2012

Nanostructural and Chemical Characterization of Complex Oxide Catalysts by Analytical Electron Microscopy

Weihao Weng
Lehigh University

Nanostructural and Chemical Characterization of Complex Oxide Catalysts by Analytical Electron Microscopy

by

Weihao Weng

Presented to the Graduate and Research Committee
of Lehigh University
in Candidacy for the Degree of
Doctor of Philosophy

in

Materials Science and Engineering

Lehigh University

January 2012

Approved and recommended for acceptance as a dissertation in partial fulfillment of the requirements for the degree of Doctor of Philosophy.

_____
Date

_____
Dissertation Director

_____
Accepted Date

Committee Members:

_____
Dr. Christopher J. Kiely

_____
Dr. Masashi Watanabe

_____
Dr. Mark A. Snyder

_____
Dr. Graham J. Hutchings

Acknowledgement

First and foremost I would like to thank my Ph.D. advisor, Dr. Christopher J. Kiely, for the opportunity to work in his research group for the past four years. The guidance, patience, encouragement and advice provided by Dr. Christopher J. Kiely are much appreciated. All his contributions of time, ideas and funding made my PhD experience productive and stimulating. It was a great honor to work with him. I would also like to acknowledge Dr. Masashi Watanabe, Dr. Mark A. Snyder and Dr. Graham J. Hutchings for their generous participation as my committee members. Additionally I acknowledge the NSF - Materials World Network Program (Grant # DMR-0709887) for providing the financial support.

I also owe thanks to my collaborators who provided me with the samples and helped me in every possible way they could. The most significant of them was Dr. Graham J. Hutchings and his group in the Department of Chemistry at Cardiff University, UK. These include Gareth Whiting, Mosaed Alhumaimess, Dr. Umacaran Sithamparappillai, Dr. Nicholas F. Dummer, Dr. Raja Al Otaibi, Dr. Marco Conte, Dr. Zhongjie Lin, Dr. Matthew Davies, Dr. Benjamin Solsona, Dr. Albert F. Carley, Dr. Jonathan K. Bartley, Dr. Stuart H. Taylor and Dr. Graham J. Hutchings. In addition I am thankful to Dr. Guojie Jin from Shanghai Research Institute of Petrochemical Technology and Dr. Carol Kiely at Lehigh University. Without them, none of the achievements in this work were possible.

I would also like to thank the faculty and staff in the Department of Materials Science and Engineering in Lehigh University. Specifically I am thankful to David

Ackland, Dr. Robert Keyse and William Mushock for their extraordinarily generous assistance in operating various electron microscopes. My thanks also go to Dr. Masashi Watanabe for his excellent short courses covering a variety of advanced electron microscopy techniques.

Finally, I want to express my deepest thanks to my family and friends. My special thanks go to my mother and father for their love, support and encouragement since I first left for college a decade ago. Most of all, I am extremely thankful for the support, patience and love of my wonderful wife, Zhenzhen. This dissertation is dedicated for them.

Table of Contents

List of Tables

List of Figures

Abstract

Complex oxide catalysts are used as heterogeneous catalysts for producing various important organic chemicals. In this thesis, three types of complex oxide catalysts prepared using novel preparation methods have been studied. Each of them has been evaluated for its catalytic performance, namely (i) the selective oxidation of *n*-butane to maleic anhydride over vanadium phosphate (V-P-O) materials; (ii) the oxidative dehydrogenation (ODH) of ethane to ethylene over niobium phosphate (Nb-P-O) materials, and (iii) the oxidation of methanol to formaldehyde over iron molybdate (Fe-Mo-O) materials. Analytical electron microscopy, X-ray diffraction and other related characterization techniques have been used to provide useful information regarding the morphology, crystallography and chemical composition of these complex oxide catalysts. The underlying aim of this work is to uncover meaningful synthesis-structure-performance relationships for these three complex catalyst systems.

Firstly, a standard methodology for generating V-P-O materials, *i.e.* the *VPD route*, has been revisited and modified. A variety of alkanes have been added during the alcohol reduction step of $VOPO_4 \cdot 2H_2O$, which were found to have a remarkable influence on the morphology and structure of the V-P-O materials produced. Either $VOHPO_4 \cdot 0.5H_2O$ or $VO(H_2PO_4)_2$ material can be produced depending on the precise alcohol:alkane volume ratio used in the reaction. In addition, the specific *order* in which the alkane and alcohol are added to $VOPO_4 \cdot 2H_2O$ during the VPD route has a dramatic effect on the morphology of the resultant precursor. Through detailed electron microscopy studies we have been able to unveil the epitaxial relationship between the $VOPO_4 \cdot 2H_2O$ and $VOHPO_4 \cdot 0.5H_2O$ crystalline phases as being $[001]^{VOPO_4 \cdot 2H_2O}$ //

$[001]^{VOHPO_4 \cdot 0.5H_2O}$ and $[100]^{VOPO_4 \cdot 2H_2O}$ // $[110]^{VOHPO_4 \cdot 0.5H_2O}$. A two-step mechanism by which the topotactic transformation from $VOPO_4 \cdot 2H_2O$ to $VOHPO_4 \cdot 0.5H_2O$ occurs has been proposed.

Secondly, three different novel synthesis routes have been explored for producing V-P-O catalysts. The first route, involving the addition of various V-P-O 'seeds' during the VPD process, was found to have a profound effect on the morphology of the V-P-O precursor and on inducing certain unexpected phase transformations. Specifically, the V-P-O seed was found to induce the transformation of $VO(H_2PO_4)_2$ to $VOHPO_4 \cdot 0.5H_2O$ in a 3-octanol solution. The second route, namely the use of a di-block copolymer template in the VPO route, was found to generate a more crystalline $VOHPO_4 \cdot 0.5H_2O$ precursor with a rhomboidal morphology, which could be activated in a much shorter time period as compared to conventional V-P-O precursors. The third route involved encapsulating the fragile V-P-O rosette-type catalysts within a mechanically protective SiO_2 shell. When used in a circulating fluidized bed reactor, these core/shell V-P-O catalysts showed a promising initial catalytic performance, but suffered a severe degradation in performance after two years-on-line. We have been able to attribute this degradation to three contributing factors; namely (i) the generation of inactive V^{5+} (*e.g.* β-$VOPO_4$) phases, (ii) densification of the SiO_2 shell and (iii) loss of core V-P-O materials. In addition, through this latter study, the novel X-ray ultramicroscopy (XuM) technique has been shown to have great potential for the non-destructive study of micron-scale catalyst particles.

Thirdly, three different niobium phosphate materials, namely the $Nb_2P_4O_{15}$, $NbOPO_4$ and $Nb_{1.91}P_{2.82}O_{12}$ phases, have been synthesized. Each of them was evaluated

for the ODH of ethane to ethylene and the oxidation of methanol to formaldehyde, respectively. It was found that the $Nb_{1.91}P_{2.82}O_{12}$ phase is the most desirable structure for ethane ODH, whereas the $NbOPO_4$ phase is more effective for methanol oxidation. The morphological and structural changes induced by both reactions on these Nb-P-O catalysts have been monitored, and correlated to the measured changes in their catalytic performance.

Finally, a highly active $Fe_2(MoO_4)_3/MoO_3$ catalyst for methanol oxidation has been prepared using a novel impregnation method. This catalyst consists of MoO_3 nanorods on which epitaxial $Fe_2(MoO_4)_3$ islands are supported. Based on our microstructural characterization studies, a mechanism has been proposed for the formation of this fascinating nanorod/island morphology which involves a thermally induced solid-state diffusive reaction accompanied by the Kirkendall effect. The excellent catalytic performance of this catalyst is thought to result from the synergistic behaviour between the active surface $Fe_2(MoO_4)_3$ islands and the underlying MoO_3 reservoir.

Chapter 1 An introduction to complex oxide catalysts

1.1 General overview of catalysis

Dating back to 19th century a number of chemical reactions were found to be affected by small amounts of materials that sustained the reaction. For example, the decomposition of hydrogen peroxide was affected by trace amounts of metal ions. Such phenomena were first described by Berzelius[1] in 1836 stating that "*I shall therefore call it the catalytic power of substances, and the decomposition by means of this power catalysis, just as we use the word analysis to denote the separation of the component parts of bodies by means of ordinary chemical forces. Catalytic power actually means that substances are able to awake affinities which are asleep at this temperature by their mere presence and not by their own affinity.*" The word 'catalysis' has appeared in human history since then.

Catalysis is involved in most industrially operated chemical processes and the majority of commodity chemicals produced depend heavily on the use of catalyst materials. It is estimated that catalysis creates more than $1 trillion in annual revenues and approximately 850,000 tonnes of catalysts were used in 2007. Nowadays a *catalyst* is usually defined as a substance that can change the rate of a chemical reaction without itself being consumed by the reaction. *Catalysis* is the phenomenon caused by the presence of a catalyst. The significant importance of the catalyst (this project is focused on positive catalysts) is known as its ability to increase the reaction rate of a specific reaction by lowering the activation energy as shown in Figure 1.1.

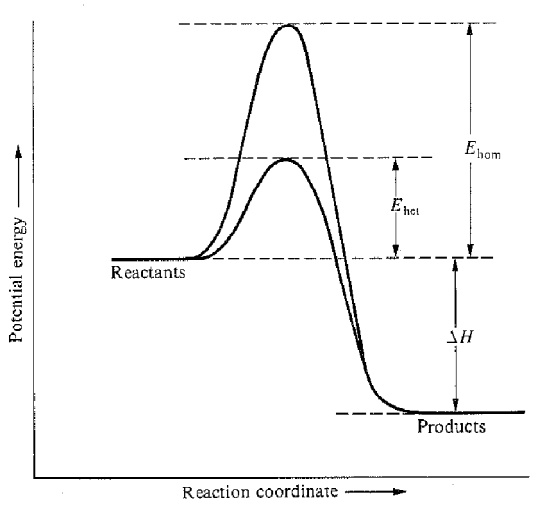

Figure 1.1 Potential energy plot against reaction coordinate for an exothermic reaction showing the lowering of the activation energy for catalyzed chemical reactions compared to uncatalyzed. [2]

Normally catalysts can be divided into two major categories:

(i) homogeneous catalysts which are in the same physical state as the reactants and no phase boundary exists, *e.g.* all are in the gas phase, and

(ii) heterogeneous catalysts which are in a different physical state from the reactants and a phase boundary exists between the catalysts and the reactants.

The most commonly used heterogeneous catalysts exist in the solid state and interact with gas and/or liquid reactants. Heterogeneous catalysts are also widely used in industrial chemical reactions because of their higher stability and ease of separation from the reactants and products. During the course of this research program, we will focus on the applications and studies of the heterogeneous catalysts.

A few important terms used to describe the performance of catalysts are *activity*, *selectivity* and *lifetime*. The *activity*, also known as the conversion, is a measure of the rate of consumption of the reactant. The *selectivity* is the proportion of the desired

product obtained after the reaction. The *lifetime* of a catalyst is the time period during which the catalyst effectively produces the desired product. Usually a catalyst consists of more than one chemical component, namely the *active phase*, *promoter* or *support*. The *active phase* is responsible for the catalytic activity, which could either be a single phase or a combination of different phases. The *promoter* is not a catalyst by itself but is used to maximize the catalytic performance of the active phase by favorably modifying the structure (*i.e.* structural promoters) or the chemistry (*i.e.* electronic promoters) of the catalyst. The *support* is usually catalytically inactive, which serves as a carrier for the active phase and promoter. It can provide a high surface area matrix where the active components can be widely spread. In an industrial catalysis process, a support having catalysts on the surface can be made into different physical forms to fit into the shape of reaction chamber in catalytic reactors. Some of the support materials can also participate in the catalytic reaction by influencing the catalytically active components.

As stated by Thomas and Thomas,[3] "*Catalysis must always be preceded by adsorption. At least one of the reactants in all heterogeneously catalyzed process must be attached for a significant period of time to the exterior surface of the solid catalyst.*" It is well known that most catalytic reactions are surface reactions occurring on the exterior surface of catalysts. Two distinct mechanistic scenarios for heterogeneous catalysis process on the surface can be concluded as: (i) the Langmuir-Hinshelwood mechanism in which both reactants A and B are adsorbed onto the surface and reacted to form a product C (Fig. 1.2(a)) and (ii) the Eley-Rideal mechanism where A is attached and is then impinged by entity B from the gas phase to form a product C (Fig. 1.2(c)).[3] It is worth mentioning that there are two different absorptions, namely the physical adsorption (or

physisorption) and the chemical adsorption (or chemisorption). Physical adsorption processes occur due to van der Waals force interaction with an enthalpy change typically in the range of 8 - 20 kJ mol^{-1}. Chemical adsorption, on the other hand, occrus because of the rearrangement of the electrons within the molecule resulting in the formation and breaking of chemical bonds, which shows an enthalpy change within 80 - 400 kJ mol^{-1}.

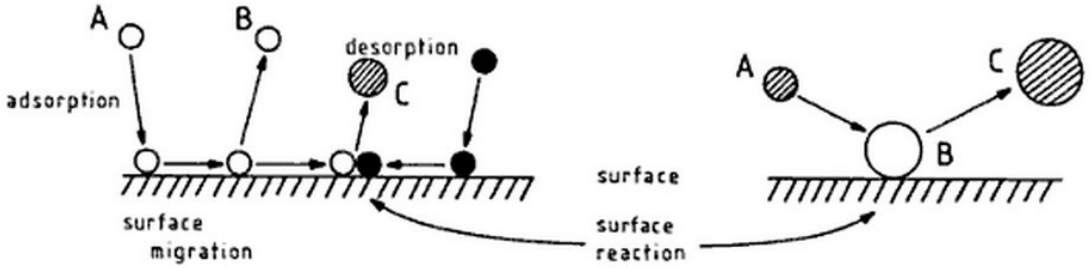

Figure 1.2 Two possible mechanistic scenarios for heterogeneous catalysis process on the surface: (a) Langmuir-Hinshelwood mechanism and (b) Eley-Rideal mechanism.[3]

In an industrial process three different types of heterogeneous catalysts are usually encountered, that is to say, metals, oxides and sulfides. In this project I will focus on the study of oxide catalysts. Specifically three distinct catalyst systems that will be discussed are:-

(a) Vanadium phosphate (V-P-O) catalysts for the selective oxidation of *n*-butane to maleic anhydride (MA),

(b) Niobium phosphate (Nb-P-O) catalysts for the oxidative dehydrogenation of ethane to ethylene and for the selective oxidation of methanol to formaldehyde,

(c) Iron molybdate (Fe-Mo-O) catalysts for the selective oxidation of methanol to formaldehyde. Each of these specific catalyst systems will be reviewed in the following sub-section.

1.2 Vanadium phosphate (V-P-O) catalyst system

1.2.1 The selective oxidation of *n*-butane to maleic anhydride over V-P-O catalysts

The selective oxidation of *n*-butane (C_4H_{10}) to maleic anhydride ($C_4H_2O_3$) using vanadium phosphate (V-P-O) catalysts was discovered in late 1960's[4] and is shown in equantion 1.1. It has been extensively studied over the intervening decades. Maleic anhydride (MA) is a highly reactive and versatile raw chemical, which is largely used in the production of unsaturated polyester resins (UPR). These resins are employed primarily in the automobile, boating and construction industries. Maleic anhydride can also be used in the production of paints, coatings, lubricant additives, agricultural chemicals, maleic acid, copolymers, Lycra and fumaric acid. The chemical reaction (eqn. 1.2) of the selective oxidation of *n*-butane to maleic anhydride involves the removel of 8 hydrogen atoms and insertion of 3 oxygen atoms. Since this oxidation reaction is exothermic and is accompanied by other non-selective side reactions, such as those shown in equations 1.3 and 1.4, it is imperative to use an efficient catalyst (*i.e.* V-P-O) that increases the selectivity as well as the activity of the main reaction (eqn. 1.2).

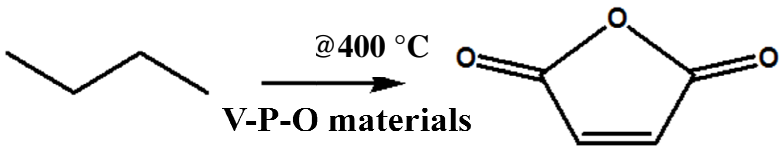

n-butane maleic anhydride (1.1)

$$C_4H_{10} + 3.5\ O_2 \rightarrow C_4H_2O_3 + 4H_2O \quad (1.2)$$

$$C_4H_{10} + 6.5\ O_2 \rightarrow 4CO_2 + 5H_2O \quad (1.3)$$

$C_4H_{10} + 4.5\ O_2 \rightarrow 4CO + 5H_2O$ (1.4)

In industrial processes, this *n*-butane oxidation is normally carried out in a fixed bed or fluidised bed reactor[5] in the presence of a V-P-O catalyst. The starting V-P-O catalyst is usually in the form of a catalyst precursor, which is known as the vanadyl hydrogen phosphate hemihydrate ($VOHPO_4 \cdot 0.5H_2O$). Under the reaction conditions the $VOHPO_4 \cdot 0.5H_2O$ precursor material is transformed *in-situ* into the active V-P-O catalyst.[6] An alternative way to prepare the material is to calcine the $VOHPO_4 \cdot 0.5H_2O$ precursor in air or nitrogen and then transfer the active V-P-O catalyst into the reactor. The typical catalytic reaction conditions employed are at temperature 400 -450 °C with a 1-2 mol% *n*-butane/air feed in a gas hourly space velocity (GHSV) regime of 1000 - 3000 h^{-1}. The typical activation time for the catalyst precursor to transform *in-situ* to the active catalyst is around 100 hours, which can be monitored by following the catalytic performance (*i.e.* the selectivity and conversion) of the V-P-O catalyst until it reaches a steady state value (or a plateau). The typical expected selectivity to MA of a V-P-O catalyst is around 65%, with a *n*-butane conversion of 75 %. Hence the yield to MA (i.e. the product of selectivity and conversion) is only about 50%, which means there is plenty of scope for improving the catalytic performance of V-P-O materials.

It is widely accepted that the V-P-O catalyst precursor is the $VOHPO_4 \cdot 0.5H_2O$ phase, whereas there is a lively ongoing debate on the precise nature of the active phase and hence the active sites present in V-P-O catalysts for *n*-butane oxidation. Some researchers believe that the active phase is the crystalline vanadyl pyrophosphate phase ($(VO)_2P_2O_7$),[7,8] while others attribute the active phase to a combination of the $(VO)_2P_2O_7$ (V^{4+}) phase and small amounts of other V^{5+} phases (*i.e.* $VOPO_4$ phases).[6,9] In

relation to the reaction mechanism, most researchers agree that it follows a surface redox or Mars-van-Krevelen mechanism.[10,11] This involves the weakly bonded lattice oxygen anions at the V-P-O surface being lost and incorporated into *n*-butane molecules during the oxidation reaction cycle. Then the reduced V-P-O surface will be re-oxidized by the gaseous oxygen molecules in order to maintain charge neutrality in the crystal structure. A more detailed review concerning the determination of active phase and the elucidation of reaction mechanisms will be presented in sub-section 1.2.4 and 1.2.5, respectively.

1.2.2 Preparation of V-P-O catalyst precursors

Most standard preparation methods, in which a vanadium source is reacted with phosphoric acid in the presence of a reducing agent, tend to form either $VOHPO_4 \cdot 0.5H_2O$ (the hemihydrate phase) or $VO(H_2PO_4)_2$ (the E-phase), or sometimes a mixture of the two materials. It is generally accepted that the best catalysts are based on $VOHPO_4 \cdot 0.5H_2O$ precursors which under *in-situ* activation conditions form a catalyst mainly comprising the active $(VO)_2P_2O_7$ (pyrophosphate) phase.[6,12-14] Since the transformation of the precursor to the final catalyst is topotactic in nature, the morphology of the precursor is of crucial importance in determining the eventual catalyst morphology and its performance following activation.[6], [15] Hence the preparation of V-P-O catalyst precursors is very important and is worth some discussion here. Based on the seminal work of Horowitz *et al.*[16] and Johnson *et al.*,[15] three standard preparation methodologies have been developed as outlined in equations 1.5, 1.6 and 1.7.[17]

VPA Route

$$V_2O_5 + HCl \xrightarrow[2.\ H_3PO_4]{1.\ \Delta,\ 2h} VOHPO_4.\tfrac{1}{2}H_2O \quad (1.5)$$

VPO Route

$$V_2O_5 + H_3PO_4 + \text{alcohol} \xrightarrow{\Delta,\ 16h} VOHPO_4.\tfrac{1}{2}H_2O \quad (1.6)$$

VPD Route

$$V_2O_5 + H_3PO_4 \xrightarrow[\Delta,\ 16h]{H_2O} VOPO_4.2H_2O \xrightarrow[\Delta,\ 16h]{\text{alcohol}} VOHPO_4.\tfrac{1}{2}H_2O \quad (1.7)$$

Typically in a first step, $VOHPO_4 \cdot 0.5H_2O$ is synthesized from vanadium oxide and phosphoric acid under reflux conditions in either aqueous HCl (***VPA route***, eqn. 1.5) or alcohol (*e.g.* isobutanol, ***VPO route,*** eqn. 1.6), at a reaction temperature of about 100ºC. The latter VPO route is currently the technology of choice used to produce industrial V-P-O catalysts. In an alternative method (known as the ***VPD route,*** eqn. 1.7), the vanadyl phosphate dihydrate phase ($VOPO_4 \cdot 2H_2O$) is produced from the reaction of V_2O_5 and H_3PO_4, and is then reduced with an alcohol at *ca.* 100-110ºC to form the $VOHPO_4 \cdot 0.5H_2O$ precursor.

The precursors obtained from the VPA route result in a block-type morphology with a low surface area (~ 4 m^2g^{-1}), as shown in Figure 1.3(a) and Table 1.1.[12] The $VOHPO_4 \cdot 0.5H_2O$ precursors produced from the VPO route, on the other hand, are usually found to have a rhomboidal shape platelet-type morphology (Fig. 1.3(b)) when isobutanol is used as the reducing agent.[12] Its surface area is higher than that of the VPA route material, at around 14 m^2g^{-1}. When a mixture of isobutanol and benzyl alcohol is used as the reducing agent, a rosette-type morphology is observed in the precursor material (Fig. 1.3(c)).[16] The VPD route is a more complicated method than the other two

methods. Depending on the choice of alcohols (*i.e.* primary alcohols, secondary alcohols and tertiary alcohols) used in the reduction step of $VOPO_4 \cdot 2H_2O$, three different morphologies can be generated.[18] A primary alcohol (*e.g.* octan-1-ol) can give rise to the formation of a rosette-type $VOHPO_4 \cdot 0.5H_2O$ (Fig. 1.3(c)), whereas a secondary alcohol (*e.g.* octan-2-ol) leads to the production of the $VOHPO_4 \cdot 0.5H_2O$ with a typical rhomboidal shaped platelet-type morphology. Surprisingly adding a tertiary alcohol (*e.g.* octan-3-ol) in the reduction step of $VOPO_4 \cdot 2H_2O$ generates a blocky $VO(H_2PO_4)_2$ material (also known as the E-phase) that is highly selective to MA but not very active.[8] A detailed study of materials produced by the VPD method using a mixture of alcohols and alkanes will be presented in Chapter 4 of this thesis.

In all cases, irrespective of the preparation route chosen, the hemihydrate ($VOHPO_4 \cdot 0.5H_2O$) precursor material is then transformed in a final step to the active catalyst *in-situ* under reaction conditions (1.5% *n*-butane in air, ~400ºC). The typical catalytic performance characteristics of V-P-O catalysts prepared by the VPA, VPO and VPD methods are summarized in Table 1.1.[12] All three V-P-O catalysts have a similar specific activity (even though they exhibit different activities and selectivities), which implies that the surface active structure of the activated catalysts prepared by these three standard preparation routes are rather similar.

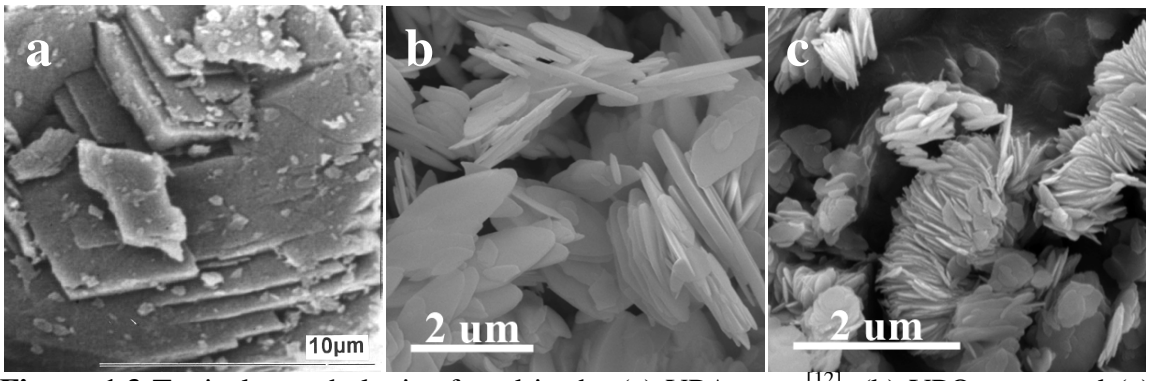

Figure 1.3 Typical morphologies found in the (a) VPA route[12], (b) VPO route and (c) VPD route catalyst materials.

Table 1.1 Typical "benchmark' catalytic performance data from the VPA, VPO and VPD route materials.[12]

Preparation Route	Conversion (%)	Selectivity (%)	Surface Area (m^2g^{-1})	Specific Activity (mol MA $m^{-2}h^{-1}$)
VPA	11	51	4	1.24×10^{-5}
VPO	27	52	14	1.35×10^{-5}
VPD	62	64	43	1.19×10^{-5}

In consideration of the surface area as a key factor in determining the activity of the V-P-O catalysts, a number of novel approaches specifically aiming at preparing higher surface area V-P-O catalysts have been investigated. The first approach was to ball mill the catalyst precursor before the *in-situ* activation. Hutchings *et al.*[19] ball milled $VOHPO_4 \cdot 0.5H_2O$ precursors in the presence of cyclohexane (solvent) and poly-12-hyroxystearic acid (dispersant) and prepared a high surface area V-P-O catalyst ($40m^2g^{-1}$). Although the catalysts produced were particularly active under fuel-rich reaction condition, they gave rise to a low MA selectivity. Later Ayub *et al.*[20] tried a similar method by ball milling Bi promoted $VOHPO_4 \cdot 0.5H_2O$ in ethanol and air, respectively. They found that the ball milling method can increase the specific surface area, but unfortunately it also destroys the crystallinity of the activated catalyst and hence reduces

the MA yield. Recently Taufiq-Yap *et al.*[21] reported that ball milling the $VOHPO_4 \cdot 0.5H_2O$ precursor produced from the VPD method can control the amount of oxygen species (O^-) extracted from the V-P-O, which participate in the *n*-butane oxidation. They deduced that surface area of the V-P-O catalysts can be increased but a large amount of O^- can reduce the conversion rate.

The second approach that has widely been investigated is to disperse the active V-P-O catalyst on a high surface area support material. Most of the methodologies tried in this respect have been unsuccessful, since the support seems to degrade the performance of the V-P-O catalyst.[22] In an early effort by Overbeek *et al.*[23], they supported V-P-O catalyst on TiO_2 by depositing a mixture solution of vanadium ions and phosphate-ions onto TiO_2. The V-P-O material generated was found to be amorphous, and the active phase interacted strongly with the TiO_2 support. This supported V-P-O/TiO_2 catalyst only showed a better activity at low temperatures (*i.e.* 200 °C) due to the higher number of oxygen atoms shared between vanadium and the TiO_2 support. At high conversion levels (> 50%) the V-P-O/TiO_2 catalyst had a low selectivity effectively making it useless. Many silica-based materials have tried as supports, which are purported to exhibit improved heat transfer characteristics, increased mechanical strength and a higher surface area-to-volume ratio of the active V-P-O component. The use of high surface area silica gels [24] and fumed silica [25] supports has also been investigated. In most cases, when compared to the unsupported $(VO)_2P_2O_7$ crystals, the MA selectivity is severely impaired for these silica supported V-P-O materials.[24] Ledoux *et al.*[26] made a breakthrough by supporting V-P-O on heat-conductive non-oxide ceramic materials (*i.e.* β-SiC, Si_3N_4 and BN). The β-SiC supported V-P-O materials in particular showed higher MA selectivity

and MA yield than unsupported V-P-O in a fixed bed reactor. This enhancement in catalytic performance was probably due to the fast heat transfer ability of the ceramic support which can avoid the formation of hot spots in the V-P-O, which if formed could further oxidize MA into CO and CO_2.

Another approach to generate a high surface area V-P-O catalyst is based on the fact that $VOPO_4 \cdot 2H_2O$ has a layer-type structure that can accommodate various type of organic molecules between layers. Kamiya and co-workers[27-30] have reported the intercalation and subsequent exfoliation of $VOPO_4 \cdot 2H_2O$ crystals using primary (*e.g.* 1-butanol and ethanol) and secondary (*e.g.* 2-butanol) alcohols. The layer-type $VOPO_4 \cdot 2H_2O$ material was heated at a low temperature in the alcohol to generate exfoliated $VOPO_4 \cdot 2H_2O$ sheets, and then was reduced and fractured to yield a nanoscale $VOHPO_4 \cdot 0.5H_2O$ precursor. The nanocrystalline $(VO)_2P_2O_7$ catalyst derived from this nanoscale precursor had a high surface area (>40 $m^2 g^{-1}$), and exhibited a MA selectivity of 78% as well as a conversion as high as 85%. [31]

Some transition metal cations, when incorporated in the $VOHPO_4 \cdot 0.5H_2O$ material, have been found to promote the catalytic activity mainly by ensuring high surface area V-P-O catalysts are obtained.[32] These promoted catalysts were generated by adding transition metal salts with V_2O_5 in the first step of the VPA route. They can also be added through impregnating the $VOHPO_4 \cdot 0.5H_2O$ precursor with metal salts in a solvent using the incipient wetness approach. Most of the promoted V-P-O materials produced have exhibited a higher surface area as compared to the un-promoted V-P-O (Fig. 1.4). Many cation dopants were found to act as a structural promoter. For example, the addition of certain dopant cations (*e.g.* Zr, Cr and Zn) can prevent the formation of

deleterious phases, such as $VO(H_2PO_4)_2$ that if present can lead to the surface area loss. It should be noted that the $VO(H_2PO_4)_2$ phase is water soluble so it can be removed by water extraction. However, Mo, as a dopant in the $(VO)_2P_2O_7$ phase, can significantly improve the specific activity of V-P-O catalysts, which is attributable to the electronic promoting effect. Due to the presence of Mo, it is easier for MA to desorb from the surface of V-P-O and/or for lattice oxygens to be inserted into the reaction intermediates.[32]

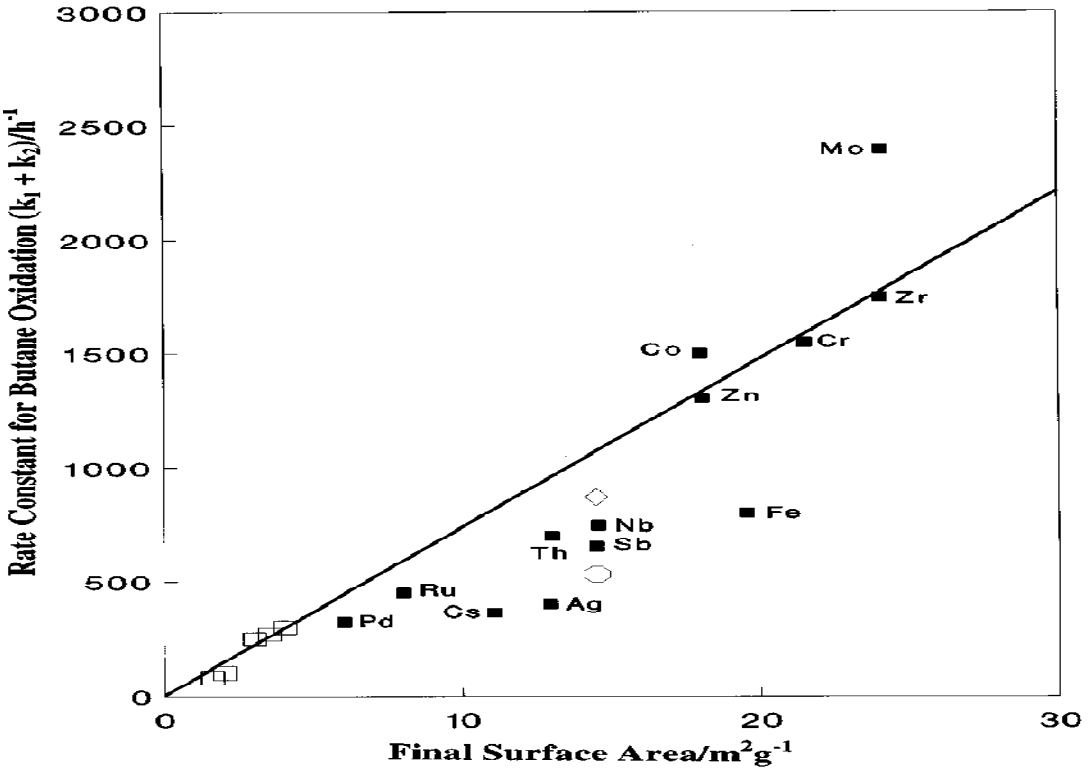

Figure 1.4 Plot of the rate constant for the *n*-butane oxidation versus the surface area of the activated V-P-O. The open symbols represent non-promoted V-P-O and closed symbols represent promoted V-P-O. The doped V-P-O materials were prepared using the VPA route.[32]

Another transition metal cation- Co is not considered to be the structural promoter as such. It can be introduced into the crystal lattice of the $(VO)_2P_2O_7$ phase at low concentrations (1-5 at%) and has been found to increase the intrinsic activity of the doped

V-P-O catalyst through interacting with the possibly active disordered V-P-O phase.[33] A few other metal cations (*e.g.* Fe) can form a solid solution with $(VO)_2P_2O_7$ in the form of $((VO)_xM_{1-x})_2P_2O_7$ where M is the metal dopant.[34,35] This solid solution was found to be active and selective for *n*-butane oxidation.[36] More details about the promoting effect of transition cations on the activated V-P-O catalysts, can be found in references [18,19,37].

1.2.3 Crystalline phases encountered in the preparation and activation stages of V-P-O catalysts.

During the preparation of V-P-O catalyst precursors and their subsequent activation under the reaction conditions, a number of different V-P-O phases can be formed. Many well characterized, crystalline vanadium phosphate phases have been identified whose structure and catalytic properties have now been well documented.[17][18] Some of the most widely studied components are the V^{5+} vanadyl orthophosphates (α-, β-, γ-, δ-, ε- and ω-$VOPO_4$, $VOPO_4 \cdot H_2O$ and $VOPO_4 \cdot 2H_2O$), and the V^{4+} vanadyl hydrogen phosphates ($VOHPO_4 \cdot 4H_2O$, $VOHPO_4 \cdot 0.5H_2O$, $VO(H_2PO_4)_2$), vanadyl pyrophosphate ($(VO)_2P_2O_7$) and vanadyl metaphosphate ($VO(PO_3)_2$).[17] A Table summarizing the crystallographic and morphological data on some of these standard phases is shown in Table 1.2. It is worth mentioning that most V-P-O phases are sensitive to the electron beam and may be amorphosized within seconds. Amongst these V-P-O phases, the two most important phases, which will be encountered many times in this dissertation, are the $VOHPO_4 \cdot 0.5H_2O$ (V^{4+}) and $(VO)_2P_2O_7$ (V^{4+}) phases.

Table 1.2 Crystallographic and morphological data on standard V-P-O phases.[12]

Compound	Crystal group[a]	Lattice parameters[a]/Å	Moisture sensitive[b]	Morphology[c,d]	Electron beam sensitivity[d]	Potential for HREM studies
$VOHPO_4 \cdot 1/2H_2O$ (hemihydrate)	Orthorhombic (Pmmn)	a = 7.416 b = 9.592 c = 5.689	No	Highly dependent on precise preparation route	High	Yes
α_I-$VOPO_4$	Tetragonal (P4/nmm)	a = 6.200 c = 4.110	Yes (45 min for hydration)	Platelets with (001) normal—Fig. 1a (TEM: featureless platelets)	High	Yes
α_{II}-$VOPO_4$	Tetragonal (P4/nmm)	a = 6.014 c = 4.434	Yes (10 h for hydration)	Platelets with (001) normal—Fig. 1b (TEM: platelets with distinctive surface texture)	High	Yes
β-$VOPO_4$	Orthorhombic (Pnma)	a = 7.770 b = 6.143 c = 6.965	No	Dense agglomerates of randomly oriented angular platelets—Fig. 1c	Low	Yes
γ-$VOPO_4$	Monoclinic (space-group unknown)	a = 9.64 b = 15.33 c = 16.62 β = 95.04°	Yes (3 h for hydration)	Dense agglomerates of platelets showing "desert rose" type structure—Fig. 1d	Extreme	No
δ-$VOPO_4$	Orthorhombic (space-group unknown)	a = 6.260 b = 6.420 c = 9.090	Yes (3 h for hydration)	Random clusters of irregular platelets—Fig. 1e (TEM: platelets frequently exhibit parallel "slashes")	Extreme	No
$(VO)_2P_2O_7$ (pyrophosphate)	Orthorhombic ($Pca2_1$)	a = 7.725 b = 9.576 c = 16.576	No	Facetted needle-like crystals—Fig. 1f Basal (100) plane often exposed	Moderate	Yes

As can be seen from Table 1.2, the structural complexity of the V-P-O catalyst system is potentially very high, and the identification of each V-P-O phase using electron diffraction and X-ray diffraction is challenging. In view of this, an atlas of various standard V-P-O phases (*e.g.* $VOPO_4 \cdot 2H_2O$, $VOHPO_4 \cdot 0.5H_2O$, $(VO)_2P_2O_7$, $VO(PO_3)_2$, $VO(H_2PO_4)_2$, α-, β-, δ- and ω-$VOPO_4$) has been built by Sajip.[18] In this atlas, the structural data as well as the simulated diffraction patterns (*i.e.* electron diffraction patterns and X-ray diffraction patterns) can be easily found, making it a very important reference database for the study of V-P-O materials. A typical example of an atlas entry for the $VOHPO_4 \cdot 0.5H_2O$ phase is shown in Figure 1.5. The atomic model and electron diffraction patterns were generated using CaRine software (v3.1). The $VOHPO_4 \cdot 0.5H_2O$ phase is composed of $VOPO_4$ sheets that are connected along the [001] direction through

interlayer water molecules. Each $VOPO_4$ sheet consists of pairs of face sharing VO_6 octahedra that are interlinked by PO_4 tetrahedra as shown in Figure 1.5(a).[15,38,39]

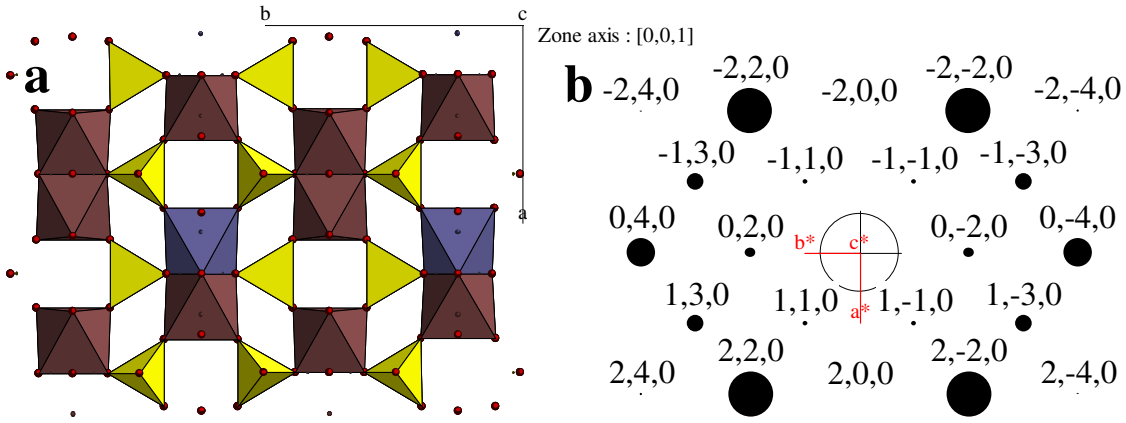

Figure 1.5 (a) Atomic model of $VOHPO_4 \cdot 0.5H_2O$ viewed along the [001] projection and (b) simulated and indexed electron diffraction patterns of the [001] projection of $VOHPO_4 \cdot 0.5H_2O$. (Brown octahedra represent VO_6 octahedra; Yellow tetrahedra represent PO_4 tetrahedra.)[18]

1.2.4 Determination of the active phase and the surface composition in the V-P-O catalyst system

Various structures and polymorphs are observed in the V-P-O catalyst system, which can show different selectivities and activities for *n*-butane oxidation to MA. This makes the determination of the active phase in V-P-O catalyst system rather complicated. Most research groups now agree that $(VO)_2P_2O_7$ is the most selective and active phase amongst the various V-P-O phases. Both Shimoda *et al.*[7] and Sananes *et al.*[8] claimed that V-P-O catalysts composed of pure $(VO)_2P_2O_7$ exhibit far superior catalytic performances than other V-P-O phases (*e.g.* $VO(H_2PO_4)_2$ and $VOPO_4$ polymorphs). Guliants *et al.*[40] agreed, stating that $(VO)_2P_2O_7$ with a degree of stacking order is the most active phase. Later Guliants *et al.*[41] showed that the (100) basal plane of the $(VO)_2P_2O_7$ (V^{4+}) structure is the most active plane for *n*-butane oxidation. However Volta

et al.[9] believed that the presence of some V^{5+} ions on the surface of V-P-O is closely related to its catalytic performance. The importance of V^{5+} species for the *n*-butane oxidation by V-P-O catalysts is further supported by Aït-Lachgar *et al.*,[42] who observed an increase of the selectivity to MA with oxidation time for $(VO)_2P_2O_7$, and attributed this improved selectivity to the presence of the bulk V^{4+} and surface V^{5+} species, which cause structural defects in $(VO)_2P_2O_7$. These V^{5+} species could be crucial for the insertion of oxygen into *n*-butane and the formation of MA. Zhanglin *et al*.[43] pointed out that the best V-P-O catalyst is composed of a small number of V^{5+} ions that are contained in the (100) plane of $(VO)_2P_2O_7$. Using *in-situ* Raman spectroscopy Hutchings *et al*.[44] proposed that a mixture of V^{4+} and V^{5+} phases in V-P-O is beneficial for its catalytic performance. However the exact mechanism for this is not well understood. Koyano *et al*.[45] suggested that the δ-$VOPO_4$ phase can participate in the surface redox reaction of $(VO)_2P_2O_7$ during *n*-butane oxidation. Actually both the γ- and δ-$VOPO_4$ phases were found to be catalytically active for the oxidation of *n*-butane to MA, but the particular polymorphs however are rarely present in the V-P-O catalysts after being activated and used for hundreds of hours.[46,47] Both Ebner *et al*.[48] and Hutchings *et al*.[14] proposed that a redox couple composed of V^{4+}/V^{5+} can be formed on the surface of V-P-O crystallites. Hutchings and co-workers[14] further concluded that this V^{4+}/V^{5+} couple is the active center for the selective oxidation of *n*-butane to maleic anhydride, which can be found on a range of V-P-O materials produced by either the VPA, VPO or VPD route.

However Gai *et al*.[49] have proposed that the O^{2-} anion vacancies on the surface of $(VO)_2P_2O_7$, which are formed under fuel rich conditions (*e.g. n*-butane only) could be the active site for the *n*-butane oxidation. Using TEM Schlögl *et al*.[50] observed that a

thin surface adlayer of amorphous material is always present on both the prismatic edges and basal planes of active $(VO)_2P_2O_7$ materials. This thin nanoscale amorphous adlayer was believed to be the termination of the $(VO)_2P_2O_7$ crystallites and a good candidate for the localization of the active sites. The existence of such an amorphous adlayer was first inferred by Hutchings *et al.*[44] using *in-situ* Raman spectroscopy during the pre-treatment of the catalyst precursor. This amorphous layer existing on the surface of the active crystalline $(VO)_2P_2O_7$ phase has since been observed in many other TEM studies.[51] In light of the observation that the active component is possibly an amorphous vanadium phosphate phase, Hutchings *et al.*[52] synthesized a completely amorphous vanadium phosphate material by adding supercritical CO_2 as an antisolvent into the vanadium phosphate/alcohol solution. The prepared catalyst consisted of discrete amorphous spherical particles which showed no crystalline features (*i.e.* diffraction contrast, lattice fringes *etc.*). When tested as catalysts for *n*-butane oxidation, this amorphous vanadium phosphate catalyst does not require an activation period to achieve the steady state performance and shows a higher intrinsic activity as compared to the standard V-P-O materials. Unlike the standard V-P-O catalysts, the amorphous V-P-O materials remained wholly amorphous during the activation and had a low surface area of 4 m^2g^{-1}. However other research groups (*e.g.* Wachs *et al.*[41]) claimed that a V-P-O catalyst with better selectivity and steady-state performance can be obtained if this amorphous layer is removed or re-crystallized.

Another important factor that is closely related to the catalytic behavior of the produced $(VO)_2P_2O_7$ catalyst is the surface P/V ratio. Aided by X-ray photoelectron spectroscopy (XPS) and low-energy ion scattering (LEIS), both of which are surface

sensitive analysis techniques, researchers were able to reveal the surface composition of the working $(VO)_2P_2O_7$ catalyst. Although the stoichiometric P/V ratio should be unity in $(VO)_2P_2O_7$, most of the surface studies have shown that there is a surface P enrichment in $(VO)_2P_2O_7$. In an early study performed by Garbassi *et al*.,[53] it was found that the specific conversion increases by an order of magnitude when the P/V ratio is slightly over 1. Such an excess in P does not result in structural changes and could delay the over-oxidation of V^{4+}. Later Harrouch Batis *et al*.[46] reported a surface P/V ratio as high as 3 in the catalyst, whereas the catalytic performance was found to drop after the P/V ratio exceeds 2.3. Delichère *et al*.[54] measured the surface of working $(VO)_2P_2O_7$ catalysts using XPS and LEIS, and reported that the surface P/V ratio is within the range of 1.5-1.9. They further pointed out that such a high P/V ratio could be due to the possible covering of the surface V dimers by carbonaceous species or the presence of V vacancies within the surface amorphous layer. In order to avoid such carbonaceous species, Jansen *et al*.[55] generated a $(VO)_2P_2O_7$ material using the aqueous VPA route and applied a surface cleaning process before the LEIS experiment. They observed that only 15% of surface P and V atoms can be detected by LEIS before cleaning, which indicates that most of the surface is covered by some carbonaceous species. They also detected a P/V ratio of 2 on the surface, which was attributed to the possible presence of α_{II}-$VOPO_4$ with $(VO)_2P_2O_7$. This finding is consistent with the previous claim that the a V^{4+}/V^{5+} couple is the active site in this catalyst system.

1.2.5 The $VOHPO_4 \cdot 0.5H_2O$ to $(VO)_2P_2O_7$ phase transformation

During the preparation and activation of V-P-O catalysts, various V-P-O phases can be formed or transformed from other V-P-O phases. Basically two different types of phase transformation can occur. Type I transformations occur between phases of two different vanadium valence states whereas type II transformations occur between phases having the same vanadium valence state. The type I transformations often occur in a reducing or oxidizing environment. A typical example is the phase transformation of $VOPO_4 \cdot 2H_2O$ (V^{5+}) to $VOHPO_4 \cdot 0.5H_2O$ (V^{4+}) by the reducing agent in the VPD route.[12] Also $VOHPO_4 \cdot 0.5H_2O$ can be transformed into V^{5+} phases, for example the thermal dehydration of $VOHPO_4 \cdot 0.5H_2O$ in air above 350 °C can form δ-$VOPO_4$.[56] A typical type II transformation occurs when $VOHPO_4 \cdot 0.5H_2O$ (V^{4+}) is converted to $(VO)_2P_2O_7$ (V^{4+}) during the activation process,[6,15,38] which is probably the most important phase transformation in the V-P-O catalyst system. It describes how the active $(VO)_2P_2O_7$ phase is produced from the $VOHPO_4 \cdot 0.5H_2O$ precursor.

The majority of researchers agree that $VOHPO_4 \cdot 0.5H_2O$ transform topotactically to $(VO)_2P_2O_7$. Johnson *et al.*[15] and Bordes *et al.*[38] noted that the structure of $VOHPO_4 \cdot 0.5H_2O$ is closely related to that of $(VO)_2P_2O_7$, whereby the *ab* plane of $VOHPO_4 \cdot 0.5H_2O$ is topologically similar to the *bc* plane of $(VO)_2P_2O_7$. Recognizing the similarity they suggested that a topotactic transformation could occur between the two phases. Using a combination of characterization techniques (*i.e.* XRD, Raman spectroscopy, XPS and ^{31}P NMR), Volta *et al.*[9] studied the activation of the $VOHPO_4 \cdot 0.5H_2O$ precursor, and observed two parallel transformation routes occurring in this activation, namely (i) the oxidation of $VOHPO_4 \cdot 0.5H_2O$ to $VOPO_4$ phases (α_{II}-, γ-

and δ-$VOPO_4$) and the subsequent reduction to $(VO)_2P_2O_7$ and (ii) the direct dehydration of $VOHPO_4 \cdot 0.5H_2O$ to $(VO)_2P_2O_7$. This finding was corroborated by Kiely *et al.*[6] using electron microscopy techniques on a series of V-P-O precursors activated for different time periods. They detected that in the interior of the platelet, $VOHPO_4 \cdot 0.5H_2O$ first transformed to δ-$VOPO_4$ embedded in a disordered matrix and then subsequently transformed to the final active $(VO)_2P_2O_7$ phase. They also observed a direct topotactic transformation from [001] $VOHPO_4 \cdot 0.5H_2O$ (Fig. 1.6(a)) to [100] $(VO)_2P_2O_7$ (Fig. 1.6(c)) occurring at the periphery of the platelet.

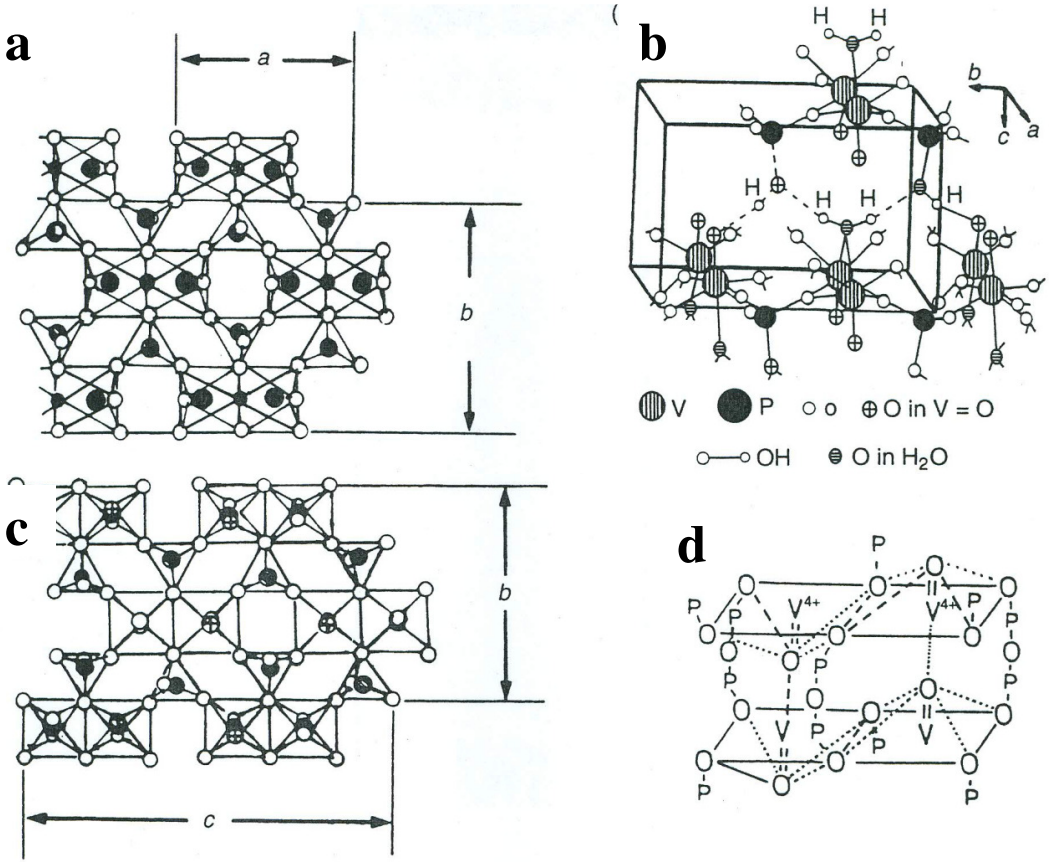

Figure 1.6 Schematic diagrams of (a) the [001] projection of the $VOHPO_4 \cdot 0.5H_2O$ phase, (b) a projection close to the (100) direction of $VOHPO_4 \cdot 0.5H_2O$ showing the interlayer water molecules, (c) the [001] projection of the $(VO)_2P_2O_7$ phase and (d) a projection close to the (021) direction of $(VO)_2P_2O_7$.[6]

The topotactic phase transformation process can be visualized as face-sharing VO_6 octahedra in $VOHPO_4 \cdot 0.5H_2O$ become edge-sharing and then the escape of interlayer water molecules from the structure leads to the collapse of the $VOHPO_4 \cdot 0.5H_2O$ structure. After some re-orientation of the VO_6 octahedra and PO_4 tetrahedra, the $(VO)_2P_2O_7$ structure is produced. The epitaxial orientation relationship between the $VOHPO_4 \cdot 0.5H_2O$ and $(VO)_2P_2O_7$ phase is shown below,

$$[001]^{VOHPO_4 \cdot 0.5H_2O} \; // \; [100]^{(VO)_2P_2O_7}$$

$$[010]^{VOHPO_4 \cdot 0.5H_2O} \; // \; [010]^{(VO)_2P_2O_7}$$

Such an epitaxial relationship was also corroborated by Duvauchelle *et al.*[57] who heated the $VOHPO_4 \cdot 0.5H_2O$ precursor in a flow of N_2 gas at various temperatures for different time periods. They also proposed such relationship. Recently Imai *et al.*[58] reported that nano-sized $VOHPO_4 \cdot 0.5H_2O$ crystallites can be transformed into nanocrystalline $(VO)_2P_2O_7$ via an amorphous intermediate in a 1.5% *n*-butane/17% O_2/81.5% He reaction environment. No $VOPO_4$ phases were formed during this transformation, which was attributed to the small size of the $VOHPO_4 \cdot 0.5H_2O$ crystallites resulting in a more uniform dehydration process.

Another important phase transformation is that of $VOPO_4 \cdot 2H_2O$ to $VOHPO_4 \cdot 0.5H_2O$ which occurs in the VPD route. Unfortunately, this particular transformation has not been well studied. O'Mahony *et al.*[59,60] used *in-situ* XRD and *ex-situ* XPS to monitor the formation of $VOHPO_4 \cdot 0.5H_2O$ produced by the reaction of V_2O_5 and H_3PO_4 (*i.e.* the VPO route). They observed that $VOPO_4 \cdot 2H_2O$ and $VOPO_4 \cdot H_2O$ phases are formed at short reaction times and subsequently transformed into $VOHPO_4 \cdot 0.5H_2O$. They did not however propose a detailed structural mechanism for the

phase transformation of $VOPO_4 \cdot 2H_2O$ to $VOHPO_4 \cdot 0.5H_2O$. In section 4.4 of this thesis, this particular phase transformation will be discussed in some detail.

1.2.6 Comments on the reaction mechanism of the selective oxidation of *n*-butane to maleic anhydride over V-P-O catalysts

Previously in section 1.2.1 it was noted that the *n*-butane oxidation over V-P-O follows a Mars-van-Krevelen mechanism. However this is only one part of this complicated story. The other aspect is how the *n*-butane gets oxidized into maleic anhydride through the coordinated abstraction of 8 H atoms and insertion of 3 O atoms during the reaction cycle. A variety of reaction mechanisms have been proposed, such as the redox couple mechanism suggested by Centi *et al*.,[61] the consecutive alkoxide route proposed by Zhanglin *et al*.,[43] and the redox Langmuir-Hinshelwood model suggested by Bej and Rao[62]. One of the most plausible reaction mechanisms for the selective oxidation of *n*-butane is the consecutive alkenyl mechanism, which has been proposed and modified by many research groups.[11,63,64][65][66][67] A schematic diagram of this reaction mechanism is shown in Figure 1.7.[65] Starting from the *n*-butane, intermediates such as 1-butene, 1-3 butadiene, dihydrofuran and asymmetric lactone are formed consecutively, and the MA is produced in the final step. However the exact reaction mechanism for *n*-butane oxidation is still an open issue due to its complexity. It will not be discussed in detail here, but the interested readers can get more details concerning the reaction mechanism of *n*-butane oxidation to MA in references. [11,63,64][65][66][67]

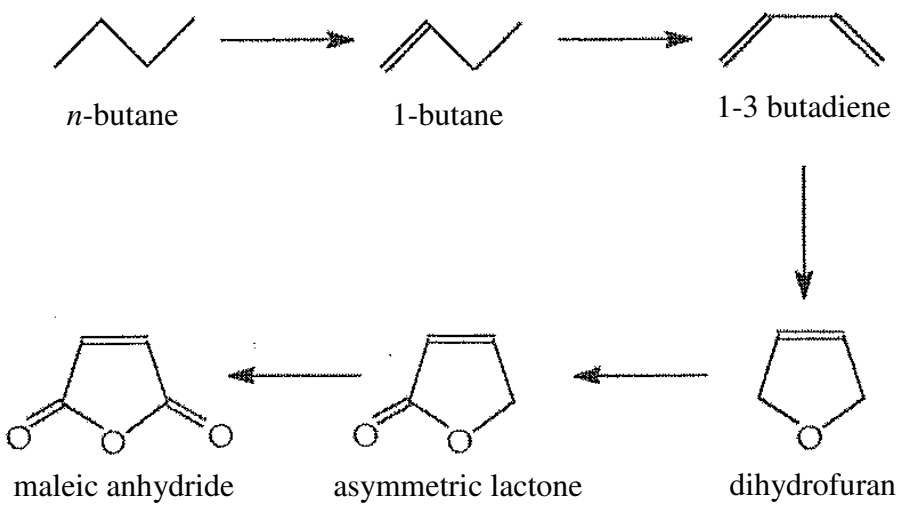

Figure 1.7 The consecutive alkenyl mechanism for the selective oxidation of *n*-butane to maleic anhydride proposed by Cleaves *et al.*[37,65]

In this thesis, two chapters (*i.e.* Chapters 4 and 5) will be focused on the study of the V-P-O catalyst system. Specifically Chapter 4 aims for obtaining a better understanding of the VPD route, while Chapter 5 will discuss some novel preparation routes for the synthesis of the $VOHPO_4 \cdot 0.5H_2O$ precursor. Further details about the study to be performed on V-P-O system can be found in section 1.5.

1.3 Niobium phosphate (Nb-P-O) catalyst system

Vanadium phosphate (V-P-O) materials are known to be effective catalysts for the selective oxidation of *n*-butane to maleic anhydride and have been used commercially since 1960's for the production of maleic anhydride worldwide[68]. They represent the most well studied heterogeneous complex oxide catalyst. Thousands of articles have been published regarding their preparation routes, the nature of the active vanadium phosphate phase and their reaction mechanisms. In recent years niobium phosphates, where niobium is in the same periodic table group (VA) as vanadium, are beginning to receive some

attention from academic researchers. It is well known that niobium phosphate presents similar acidic and catalytic characteristics to niobium oxide, the latter of which has been widely used as a solid acid catalyst due to its strong surface acidity.[69,70] Although niobium oxide has been studied by many researchers in the last 20 years, its related niobium compound - niobium phosphate has received relatively little attention. In consideration of the Nb-P-O's close relationship with two well studied catalysts, *i.e.* V-P-O and niobium oxide, Nb-P-O materials will be the studied material in this part of the project. A brief review concerning the catalytic applications, the crystalline phases of Nb-P-O and its potential catalytic ability for the oxidative dehydrogenation of ethane to ethylene is presented below.

1.3.1 General catalytic applications of Nb-P-O materials

A couple of catalytic applications of niobium phosphates have been assessed, whereas the structural and compositional changes that occur when they are used as catalysts are still not well understood [71,72]. Niobium phosphate (Nb-P-O) materials can serve as catalyst components for many reactions. For instance de Farias *et al.* [71] prepared V-Nb-P-O by doping vanadium phosphates with Nb. The resultant complex oxides show an enhanced *n*-butane conversion to maleic anhydride. By supporting CuO on $NbOPO_4$, Gervasini *et al.* [72] found that this catalyst formulation had enhanced reaction selectivity for N_2O decomposition. Mixing niobium phosphate with $CuZnO/Al_2O_3$ can greatly improve the conversion of dimethoxymethane to H_2 with high selectivity [73]. Recently Carniti *et al.* [74,75] have studied the intrinsic and effective surface acidity of niobium phosphates and found that they could be used as effective catalysts for the fructose

dehydration reaction. Rocha *et al.*[76] used niobium phosphates as catalysts in the alkylation of anisole with benzyl alcohol. Some important applications documented so far of the usef of Nb-P-O as catalyst materials are summarized in Table 1.3. In these studies, the Nb-P-O materials were mostly prepared by mixing Nb_2O_5 or $NbCl_5$ with H_3PO_4. The catalytic activity of Nb-P-O is primarily attributable to its surface acidity (*i.e.* the presence of Brönsted and/or Lewis acid sites on the surface), which accept electrons that are formed during the catalytic reaction cycle.[77] A Brönsted acid is an acid that donates protons (H^+ ions) (which is also known as a proton donor), whereas a Lewis acid is an electron acceptor.

Table 1.3 Catalytic applications of Nb-P-O materials

Catalyst precursor	**Catalytic reaction**	**Nb-P-O crystal structure**	**Electron microscopy studies**	**Ref. #**
V-Nb-P-O	selective oxidation of *n*-butane	unknown	SEM and BF-TEM	[71]
CuO/ $NbOPO_4$	decomposition of N_2O	amorphous	SEM	[72]
$CuZnO/Al_2O_3$/Nb-P-O	dimethoxymethane → H_2 + hydrocarbons	amorphous	BF-TEM	[73]
$NbOPO_4$	dehydration of fructose	amorphous	none attempted	[74,75]
$NbOPO_4 \cdot nH_2O$	alkylation of anisole	triclinic	none attempted	[76]
$[Nb_{1.0}(PO_4)_{1.0}](HPO_4)_{0.13}Cl_{0.74}$	hydroxylation of phenol	hexagonal	BF-TEM	[78]
$NbO(O_2)_{0.5}PO_4 \cdot 2H_2O$	benzylation of aromatic compounds	tetragonal	none attempted	[79]
Nb-P-O	hydroxylation of 1-naphthol	hexagonal	BF-TEM	[80]

1.3.2 Preparation of Nb-P-O materials

Most of the Nb-P-O materials used for catalytic applications have been as-received commercial products. The physic-chemical properties of niobium phosphate (NBP) as well as niobium oxide (NBO) supplied by CBMM (Companhia Brasileira De Metalurgia e Mineracao) are presented in Table 1.4.[74,75] Rocha *et al.*[76] prepared niobium phosphate materials using different methods and tested their catalytic activity in the alkylation of anisole with benzyl alcohol. Four Nb-P-O materials were produced by these authors,[76] namely (i) a commercial calcined Nb-P-O material, (ii) a commercial recrystallized Nb-P-O material, (iii) a crystalline Nb-P-O material synthesized by reacting niobic acid with HF and H_3PO_4 and (iv) a microporous Nb-P-O material generated by mixing $NbCl_5$ with H_3PO_4 and *n*-hexadecylamine[78]. Among them the microporous Nb-P-O material exhibited the best catalytic activity which they attributed to its large surface area and a high density of surface Brønsted acid sites. Da Silva *et al.*[81] synthesized a crystalline layer type hydrated niobium phosphate through the reaction of orthophosphoric acid and potassium niobate. The resultant $NbOPO_4{\cdot}0.4H_3PO_4{\cdot}1.0H_2O$ material had a triclinic structure. After being calcined at temperatures as high as 1000 °C, the $NbOPO_4{\cdot}0.4H_3PO_4{\cdot}1.0H_2O$ phase transformed to the tetragonal α-$NbOPO_4$ phase.

Table 1.4 Physicochemical properties of niobium phosphate and niobium oxide supplied by CBMM [74,75]

Catalyst	Composition [wt.%]		B.E.T. surface [$m^2\ g^{-1}$]
NBO	Nb_2O_5	80	108
	H_2O	20	
NBP	Nb_2O_5	66.7	
	P_2O_5	15.9	142
	K_2O	2.1	

1.3.3 Crystalline phases encountered in the preparation and activation stages of Nb-P-O catalysts

Most of the commercial Nb-P-O materials exist in amorphous state as shown in Table 1.4, which could be transformed into a triclinic structure after recrystallization.[76] A number of different crystalline Nb-P-O phases are known to exist such as α-$NbOPO_4$ [82], $NbPO_5$ [83], NbP_2O_7 [84], $Nb_{1.91}(PO_4)_{2.82}O_{0.72}$ [85]. These may form during the precursor preparation stage, precursor activation, or even during the oxidative dehydrogenation reaction. A typical example for α-$NbOPO_4$ is shown in Figure 1.8, which includes an experimentally determined structure (Fig. 1.8(a)), an atomic model built by CaRIne (Fig. 1.8(b)) and the simulated and indexed electron diffraction pattern rendered by CaRIne (Fig. 1.8(c)).

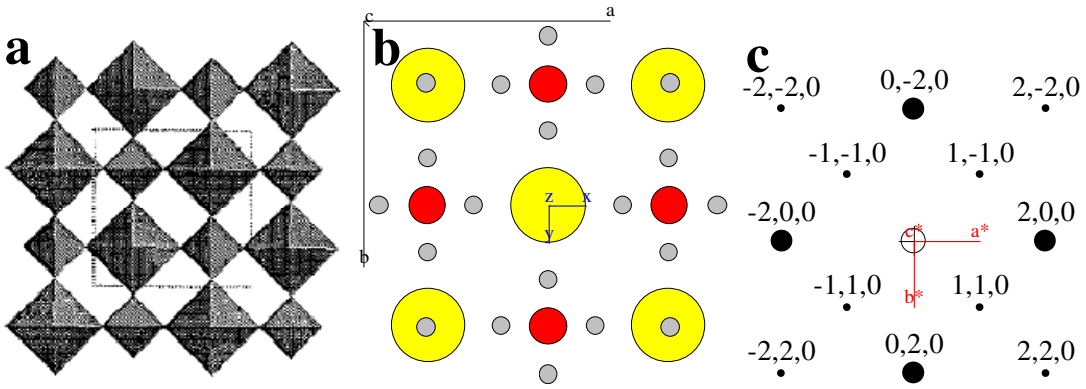

Figure 1.8 Schematic diagram of α-$NbOPO_4$ showing (a) interlinked PO_4 tetrahedra and NbO_6 octahedra viewed along the [001] direction (taken from [86]; small squares represent PO_4 tetrahedra and larger squares represent NbO_6 octahedra.); (b) the simulated atomic model viewed along the [001] direction (yellow circles represent Nb atoms; red circles represent P atoms and grey circles represent O atoms.); and (c) the simulated and indexed electron diffraction pattern of the [001] projection of α-$NbOPO_4$.

Amos *et al.*[86] determined the crystal structure of α-$NbOPO_4$ using X-ray powder diffraction and neutron powder diffraction. The α-$NbOPO_4$ has a tetragonal symmetry in space group *P*4/*nmm* with a = 6.4043 Å and c = 4.1217 Å. The structure consists of

chains of corner-sharing NbO_6 octahedra along the *c* axis while these chains are interlinked by PO_4 tetrahedra as shown in Figure 1.8(a). The atomic model (Fig. 1.8(b)) and the electron diffraction patterns (Fig. 1.8(c)) match well with the experimental data.

1.3.4 Oxidative dehydrogenation of ethane to ethylene over Nb-P-O catalysts

In this project two specific catalytic applications of Nb-P-O materials will be discussed, namely (i) the oxidative dehydrogenation (ODH) of ethane to ethylene and (ii) the methanol oxidation. Ethylene (C_2H_4) is one of the most important chemical building blocks, and it ranks as the highest worldwide volume organic chemical produced.[87] Current olefin demand is achieved commercially through steam cracking of hydrocarbons, mainly naphtha and ethane (C_2H_6).[88] Oxidative dehydrogenation (ODH) is a process that potentially offers both energy and economic advantages over traditional cracking technologies. However, before the ethane oxidative dehydrogenation,

$$C_2H_6 + O \rightarrow C_2H_4 + H_2O \quad (1.8)$$

can be considered as a viable alternative process, catalysts producing high ethylene yields need to be developed.

In recent years there has been an increased research effort to identify new catalysts for the oxidative dehydrogenation of ethane. In some cases higher yields to ethylene than those obtained by steam cracking have been achieved.[89] However, ethylene manufacturers have been reluctant to adopt the ODH process, and currently there are no commercial plants using the approach. This is most likely due to the familiarity and trust in the tried and tested steam cracking process. Therefore, if catalytic

ODH is to become a viable competing route for ethylene production, the identification and development of improved catalysts is required.

Vanadium oxide based catalysts have been considered for many years the catalysts of choice for the oxidative dehydrogenation of ethane to ethylene.[90,91] However, some mixed metal oxide catalysts containing niobium, in combination with a range of other elements, have shown promising performance for ethane ODH. Oxides of Mo-V-Nb,[92] Mo-V-Te-Nb,[93] and Ni-Nb[94] demonstrate higher selectivity to ethylene and operate at lower temperatures than conventional supported vanadium oxide catalysts. As long ago as 1978, Thorsteinson and co-workers[92] reported that mixed molybdenum vanadium oxide catalysts containing niobium could activate ethane very selectively towards ethylene. Many years later Mo-V-Te-Nb oxide catalysts[93] were developed and showed even better catalytic performance, and are, to date, the catalytic system with the highest yield to ethylene reported.[89] Mo-V-Te-Nb oxide catalysts are characterized by the presence of an active and selective crystalline phase, *i.e.* the orthorhombic $Te_2M_{20}O_{57}$ (M = Mo, V, Nb), the so-called M1 phase.[95,96] The M1 structure can be formed in the absence of Nb, but the presence of Nb greatly improves the catalytic performance. Although an explanation for the promotional effect is still not clear, it is possible that the acid character of Nb can favor the desorption of both ethane and ethylene from the surface of the catalysts, thus decreasing the consecutive over-oxidation to CO_2.[97] Furthermore, mixed nickel niobium oxide catalysts have also shown promising ODH catalytic activity.[94,98] Nickel oxide alone is very reactive and it activates ethane at very low temperatures, but produces CO_2 with high selectivity. However, the incorporation of niobium favors the formation of a Ni-Nb-O solid solution, which is very efficient for

oxidative dehydrogenation of ethane, and significantly reduces the formation of CO_2. Hence, it was proposed that the addition of niobium oxide to nickel oxide eliminates the unselective electrophyllic O species.[94,98] Although the presence of niobium in the former materials is very important, niobium oxide alone shows low activity, and apparently needs an accompanying element, such as vanadium, molybdenum or nickel to activate the alkane.

The majority of catalysts used for ethane ODH, and the ODH of other alkanes, are based on metal oxides. However, some of the most successfully exploited selective alkane oxidation catalysts are vanadium phosphates, which are used commercially for the selective oxidation of butane to maleic anhydride.[12,17] The role of phosphorus for *n*-butane selective oxidation is crucial, and it has also been demonstrated that it is important for alkane oxidative dehydrogenation. The addition of phosphorus has improved the ODH performance for ethane to ethylene using molybdenum oxide based catalysts,[99] and propane to propylene on vanadium oxide based catalysts.[100] Matsuura and Kimura[101] have also studied a range of metal phosphate catalysts for the selective oxidation of propane to propylene. They studied several $M^{5+}OPO_4$ phases and interestingly $NbOPO_4$ was reported to be active and relatively selective towards propylene. Against this background, it is surprising that niobium phosphates have not been more widely investigated as catalysts, especially considering the importance of niobium and phosphorus for the ODH of ethane and propane. Furthermore, niobium phosphates have a range of properties and structures that are considered desirable for selective oxidation catalysts. In Chapter 6 of this thesis we will address some of these

deficiencies and study three niobium phosphate materials. Their relative activities for the selective oxidative dehydrogenation of ethane to ethylene will also be determined.

1.4 Iron molybdate (Fe-Mo-O) catalyst system

1.4.1 The oxidation of methanol to formaldehyde over Fe-Mo-O catalysts

Formaldehyde, $H_2C=O$ is one of the most important basic chemicals, and is used to produce a large number of industrial and consumer products. Large volumes of formaldehyde are employed to make resins with urea, phenol and melamine.[102] Two processes are generally used in the industry to produce formaldehyde, which are referred as to the silver and iron molybdate process, respectively. In comparison with catalysis over Ag,[103,104] the oxidation of methanol over iron molybdate[105-107] is carried out at lower temperatures, so the catalyst is less sensitive to contamination by normal methanol impurities. It also provides a superior yield to formaldehyde which can be as high as 90%.[107] So, although currently both processes account for roughly an equal fraction of the total formaldehyde produced, it is clear that most of the new capacity that is being brought into operation will be based on the iron molybdate oxide process.

The bulk iron molybdate (Fe-Mo-O) catalyst was first reported to be active and selective for the oxidation of methanol to formaldehyde in 1931,[108] and began to be employed as commercial catalyst to this process in the 1950's.[109] Two stoichiometric iron molybdate phases, namely ferric molybdate ($Fe_2(MoO_4)_3$) and ferrous molybdate ($FeMoO_4$) are normally found in the catalyst.[107] The former phase is usually effective for the oxidation of methanol to formaldehyde, whereas the latter phase is normally found in used catalysts due to its generation during the redox process. Herein unless stated in

the context, the iron molybdate catalyst is referred as the ferric molybdate phase ($Fe_2(MoO_4)_3$). The commercial iron molybdate catalyst is composed of two crystal phases, *i.e.* $Fe_2(MoO_4)_3$ and excess MoO_3.[106,107] It is believed both $Fe_2(MoO_4)_3$ and excess MoO_3 are essential for the Fe-Mo-O catalyst in order to obtain good catalytic activity, selectivity and be long-lasting.[107]

1.4.2 Preparation of Fe-Mo-O catalysts

Iron molybdate catalysts are mainly prepared by the co-precipitation method in aqueous solution. By reacting ferrous malate, ammonium molybdate and ammonium hydroxide solutions with steel balls, in 1931 Adkins and Peterson[108] prepared the iron-molybdenum oxide catalyst and found that it was active and selective to the oxidation of methanol to formaldehyde. Kerr *et al*.[110] prepared iron molybdate in 1963 using the co-precipitation method in which sodium molybdate and ferric chloride solutions were mixed. In order to avoid sodium and chlorine contamination, most other researchers have generated iron molybdate catalysts by reacting ferric nitrate and ammonium heptamolybdate solutions.[111-113] There are some other reports[114,115] regarding the preparation of iron molybdate catalysts from iron chloride and ammonium heptamolybdate solutions, which is also used in the production of the industrial catalyst. A number of variables were found to have an influence on the catalytic performance of the generated iron molybdate catalysts from the precipitation method, such as the pH value of the mixed solution,[114] the Mo/Fe atomic ratio of the catalyst[116] and the calcination conditions (*i.e.* calcination temperature and calcination time)[117] for the co-precipitated iron molybdates.

There are other preparation methods reported in the literature besides the co-precipitation method. Soares *et al.*[118] prepared iron molybdate catalysts by the sol-gel method. A sol mixture of Fe precursor solution and Mo precursor solution in organic acid medium was heated and the formed gel was then calcined with and without air, respectively. The Fe-Mo-O catalyst generated showed a higher surface area than those produced by the co-precipitation method. Li *et al.*[119] compared the preparation of Fe-Mo-O from dry mixing of $Fe(NO)_3 \cdot 9H_2O$ and $(NH_4)_6Mo_7O_{24} \cdot 4H_2O$ salts and wet mixing of the same salt dissolved in water, respectively. They found that the wet mixing provides a better catalyst in terms of reactivity, reproducibility and thermal stability.

It should be noted that the Fe-Mo-O catalysts described above are unsupported, which makes them only suitable for fixed bed reactors. In order to minimize the hot spots, fluidized bed reactors are normally used, which requires that the catalysts are mechanically resistant. In order to achieve a higher mechanical resistance to abrasion, Fe-Mo-O catalysts have been deposited onto supports (*e.g.* SiO_2 or Al_2O_3). However these supported Fe-Mo-O catalysts are found to be less active than the unsupported ones, which could be due to strong interactions between the support and the active component.[120] Caiarati *et al.*[121] reported that the electronic properties of iron components in Fe-Mo-O catalysts were changed after deposition on SiO_2 supports. There are studies[122] showing that when the support surface area is increased the supported catalysts exhibit a lower catalytic activity, which was more dramatic on Al_2O_3 supports as compared to SiO_2 supports. This effect could be related to the formation of Anderson-type $[Al(OH)_6Mo_6O_{18}]^{3-}$ ions from the interaction between Mo solution and Al_2O_3 support which could give rise an Fe rich surface in Fe-Mo-O catalysts.[122]

1.4.3 Fe-Mo-O crystalline phases encountered in the preparation and the methanol oxidation

Usually ferric molybdates ($Fe_2(MoO_4)_3$) and ferrous molybdates ($FeMoO_4$) are observed in Fe-Mo-O catalysts. Ferric molybdates ($Fe_2(MoO_4)_3$), which is believed to be the active component, was structurally characterized by Plyasova *et al.*[123] in 1966. They found that it contained eight $Fe_2(MoO_4)_3$ molecules in a unit cell having the monoclinic structure (space group: $P2_1/a$), in which Fe octahedra and Mo tetrahedra share corners. This structure was further refined by Rapposch *et al.*[124] by comparing the crystalline structure of $Fe_2(MoO_4)_3$ to that of $Sc_2(WO_4)_3$. It was found that the monoclinic $Fe_2(MoO_4)_3$ has the space group $P2_1$ with a = 15.693 (3) Å, b = 9.235 (1) Å, c = 18.218 (4) Å and β = 125.21 (1) °. Each unit cell was composed of sixteen FeO_6 octahedra with a average Fe-O distance at 1.992 Å and twenty four MoO_4 tetrahedra with an overall average Mo-O distance at 1.756 Å (see Figure 1.9(a)). Each pair of FeO_6 octahedra and MoO_4 tetrahedra are interlinked by one oxygen atom, which results in a open structure where the nearest Fe-Fe distance at 5.03 Å. The 3D atomic model of monoclinic $Fe_2(MoO_4)_3$, as well as the simulated and indexed electron diffraction patterns of the [100] projection of monoclinic $Fe_2(MoO_4)_3$ are shown in Figures 1.9(a) and (b), respectively.

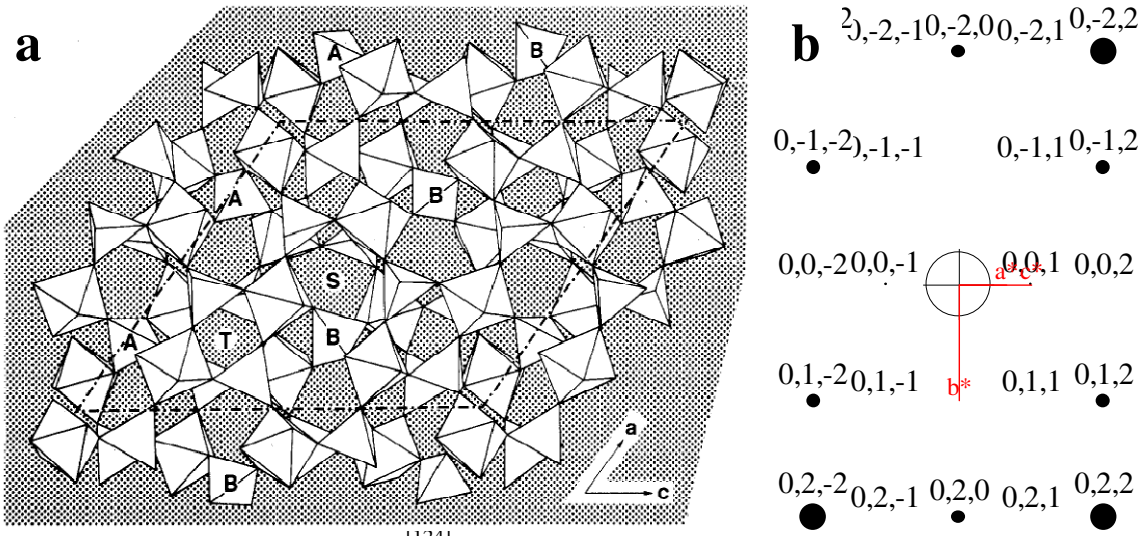

Figure 1.9 (a) 3D atomic model[124] of monoclinic $Fe_2(MoO_4)_3$ showing chains (A and B) and two cavities (S and T) and (b) the simulated and indexed electron diffraction patterns of the [100] projection of monoclinic $Fe_2(MoO_4)_3$.

Ferrous molybdates have been found to exist in three different forms, namely α-$FeMoO_4$, β-$FeMoO_4$ and $FeMoO_4$-II by magnetic susceptibility, Mössbauer effect and XRD studies.[125] α-$FeMoO_4$, which is a low temperature and low pressure phase, is iso-structural with the low temperature $NiMoO_4$ and $CoMoO_4$ phases. β-$FeMoO_4$, which is a high temperature and low pressure phase, is iso-structural with α-$MnMoO_4$. $FeMoO_4$-II, which is a high pressure phase, can be represented by a triclinic distortion of the monoclinic $NiMoO_4$-type structure.[125]

1.4.4 Active sites in the Fe-Mo-O catalysts for the oxidation of methanol to formaldehyde

There is still much discussion regarding the nature of the active site for the oxidation of methanol to formaldehyde, although it does appear that Mo plays an important role in the catalysis.[107] Different explanations for this have been presented in the literature. One general consensus is that the coexistence of both the $Fe_2(MoO_4)_3$ and

MoO_3 phases are necessary for a good catalyst. One popular explanation is that $Fe_2(MoO_4)_3$ is the active phase[126,127] while MoO_3 is required to ensure that iron rich phase is not formed on the surface.[128,129] Temperature programmed desorption (TPD) of methanol from stoichiometric bulk iron molybdate catalysts found that bulk $Fe_2(MoO_4)_3$ is 2-4 times more active than bulk MoO_3 for formaldehyde formation.[130] Physiochemical characterization shows that excess Mo brings about an increase in the surface area. On the other hand, excess Mo does not result in significant changes in the activity for methanol oxidation per unit surface area.[106] This provides convincing evidence that $Fe_2(MoO_4)_3$ is indeed the active phase of the catalyst. Catalysts with excess Mo tend to have a higher selectivity for HCHO and a reduction in selectivity to dimethyl ether. This is attributed to larger oxygen availability at the catalyst surface and the enhancement of the oxidation potential of the catalyst.[106] More recently, Söderhjelm *et al.*[131] reported that a synergy effect is observed in the catalysts having a mixture of MoO_3 and $Fe_2(MoO_4)_3$ crystalline phases. They proposed that the active structure may be an amorphous overlayer with a higher Mo/Fe ratio as compared to the bulk catalyst, in which Mo is in octahedral coordination on the surface of the crystalline iron molybdate.

Routray *et al.*[132] studied the oxidation of methanol to formaldehyde on MoO_3, Fe_2O_3, $Fe_2(MoO_4)_3$, MoO_3/ $Fe_2(MoO_4)_3$ and a model supported MoO_3/Fe_2O_3 catalyst in order to understand the origin of the enhanced catalytic performance of bulk iron molybdate catalysts with excess crystalline MoO_3. They attributed the enhanced catalytic performance to the formation of a surface MoO_x monolayer on the bulk $Fe_2(MoO_4)_3$ phase and proposed that the catalytically active phase is in fact a surface MoO_x monolayer supported on the $Fe_2(MoO_4)_3$ bulk. The excess MoO_3 in the Fe-Mo-O

catalysts is required to balance the loss of MoO_x from the surface. Recently House *et al.*[116] examined the oxidation of methanol to formaldehyde over bulk iron molybdate catalysts as a function of Mo/Fe ratios in the range of 0.02 to 4. They found that Mo/Fe ratios greater than 1.5 are required for higher catalytic activity and selectivity. And they also reached a similar conclusion in that the excess crystalline MoO_3 is required mainly to replenish any surface molybdenum oxide that is volatilized during methanol oxidation at high temperatures.

1.4.5 Comments on the reaction mechanism for the oxidation of methanol to formaldehyde on Fe-Mo-O catalysts

It is widely accepted that the oxidation of methanol to formaldehyde on Fe-Mo-O catalysts is a surface redox process, which follows a Mars-van Krevelen type reaction mechanism. Bowker *et al.*[128] presented a detailed kinetic study on this reaction over three different oxide catalysts, namely iron molybdate (Fe-Mo-O), Fe_2O_3 and MoO_3 and found that only CO_2 and H_2 were formed on Fe_2O_3 indicating that a formate intermediate is present. Formaldehyde was only formed with a high selectivity on molybdenum-containing catalysts, in which the iron molybdate is more active than the MoO_3. Pernicone *et al.*[133] proposed a similar reaction mechanism on Fe-Mo-O catalysts based on the Mars-van Krevelen mechnism as shown below:

step 1: $CH_3OH + [\ ] + O_2 \leftrightarrow (CH_3O - [\ ])^- + OH^-$

step 2: $(CH_3O - [\ ])^- + O^{2-} \leftrightarrow (CH_2O - [\ ])^{2-} + OH^-$

step 3: $2\ OH^- \leftrightarrow H_2O + O_{2-} + [\ ]$

step 4: $(CH_2O - [\ ])^{2-} \rightarrow CH_2O + [\ ]^{2-}$

step 5: ½ O_2 + [ ]$^{2-}$ → O^{2-}

where [ ] is an anionic vacancy and O^{2-} represents a lattice oxygen. The rate determining step is believed by many researchers to be the abstraction of H from the methyl group. It should be noted that during this methanol oxidation reaction, many by-products can also be formed, such as dimethylether (DME), dimethoxymethane (DMM), methylformate (MF), CO and CO_2, where CO is the major by-product. More details about the reaction mechanism and kinetics of the oxidation of methanol to formaldehyde can be found in references [130,134-137], and shall not be discussed any further here.

1.5 Scope of this thesis

This project involves the nanostructural and compositional characterization of three different complex oxide catalysts, *i.e.* vanadium phosphate (V-P-O), niobium phosphate (Nb-P-O) and iron molybdate (Fe-Mo-O) using electron microscopy techniques as well as complementary characterization techniques. The brief literature review of these three complex oxide catalyst systems has been given in this chapter. Since this dissertation is mainly focused on the application of electron microscopy techniques to study the complex oxide catalysts, a detailed review regarding the application of various electron microscopy techniques on complex oxide catalysts, as well as the basics of these electron microscopy techniques will be presented in Chapter 2. It will mainly introduce the major electron microscopy techniques that have been often used in the study of complex oxide catalysts. This includes scanning electron microscopy (SEM), transmission electron microscopy (TEM) and scanning transmission electron microscopy (STEM). Chemical analysis techniques in the electron microscope, such as

X-ray energy dispersive spectroscopy (XEDS) and electron energy loss spectroscopy (EELS), are also described.

In chapter 3, the basics of two electron microscopy techniques (*i.e.* X-ray ultra-Microscopy (XuM) and energy-filtered transmission electron microscopy (EFTEM)) that are rarely used to study complex oxide catalysts will be described. Then the basic principles of other complementary characterization methods will be briefly introduced, which includes BET surface area measurement, X-ray diffraction (XRD), X-ray photoelectron spectroscopy (XPS) and Laser Raman spectroscopy (LRS).

V-P-O system

Depending on the types of alcohols used in the reduction step of $VOPO_4 \cdot 2H_2O$ in the VPD method, different vanadium phosphate materials with different morphologies can be produced. Unfortunately there are not reports that provide a detailed understanding of the VPD route. In the present study, adding a variety of alkanes during the alcohol reduction step of $VOPO_4 \cdot 2H_2O$ shows a significant influence on the materials produced. The effect of the alkanes on the generation of different V-P-O materials will be discussed. In addition the specific *order* of alkane and alcohol added in the reduction stage of $VOPO_4 \cdot 2H_2O$ will be investigated. This Chapter 4 aims at obtaining a better understanding of the synthesis-structure relationship in the VPD route. Although the topotactic phase transformation from the $VOHPO_4 \cdot 0.5H_2O$ to the $(VO)_2P_2O_7$ phase has been well investigated, another important phase transformation, namely $VOPO_4 \cdot 2H_2O$ to $VOHPO_4 \cdot 0.5H_2O$ (*i.e.* platelet-type and rosette-type morphologies) is still not well documented. In Chapter 4, this particular phase transformation will be explained on the basis of detailed electron microscopy studies.

It is well known that the active $(VO)_2P_2O_7$ phase is formed topotactically from the $VOHPO_4 \cdot 0.5H_2O$ precursor. Hence it is very important to control the morphology of the precursor through the preparation route in order to generate an active V-P-O material which has a better catalytic performance. Three novel preparation methodologies have been used in this project, *i.e.* (i) the use of V-P-O 'seed' crystals in the VPD route, (ii) the use of a di-block copolymer template in V-P-O production and (iii) the use of a mechanically resistant SiO_2 shell for encapsulating fragile V-P-O catalysts. Each of the methods has shown advantages over the conventional routes (*i.e.* the VPA, VPO and VPD route.) as shown in Chapter 5. The details of the synthesis and the structure-performance relationship of the produced V-P-O materials will also be discussed in Chapter 5.

Nb-P-O system

The application of V-P-O catalysts in the selective oxidation of *n*-butane to MA has been studied for decades. Recently niobium phosphates, a close relative to V-P-O, are beginning to receive some attention from some research groups. In Chapter 6, two catalytic applications of niobium phosphate (Nb-P-O) materials, namely the oxidative dehydrogenation of ethane to ethylene and the oxidation of methanol to formaldehyde, will be investigated. The relationship between the Nb-P-O morphologies and phases (*i.e.* cubic $Nb_2P_4O_{15}$, tetragonal $NbOPO_4$ and orthorhombic $Nb_{1.91}P_{2.82}O_{12}$ phases) produced and their catalytic performance will be discussed.

Fe-Mo-O system

In Chapter 7 the application of a novel hydrothermal synthesis and impregnation technique to prepare $Fe_2(MoO_4)_3/MoO_3$ nanorod catalysts for the oxidation of methanol

to formaldehyde will be discussed. By depositing iron salt precursors to pre-synthesized MoO_3 nanorods, a novel $Fe_2(MoO_4)_3/MoO_3$ island/nanorod morphology can be produced. The effect of Mo/Fe atomic ratio and duration of calcination time during the course of catalyst preparation on the physical structure, chemical composition and catalytic performance will be systemically investigated. The catalysts generated will be shown to exhibit a comparable catalytic performance to industrial Fe-Mo-O catalysts, showing a conversion of nearly 100% while maintaining the selectivity as high as 90%. The formation mechanism involved in the generation of these novel island/nanorod catalysts will be discussed.

1.6 References

1. M. Berzelius, "Considerations respecting a new power which acts in the formation of organic bodies," *Edinburgh New Philosophical Journal,* **21,** 223-236 (1836).

2. G. C. Bond, Heterogeneous catalysis: principles and applications (Clarendon Press, 2nd Edition, 1987).

3. J. M. Thomas and W. J. Thomas, Principles and practice of heterogeneous catalysis (Vch, 1996).

4. R. L. Bergman and N. W. Frisch, "Process for preparing phosphorus-vanadium-oxygen catalysts,"3 293 268 (1966).

5. E. Bordes and R. M. Contractor, "Adaptation of the microscopic properties of redox catalysts to the type of gas-solid reactor," *Topics in Catalysis,* **3,** 365-375 (1996).

6. C. J. Kiely, A. Burrows, G. J. Hutchings, K. E. Bere, J. C. Volta, A. Tuel, and M. Abon, "Structural transformation sequences occurring during the activation of vanadium phosphorus oxide catalysts," *Faraday Discussions,* **105,** 103-118 (1996).

7. T. Shimoda, T. Okuhara, and M. Misono, "Preparation of vanadium-phosphorus mixed-oxide (P/V=1) catalysts and their application to oxidation of butane to maleic-anhydride," *Bulletin of the Chemical Society of Japan,* **58,** 2163-2171 (1985).

8. M. T. Sananes, G. J. Hutchings, and J. C. Volta, " *n*-Butane oxidation to maleic-anhydride and furan with no carbon oxide formation using a catalyst derived from $VO(H_2PO_4)_2$," *Journal of the Chemical Society-Chemical Communications,* 243-244 (1995).

9. J. Volta, "Dynamic processes on vanadium phosphorous oxides for selective alkane oxidation," *Catalysis Today,* **32,** 29-36 (1996).

10. M. Abon, K. E. Béré, and P. Delichère, "Nature of active oxygen in the n-butane selective oxidation over well-defined V-P-O catalysts: an oxygen isotopic labelling study," *Catalysis Today,* **33,** 15-23 (1997).

11. G. Centi, "Vanadyl pyrophosphate - a critical overview," *Catalysis Today,* **16,** 5-26 (1993).

12. C. J. Kiely, A. Burrows, S. Sajip, G. J. Hutchings, M. T. Sananes, A. Tuel, and J. C. Volta, "Characterisation of variations in vanadium phosphate catalyst microstructure with preparation route," *Journal of Catalysis,* **162,** 31-47 (1996).

13. G. J. Hutchings, A. Burrows, S. Sajip, C. J. Kiely, K. E. Bere, J. C. Volta, A. Tuel, and M. Abon, "Understanding the microstructural transformation mechanism which takes place during the activation of vanadium phosphorus oxide catalysts," *3rd World Congress on Oxidation Catalysis,* **110,** 209-218 (1997).

14. G. J. Hutchings, C. J. Kiely, M. T. Sananes-Schulz, A. Burrows, and J. C. Volta, "Comments on the nature of the active site of vanadium phosphate catalysts for butane oxidation," *Catalysis Today,* **40,** 273-286 (1998).

15. J. W. Johnson, D. C. Johnston, A. J. Jacobson, and J. F. Brody, "Preparation and characterization of $VO(HPO_4)\cdot 0.5H_2O$ and its topotactic transformation to $(VO)_2P_2O_7$," *Journal of the American Chemical Society,* **106,** 8123-8128 (1984).

16. H. S. Horowitz, C. M. Blackstone, A. W. Sleight, and G. Teufer, "V-P-O catalysts for oxidation of butane to maleic-anhydride - Influence of $(VO)_2H_4P_2O_9$ precursor morphology on catalytic properties," *Applied Catalysis,* **38,** 193-210 (1988).

17. G. J. Hutchings, "Vanadium phosphate: a new look at the active components of catalysts for the oxidation of butane to maleic anhydride," *Journal of Materials Chemistry,* **14,** 3385-3395 (2004).

18. S. Sajip, "Electron microscopy studies of vanadium phosphorus oxide catalysts," PhD Thesis, University of Liverpool (1998).

19. G. J. Hutchings and R. Higgins, "Selective oxidation of n-butane to maleic anhydride with vanadium phosphorus catalysts prepared by comminution in the presence of dispersants," *Applied Catalysis A-General,* **154,** 103-115 (1997).

20. I. Ayub, D. S. Su, M. Willinger, A. Kharlamov, L. Ushkalov, V. A. Zazhigalov, N. Kirillova, and R. Schlogl, "Tribomechanical modification of Bi promoted vanadyl phosphate systems 1: An improved catalyst and insight into structure-function relationship," *Physical Chemistry Chemical Physics,* **5,** 970-978 (2003).

21. Y. H. Taufiq-Yap, C. K. Goh, G. J. Hutchings, N. Dummer, and J. K. Bartley, "Effects of mechanochemical treatment to the vanadium phosphate catalysts derived from $VOPO_4\cdot 2H_2O$," *Journal of Molecular Catalysis A-Chemical,* **260,** 24-31 (2006).

22. R. A. Overbeek, A. R. C. J. Pekelharing, A. J. vanDillen, and J. W. Geus, "Preparation, characterization and testing of newly developed silica-supported V-P-O catalysts," *Applied Catalysis A-General,* **135,** 231-248 (1996).

23. R. A. Overbeek, P. A. Warringa, M. J. D. Crombag, L. M. Visser, A. J. vanDillen, and J. W. Geus, "Preparation, characterization and testing of newly developed titania supported V-P-O catalysts," *Applied Catalysis A-General,* **135,** 209-230 (1996).

24. J. M. C. Bueno, G. K. Bethke, M. C. Kung, and H. H. Kung, "Supported VPO catalysts for selective oxidation of butane III: Effect of preparation procedure and SiO_2 support," *Catalysis Today,* **43,** 101-110 (1998).

25. C. Y. Xiao, X. Chen, Z. Y. Wang, W. J. Ji, Y. Chen, and C. T. Au, "The novel and highly selective fumed silica-supported VPO for partial oxidation of *n*-butane to maleic anhydride," *Catalysis Today,* **93-5,** 223-228 (2004).

26. M. J. Ledoux, C. Crouzet, C. Pham-Huu, V. Turines, K. Kourtakis, P. L. Mills, and J. J. Lerou, "High-yield butane to maleic anhydride direct oxidation on vanadyl pyrophosphate supported on heat-conductive materials: beta-SiC, Si_3N_4, and BN," *Journal of Catalysis,* **203,** 495-508 (2001).

27. H. Imai, Y. Kamiya, and T. Okuhara, "Selective oxidation of *n*-butane over nanosized crystallites of $(VO)_2P_2O_7$ synthesized by an exfoliation-reduction process of $VOPO_4 \cdot 2H_2O$ in a mixture of 2-butanol and ethanol," *Journal of Catalysis,* **251,** 195-203 (2007).

28. H. Imai, Y. Kamiya, and T. Okuhara, "Synthesis of $(VO)_2P_2O_7$ catalysts via exfoliation-reduction of $VOPO_4 \cdot 2H_2O$ in butanol in the presence of ethanol," *Research on Chemical Intermediates,* **34,** 669-677 (2008).

29. N. Yamamoto, N. Hiyoshi, and T. Okuhara, "Thin-layered sheets of $VOHPO_4 \cdot 0.5H_2O$ prepared from $VOPO_4 \cdot 2H_2O$ by intercalation-exfoliation-reduction in alcohol," *Chemistry of Materials,* **14,** 3882-3888 (2002).

30. Y. Kamiya, S. Ueki, N. Hiyoshi, N. Yamamoto, and T. Okuhara, "Preparation of catalyst precursors for selective oxidation of *n*-butane by exfoliation-reduction of $VOPO_4 \cdot 2H_2O$ in primary alcohol," *Catalysis Today,* **78,** 281-290 (2003).

31. Y. Kamiya, H. Imai, and T. Okuhara, "Selective oxidation of *n*-butane over highly crystalline vanadyl pyrophosphate catalyst synthesized by intercalation-exfoliation-reduction of layered vanadyl phosphate dihydrate," *Journal of the Japan Petroleum Institute,* **52,** 81-89 (2009).

32. G. J. Hutchings and R. Higgins, "Effect of promoters on the selective oxidation of *n*-butane with vanadium-phosphorus oxide catalysts," *Journal of Catalysis,* **162,** 153-168 (1996).

33. S. Sajip, J. K. Bartley, A. Burrows, M. T. Sanenes-Schulz, A. Tuel, J. C. Volta, C. J. Kiely, and G. J. Hutchings, "Structure-activity relationships for Co- and Fe-promoted vanadium phosphorus oxide catalysts," *New Journal of Chemistry,* **25,** 125-130 (2001).

34. M. Brutovsky and S. Gerej, "Effect of various modifying elements on the catalytic properties of vanadium-phosphorus catalysts in oxidation of butane," *Collection of Czechoslovak Chemical Communications,* **47,** 403-408 (1982).

35. M. Brutovsky, S. Gerej, F. Vasilco, and J. Gerejova, "X-Ray diffractograms and Ir-spectra of modified vanadium-phosphate catalysts," *Collection of Czechoslovak Chemical Communications,* **47,** 1290-1300 (1982).

36. M. Otake, "Solid-solution type crystalline oxides and their precursors," US Patent4 337 173 (1982).

37. A. Delimitis, "Electron microscopy studies of doped vanadium phosphorus oxide catalysts," PhD Thesis, University of Liverpool (2002).

38. E. Bordes, P. Courtine, and J. W. Johnson, "On the topotactic dehydration of $VOHPO_4 \cdot 0.5H_2O$ into vanadyl pyrophosphate," *Journal of Solid State Chemistry,* **55,** 270-279 (1984).

39. M. E. Leonowicz, J. W. Johnson, J. F. Brody, H. F. Shannon, and J. M. Newsam, "Vanadyl hydrogenphosphate hydrates - $VO(HPO_4) \cdot 4H_2O$ and $VO(HPO_4) \cdot 0.5H_2O$," *Journal of Solid State Chemistry,* **56,** 370-378 (1985).

40. V. V. Guliants, J. B. Benziger, S. Sundaresan, I. E. Wachs, J. M. Jehng, and J. E. Roberts, "The effect of the phase composition of model VPO catalysts for partial oxidation of n-butane," *Catalysis Today,* **28,** 275-295 (1996).

41. V. V. Guliants, S. A. Holmes, J. B. Benziger, P. Heaney, D. Yates, and I. E. Wachs, "In situ studies of atomic, nano- and macroscale order during $VOHPO_4 \cdot 0.5H_2O$ transformation to $(VO)_2P_2O_7$," *Journal of Molecular Catalysis A-Chemical,* **172,** 265-276 (2001).

42. K. Aït-Lachgar, M. Abon, and J. C. Volta, "Selective oxidation of *n*-butane to maleic anhydride on vanadyl pyrophosphate," *Journal of Catalysis,* **171,** 383-390 (1997).

43. Y. Zhanglin, M. Forissier, J. C. Vedrine, and J. C. Volta, "On the mechanism of *n*-butane oxidation to maleic anhydride on VPO catalysts .II. Study of the evolution of the VPO catalysts under *n*-butane, butadiene, and furan oxidation conditions," *Journal of Catalysis,* **145,** 267-275 (1994).

44. G. J. Hutchings, A. Desmartinchomel, R. Olier, and J. C. Volta, "Role of the product in the transformation of a catalyst to its active state," *Nature,* **368,** 41-45 (1994).

45. G. Koyano, T. Okuhara, and M. Misono, "Redox processes of surface of vanadyl pyrophosphate in relation to selective oxidation of *n*-butane," *Catalysis Letters,* **32,** 205-213 (1995).

46. N. H. Batis, H. Batis, A. Ghorbel, J. C. Vedrine, and J. C. Volta, "Synthesis and characterization of new VPO catalysts for partial n-Butane oxidation to maleic anhydride," *Journal of Catalysis,* **128,** 248-263 (1991).

47. E. Bordes, "Nature of the active and selective sites in vanadyl pyrophosphate, catalyst of oxidation of *n*-butane, butene and pentane to maleic anhydride," *Catalysis Today,* **16,** 27-38 (1993).

48. J. R. Ebner and M. R. Thompson, "An active-Site hypothesis for well-crystallized vanadium phosphorus oxide catalyst systems," *Catalysis Today,* **16,** 51-60 (1993).

49. P. L. Gai and K. Kourtakis, "Solid-state defect mechanism in vanadyl pyrophosphate catalysts - implications for selective oxidation," *Science,* **267,** 661-663 (1995).

50. H. Bluhm, M. Havecker, E. Kleimenov, A. Knop-Gericke, A. Liskowski, R. Schlogl, and D. S. Su, "In situ surface analysis in selective oxidation catalysis: *n*-butane conversion over VPP," *Topics in Catalysis,* **23,** 99-107 (2003).

51. G. J. Hutchings, J. K. Bartley, J. M. Webster, J. A. Lopez-Sanchez, D. J. Gilbert, C. J. Kiely, A. F. Carley, S. M. Howdle, S. Sajip, S. Caldarelli, C. Rhodes, J. C. Volta, and M. Poliakoff, "Amorphous vanadium phosphate catalysts from supercritical antisolvent precipitation," *Journal of Catalysis,* **197,** 232-235 (2001).

52. G. J. Hutchings, J. A. Lopez-Sanchez, J. K. Bartley, J. M. Webster, A. Burrows, C. J. Kiely, A. F. Carley, C. Rhodes, M. Havecker, A. Knop-Gericke, R. W. Mayer, R. Schlogl, J. C. Volta, and M. Poliakoff, "Amorphous vanadium phosphate catalysts prepared using precipitation with supercritical CO_2 as an antisolvent," *Journal of Catalysis,* **208,** 197-210 (2002).

53. F. Garbassi, J. C. J. Bart, R. Tassinari, G. Vlaic, and P. Lagarde, "Catalytic *n*-butane oxidation activity and physicochemical characterization of vanadium-phosphorus oxides with variable P/V ratio," *Journal of Catalysis,* **98,** 317-325 (1986).

54. P. Delichère, K. E. Béré, and M. Abon, "Vanadyl pyrophosphate catalysts: Surface analysis by XPS and LEIS," *Applied Catalysis A: General,* **172,** 295-309 (1998).

55. W. P. A. Jansen, M. Ruitenbeek, A. W. Denier v.d. Gon, J. W. Geus, and H. H. Brongersma, "New insights into the nature of the active phase of VPO catalysts—a quantitative static LEIS study," *Journal of Catalysis,* **196,** 379-387 (2000).

56. L. O'Mahony, T. Curtin, J. Henry, D. Zemlyanov, M. Mihov, and B. K. Hodnett, "Phase development and morphology during the thermal treatment of $VOHPO_4 \cdot 0.5H_2O$," *Applied Catalysis A: General,* **285,** 36-42 (2005).

57. N. Duvauchelle, E. Kesteman, F. Oudet, and E. Bordes, "Mosaic crystals of vanadyl pyrophosphate obtained by oriented nucleation and growth," *Journal of Solid State Chemistry,* **137,** 311-324 (1998).

58. H. Imai, Y. Kamiya, and T. Okuhara, "Transformation of nano-sized vanadyl hydrogen phosphate hemihydrate crystallites to vanadyl pyrophosphate during activation in the presence of *n*-butane and oxygen," *Journal of Catalysis,* **255,** 213-219 (2008).

59. L. O'Mahony, J. Henry, D. Sutton, T. Curtin, and B. K. Hodnett, "Crystallisation of $VOHPO_4 \cdot 0.5H_2O$," *Applied Catalysis A-General,* **253,** 409-416 (2003).

60. L. O'Mahony, T. Curtin, D. Zemlyanov, M. Mihov, and B. K. Hodnett, "Surface species during the crystallization of $VOHPO_4 \cdot 0.5H_2O$," *Journal of Catalysis,* **227,** 270-281 (2004).

61. G. Centi, G. Fornasari, and F. Trifirò, "On the mechanism of *n*-butane oxidation to maleic anhydride: Oxidation in oxygen-stoichiometry-controlled conditions," *Journal of Catalysis,* **89,** 44-51 (1984).

62. S. K. Bej and M. S. Rao, "Selective oxidation of normal-butane to maleic-anhydride .2. Identification of rate expression for the reaction," *Industrial & Engineering Chemistry Research,* **30,** 1824-1828 (1991).

63. B. Schiott, K. A. Jorgensen, and R. Hoffmann, "Formation of maleic-anhydride on a vanadyl pyrophosphate surface - a theoretical-study of the mechanism," *Journal of Physical Chemistry,* **95,** 2297-2307 (1991).

64. T. Okuhara and M. Misono, "Key reaction steps and active surface phase of vanadyl pyrophosphate for selective oxidation of butane," *Catalysis Today,* **16,** 61-67 (1993).

65. J. T. Cleaves and G. Centi, "The reaction mechanism of alkane selective oxidation on vanadyl pyrophosphate catalysts. Features gleaned from TAP reactor transient response studies," *Catalysis Today,* **16,** 69-78 (1993).

66. G. Busca and G. Centi, "Surface dynamics of adsorbed species on heterogeneous oxidation catalysts - evidence from the oxidation of C4 and C5 alkanes on vanadyl pyrophosphate," *Journal of the American Chemical Society,* **111,** 46-54 (1989).

67. G. Centi and F. Trifiro', "Surface kinetics of adsorbed intermediates: selective oxidation of C4-C5 alkanes," *Chemical Engineering Science,* **45,** 2589-2596 (1990).

68. R. L. Bergman and N. W. Frisch, "Process for Preparing Phosphorus-Vanadium-Oxygen Catalysts,"3293268 (1966).

69. K. Tanabe, "Catalytic application of niobium compounds," *Catalysis Today,* **78,** 65-77 (2003).

70. I. Nowak and M. Ziolek, "Niobium compounds: Preparation, characterization, and application in heterogeneous catalysis," *Chemical reviews,* **99,** 3603-3624 (1999).

71. A. M. D. de Farias, W. D. Gonzalez, P. G. P. de Oliveira, J. G. Eon, J. M. Herrmann, M. Aouine, S. Loridant, and J. C. Volta, "Vanadium phosphorus oxide catalyst modified by niobium doping for mild oxidation of n-butane to maleic anhydride," *Journal of Catalysis,* **208,** 238-246 (2002).

72. A. Gervasini, P. Carniti, S. Bennici, and C. Messi, "Influence of the chemical nature of the support (niobic acid and niobium phosphate) on the surface and catalytic properties of supported CuO," *Chemistry of Materials,* **19,** 1319-1328 (2007).

73. Q. Sun, A. Auroux, and J. Shen, "Surface acidity of niobium phosphate and steam reforming of dimethoxymethane over $CuZnO/Al_2O_3$-NbP complex catalysts," *Journal of Catalysis,* **244,** 1-9 (2006).

74. P. Carniti, A. Gervasini, S. Biella, and A. Auroux, "Intrinsic and effective acidity study of niobic acid and niobium phosphate by a multitechnique approach," *Chemistry of Materials,* **17,** 6128-6136 (2005).

75. P. Carniti, A. Gervasini, S. Biella, and A. Auroux, "Niobic acid and niobium phosphate as highly acidic viable catalysts in aqueous medium: Fructose dehydration reaction," *Catalysis Today,* **118,** 373-378 (2006).

76. A. S. Rocha, A. M. S. Forrester, M. H. C. de la Cruz, C. T. da Silva, and E. R. Lachter, "Comparative performance of niobium phosphates in liquid phase anisole benzylation with benzyl alcohol," *Catalysis Communications,* **9,** 1959-1965 (2008).

77. F. Arena, R. Dario, and A. Parmaliana, "A characterization study of the surface acidity of solid catalysts by temperature programmed methods," *Applied Catalysis A: General,* **170,** 127-137 (1998).

78. N. K. Mal, A. Bhaumik, P. Kumar, and M. Fujiwara, "Microporous niobium phosphates and catalytic properties prepared by a supramolecular templating mechanism," *Chemical Communications,* 872-873 (2003).

79. M. H. C. de la Cruz, J. F. C. da Silva, and E. R. Lachter, "Liquid phase benzylation of aromatic compounds with benzyl alcohol catalyzed by niobium phosphate," *Applied Catalysis A-General,* **245,** 377-382 (2003).

80. N. K. Mal and M. Fujiwara, "Synthesis of hexagonal and cubic super-microporous niobium phosphates with anion exchange capacity and catalytic properties," *Chemical Communications,* 2702-2703 (2002).

81. J. Da Silva, M. Vieira, W. Andrade, and A. Dos Santos, "Chemical and structural aspects of a layered acid niobium (V) phosphate," *Journal of Materials Science,* **40,** 4455-4460 (2005).

82. J. M. Longo and Kierkega.P, "Crystal Structure of Nbopo4," *Acta chemica Scandinavica,* **20,** 72-& (1966).

83. D. L. Serra and S. J. Hwu, "Structure of Orthorhombic Nbpo5," *Acta Crystallographica Section C-Crystal Structure Communications,* **48,** 733-735 (1992).

84. H. Fukuoka, H. Imoto, and T. Saito, "Preparation of Cubic Niobium Pyrophosphate Containing Nb(iv) and Topotactic Extraction of Phosphorus Atoms," *Journal of Solid State Chemistry,* **119,** 98-106 (1995).

85. J. J. Zahletho, A. Verbaere, A. Jouanneaux, F. Taulelle, Y. Piffard, and M. Tournoux, "Nb2-Xp3-Yo12, a Novel Nb-V Oxophosphate with Disordered Cation Vacancies in a Sc-2(wo4)(3)-Type Structure," *Journal of Solid State Chemistry,* **116,** 335-342 (1995).

86. T. G. Amos, A. Yokochi, and A. W. Sleight, "Phase transition and negative thermal expansion in tetragonal $NbOPO_4$," *Journal of Solid State Chemistry,* **141,** 303-307 (1998).

87. A. M. Thayer, "Ethylene producers add capacity to buffer cyclical markets, meet demand," *Chemical & Engineering News,* **74,** 15-17 (1996).

88. H. H. Kung, "Oxidative dehydrogenation of light (C-2 to C-4) alkanes," *Advances in Catalysis, Vol 40,* **40,** 1-38 (1994).

89. F. Cavani, N. Ballarini, and A. Cericola, "Oxidative dehydrogenation of ethane and propane: How far from commercial implementation?" *Catalysis Today,* **127,** 113-131 (2007).

90. M. A. Banares and S. J. Khatib, "Structure-activity relationships in alumina-supported molybdena-vanadia catalysts for propane oxidative dehydrogenation," *Catalysis Today,* **96,** 251-257 (2004).

91. J. M. Lopez Nieto, "The selective oxidative activation of light alkanes. From supported vanadia to multicomponent bulk V-containing catalysts," *Topics in Catalysis,* **41,** 3-15 (2006).

92. E. M. Thorsteinson, T. P. Wilson, F. G. Young, and P. H. Kasai, "The oxidative dehydrogenation of ethane over catalysts containing mixed oxides of molybdenum and vanadium," *Journal of Catalysis,* **52,** 116-132 (1978).

93. B. Solsona, M. I. Vazquez, F. Ivars, A. Dejoz, P. Concepcion, and J. M. L. Nieto, "Selective oxidation of propane and ethane on diluted Mo-V-Nb-Te mixed-oxide catalysts," *Journal of Catalysis,* **252,** 271-280 (2007).

94. E. Heracleous and A. A. Lemonidou, "Ni-Nb-O mixed oxides as highly active and selective catalysts for ethene production via ethane oxidative dehydrogenation. Part I: Characterization and catalytic performance," *Journal of Catalysis,* **237,** 162-174 (2006).

95. J. M. M. Millet, M. Baca, A. Pigamo, D. Vitry, W. Ueda, and J. L. Dubois, "Study of the valence state and coordination of antimony in MoVSbO catalysts determined by XANES and EXAFS," *Applied Catalysis A: General,* **244,** 359-370 (2003).

96. H. Murayama, D. Vitry, W. Ueda, G. Fuchs, M. Anne, and J. L. Dubois, "Structure characterization of orthorhombic phase in MoVTeNbO catalyst by powder X-ray diffraction and XANES," *Applied Catalysis A: General,* **318,** 137-142 (2007).

97. J. M. López Nieto, P. Botella, P. Concepción, A. Dejoz, and M. I. Vázquez, "Oxidative dehydrogenation of ethane on Te-containing MoVNbO catalysts," *Catalysis Today,* **91-92,** 241-245 (2004).

98. E. Heracleous and A. A. Lemonidou, "Ni–Me–O mixed metal oxides for the effective oxidative dehydrogenation of ethane to ethylene – Effect of promoting metal Me," *Journal of Catalysis,* **270,** 67-75 (2010).

99. N. Haddad, E. Bordes-Richard, and A. Barama, "MoO_x-based catalysts for the oxidative dehydrogenation (ODH) of ethane to ethylene: Influence of vanadium and phosphorus on physicochemical and catalytic properties," *Catalysis Today,* **142,** 215-219 (2009).

100. R. P. Singh, M. A. Bañares, and G. Deo, "Effect of phosphorous modifier on V_2O_5/TiO_2 catalyst: ODH of propane," *Journal of Catalysis,* **233,** 388-398 (2005).

101. I. Matsuura and N. Kimura, "Oxidation and ammoxidation of propane over tetragonal type $M(5+)OPO_4$ catalysts," *New Developments in Selective Oxidation Ii,* **82,** 271-279 (1994).

102. M. Bohnet, Ullmann's encyclopedia of industrial chemistry (Wiley-VCH, 6th Edition, 2003).

103. M. Qian, M. A. Liauw, and G. Emig, "Formaldehyde synthesis from methanol over silver catalysts," *Applied Catalysis A: General,* **238,** 211-222 (2003).

104. A. N. Pestryakov, N. E. Bogdanchikova, and A. Knop-Gericke, "Alcohol selective oxidation over modified foam-silver catalysts," *Catalysis Today,* **91-92,** 49-52 (2004).

105. V. Diakov, D. Lafarga, and A. Varma, "Methanol oxidative dehydrogenation in a catalytic packed-bed membrane reactor," *Catalysis Today,* **67,** 159-167 (2001).

106. A. P. V. Soares, M. F. Portela, A. Kiennemann, L. Hilaire, and J. M. M. Millet, "Iron molybdate catalysts for methanol to formaldehyde oxidation: effects of Mo excess on catalytic behaviour," *Applied Catalysis A-General,* **206,** 221-229 (2001).

107. A. Soares and M. Portela, "Methanol selective oxidation to formaldehyde over iron-molybdate catalysts," *Catalysis Reviews-Science and Engineering,* **47,** 125-174 (2005).

108. H. Adkins and W. R. Peterson, "The oxidation of methanol with air over iron, molybdenum, and iron-molybdenum oxides," *Journal of the American Chemical Society,* **53,** 1512-1520 (1931).

109. A. R. Chauvel, P. R. Courty, R. Maux, and C. Petitpas, "Select best formaldehyde catalyst," *Hydrocarbon Processing,* **52,** 179-184 (1973).

110. P. F. Kerr, A. W. Thomas, and A. M. Langer, "The nature and synthesis of ferrimolybdite," *The American Mineralogist,* **48,** 14-32 (1963).

111. G. Alessandrini, L. Cairati, P. Forzatti, P. L. Villa, and F. Trifiro, "Chemical, structural and catalytic modifications of pure and doped iron (III) molybdate," *Journal of the Less-Common Metals,* **54,** 373-386 (1977).

112. M. Carbucicchio, "Mossbauer analysis of Fe_2O_3-MoO_3 supported on SiO_2 and Al_2O_3 ," *Journal of Chemical Physics,* **70,** 784-787 (1979).

113. P. Forzatti, P. L. Villa, N. Ferlazzo, and D. Jones, "Multicomponent catalysts for the oxidation of propylene to acrolein - $Fe_2(MoO_4)_3$ doped with Bi or Te," *Journal of Catalysis,* **76,** 188-207 (1982).

114. N. Pernicone, "MoO_3-$Fe_2(MoO_4)_3$ catalysts for methanol oxidation," *Journal of the Less Common Metals,* **36,** 289-297 (1974).

115. F. Trifiro, S. Notarbar, and I. Pasquon, "Nature of active component in a Fe_2O_3-MoO_3 Catalyst .II. Variations occurring during high temperature treatment," *Journal of Catalysis,* **22,** 324-& (1971).

116. M. P. House, A. F. Carley, R. Echeverria-Valda, and M. Bowker, "Effect of varying the cation ratio within iron molybdate catalysts for the selective oxidation of methanol," *Journal of Physical Chemistry C,* **112,** 4333-4341 (2008).

117. J. Aruanno and S. Wanke, "Effect of high temperature treatment on the properties of Fe-Mo oxide catalysts," *The Canadian Journal of Chemical Engineering,* **53,** 301-307 (1975).

118. A. P. V. Soares, M. F. Portela, and A. Kiennemann, "A comparison of iron molybdate catalysts for methanol oxidation prepared by coprecipitation and new sol-gel method," *3rd World Congress on Oxidation Catalysis,* **110,** 807-816 (1997).

119. J. Li, Y. Zhang, C. Liu, and Q. Zhu, "Improvement in reactivity, reproducibility and stability of Fe-Mo catalysts by wet mixing," *Catalysis Today,* **51,** 195-199 (1999).

120. P. Forzatti, "On the deactivation of Fe_2O_3-MoO_3/SiO_2 catalysts in the oxidation of methanol to formaldehyde," *Reaction Kinetics and Catalysis Letters,* **20,** 213-218 (1982).

121. L. Cairati, M. Carbucicchio, O. Ruggeri, and F. Trifiro, "Study of the interaction of Fe_2O_3-MoO_3 with several supports," in *Studies in Surface Science and Catalysis*, B. Delmon, P. Grange,P.Jacobs and G.Poncelet, ed., 279-292 (Elsevier, 1979).

122. X. Carner, J. F. Lambert, and M. Che, "Geochemistry and catalysts preparation: Alumina as a chemical reactant in the synthesis of MoO_x/Al_2O_3 and WO_x/Al_2O_3 systems," in *Studies in Surface Science and Catalysis*, Avelino Corma, Francisco V. Melo,Sagrario Mendioroz and José Luis G.Fierro, ed., 1049-1054 (Elsevier, 2000).

123. L. M. Plyasova, R. F. Klevtsov, S. V. Borisov, and L. M. Kefelo, "Crystal structure of iron molybdate," *Doklady Akademii nauk SSSR,* **167,** 84-& (1966).

124. M. H. Rapposch, J. B. Anderson, and E. Kostiner, "Crystal-structure of ferric molybdate, $Fe_2(MoO_4)_3$," *Inorganic chemistry,* **19,** 3531-3539 (1980).

125. A. W. Sleight, B. L. Chamerl, and J. F. Weiher, "Magnetic mossbauer and structural studies on 3 modifications of $FeMoO_4$," *Inorganic chemistry,* **7,** 1093-& (1968).

126. A. Andersson, M. Hernelind, and O. Augustsson, "A study of the ageing and deactivation phenomena occurring during operation of an iron molybdate catalyst in formaldehyde production," *Catalysis Today,* **112,** 40-44 (2006).

127. T. Kim, B. Ramachandra, J. Choi, M. Saidutta, K. Choo, S. Song, and Y. Rhee, "Selective oxidation of methanol to formaldehyde using modified iron-molybdate catalysts," *Catalysis Letters,* **98,** 161-165 (2004).

128. M. Bowker, R. Holroyd, A. Elliott, P. Morrall, A. Alouche, C. Entwistle, and A. Toerncrona, "The selective oxidation of methanol to formaldehyde on iron molybdate catalysts and on component oxides," *Catalysis Letters,* **83,** 165-176 (2002).

129. M. P. House, M. D. Shannon, and M. Bowker, "Surface segregation in iron molybdate catalysts," *Catalysis Letters,* **122,** 210-213 (2008).

130. W. E. Farneth, F. Ohuchi, R. H. Staley, U. Chowdhry, and A. W. Sleight, "Mechanism of partial oxidation of methanol over MoO_3 as studied by temperature-programmed desorption," *Journal of Physical Chemistry,* **89,** 2493-2497 (1985).

131. E. Soderhjelm, M. P. House, N. Cruise, J. Holmberg, M. Bowker, J. Bovin, and A. Andersson, "On the synergy effect in MoO_3-$Fe_2(MoO_4)_3$ catalysts for methanol oxidation to formaldehyde," *Topics in Catalysis,* **50,** 145-155 (2008).

132. K. Routray, W. Zhou, C. J. Kiely, W. Grünert, and I. E. Wachs, "Origin of the synergistic interaction between MoO_3 and iron molybdate for the selective oxidation of methanol to formaldehyde," *Journal of Catalysis,* **275,** 84-98 (2010).

133. N. Pernicone, F. Lazzerin, G. Liberti, and G. Lanzavecchia, "On the mechanism of CH_3OH oxidation to CH_2O over MoO_3/$Fe_2(MoO_4)_3$ catalyst," *Journal of Catalysis,* **14,** 293-302 (1969).

134. G. Liberti, N. Pernicon, and S. Soattini, "Pulse microreactor study of methanol oxidation over MoO_3-$Fe_2(MoO_4)_3$ catalyst," *Journal of Catalysis,* **27,** 52-57 (1972).

135. Y. H. Ma and S. J. Kmiotek, "Deactivation kinetics of ferric molybdate catalysts," *Journal of Catalysis,* **109,** 132-142 (1988).

136. M. Niwa, M. Mizutani, M. Takahashi, and Y. Murakami, "Mechanism of methanol oxidation over oxide catalysts containing MoO_3 ," *Journal of Catalysis,* **70,** 14-23 (1981).

137. E. Santacesaria, M. Morbidelli, and S. Carra, "Kinetics of the catalytic-oxidation of methanol to formaldehyde," *Chemical Engineering Science,* **36,** 909-918 (1981).

Chapter 2 Introduction to electron microscopy techniques and their application to complex oxide catalysts

2.1 Introduction

Electron microscopy has and continues to be a valuable tool for the study of catalyst materials for revealing their morphology, crystallography, microstructure and chemical composition from the macroscopic to the atomic scale. Most complex oxide heterogeneous catalyst materials are composed of more than one phase that often exhibit different morphologies. Some examples of the V-P-O, Nb-P-O and Fe-Mo-O catalyst systems have been described in Chapter 1, in which a number of various phases can co-exist. Usually scanning electron microscopy and transmission electron microscopy are firstly used to observe the general morphology of the materials. Electron diffraction can then be used for the structural characterization of these materials in order to determine the presence (or absence) of a specific phase and the orientation of the crystal. High resolution transmission electron microscopy and scanning transmission electron microscopy allow one to further examine local structure at the surface or within the bulk of these materials at the atomic level. X-ray energy dispersive spectroscopy and electron energy loss spectroscopy in the TEM can provide elemental analysis and chemical information (*e.g.* chemical bonding and oxidation states). In view of the importance of electron microscopy, a review of the literatures with respect to its applications to complex oxide catalyst systems is warranted. The electron microscopy applications described here will mainly focus on the studies of V-P-O, Fe-Mo-O, niobium-containing complex oxides and other related complex oxide catalysts.

2.2 Scanning electron microscopy and its application to the complex oxide catalysts

Scanning electron microscopy (SEM) is one of the most intuitive techniques available to image a sample. A schematic diagram of a typical scanning electron microscope is presented in Figure 2.1. In SEM, an electron beam produced by an electron gun (*i.e.* thermionic, Schottky or field emission) is accelerated down the column at a potential of 0.5 - 30 kV. The beam is focused into a small probe by condenser lenses and then rastered across the specimen surface by scan coils. Through various electron beam-specimen interactions, secondary electrons (SE) and/or backscattered electrons (BSE) exiting the surface of the specimen are captured by the corresponding electron detector (either SE or BSE detector). The captured signals at each pixel are used to modulate the intensity of a synchronously rastered image on a TV screen. The magnification (M) of the SEM micrograph is given by the equation 2.1:

$$M = A_{scr}/A_{sca} \quad (2.1)$$

where A_{sca} is the scanned area on the specimen and A_{scr} is the corresponding area of the display screen. The spatial resolution of a SEM is mainly determined by the size of the electron probe: the smaller the probe diameter, the higher resolution in the SEM image.

The interpretation of an SEM micrograph to a first approximation is reasonably straightforward. The contrast observed in a typical SEM micrograph is mainly due to the surface topology if the SE signal is captured or due to the atomic number differences if the BSE signal is employed. SEM has been used frequently in this project to obtain information about the general morphology of powder catalyst specimens.

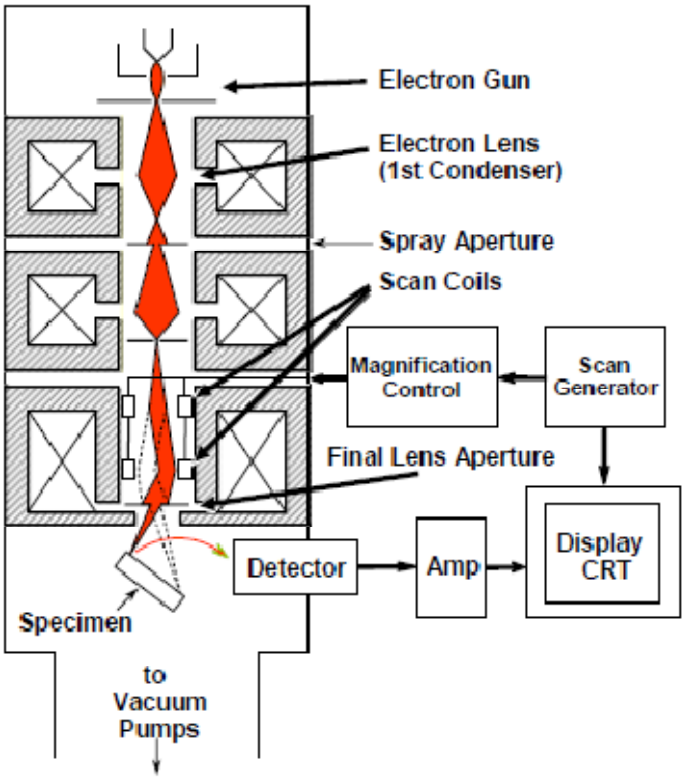

Figure 2.1 Schematic diagram of a typical scanning electron microscope showing the electron gun, lenses, scan coils and detector.[1]

The application of SEM to reveal the morphology of V-P-O materials can be found in many studies. In Chapter 1, sub-section 1.2.2, Figure 1.5, three typical morphologies of $VOHPO_4 \cdot 0.5H_2O$ materials observed by SEM are presented, namely the block-type morphology obtained from the VPA route, the rhomboidal shaped platelet-type morphology produced from the VPO route and the rosette-type morphology generated from the VPD route (when the primary alcohol is used.). The diversity of the morphologies in the V-P-O catalyst system has been further illustrated by Kiely *et al.*[2] They showed that α_I-$VOPO_4$ and α_{II}-$VOPO_4$ tend to form platelet-type morphologies (Figs. 2.2(a)(b)), whereas β-$VOPO_4$ adopts an angular morphology (Fig. 2.2(c)). γ-

$VOPO_4$ is mainly composed of thin platelets (Fig. 2.2(d)) and δ-$VOPO_4$ consists of irregularly shaped particles (Fig. 2.2(e)).

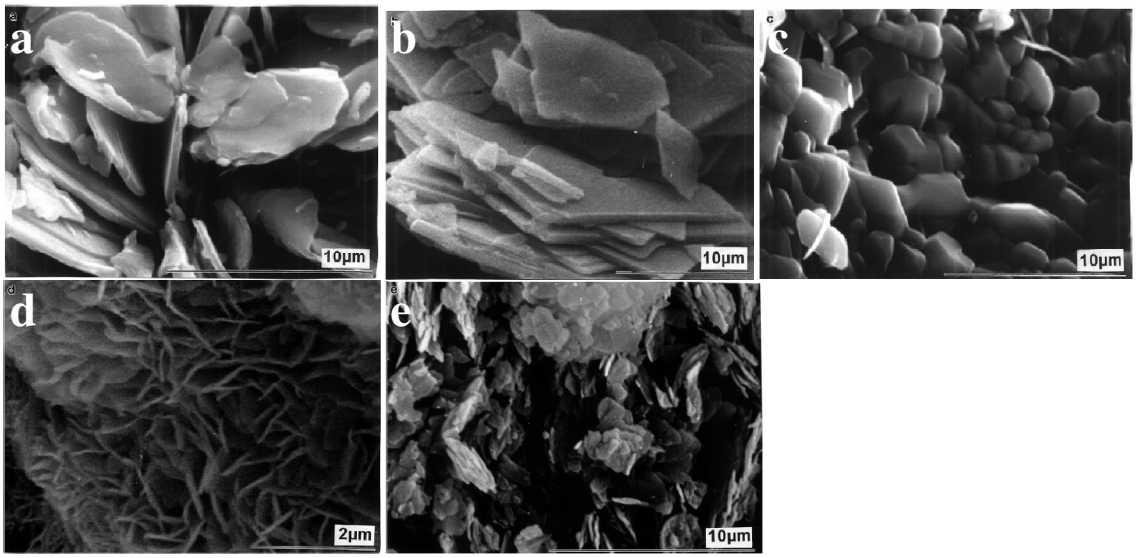

Figure 2.2 Representative SEM micrographs of standard $VOPO_4$ phases, such as (a) α_I-$VOPO_4$, (b) α_{II}-$VOPO_4$, (c) β-$VOPO_4$, (d) γ-$VOPO_4$ and (e)δ-$VOPO_4$.[2]

2.3 Transmission Electron Microscopy

Transmission Electron Microscopy (TEM) not only provides morphological information of samples at a much higher magnification than SEM, but can also reveal the crystalline structure of the sample by electron diffraction. The major operating difference in TEM from SEM is that a parallel beam of incident electrons is kept stationary and transmitted through a thin specimen, instead of being focused and rastered across a bulk specimen. A schematic illustration of a typical TEM column is shown in Figure 3.3. A coherent beam of electrons produced by an electron gun (*i.e.* thermionic, Schottky or field emission) with energies between 80kV and 200kV is transferred down to the specimen via the condenser lens system. This incident electron beam can be either a parallel beam or a focused probe depending on the particular technique to be applied.

After the incident electrons have interacted with the specimen, the transmitted electrons are first transferred by the lower objective lens, and then further transferred by a set of intermediate and projector lens to form either an image or a diffraction pattern on the fluorescent screen. Typically the transmitted electrons (*i.e.* non-scattered and elastically scattered electrons) passing through the thin specimen contain the morphological and crystallographic information on the sample, while the in-elastically scattered electrons contain the compositional information.

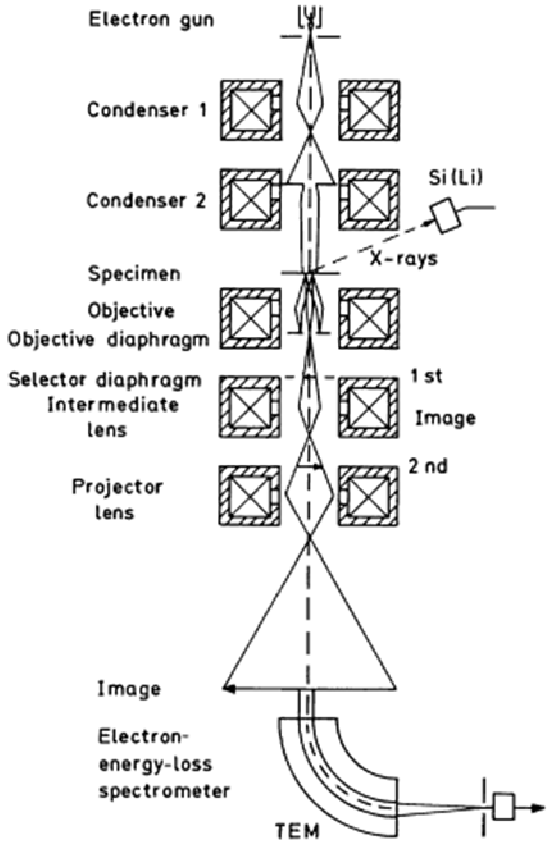

Figure 2.3 Schematic illustration of a transmission electron microscope showing basic components including the electron gun, condenser lenses, the specimen, the objective lens, the intermediate lens, the projector lens and chemical analysis components (*i.e.* energy-dispersive X-ray spectroscometer (XEDS) and electron energy loss spectrometer (EELS) which will be described later).[3]

2.3.1 Bright Field and Dark Field imaging in TEM

In a conventional TEM, image contrast is formed because of spatial variations in the intensities of electrons detected by the recording device. The three primary contrast mechanisms at play are (i) mass/thickness contrast, (ii) diffraction contrast and (iii) phase contrast. Mass/thickness contrast is formed due to the fact that thicker or higher-Z regions of the specimen absorb and/or scatter more electrons off the optic axis. Hence fewer electrons from these regions are captured by the fluorescent screen giving rise to darker areas in bright field images. Diffraction contrast is normally observed when a particular set of Bragg-scattered electrons are used to form an image, which show brighter areas (specific to region exhibiting strong Bragg-scattering) and darker areas (where Bragg diffractions are weak or non-existent). Phase contrast is achieved by allowing two or more electron beams with different phases to pass through the objective aperture, and interfere with each other to form a final image. This latter type of contrast is often displayed as moiré fringes and Fresnel fringes in low magnification TEM images, and lattice fringes in high resolution TEM (HR-TEM) which will be described later. Further details of these various image contrast mechanisms can be found in Williams and Carter.[4]

When the TEM is operated in the imaging mode, an objective aperture is placed on the back focal plane (BFP) of the objective lens, which selects either the direct beam or a diffracted beam to form an image. When the direct beam is selected by the objective aperture (Fig. 2.4(a)), the diffracted electrons are excluded and only the non-scattered and low angle inelastically scattered electrons are included in a bright field transmission electron microscopy (BF-TEM) image. When a diffracted beam selected by the objective

aperture is used (Fig. 2.4(b)(c)), the image formed is known as the dark field transmission electron microscopy (DF-TEM) image. Two different DF-TEM imaging modes are normally used, namely (i) displaced aperture DF-TEM in which the objective aperture is displaced to select the off-axis diffracted beam (Fig. 2.4(b)) and (ii) centered DF-TEM in which objective aperture is centered but the diffracted beam is tilted passing through the objective aperture (Fig. 2.4(c)). DF-TEM, to a first approximation, shows a complementary contrast to BF-TEM images.

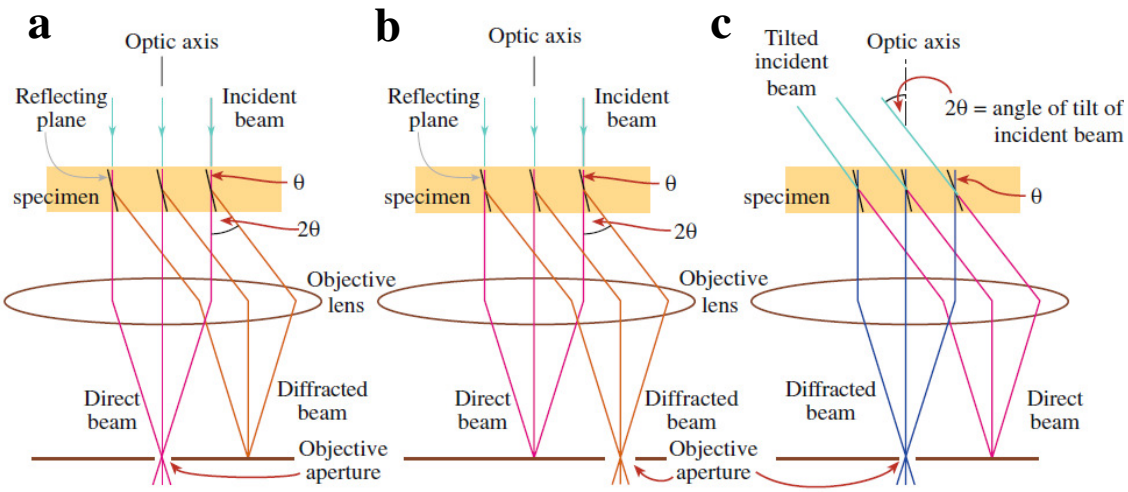

Figure 2.4 Ray diagrams in the TEM of (a) BF imaging mode, (b) DF imaging mode (displaced objective aperture) and (c) DF imaging mode (centered objective aperture).[4]

2.3.2 Selected area electron diffraction in TEM

Electron diffraction in the TEM bears a similarity to X-ray diffraction and follows Bragg's law, where

$$n\lambda = 2d_{hkl}\sin\theta \qquad (2.2)$$

In equation 2.2, n is an integer, λ is the wavelength of the incident electron beam, d_{hkl} is the spacing between the specific *hkl* planes and θ is the angle between the incident beam and the scattering planes. Bragg's law is a manifestation of the constructive interference

of elastically scattered coherent electrons in a periodic crystalline lattice. A structure factor, F_{hkl} (see eqn. 2.3), is often used to describe the elastic scattering of these coherent electrons from a unit cell of a thin crystal.

$$F_{hkl} = \sum_i f_i e^{2\pi i(hx_i + ky_i + lz_i)} \quad (2.3)$$

In equation 2.3 f is the atomic scattering factor which is related to the amplitude of a scattered wave, *hkl* is the index of a specific plane and x,y,z represent the fractional atomic coordinates of atoms in the unit cell. This equation implies that structure factors can be evaluated by multiplying the atomic scattering factor f_i for each atom i with a coordinate (x_i,y_i,z_i), with a phase factor that takes into account the phase difference of electrons scattered by different *hkl* planes. Hence the intensity of each *hkl* spots in the electron diffraction pattern can be simulated by the calculation of such structure factors for this given structure as $I \sim (F_{hkl})^2$. It should be noted that this type of the simulated electron diffraction pattern is known as the 'kinematical' diffraction pattern. Kinematical diffraction theory mainly ignores the effect of multiple scattering events (dynamical scattering) that can occur during the passage of electrons through the thin specimen. Kinematical theory considers the specimen to be very thin and flat. In reality, the kinematical theory needs to be modified to take into account the multiple scattering effects and leads to a more accurate theory- dynamical diffraction theory. One of the most successful mathematical discriptions of this dynamical theory is presented by Howie and Whelan[5] using coupled partial differential equations (or the so-called Howie-Whelan equations), in which only the interactions between two beams, namely the incident beam and the Bragg-diffracted beam are considered.

In the diffraction mode of TEM, a selected area electron diffraction (SAED) aperture is located in the image plane of the objective lens, which can be used to select a specific area of the specimen for analysis. A diffraction pattern from this selected area can then be displayed on the fluorescent screen. This technique is known as the selected area electron diffraction (SAED) and the diffraction patterns recorded are termed the selected area electron diffraction patterns (SADP's). The SAED technique is very useful for determining the crystallographic structure and orientation relative to the incident beam direction of individual particles in complex oxide catalysts.

The two operating modes- the imaging mode and the diffraction mode in TEM are shown schematically in Figure 2.5. In the imaging mode (Fig. 2.5(a)), an objective aperture is placed on the back focal plane (BFP) of the objective lens to select either the direct beam or the diffracted beam from which to form an image. The strength of the intermediate/projector lens system is automatically adjusted to select the image plane of the objective lens as its object and then projects a magnified image on the screen. In diffraction mode (Fig. 3.5(b)) however, the SAED aperture is located on the image plane and the intermediate/projector lens system is adjusted to select the back focal plane of the objective lens as its object, which then projects an electron diffraction pattern of the specimen onto the screen.

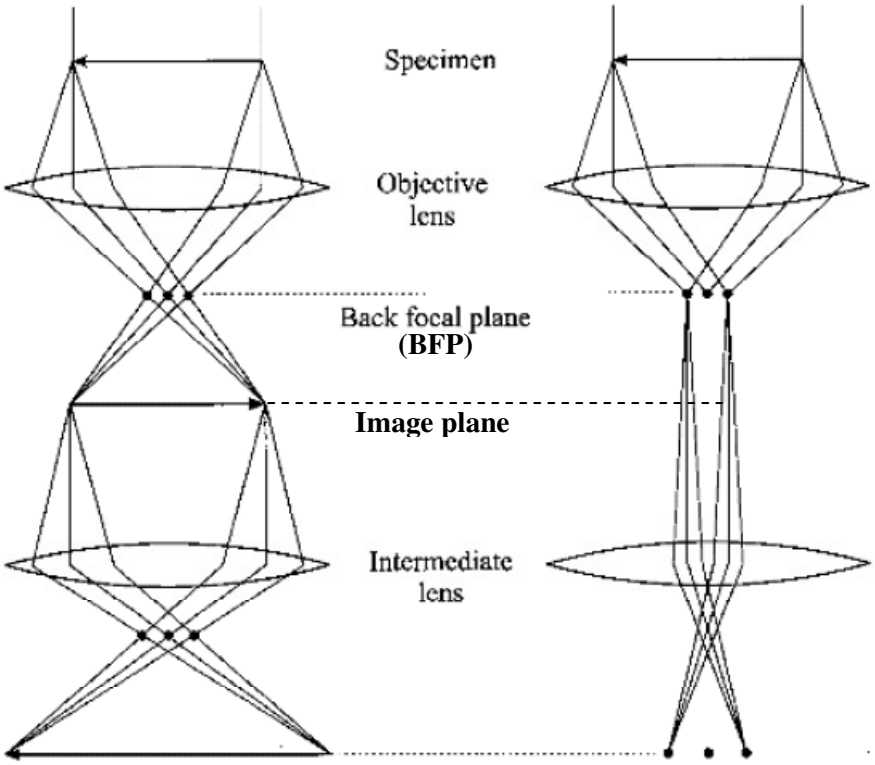

Figure 2.5 Simplified schematic diagram showing two basic modes in TEM: (a) the imaging mode- where the image plane of the objective lens is projected onto the screen and (b) the diffraction mode- where the back focal plane (BFP) of the objective lens is projected onto the screen.[6]

2.4 Chemical analysis in the electron microscope

2.4.1 X-ray energy dispersive spectroscopy

X-ray energy dispersive spectroscopy (XEDS; also known as EDS or EDX) is one the most widely used compositional analysis method in the analytical electron microscopy (AEM). A high energy incident electron collides with an atom of the sample and ejects an inner orbital electron thus leaving a hole in that shell (*e.g.* the K shell in Fig. 2.6). This hole would then be filled by an electron dropping down from a higher energy shell (*e.g.* the L shell in Fig. 2.6) resulting in an energy loss between the two shells, which is known as a relaxation process. This excess energy can be emitted either by (i)

the ejection of a second electron - an Auger electron or by (ii) the emission of a characteristic X-ray, which is captured by an XEDS spectrometer (*e.g.* Si(Li) detector). The energy of this characteristic X-ray is given by eqn. 2.4:

$$\Delta E = h\nu = E_2 - E_1 \qquad (2.4)$$

where E_1 and E_2 represent the electron energies at the initial state and final state for the electron undergoing the transition, respectively, h is Planck's constant and ν is the frequency of this characteristic X-ray.

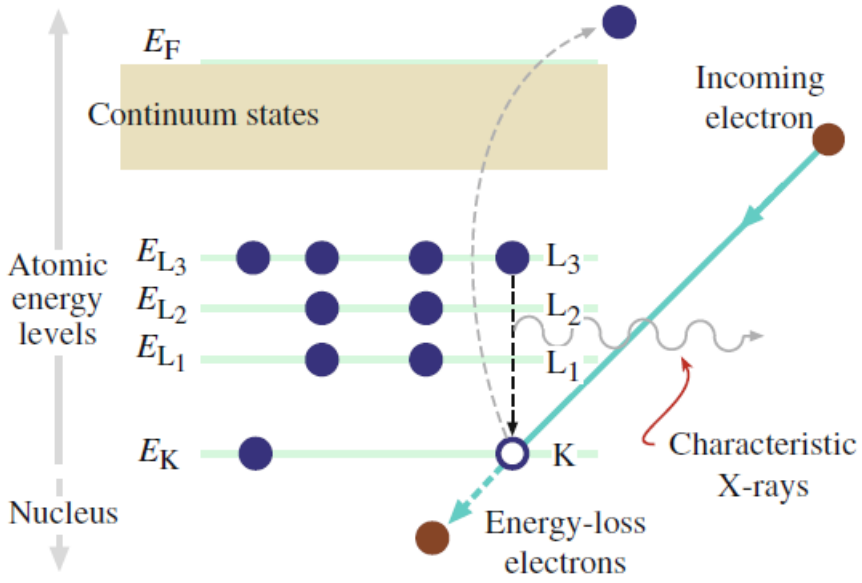

Figure 2.6 Schematic illustration of the generation of characteristic X-rays and energy-loss electrons.[4]

2.4.2 Electron energy loss spectroscopy

Another powerful analytical method incorporated in the AEM is electron energy loss spectroscopy (EELS). For the same ionization process described above (Fig. 2.6), those inelastically scattered energy-loss electrons of the incident beam are collected by a post specimen spectrometer to form an EELS spectrum. A typical EELS spectrum plots energy loss on the horizontal axis and electron counts on the vertical axis. The energy

loss of the incident electron is closely related to the binding energy and kinetic energy of the ejected electron, which can be used to determine local chemical, bonding and electronic information of the sample under examination. It should be noted that EELS is often used as a complementary technique to XEDS in terms of elemental analysis. XEDS is easy to use, intuitive to interpret and sensitive to most elements, especially heavy elements due to the fact that the characteristic X-ray generation efficiency increases with increasing atomic number (Z). The EELS spectrum, however is more difficult to interpret, but can provide a larger amount of chemical information (*e.g.* chemical composition, ionization state, dielectric constant and specimen thickness), and is much more sensitive to lighter elements.

It should be noted that both the XEDS and EELS techniques are available in the TEM and STEM (see section 2.6) microscopes and can provide elemental and chemical information from the micron down to nano-scale. In addition STEM-XEDS and STEM-EELS, due to the development of the probe corrector, now offer the ability to perform atomic scale chemical analysis.

2.5 Example applications of imaging, SAED analysis and chemical analysis in TEM to complex oxide catalysts

Using such methods (BF-/DF-TEM and SAED) the structural transformation of the $VOHPO_4 \cdot 0.5H_2O$ precursor to the $(VO)_2P_2O_7$ activated catalyst has been investigated.[7] In this particular study performed by Kiely *et al.*,[7] a $VOHPO_4 \cdot 0.5H_2O$ platelet type precursor was prepared via the VPO route and then activated under identical reaction conditions (400 °C, 1.5% *n*-butane/air) for four different times-on-stream,

namely 0.1, 8, 84 and 132 hours. The four partially activated catalysts, denoted as VPO-0.1, VPO-8, VPO-84 and VPO-132, respectively, were then examined in the TEM to follow any substantial phase and microstructural changes that occur during activation (see Fig. 2.7). A direct topotactic transformation from [001] $VOHPO_4 \cdot 0.5H_2O$ to [100] $(VO)_2P_2O_7$ was observed to occur at the periphery of the platelet (Figs. 2.7 and 2.8(b)). In the interior of the platelet, $VOHPO_4 \cdot 0.5H_2O$ (Fig. 2.8(a)) first transformed to the δ-$VOPO_4$ polymorph embedded in a disordered matrix (Fig. 2.8(c)) and then subsequently transformed to the final active $(VO)_2P_2O_7$ phase (Fig. 2.7(e)).

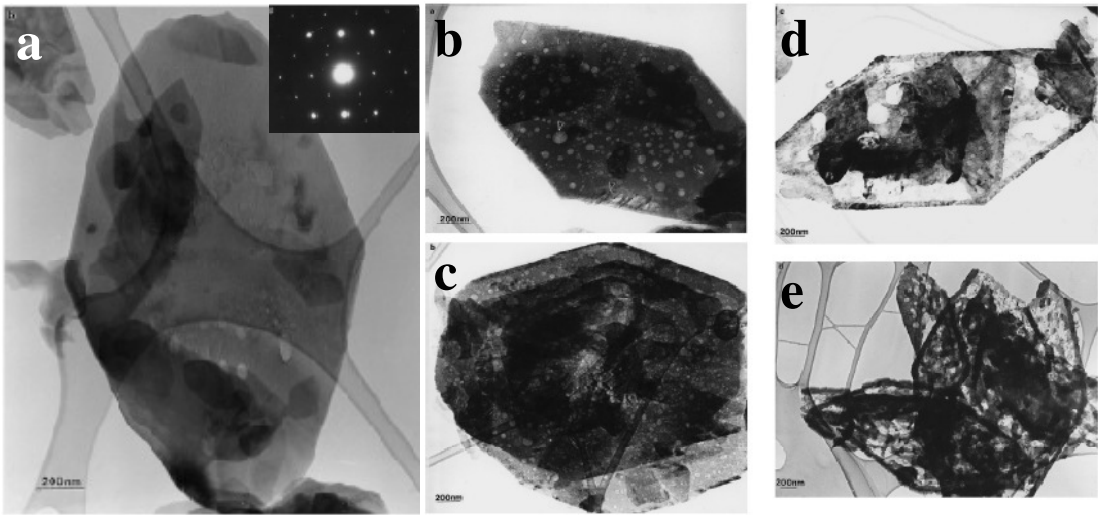

Figure 2.7 BF-TEM micrographs of (a) the $VOHPO_4 \cdot 0.5H_2O$ materials (inset SADPs correspond to [001] $VOHPO_4 \cdot 0.5H_2O$), (b) VPO-0.1, (c) VPO-8, (d) VPO-84 and (e) VPO-132 activated catalysts. [7]

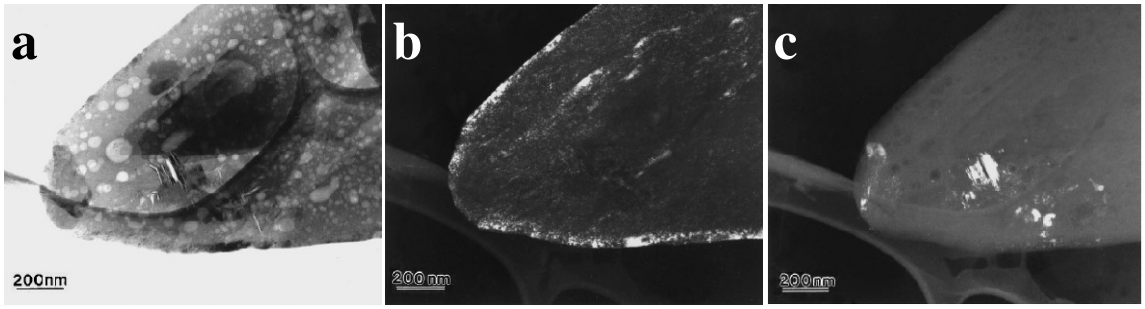

Figure 2.8 (a) BF-TEM micrograph of the VPO-0.1 sample showing a typical platelet from; corresponding DF-TEM micrographs taken in (b) $\mathbf{g}^{(VO)_2P_2O_7}$ = 024 reflection of $(VO)_2P_2O_7$ and (c) the $\mathbf{g}^{\delta\text{-}VOPO_4}$ = 022 reflection of δ-$VOPO_4$.[7]

Delimitis *et al.*[8] studied V-P-O catalysts doped with gallium, cobalt and iron, respectively, using electron microscopy. Both the undoped and doped $VOHPO_4 \cdot 0.5H_2O$ precursors were prepared by the VPO route, in which the dopant elements were refluxed with alcohols and then added into the reacting slurry. In the case of gallium-doped V-P-O catalysts,[9] materials with four different nominal Ga/V atomic ratios, namely 0.1, 0.5, 1.0 and 5.0 were prepared, catalytically tested and examined by TEM. It was found that the four doped $VOHPO_4 \cdot 0.5H_2O$ precursors show {120}-, {010}- and {100}- type forbidden reflections in the SADP's as a direct consequence of an increased point defect population caused by the Ga doping (Fig. 2.9). The perfect $VOHPO_4 \cdot 0.5H_2O$ material does not show forbidden reflections in the SADP's (Fig. 2.9(a)(b)). However, after being doped with 0.1 at% Ga, both experimental and simulated SADP's show forbidden reflections at {120}, {010} and {100} positions because of the point defect populations (*i.e.* substitutional Ga^{3+} ions and O^{2-} vacancies).

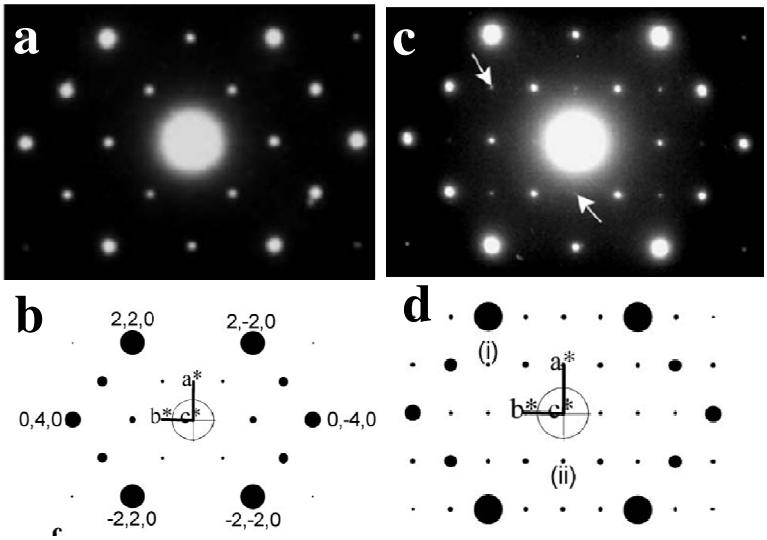

Figure 2.9 SADP's obtained along the [001] platelet normal of $VOHPO_4 \cdot 0.5H_2O$ for (a) the undoped precursor and (c) the VPO-0.1Ga precursor materials; simulated and indexed SADP's for the [001] projection of (b) the perfect $VOHPO_4 \cdot 0.5H_2O$ crystal and (d) the doped $VOHPO_4 \cdot 0.5H_2O$ containing point defects showing forbidden reflections at (i) and (ii) corresponding to {120} and {100}, respectively. [9]

In addition using the EELS technique Ayub *et al.*[10] studied the vanadium oxidation states in Bi promoted $VOHPO_4 \cdot 0.5H_2O$ and $(VO)_2P_2O_7$ materials. Their results indicate that the energy shifts of V-*L* edges correspond to the alteration in the vanadium oxidation states, which is helpful for identifying the different V-P-O phases in the active catalyst (which can have V^{4+}, V^{5+} or even V^{3+} oxidation states).

Compared with numerous electron microscopy analyses performed on V-P-O materials, only a relatively few TEM imaging and SAED analyses have been carried out on Nb-P-O and Fe-Mo-O materials. Mal *et al.*[11] synthesized hybrid and organic free mesoporous niobium oxophosphate using phenylphosphonic acid and $NbCl_5$ as precursors and sodium dodecylsulfate (SDS) as the surfactant. Following this study, Sarkar *et al.*[12] reported the synthesis of a high surface area mesoporous Nb-P-O (427 m^2g^{-1}) using niobium tartrate complex and diammonium hydrogen phosphate as precursors and tetradecyl trimethylammonium bromide (TTBr) as the template. BF-TEM imaging allowed both group to observe a mesoporous structure in the Nb-P-O material generated. Both Nb-P-O materials show a narrow pore size distribution as illustrated in Figure 2.10.

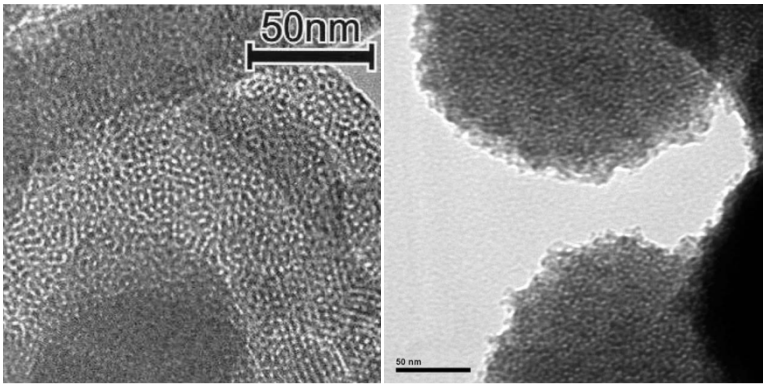

Figure 2.10 BF-TEM micrographs of (a) the mesoporous hybrid Nb-P-O material produced by Mal *et al.*[11] and (b) the mesoporous calcined Nb-P-O material produced by Sarkar *et al.*[12]

Wang *et al.*[13] have used the BF-TEM imaging as well as SAED analysis to investigate ferric molybdate nanotubes, which were produced by depositing iron hydroxide onto pre-synthesized MoO_3 nanorods and then heating them in air. BF-TEM images of the pre-synthesized MoO_3 nanorods are shown in Figure 2.11(a), and after iron hydroxide deposition core/shell $MoO_3/Fe(OH)_3$ nanorods with a shell thickness of 40 nm were produced (Fig. 2.11(b)). After calcination in air at 420 °C, a novel $Fe_2(MoO_4)_3$ nanotube is generated through a combination of the solid state diffusion reaction and the Kirkendall effect.

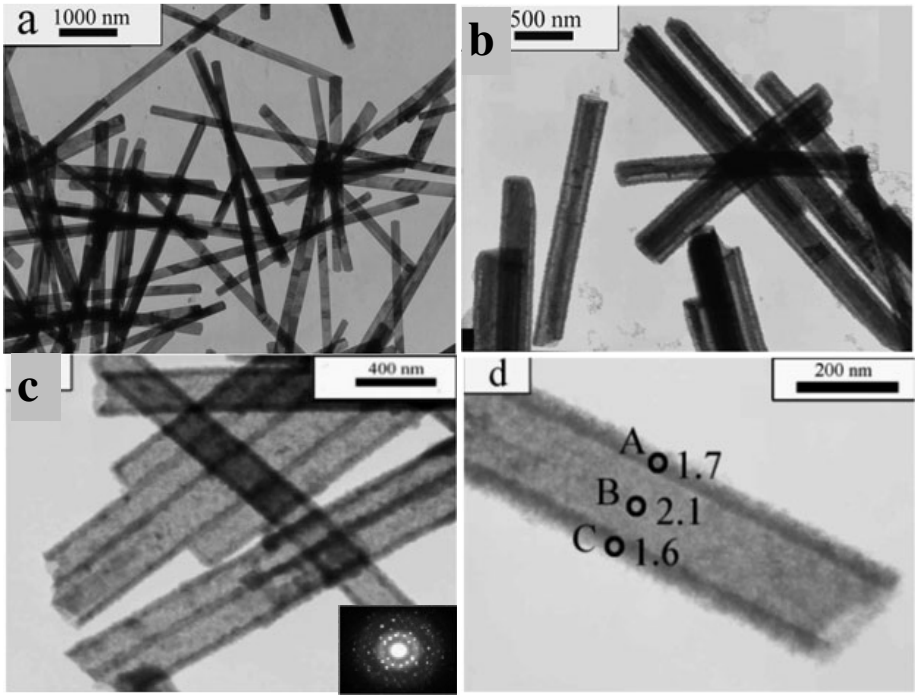

Figure 2.11 BF-TEM micrographs of (a) MoO_3 nanorods, (b) core/shell $MoO_3/Fe(OH)_3$ nanorods with a 40 nm shell, (c) $Fe_2(MoO_4)_3$ nanotubes obtained by heating samples in (b) at 420 °C in air (inset, SADP corresponds to the monoclinic $Fe_2(MoO_4)_3$ phase) and (d) enlargement of (b) showing hollow tubular structure and different Mo/Fe ratios at different positions as determined by XEDS analysis.[13]

The SADP (Fig. 2.11(c), inset) taken from the nanotube confirmed that they are the monoclinic $Fe_2(MoO_4)_3$ phase. XEDS analysis (Fig. 2.11(d)) showed that the Mo/Fe

atomic ratio at the rim region (A: 1.7 and C: 1.6) is lower than that of the central region (B: 2.1), which was attributed to a radial gradient distribution of Mo and Fe components that developed under the low calcination temperature conditions employed.[14]

2.6 High resolution transmission electron microscopy and its application to the complex oxide catalysts

2.6.1 The high resolution transmission electron microscopy

The real-space specimen information obtained using the BF-TEM and DF-TEM imaging techniques do not provide information down to the atomic level. Using high resolution transmission electron microscopy (HR-TEM), it is possible to acquire atomic scale structural information from a crystalline material. In the HR-TEM technique, lattice fringes can be produced via the phase contrast mechanism, which is achieved by the interference of two or more electron beams with different phases at the image plane. This interference finally shows an array of overlapping lattice fringes on the fluorescent screen. It should be noted that such array of intersecting lattice fringes might look like the projected atomic structure in the crystal. However it is not a direct representation of the atoms, and merely shows spacing and intersection angle information of the projected crystal plane. In order to better relate the crystal structure to its corresponding HR-TEM image, the use of image simulations is required.

Image formation in HR-TEM technique can be understood by introducing a very important function, the *Contrast Transfer Function (CTF)* of the TEM, which describes how the limiting apertures and aberrations affect the interference of various electron waves. A TEM is an optical system that conveys the information on the specimen to the

final image. Each point of the final image contains the information from many points of the specimen. Mathematically the specimen can be represented by a periodic specimen function- f(**r**) and the image can be defined as the image function- g(**r**). Hence the image function is given by equation 2.5,

$$g(\mathbf{r}) = \int f(\mathbf{r}') \, h(\mathbf{r}-\mathbf{r}')d\mathbf{r}' = f(\mathbf{r}) \lozenge h(\mathbf{r}) \qquad (2.5)$$

where h(**r**) is known as the point-spread function which describes how the image function is related back to the specimen function, and ◊ is the convolution operator. Fourier transforms of equation 2.5 gives a new equation 2.6,

$$G(\mathbf{u}) = F(\mathbf{u}) \, H(\mathbf{u}) \qquad (2.6)$$

where G(**u**) is the Fourier transform of g(**r**), F(**u**) is the Fourier transform of f(**r**), H(**u**) is the Fourier transform of h(**r**) and **u** is the spatial frequency for a particular direction. Here H(**u**) can be expressed as the product of three factors, namely (i) the apertures (the aperture function- A(**u**)), (ii) the attenuation of the wave due to the chromatic aberration (C_c) and the spatial coherence of the electron gun (the envelope function- E(**u**)) and (iii) the aberration of the lens (the aberration function B(**u**)).

If the specimen is simply considered as a "phase object" which is so thin that the absorption of electrons can be neglected, we are in a regime known as the weak-phase-object approximation (WPOA). Then the specimen function f(**r**) or f(x,y) can be expressed as:-

$$f(x,y) = 1 - i\sigma V(x,y) \qquad (2.7)$$

where V(x,y) is the crystal potential projected in the z direction and σ is the interaction constant. The specimen function now becomes a linear function with the projected crystal potential when the weak-phase-object approximation (WPOA) is applied. Substituting

this specimen function expression (eqn. 2.7) into equation 2.5, the image function can be rearranged as:-

$$\psi(x,y) = [1 - i\sigma V(x,y)] \lozenge h(x,y) \quad (2.8)$$

Considering that

$$h(x,y) = \cos(x,y) + i \sin(x,y) \quad (2.9)$$

and the intensity of the image on the screen is

$$I = \psi \psi^* = |\psi|^2 \quad (2.10)$$

then the image intensity in the HR-TEM micrographs can be expressed as:-

$$I = 1 + 2\sigma V(x,y) \lozenge \sin(x,y) \quad (2.11)$$

which is closely related to the convolution of the projected crystal potential and the imaginary part of the contrast transfer function. Hence the contrast transfer function can be re-defined only in consideration of the imaginary part of B(**u**) (which is also the imaginary part of h(x,y)),

$$T(\mathbf{u}) = A(\mathbf{u})\, E(\mathbf{u})\, 2 \sin \chi(\mathbf{u}) \quad (2.12)$$

This is known as the objective lens transfer function, where

$$\chi(u) = 2\pi/\lambda\, (C_s\lambda^4u^4/4 + \Delta f\lambda^2u^2/2) = \pi\, \Delta f\, \lambda\, u^2 + \tfrac{1}{2}\, \pi\, C_s\, \lambda^3\, u^4 \quad (2.13)$$

The above equations (equations 2.7 - 2.12) tell us that in the WPOA regime, the objective lens transfer function T(**u**) and therefore the contrast transfer function H(**u**), is mainly dependent on the phase-distortion function $\chi(u)$. This $\chi(u)$ function is expressed in the form of a phase shift- $2\pi/\lambda$ times the path difference of electron waves, which is mainly affected by the defocus (Δf) and spherical aberration (C_s). In this equation the astigmatism (C_a) is neglected due to the fact that it can be easily corrected experimentally. The effect of terms- C_s, Δf, λ and **u** on the transfer function, T(**u**), is usually presented as

a plot of T(**u**) versus **u** as described in detail by Williams and Carter.[4] The effect of the defocus (Δf) on T(**u**) as an example is shown in Figure 2.12. Those plots were generated by Java Electron Microscopy image Simulation (JEMS) for E_0 = 200 kV and C_s = 0.5 mm on JEOL JEM-2100F.

The plot of T(**u**) versus **u** in Figure 2.12 shows maximum, minimum and zero values, which resembles the sinusoidal wave function. The sign of T(**u**) (either positive or negative) indicates the image contrast of atomic columns in the HR-TEM micrographs; namely a negative T(**u**) gives rise to dark atomic column contrast with a white background, and vice versa. In order to obtain a higher resolution HR-TEM micrograph with a better image contrast, the T(**u**) value needs to keep high while having a broad range of spatial frequencies **u** (units: nm^{-1}) as shown in Figure 2.12(b).

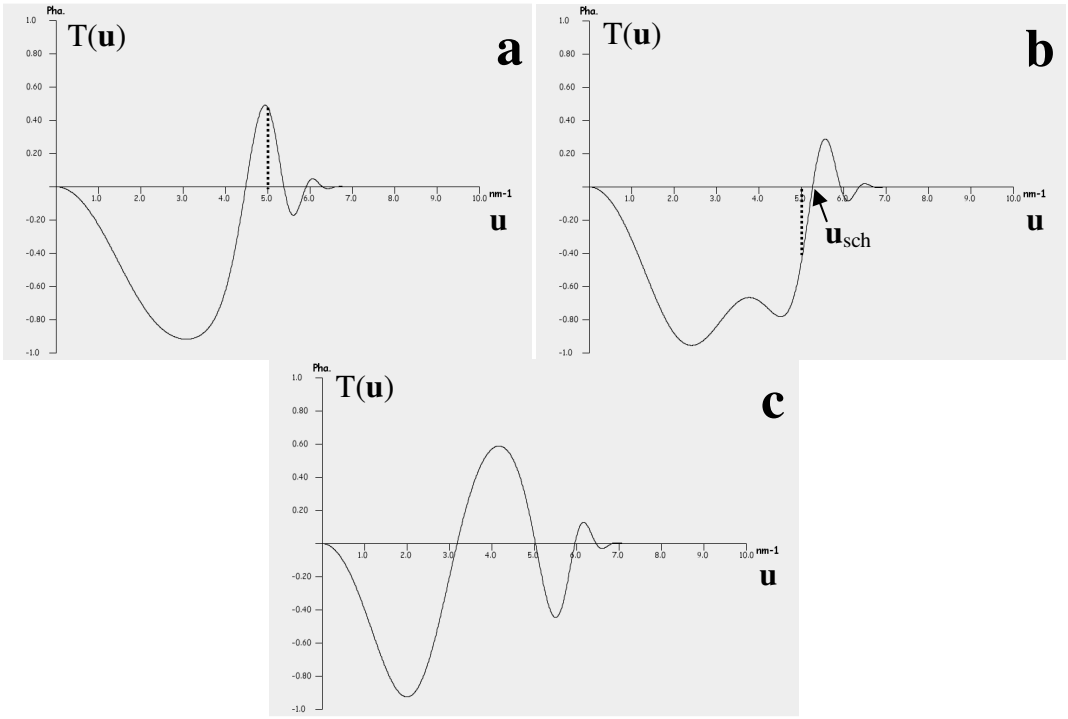

Figure 2.12 Plots of T(**u**) versus **u** at different defocus values for the JEOL JEM-2100F TEM: (a) Δf = 31.4 nm, (b) Δf_{sch} = 43.4 nm and (c) Δf = 55.4 nm. (underfocus is positive.)

Such a condition can be achieved when the first derivative of $\chi(\mathbf{u})$ over $\mathbf{u}$ equals to zero, which gives the following result:-

$$\Delta f_{sch} = - 1.2 (C_s \lambda)^{½} \quad (2.14)$$

At this special defocus value, all electron beams have almost the same constant value of the transfer function up to the first point that $T(\mathbf{u})$ crosses the zero axis at $\mathbf{u}_{sch}$. Hence nearly all electron beams are transferred through the electron microscope with identical phase, which contribute positively to the final HR-TEM image. This particular Δf_{sch} defocus condition (eqn. 2.14), which was discovered by Scherzer in 1949, is known as Scherzer defocus.[15] It can effectively offset the spherical aberration of the objective lens by underfocusing the electron microscope by tens of nanometers (*i.e.* 43.4 nm in this case, Figure 2.12(b)). The $\mathbf{u}_{sch}$ value at the Scherzer defocus condition defines the largest spatial frequency (or the smallest interplanar spacing) of a HR-TEM that is interpretable in the image, which is also known as the instrumental resolution limit. The resolution limit (r_{sch}) can be expressed as the reciprocal of $\mathbf{u}_{sch}$,

$$r_{sch} = 0.66 C_s^{0.25} \lambda^{0.75} \quad (3.15)$$

It should be noted that both the aperture function- $A(\mathbf{u})$ and the envelope function- $E(\mathbf{u})$ will also affect the transfer function. The value of $A(\mathbf{u})$ can be either 0 or 1 depending on whether the objective aperture excludes certain beams ($A(\mathbf{u}) = 0$) or includes certain beams ($A(\mathbf{u}) = 1$) for the image formation in the HR-TEM micrograph. The more complicated $E(\mathbf{u})$ function effectively damps out the higher spatial frequencies (Fig. 2.13) because of chromatic effects (the temporal envelope) and the spatial coherence (the spatial envelope) of the electron source. A consequence of the sinusoidal shape of the transfer function is that the image contrast in HR-TEM can potentially

reverse when the defocus value is changed, which makes the image interpretation more challenging. A good example of this effect is shown in Figure 2.12. Assuming there is a feature with a 0.2 nm interplanar spacing (u = 5.0 nm^{-1}) in the HR-TEM image, such feature would have a positive T(u) value in Figure 2.12(a) at defocus = 33.4 nm, but a negative T(u) value in Figure 2.12(b) at defocus = 43.4 nm. In addition other parameters such as sample thickness, aberration coefficient and beam tilt can also change the details of an HR-TEM image. Hence computer simulations of HR-TEM images are normally performed in order to better understand the relationships between the details of an image and the real projected atomic structure of the specimen. The principles of image simulations used in this project will be described in Chapter 3, section 3.4. More details about the HR-TEM can be found in the excellent book authored by Spence.[16]

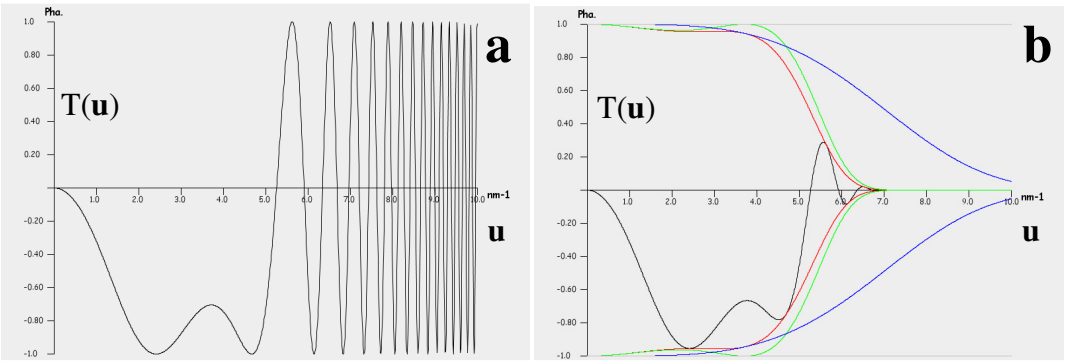

Figure 2.13 Plots of T(**u**) versus **u** (a) without the envelope function included and (b) with the envelope function included (blue- temporal envelope, green- spatial envelope, red- products of both envelopes and black- the damped T(u). (These plots were rendered by JEMS.)

2.6.2 Example applications of HR-TEM to complex oxide catalysts

HR-TEM has been widely used for identifying the crystal structure, crystal defects and the surface structure of complex oxide catalysts at the atomic scale. In Figure 2.2, BF-TEM micrographs show the phase transformation from a uniform

$VOHPO_4 \cdot 0.5H_2O$ platelet to the $(VO)_2P_2O_7$ material with block-type crystallites (ca. 50 - 100 nm) at the periphery.[7] HR-TEM allowed Kiely *et al*. to identify these crystallites to be the $(VO)_2P_2O_7$ phase viewed along the [100] direction with (010) and (001) lattice planes resolved (Figs. 2.14(a)(b)).[7] In another study of V-P-O catalysts performed by the same authors, two different projections of the block-type $(VO)_2P_2O_7$ crystallites were observed, namely the [100] projection of $(VO)_2P_2O_7$ and the [021] projection of $(VO)_2P_2O_7$ with the (200) and $(02\bar{4})$ lattice planes resolved (Fig. 2.14(c)).[2] These different atomic projections allowed them to propose a model of the oblong $(VO)_2P_2O_7$ crystallite exposing (100), (021) and $(01\bar{2})$ facets as shown in Figure 2.14(d).

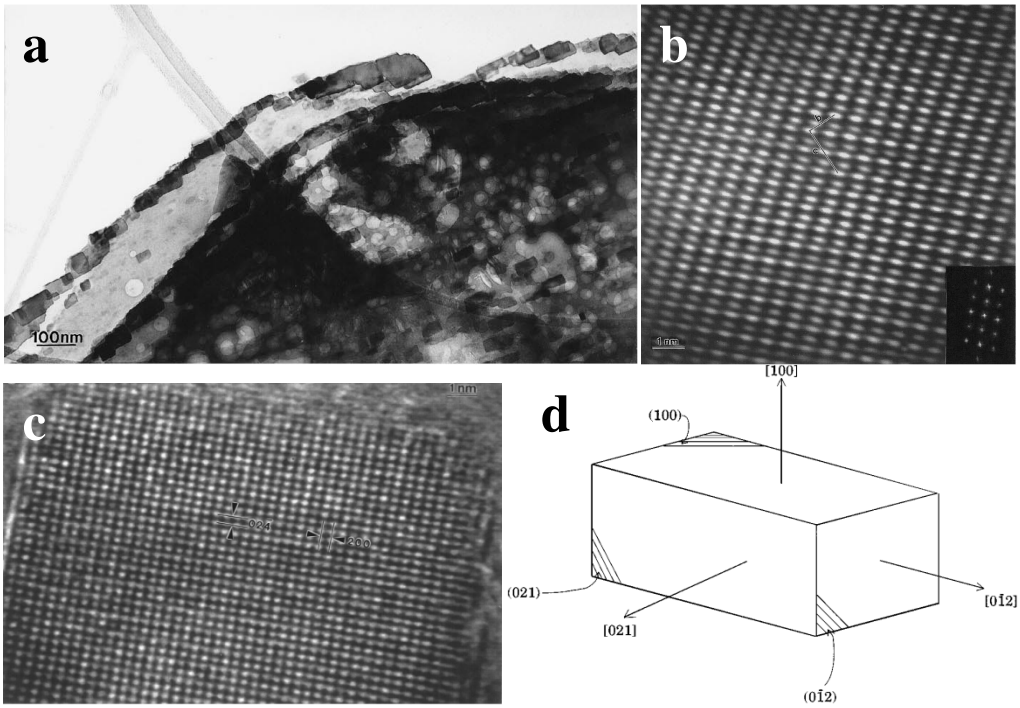

Figure 2.14 (a) BF-TEM micrograph of the rim region of the VPO-84 platelet and (b) HR-TEM micrograph of the block-type crystallites corresponding to the [100] projection of $(VO)_2P_2O_7$;[7](c) HR-TEM micrograph of the [021] projection of $(VO)_2P_2O_7$ and (d) schematic diagram of the block-type $(VO)_2P_2O_7$ crystallites.[2]

It is well known that the catalytic reactions occur on the surface of the active catalysts. HR-TEM is widely used for observing the surface structure of complex oxide catalysts. Using HR-TEM Bluhm *et al*.[17] observed that a thin adlayer of non-crystalline material (ca. 1-3 nm in thickness) is present on both the prismatic edges and basal surface planes of the active $(VO)_2P_2O_7$ crystallites. This terminating thin amorphous adlayer was believed to be a good candidate for the localization of the active sites. Such an amorphous overlayer existing on the surface of the active crystalline $(VO)_2P_2O_7$ phase has also been observed in several other TEM studies,[18,19] and a consensus is building that it may be the active material for the selective oxidation of *n*-butane to MA.

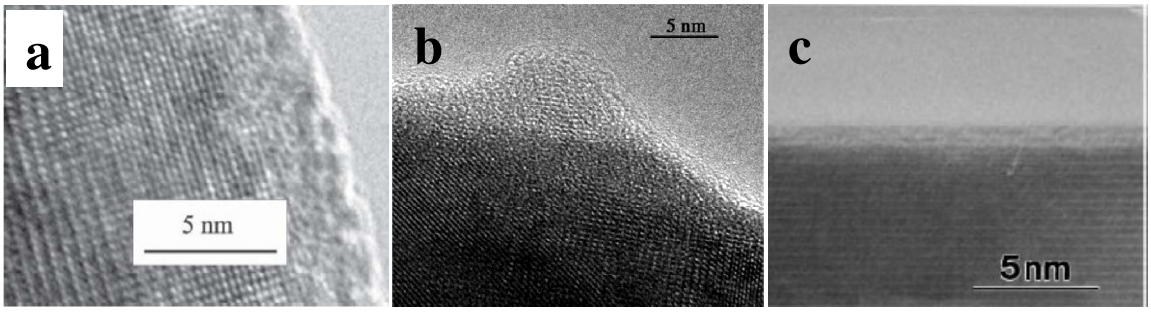

Figure 2.15 HR-TEM micrographs of (a) the activated $(VO)_2P_2O_7$ particles with a non-crystalline adlayer as observed by Bluhm *et al*.,[17] (b) the disorderd surface on the well-crystallized $(VO)_2P_2O_7$ particles reported by Hävecker *et al*.[19] and (c) the amorphous overlayer on the activated $(VO)_2P_2O_7$ crystallites as detected by Hutchings *et al*.[18]

These amorphous layers on the surface of complex oxide catalysts have also been observed in other complex oxide catalyst systems. Routray *et al*.[20] reported that a surface amorphous layer (~ 1 nm thick) is present on the surface of catalytically active stoichiometric $Fe_2(MoO_4)_3$, which is enriched in MoO_x. This MoO_x enriched amorphous overlayer is now believed to be active for the oxidation of methanol to formaldehyde. The same authors also observed an amorphous VO_x enriched layer on the surface of a $FeVO_4$ catalyst, which was attributed to be the active phase for the methanol oxidation.[21]

The presence of a disordered surface layer in complex oxide catalyst systems is not surprising, since the catalytic reactions on the aforementioned (*e.g.* V-P-O, Fe-Mo-O and Fe-V-O) are all believed to follow the Mars-van-Krevelen mechanism. According to this surface redox mechanism, lattice oxygen from the complex oxide lattice participates in the gas-phase reaction and is physically removed from the first few layers of the crystal surface, which would naturally leave vacancies in the surface structure. Eventually the surface of the crystal structure may degenerate into an amorphous overlayer. It should be noted however that most of these complex oxide catalysts are sensitive to electron beam damage, and although low electron dose settings were employed in the aforementioned studies, the possibility of having an electron induced contribution to the amorphous layer was not ruled out by any of the authors.

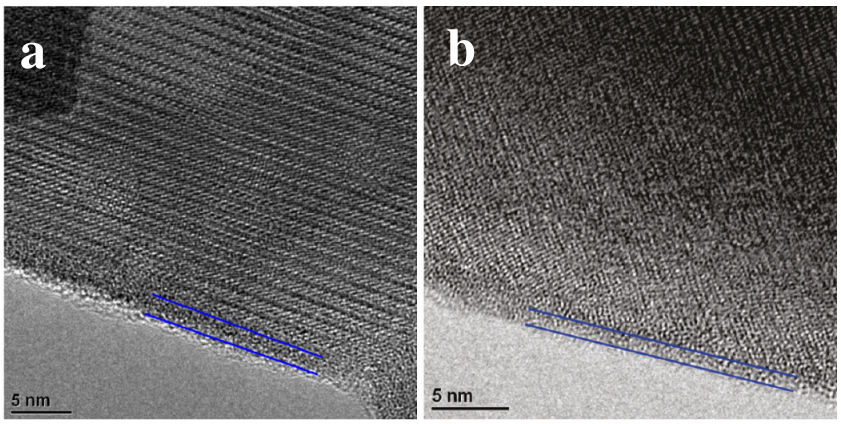

Figure 2.16 HR-TEM micrographs of (a) the bulk $Fe_2(MoO_4)_3$ catalyst with an amorphous overlayer[20] and (b) the $FeVO_4$ catalyst with an amorphous overlayer[21].

HR-TEM aided by image simulations has allowed researchers to determine the crystal structure of certain oxides by comparing the experimental HR-TEM image with the simulated HR-TEM image. A good example of this application is shown in Figure 2.17 for the investigation of the Mo-V-Nb-Te-O catalyst. This catalyst system has two phases (*i.e.* M1 and M2 phases), which are active and selective for the propane

ammoxidation.[22] The structures of both phases are rather complicated and are still under investigation. HR-TEM analysis allowed DeSanto *et al*.[23] to obtain atomically resolved lattice images of both phases as shown in Figure 2.17(a)(d). Through the image simulation using the atomic models presented in Figure 2.17(b)(e), a good agreement between the simulated image (the proposed model) and the experimental image was achieved for both M1 and M2 phases, respectively. This confirmed proposed structures of the M1 and M2 phases as derived from X-ray diffraction and neutron diffraction studies. In another example, aided by HR-TEM and image simulations, Burrows *et al*.[24] were able to observe that a cubic spinel (MgV_2O_4) phase epitaxially grows on an MgO support by matching the simulated images of MgV_2O_4/MgO and $Mg_3V_2O_8$/MgO, respectively, with experimentally obtained images.

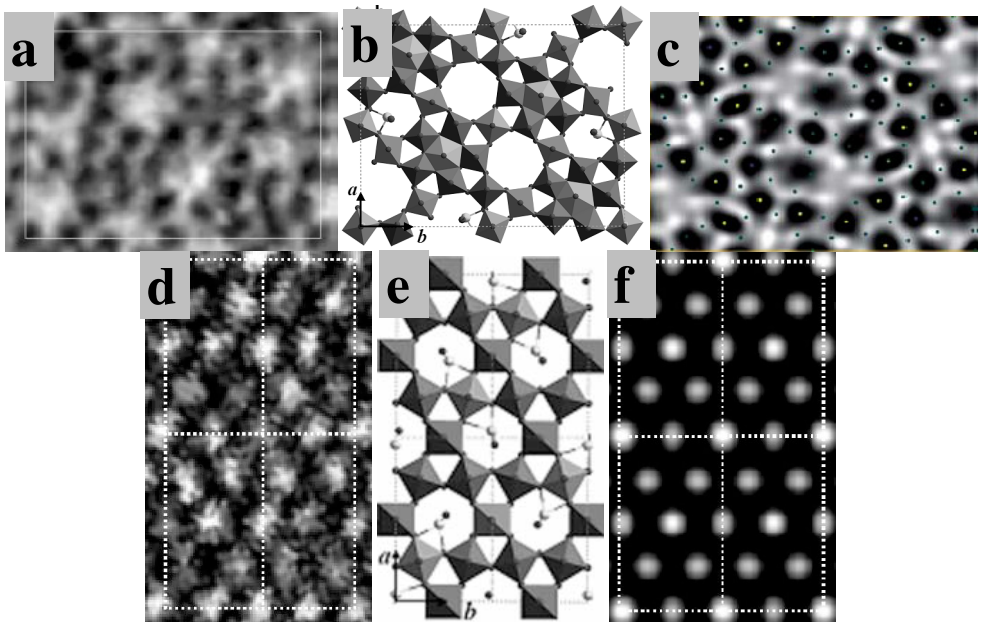

Figure 2.17 M1 phase in the [001] projection (*row 1*): (a) experimental HR-TEM micrograph, (b) the proposed atomic model and (c) the simulated HR-TEM micrograph obtained at Δf = -43nm and t = 40Å; M2 phase in the [001] projection (*row 2*): (d) experimental HR-TEM micrograph, (e) the proposed atomic model and (f) the simulated HR-TEM micrograph obtained at Δf = -43nm and t = 92Å.[23]

2.7 *In-situ* transmission electron microscopy and its application to complex oxide catalysts

The electron microscopy approaches described above are all *ex-situ* techniques, which means the samples after use in a catalytic reaction will have to be transferred from the reactor to the microscope. During this transfer step, the material would be exposed to air, which may introduce hydration or oxidation effects to the specimen, resulting in errors in the interpretation. In addition it is well known that catalysis is a dynamical process, in which the morphology and local structure of the catalyst surface can change under reaction conditions. Such changes are often vital for their catalytic behaviour. Hence the development of the *in-situ* transmission electron microscope was deemed necessary for the study of catalysts. Such an instrument can in principle provide a direct observation of the dynamical interactions (*e.g.* transient phases and surface structure modifications) between solid catalysts and gas phase reactants under slightly more realistic reaction conditions. The *in-situ* electron microscopes developed to date include *in-situ* SEM, *in-situ* TEM and *in-situ* STEM. Since the *in-situ* TEM has been the most widely applied in the study of complex oxide catalysts, the basics of *in-situ* TEM instrumentation will be outlined here.

A typical *in-situ* TEM system is shown in Figure 2.18. This instrument was developed by Gai and Boyes[25-28] by incorporating a differentially pumped gas reaction cell (also known as environmental cell or ECELL) into the electron microscope column as delineated by a rectangular frame in Figure 2.18. This ECELL mainly consists of a reaction chamber, a heating stage, a gas inlet and outlet system, a mass spectrometer and some differential pumps. A high gas pressure ranging from a few millibars to a fraction

of 1 atm can be maintained within the ECELL region while the rest of the microscope column is kept under high vacuum. This design allows the dynamic observation of samples at atomic resolution when the gas pressure is kept below a few millibars. However it should be noted that in the ECELL electrons may interact with reaction gas to produce a plasma, which is not an entirely realistic catalytic reaction atmosphere. The small gas pressure present in the ECELL inevitably causes electrons to be scattered by reactant gas molecules, effectively reducing the imaging resolution of the microscope. In order to minimize these effects, low dose illumination conditions are usually employed during the *in-situ* experiment.

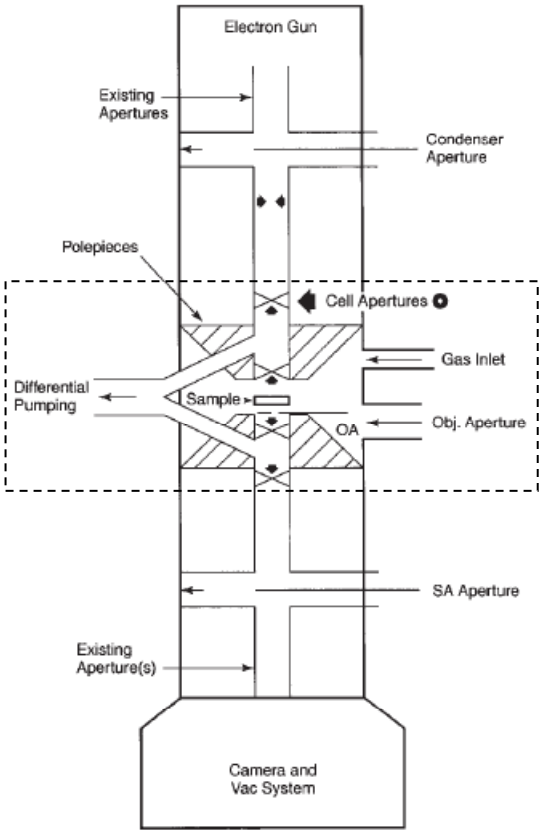

Figure 2.18 Schematic diagram of the *in situ* TEM system developed by Gai and Boyes. The ECELL is delineated by the rectangular frame.[28]

Using *in-situ* environmental TEM (ETEM) Gai *et al.*[28,29] were able to study the V-P-O catalysts under the simulated reaction conditions. By activating the $VOHPO_4 \cdot 0.5H_2O$ in N_2, they dynamically observed the topotactic phase transformation occurring as the $VOHPO_4 \cdot 0.5H_2O$ phase converts to the $(VO)_2P_2O_7$ phase.[28] A sequence of SADP's, showing the starting $VOHPO_4 \cdot 0.5H_2O$ materials (Fig. 2.19(a)), the partially transformed $VOHPO_4 \cdot 0.5H_2O$ and $(VO)_2P_2O_7$ (Fig. 2.19(b)) and the final $(VO)_2P_2O_7$ structure (Fig. 2.19(c)), are shown in Figure 2.19. This finding agrees with that reported previously by Kiely *et al.*[7]

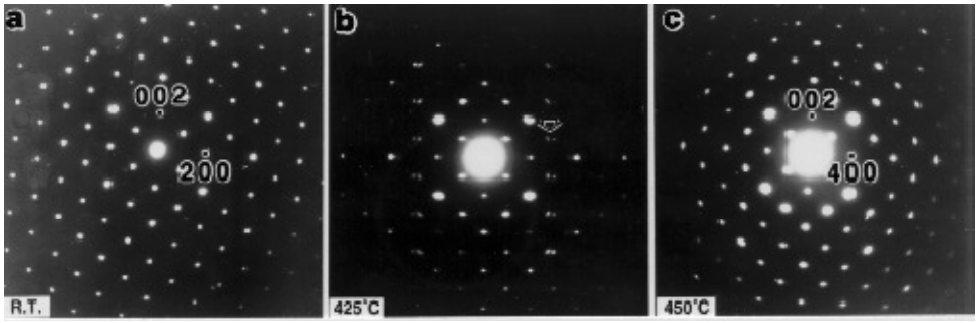

Figure 2.19 Dynamical SADPs showing the topotactic transformation from the $VOHPO_4 \cdot 0.5H_2O$ precursor to the $(VO)_2P_2O_7$ catalyst. (a) The [010] projection of $VOHPO_4 \cdot 0.5H_2O$ at room temperature (RT), (b) intermediate SADPs showing a mixture of $VOHPO_4 \cdot 0.5H_2O$ and $(VO)_2P_2O_7$ at 425 °C and (c) the [010] projection of the final $(VO)_2P_2O_7$ at 450 °C.[28]

Using *in-situ* ETEM together with the HR-TEM, Gai *et al.*[29] also reported the surface structural evolution that occurs due to the catalyst anion (O^{2-}) loss when the $(VO)_2P_2O_7$ material was used to oxidize pure *n*-butane into maleic anhydride. Figure 2.20(a) shows a HR-TEM micrograph of the $(VO)_2P_2O_7$ phase with the (201) planes resolved. The formation of extended defects along the <201> directions is shown in Figure 2.20(b), as evidenced by the inset SADP which show streaks along the <201> directions confirming that the structural disorder is present due to the defects on (201) planes. Figure 2.20(c) shows evidence of (201) lattice displacements near the surface

with defects P1 and P2 formed by a novel glide shear mechanism.[29] This glide shear can be understood as follows:- under the reducing reaction conditions a large fraction of lattice oxygen of $(VO)_2P_2O_7$ escapes from the structure and just sub-surface region leaving behind anion vacancies. To minimize the strain energy introduced by these anion vacancies, the $(VO)_2P_2O_7$ crystal simply glides along the <201> directions giving rise to extended defects in the reduced surface region, while the underlying $(VO)_2P_2O_7$ matrix remains intact. Figures 2.20(d)(e)(f) illustriate how the surface structure of $(VO)_2P_2O_7$ develops under an reducing environment. A structure with reduced anion-deficient surface layers and perfect $(VO)_2P_2O_7$ matrix (Fig. 2.20(f)) is formed through a pure glide shear mechanism along <201> directions (as arrowed in Fig. 2.20(e)). It should be noted that this experiment was carried out in a very highly reducing environment (*n*-butane), which cannot fully represent the realistic reaction conditions (1.5% *n*-butane/air). In addition the assignment of the zone axis by these authors in Figures 2.19 and 2.20 was incorrect, namely the [010] projection of $VOHPO_4 \cdot 0.5H_2O$ should be the [001] projection of $VOHPO_4 \cdot 0.5H_2O$, the [010] projection of $(VO)_2P_2O_7$ should be the [100] projection of $(VO)_2P_2O_7$. Furthermore the (201) and <201>- directions should be changed to (210) and <210>, respectively.

Gai and Labun[30] also studied the $Fe_2(MoO_4)_3$ catalysts under reaction conditions (H_2/He as well as CH_3OH/He or CH_3OH/O_2) at temperatures of ≥ 300 °C. They reported that in the reducing condition (*i.e.* under H_2/He, as well as CH_3OH/He) the defect-free $Fe_2(MoO_4)_3$ is reduced into aggregates of either β-$FeMoO_4$, α-Fe_2O_3 or a spinel (Fe_2MoO_4/Fe_3O_4). In the CH_3OH/O_2 oxidizing condition, the decomposition of $Fe_2(MoO_4)_3$ follows the same route but is not as fast as that observed in the reduction

cycle. More details concerning *in-situ* electron microscopy and its applications to various materials can be found in a book edited by Banhart.[31]

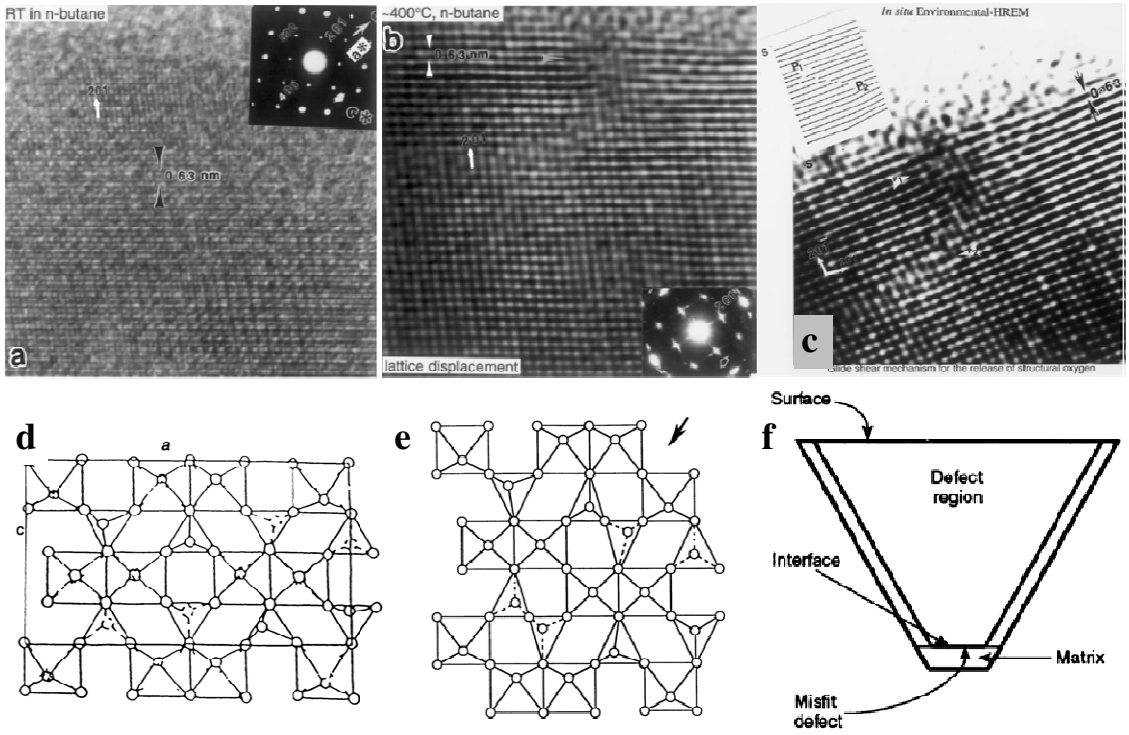

Figure 2.20 *In situ* atomic-resolution ETEM micrograph of (a) [010] $(VO)_2P_2O_7$ in *n*-butane at RT with (201) planes resolved; (b) [010] $(VO)_2P_2O_7$ in *n*-butane at 400 °C showing lattice displacement (inset SADPs shows streaks along the <201> directions); (c) surface structure of (b) showing the (201) lattice displacements close to the surface S. The resulting defects P1 and P2 are formed by a novel glide-shear mechanism. Schematic diagrams of (d) $(VO)_2P_2O_7$ in the [010] planar projection. The structure consists of edge-shared VO_6 octahedra interlinked by PO_4 tetrahedra; (e) the [010] planar projection of one layer of the $(VO)_2P_2O_7$, showing a possible pure shear model along <201> (arrowed). (f) Misfit defects extended by glide shear showing an interface between reduced anion-deficient surface regions and the $(VO)_2P_2O_7$ matrix.[26,28,29]

2.8 Scanning transmission electron microscopy based imaging and chemical analysis techniques

2.8.1 Aberration-corrected scanning transmission electron microscopy

The scanning transmission electron microscope (STEM) has features that are common to both the SEM and TEM. It differs from imaging in the conventional TEM, where a stationary parallel electron beam is used to illuminate a large area of the thin specimen. The STEM utilizes a highly focused electron beam formed by the condenser lens, which is rastered across the thin specimen using x and y scan coils. It should be noted that the scanned beam in STEM is parallel to the optic axis whereas in SEM beam scanning is achieved via tilting the electron beam. By facilitating this raster in STEM, a stationary electron diffraction pattern can be obtained in the BFP of the lower objective lens even when the beam is scanned. It is therefore analogous to using the parallel beam in a TEM. After the electron beam-specimen interactions have occurred, a number of different signals can be collected and analyzed simultaneously by a variety of recording devices, which makes the STEM one of the most powerful analytical instruments available to the electron microscopist. In this section, the various STEM imaging modes as well as some applications of STEM to complex oxide catalysts will be introduced.

Depending on the position and geometry of the post-specimen detector, three different imaging modes can be obtained in the STEM as shown schematically in Figure 2.21. From those electrons scattered at a very small angle (< 10 mrads), a bright field (BF) STEM image can be formed using the on-axis BF detector, which is comparable to the corresponding BF-TEM image. It is worth noting that these electrons near the optic axis

can also be utilized in electron energy loss spectroscopy (EELS). The annular dark field (ADF) image formed using electrons scattered further away from the optic axis, *i.e.* in the 10 - 50 mrad angular range, is similar to that of the corresponding DF-TEM image. Finally electrons scattered out to angles larger than 50 mrads can be collected by a high angle annular dark field (HAADF) detector, and are used to form an HAADF image. These large angle scattered electrons are generated mainly through Rutherford scattering from the nucleaus, and their prevalence are proportional to the 1.7 power of the atomic number ($Z^{1.7}$) of the atoms making up the specimen.[32] Hence these HAADF-STEM images are also commonly referred to Z-contrast images.

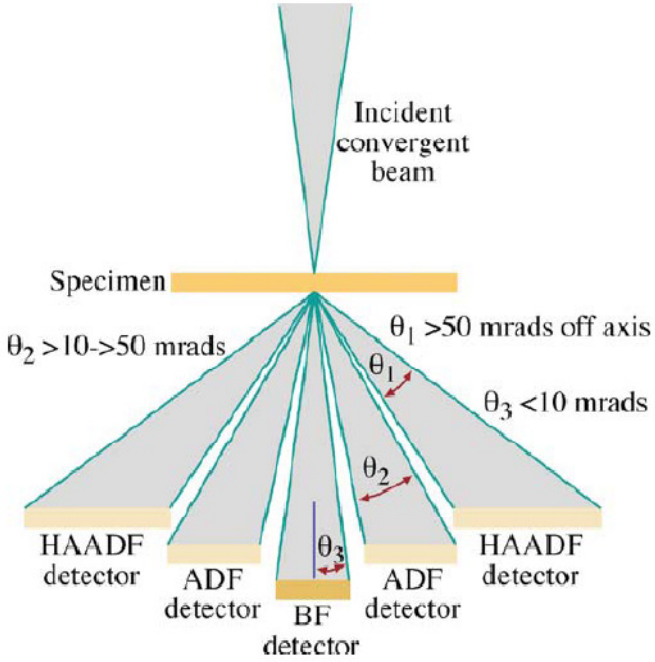

Figure 2.21 Schematic diagram showing a BF detector, an ADF detectors and an HAADF detector and their respective collection angles in a typical STEM instrument.[4]

STEM analysis can provide a wide range of structural and chemical information on the material. However the probe size of electron beam, which determines the spatial resolution obtainable in imaging and chemical analysis in the STEM mode, does not

reach the atomic level in uncorrected instrument mainly due to limitations imposed by the third order spherical aberration (C_s) of the objective lens as shown in Figure 2.22. The recent development of a probe aberration corrector in the STEM instruments has now overcome this limitation.[33-35][33] As we know, the magnetic lenses used in STEM instruments should be rotationally symmetric. However in order to correct C_s, Scherzer[36] proposed using a series of non-round magnetic components (*i.e.* quadrapole, hexapole and octapole lenses) to break the rotational symmetry of the electromagnetic lenses. These non-round lenses can produce a negative C_s value, which can then be used to offset the positive C_s value generated from the conventional cylindrical lenses.

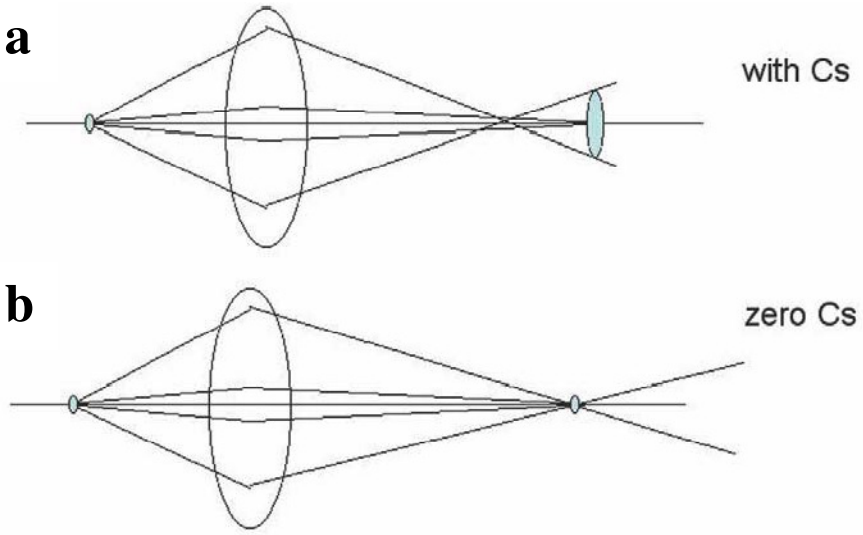

Figure 2.22 Schematic diagram showing an electron lens (a) with spherical aberration (C_s) in which electron trajectories at different angles are focused at different points on the optical axis, and (b) without spherical aberration (C_s) in which electron trajectories at different angles are all focused at the same point on the optical axis.[37]

Nowadays two different types of spherical aberration correctors (also known as C_s-correctors) are available, *i.e.* the image corrector and the probe corrector. Two brands of the probe corrector are currently on the market, namely the quadrupole-octupole (QO) corrector from Nion Co.[33,34] and the hexapole corrector from Corrected Electron Optical

Systems (CEOS) GmbH.[35] The third-generation QO corrector developed by Nion Co.,[34] which was designed for a dedicated VG STEM, consists of four quadrupoles, one combined quadrupole-octupole and one octupole. When placed between the condenser lens and the scan coils in a VG instrument, it can correct the third-order C_s, as well as fifth-order spherical aberration (C_5) and chromatic aberration (C_c). The hexapole corrector is composed of a pair of hexapoles and additional transfer lenses. It is also located between condenser lenses and objective lens of the most modern S/TEM instruments (*e.g.* the JEOL JEM-2200FS at Lehigh University).

As a combined TEM/STEM instrument with the C_s corrector, the JEOL JEM-2200FS at Lehigh University is a state-of-the-art microscope. The specimen stage is located between two objective lenses that act as the imaging lens (the lower lens) in TEM mode and probe-forming lens (the upper lens) in STEM mode. When the C_s-corrector is turned on, it offers an electron beam with a much higher probe current and a smaller probe size (Fig. 2.23(b)(d)) than can be achieved with the C_s-corrector turned-off (Fig. 2.23(a)(c)). This implies that the spatial resolution in HAADF-STEM images as well as the detection efficiency in chemical analyses (*i.e.* XEDS and EELS) can be significantly improved.[38] A good example is shown in Figure 2.23 where the Si <110> dumbbell structure with a 1.36Å interplanar spacing can easily be resolved in this probe corrected microscope.

It should be noted that nowadays modern instruments can be corrected up to fifth order aberrations. The main limitations in the performance of an electron microscope lie with higher order aberrations (*i.e.* chromatic aberration), microscope instabilities and the

local environment of the microscope (*e.g.* the mechanical and electromagnetic noise and thermal fluctuations).

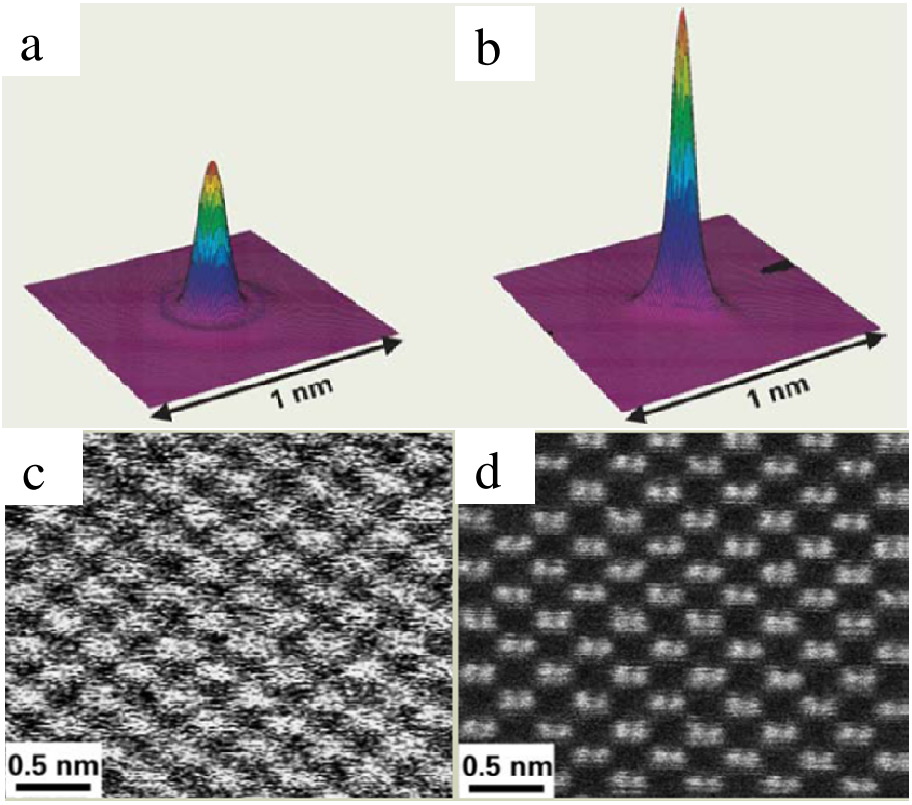

Figure 2.23 Simulated probe intensity distributions (*row 1*) and HAADF-STEM images of Si <110> dumbbell structure with a 1.36Å interplanar spacing (*row 2*) in the un-corrected condition (*column 1*) and corrected condition (*column 2*). The corrected probe has a significantly higher beam current and a considerably smaller probe size.[38]

2.8.2 Example applications of STEM based techniques to complex oxide materials

Recently STEM based techniques, such as STEM imaging (*e.g.* HAADF-STEM) and STEM chemical analysis (*i.e.* STEM-XEDS and STEM-EELS), are attracting more and more attention from academic researchers for the study of catalyst materials (*e.g.* metal nanoparticles, supported metal oxides and complex oxides). A number of applications using STEM based techniques have been reported. Herzing *et al.*[39] used aberration-corrected HAADF-STEM methods to indentify the active catalytic species in

the iron oxide supported gold CO oxidation catalysts to be Au bilayer clusters. Later using the similar approach Zhou *et al.*[40] were able to detect the presence of sub-nanometer Zr-WO_x clusters on the $WO_3/ZrO_x(OH)_{4-2x}$ catalysts and determined them to be the active species involved in the light alkane isomerization. However, very few successful HAADF-STEM studies of the active species in complex oxide catalyst materials have been reported. This is partly because of the extreme electron beam sensitivity of the complex oxide materials,[2] and more importantly because the possible active sites normally have a similar atomic number to that of the inactive matrix (*e.g.* the possible active V^{4+}/V^{5+} redox couple in the disordered surface layer on the $(VO)_2P_2O_7$ material). Hence they cannot stand out as brighter features in the HAADF-STEM micrographs.

STEM based chemical analysis of complex oxide catalysts, on the other hand, has been reported a few times. Using STEM-XEDS, Söderhjelm *et al.*[41] were able to observe the enrichment of Mo at the surface of an $Fe_2(MoO_4)_3$ particle. As shown in Figure 2.24, the Mo/Fe ratio is higher at the periphery (~2.1) as compared to the lower ratio (~1.5) in the center. House *et al.*[42] produced a stoichiometric $Fe_2(MoO_4)_3$ catalyst by the co-precipitation of iron nitrate and ammonium heptamolybdate. Using STEM-EELS they observed an enrichment of Mo on the surface of the $Fe_2(MoO_4)_3$ particles. As shown in Figure 2.25, a STEM-EELS line profile is drawn across the iron molybdate particle. On the surface the particle, a greater amount of Mo with a corresponding lower amount of Fe is detected indicating that the surface is enriched in Mo.

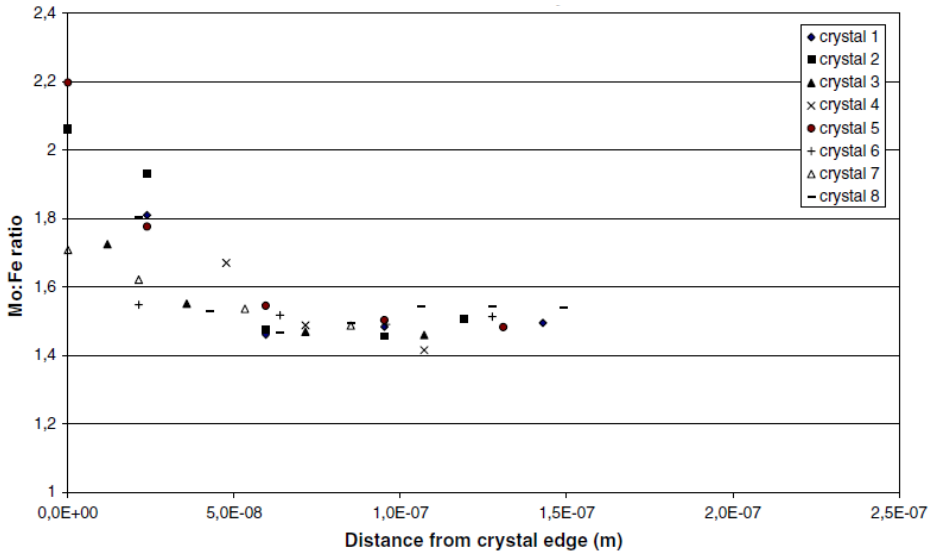

Figure 2.24 The Mo/Fe ratios of a $Fe_2(MoO_4)_3$ crystal determined by STEM-XEDS line scan analysis in the fresh catalyst.[41]

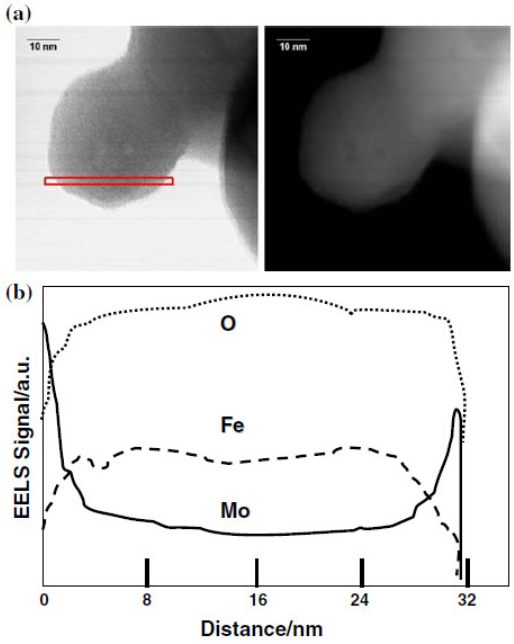

Figure 2.25 (a) BF- and HAADF- STEM micrographs of the iron molybdate particle; (b) Mo, Fe and O EELS signals across the line profile in (a).[42]

One of the most successful applications of the HAADF-STEM technique is on the Mo-V-Nb-Te-O complex oxide catalyst. Although this material is not within the scope of this thesis, it is still worth introducing it in order to illustrate the power and potential of the STEM imaging technique for the study of complex oxide catalysts. As noted

previously the Mo-V-Nb-Te-O catalyst system consists of two phases (*i.e.* the M1 and M2 phases), which are used for the propane ammoxidation.[22] HAADF-STEM experiments performed on the aberration-corrected JEOL 2100F microscope were able to provide atomic scale structural information on the cation arrangement in the M1 phase which agrees with its proposed atomic structural model (Fig. 2.26(a)(b)).[43] Pyrz *et al.*[43] observed the partial occupancy of Te in the heptagonal channels as predicted by the Rietveld model (Fig. 2.26(c)(d)). A good agreement between the HAADF-STEM micrograph and the M1 unit cell is shown in Figure 2.26(e).

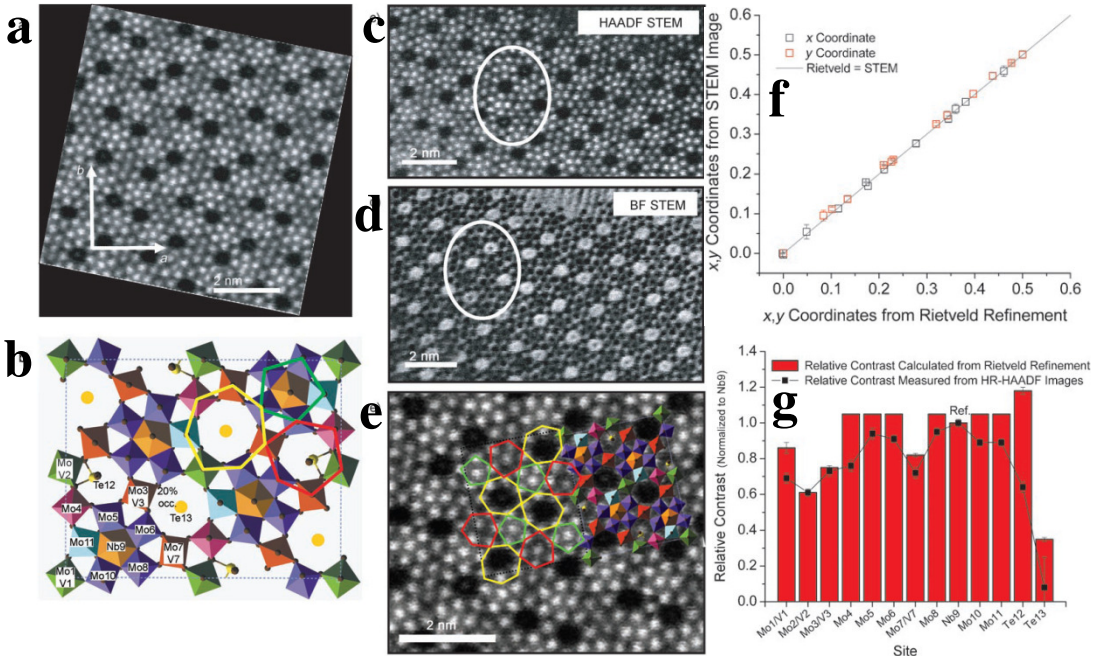

Figure 2.26 (a) HAADF-STEM micrograph of the [001] projection of the M1 phase, (b) the atomic model of the M1 phase, (c) HAADF-STEM micrograph showing areas with the occupied heptagonal channels and (d) the corresponding BF-STEM micrograph showing the same filled heptagonal channels, (e) enlargement of (c) with a M1 model superimposed; (f) Plot of the x,y coordinates from the refinement against the coordinates obtained from the STEM micrograph; (g) Comparison of contrast and occupancies calculated from STEM experiment with those from the Rietveld refinement.[43]

The HAADF-STEM micrograph also allowed them to verify the x,y coordinates of the unit cell (Fig. 2.26(f)). In addition the Z-contrast ratios on each cation position

rendered by the HAADF technique matches with those expected by the Rietveld model (Fig. 2.26(g)). Using such STEM techniques, Pyrz and co-workers[44,45] then studied the M2 phase of the Mo-V-Nb-Te-O catalyst system and the Nb or Ta substitution into the M1 phase.

2.9 Conclusions

A wide variety of electron microscopy methods have been introduced in this Chapter, as well as their recent applications to various complex oxide catalyst materials of relevance to this thesis. As demonstrated in various experiments, each electron microscopy approach is able to reveal some aspects of the structure and/or chemical composition of the complex oxide heterogeneous catalysts. In order to obtain a fuller characterization of the catalyst materials of interest in this thesis, a few more complementary characterization techniques are necessary, which will be described briefly in the next chapter.

2.10 References

1. J. Goldstein, Scanning electron microscopy and x-ray microanalysis (Kluwer Academic/Plenum Publishers, 3rd Edition, 2003).

2. C. J. Kiely, A. Burrows, S. Sajip, G. J. Hutchings, M. T. Sananes, A. Tuel, and J. C. Volta, "Characterisation of variations in vanadium phosphate catalyst microstructure with preparation route," *Journal of Catalysis,* **162,** 31-47 (1996).

3. L. Reimer and H. Kohl, Transmission electron microscopy: physics of image formation (Springer, 5th Edition, 2008).

4. D. B. Williams and C. B. Carter, Transmission electron microscopy: a textbook for materials science (Springer, 2nd Edition, 2009).

5. A. Howie and M. J. Whelan, "Diffraction contrast of electron microscope images of crystal lattice defects. II. The development of a dynamical theory," *Proceedings of the Royal Society of London.Series A: Mathematical and Physical Sciences,* **263,** 217-237 (1961).

6. P. J. Goodhew, F. J. Humphreys, and R. Beanland, Electron microscopy and analysis (Taylor & Francis, 3rd Edition, 2001).

7. C. J. Kiely, A. Burrows, G. J. Hutchings, K. E. Bere, J. C. Volta, A. Tuel, and M. Abon, "Structural transformation sequences occurring during the activation of vanadium phosphorus oxide catalysts," *Faraday Discussions,* **105,** 103-118 (1996).

8. A. Delimitis, "Electron microscopy studies of doped vanadium phosphorus oxide catalysts," PhD Thesis, University of Liverpool (2002).

9. L. Sartoni, A. Delimitis, J. K. Bartley, A. Burrows, H. Roussel, J. Herrmann, J. Volta, C. J. Kiely, and G. J. Hutchings, "Gallium-doped VPO catalysts for the oxidation of *n*-butane to maleic anhydride," *Journal of Materials Chemistry,* **16,** 4348-4360 (2006).

10. I. Ayub, D. S. Su, M. Willinger, A. Kharlamov, L. Ushkalov, V. A. Zazhigalov, N. Kirillova, and R. Schlogl, "Tribo-mechanical modification of Bi promoted vanadyl phosphate systems 1: An improved catalyst and insight into structure-function relationship," *Physical Chemistry Chemical Physics,* **5,** 970-978 (2003).

11. N. K. Mal, A. Bhaumik, M. Fujiwara, and M. Matsukata, "Novel organic-inorganic hybrid and organic-free mesoporous niobium oxophosphate synthesized in the presence of an anionic surfactant," *Microporous and Mesoporous Materials,* **93,** 40-45 (2006).

12. A. Sarkar and P. Pramanik, "Synthesis of mesoporous niobium oxophosphate using niobium tartrate precursor by soft templating method," *Microporous and Mesoporous Materials,* **117,** 580-585 (2009).

13. L. Wang, B. Peng, X. Guo, W. Ding, and Y. Chen, "Ferric molybdate nanotubes synthesized based on the Kirkendall effect and their catalytic property for propene epoxidation by air," *Chemical Communications,* 1565-1567 (2009).

14. S. Prasad and A. Paul, "Theoretical consideration on the formation of nanotube following the Kirkendall effect," *Applied Physics Letters,* **90,** 233114 (2007).

15. O. Scherzer, "The theoretical resolution limit of the electron microscope," *Journal of Applied Physics,* **20,** 20-29 (1949).

16. J. C. H. Spence, High-resolution electron microscopy (Oxford University Press, 3rd Edition, 2003).

17. H. Bluhm, M. Havecker, E. Kleimenov, A. Knop-Gericke, A. Liskowski, R. Schlogl, and D. S. Su, "In situ surface analysis in selective oxidation catalysis: *n*-butane conversion over VPP," *Topics in Catalysis,* **23,** 99-107 (2003).

18. G. J. Hutchings, J. K. Bartley, J. M. Webster, J. A. Lopez-Sanchez, D. J. Gilbert, C. J. Kiely, A. F. Carley, S. M. Howdle, S. Sajip, S. Caldarelli, C. Rhodes, J. C. Volta, and M. Poliakoff, "Amorphous vanadium phosphate catalysts from supercritical antisolvent precipitation," *Journal of Catalysis,* **197,** 232-235 (2001).

19. M. Havecker, R. W. Mayer, A. Knop-Gericke, H. Bluhm, E. Kleimenov, A. Liskowski, D. Su, R. Follath, F. G. Requejo, D. F. Ogletree, M. Salmeron, J. A. Lopez-Sanchez, J. K. Bartley, G. J. Hutchings, and R. Schlogl, "In-situ investigation of the nature of the active surface of a vanadyl pyrophosphate catalyst during *n*-butane oxidation to maleic anhydride," *Journal of Physical Chemistry B,* **107,** 4587-4596 (2003).

20. K. Routray, W. Zhou, C. J. Kiely, W. Grünert, and I. E. Wachs, "Origin of the synergistic interaction between MoO_3 and iron molybdate for the selective oxidation of methanol to formaldehyde," *Journal of Catalysis,* **275,** 84-98 (2010).

21. K. Routray, W. Zhou, C. J. Kiely, and I. E. Wachs, "Catalysis science of methanol oxidation over iron vanadate catalysts: nature of the catalytic active sites," *ACS Catalysis,* **1,** 54-66 (2011).

22. R. K. Grasselli, J. D. Burrington, D. J. Buttrey, P. DeSanto, C. G. Lugmair, A. F. Volpe, and T. Weingand, "Multifunctionality of active centers in (amm)oxidation catalysts: from Bi-Mo-O_x to Mo-V-Nb-(Te, Sb)-O_x ," *Topics in Catalysis,* **23,** 5-22 (2003).

23. P. DeSanto, D. J. Buttrey, R. K. Grasselli, C. G. Lugmair, A. F. Volpe, B. H. Toby, and T. Vogt, "Structural aspects of the M1 and M2 phases in MoVNbTeO propane ammomidation catalysts," *Zeitschrift Fur Kristallographie,* **219,** 152-165 (2004).

24. A. Burrows, C. J. Kiely, J. Perregaard, P. E. Hojlund-Nielsen, G. Vorbeck, J. J. Calvino, and C. Lopez-Cartes, "Structural characterisation of a VMgO catalyst used in the oxidative dehydrogenation of propane," *Catalysis Letters,* **57,** 121-128 (1999).

25. E. D. Boyes and P. L. Gai, "Environmental high resolution electron microscopy and applications to chemical science," *Ultramicroscopy,* **67,** 219-232 (1997).

26. P. L. Gai, "Developments in in situ environmental cell high-resolution electron microscopy and applications to catalysis," *Topics in Catalysis,* **21,** 161-173 (2002).

27. P. L. Gai and J. J. Calvino, "Electron microscopy in the catalysis of alkane oxidation, environmental control, and alternative energy sources," *Annual Review of Materials Research,* **35,** 465-504 (2005).

28. P. L. Gai, "Environmental high resolution electron microscopy of gas-catalyst reactions," *Topics in Catalysis,* **8,** 97-113 (1999).

29. P. L. Gai and K. Kourtakis, "Solid-state defect mechanism in vanadyl pyrophosphate catalysts - implications for selective oxidation," *Science,* **267,** 661-663 (1995).

30. P. L. Gai and P. A. Labun, "Electron microscopy studies relating to methanol oxidation over ferric molybdate and molybdenum trioxide catalysts," *Journal of Catalysis,* **94,** 79-96 (1985).

31. F. Banhart, In-situ electron microscopy at high resolution (World Scientific, 2008).

32. P. Hartel, H. Rose, and C. Dinges, "Conditions and reasons for incoherent imaging in STEM," *Ultramicroscopy,* **63,** 93-114 (1996).

33. O. L. Krivanek, N. Dellby, and A. R. Lupini, "Towards sub-angstrom electron beams," *Ultramicroscopy,* **78,** 1-11 (1999).

34. O. L. Krivanek, P. D. Nellist, N. Dellby, M. F. Murfitt, and Z. Szilagyi, "Towards sub-0.5 angstrom electron beams," *Ultramicroscopy,* **96,** 229-237 (2003).

35. H. Rose, "Outline of a spherically corrected semiaplanatic medium-voltage transmission electron-microscope," *Optik,* **85,** 19-24 (1990).

36. O. Scherzer, "Sphärische und chromatische Korrektur von Elektronenlinsen," *Optik,* **2,** 114-132 (1947).

37. C. Hetherington, "Aberration correction for TEM," *Materials Today,* **7,** 50-55 (2004).

38. M. Watanabe, D. W. Ackland, C. J. Kiely, D. B. Williams, M. Kanno, R. Hynes, and H. Sawada, "The aberration corrected JEOL JEM-2200FS FEGSTEM/TEM fitted with an Ω electron energy-filter: performance characterization and selected applications," *JEOL News,* **41,** 2-7 (2006).

39. A. A. Herzing, C. J. Kiely, A. F. Carley, P. Landon, and G. J. Hutchings, "Identification of active gold nanoclusters on iron oxide supports for CO oxidation," *Science,* **321,** 1331-1335 (2008).

40. W. Zhou, E. I. Ross-Medgaarden, W. V. Knowles, M. S. Wong, I. E. Wachs, and C. J. Kiely, "Identification of active Zr-WO_x clusters on a ZrO_2 support for solid acid catalysts," *Nature Chemistry,* **1,** 722-728 (2009).

41. E. Soderhjelm, M. P. House, N. Cruise, J. Holmberg, M. Bowker, J. Bovin, and A. Andersson, "On the synergy effect in MoO_3-$Fe_2(MoO_4)_3$ catalysts for methanol oxidation to formaldehyde," *Topics in Catalysis,* **50,** 145-155 (2008).

42. M. P. House, M. D. Shannon, and M. Bowker, "Surface segregation in iron molybdate catalysts," *Catalysis Letters,* **122,** 210-213 (2008).

43. W. D. Pyrz, D. A. Blom, T. Vogt, and D. J. Buttrey, "Direct imaging of the MoVTeNbO M1 phase using an aberration-corrected high-resolution scanning transmission electron microscope," *Angewandte Chemie-International Edition,* **47,** 2788-2791 (2008).

44. W. D. Pyrz, D. A. Blom, N. R. Shiju, V. V. Guliants, T. Vogt, and D. J. Buttrey, "The effect of Nb or Ta substitution into the M1 phase of the MoV(Nb,Ta)TeO selective oxidation catalyst," *Catalysis Today,* **142,** 320-328 (2009).

45. D. A. Blom, W. D. Pyrz, T. Vogt, and D. J. Buttrey, "Aberration-corrected STEM investigation of the M2 phase of MoVNbTeO selective oxidation catalyst," *Journal of electron microscopy,* **58,** 193-198 (2009).

Chapter 3 Experimental Methods

3.1 Introduction

This chapter describes the experimental methods, in addition to conventional SEM/TEM, used throughout the course of this study. It begins with an introduction to X-ray ultra-Microscopy (XuM) and energy-filtered transmission electron microscopy (EFTEM), which have rarely been used in the past for the characterization of complex oxide catalyst materials. Then the image simulation and image processing software programs used in this project are introduced. The general electron microscopy approaches employed in the project, as well as the sample preparation methods for electron microscopy studies are also briefly described. The various catalytic testing methods used in this project are then discussed. Finally complementary characterization techniques such as BET surface area measurement, X-ray diffraction (XRD), X-ray photoelectron spectroscopy (XPS) and Laser Raman spectroscopy (LRS) are briefly outlined at the end of the chapter.

3.2 X-ray ultraMicroscopy

X-ray ultra-Microscopy (XuM) is a technique carried out within the environment of a scanning electron microscope (the FEI XL30 ESEM). XuM can provide high spatial resolution X-ray images of the internal structure of samples without having to section or damage the material. A schematic diagram of the main components of the XuM is presented in Figure 3.1(a). It has three major parts, namely (i) the target (X-ray source), (ii) the sample and (iii) the X-ray detector. The X-rays are generated as the electron probe is focused onto a metal foil target (*e.g.* Pt). This provides a point source of X-rays which

can then pass through a nearby sample and generate a projection image on an X-ray sensitive CCD camera.

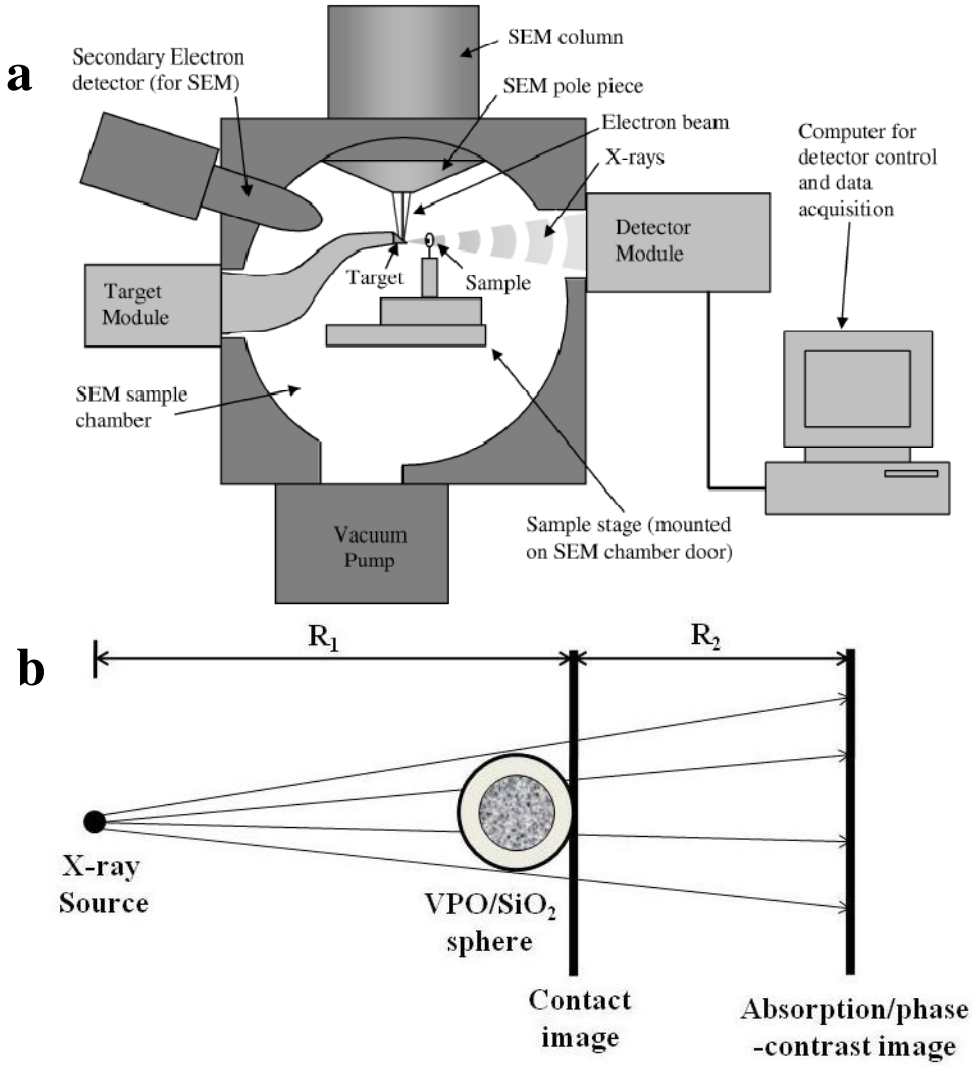

Figure 3.1 Schematic diagrams of (a) the main components of the XuM[1] and (b) the point-projection microscope geometry employed in XuM. A VPO/SiO_2 sphere is used as an example specimen in this schematic.

The point-projection microscope geometry employed in XuM (Fig. 3.1(b)) means that the magnification of an XuM image is determined by the following equation 3.1:-

$$M = (R_1 + R_2)/R_1 \quad (3.1)$$

where R_1 is the distance between the X-ray source and the particle under investigation and R_2 is the distance between the particle and the X-ray detector.

XuM micrographs include contributions from both absorption and phase contrast. Absorption contrast is largely determined by the difference in densities of the sample, where a denser material results in darker region in the X-ray image. Phase contrast arises directly from the wave properties of X-rays. Areas with a sharp refractive index change such as edges, boundaries and cracks, show such phase contrast because of the phase shift it induces in the X-rays. Additionally using the XuM technique it is possible to reconstruct a 3-dimensional representation of samples by acquiring a systematic rotational set of XuM images. More details about the XuM technique can be found in references.[1,2] This method has been used in this work for the study of V-P-O/SiO_2 core/shell morphology particles in Chapter 5.

3.3 Energy-filtered transmission electron microscopy

Energy-filtered transmission electron microscopy (EFTEM) is probably one of the most powerful AEM techniques. During the electron beam-specimen interaction, both elastic and inelastic scattering of incoming electrons can occur. The inelastically scattered energy-loss electrons can be used to obtain an EELS spectrum as described in sub-section 2.4.2. However by placing an energy filter in the microscope, one can select electrons within a specific energy range to form either an image or a diffraction pattern. Two types of energy filters are commercially available, namely the in-column Ω filter and the post-column Gatan imaging filter (GIF).[3,4] The JEM-2200FS microscope at Lehigh University is equipped with an in-column Ω filter, which is situated between the

intermediate lens and projector lens as shown in Figure 3.2(a). The filter is composed of four magnetic prisms arranged in a Ω shape and an energy selecting slit at the outlet of the filter. This slit is used to select a desired energy window and exclude undesired electrons, and acts like the objective aperture in a conventional TEM. As shown in Figure 3.2(b) in a typical EFTEM imaging experiment, electrons passing though the specimen are dispersed laterally by the filter and only electrons in a desired range of energy determined by the energy slit can pass onto the detector to form a EFTEM image.

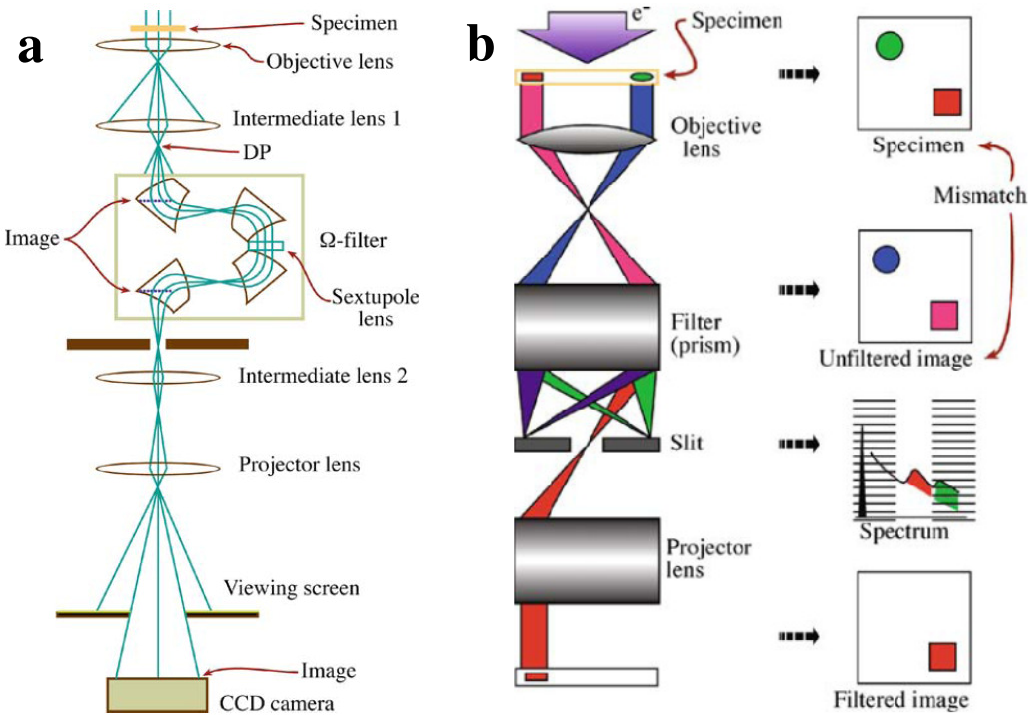

Figure 3.2 Schematic illustrations of (a) an in-column Ω filter located in a TEM and (b) steps necessary to form an EFTEM image.[3]

Depending on the energy range selected, the EFTEM image may contain spatially resolved chemical information and/or electronic information of the specimen. It should be noted that the spatial resolution of EFTEM imaging, which is around 1 nm in practice,[5]

is not as good as that obtainable in the HR-TEM or HAADF-STEM techniques. This EFTEM technique has been used for the study of Fe-Mo-O materials in Chapter 7.

3.4 Image simulation techniques

The computer simulation of HR-TEM and HAADF-STEM images has now become a routine tool allowing one to determine the object transmission function for a given electron beam and facilitating the calculation of an image intensity distribution with regard to different specimen thicknesses and microscope operating conditions. Through image simulations one can better understand the detailed microstructure observed in the image and relate it with greater confidence to the real material structure. Especially for HR-TEM experiments, it is well known that the intensity distribution in an HR-TEM image varies with parameters such as the specimen thickness, the defocus of the objective lens, the tilt angle of the crystal and many other operating parameters. This makes the image simulation step very important in the interpretation of HR-TEM images. A good example is presented in Figure 3.3 which shows how the intensity distribution in the HR-TEM image of the Rh/CeO_2 catalyst particle changes with variations in the specimen thicknesses and defocus values. For HAADF-STEM, the intensity distribution of the image does not vary as dramatically as that in HR-TEM, and in most instances it remains roughly consistent as the specimen thickness and defocus values change. Nevertheless HAADF-STEM simulations can provide a good reference for the improved understanding of the structural details in a given material (*e.g.* the intensity ratio between neighboring atomic columns with different atomic numbers).[6]

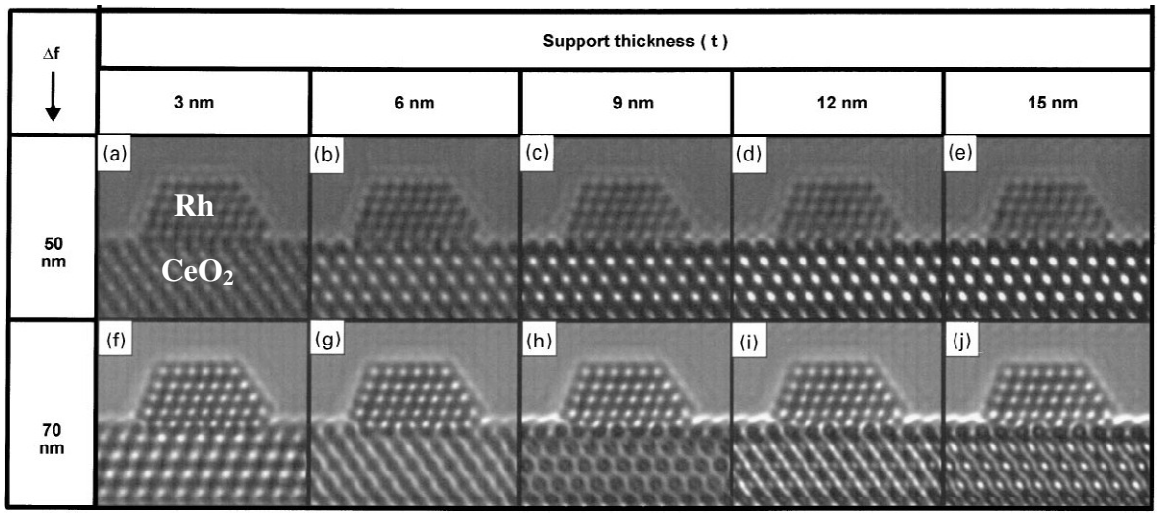

Figure 3.3 Simulated HR-TEM images of the Rh/CeO_2 catalyst particle with the CeO_2 support thickness varying from 3 to 15 nm at defocus values 50 nm (*row 1*) and 70 nm (*row 2*), respectively. Pay attention to the image contrast variation of the CeO_2 support in both sets of images.[7]

In a TEM (or STEM), electrons pass through the specimen, and in most cases they will undergo dynamical scattering as they interact with the specimen. The two principal methods utilized in calculating electron microscopy images (both HR-TEM and STEM) are known as the Bloch wave method and the multi-slice method, which will be outlined briefly in the following sub-sections. Both techniques have been described in considerable detail in books authored by De Graef[8] or Kirkland[9].

3.4.1 The Bloch wave method

Inside a crystalline material, the electron wave function is treated as a Bloch wave, which satisfies the time-independent Schrödinger equation and is in a periodic potential having the symmetry of the crystal. This Bloch-wave expression of the Schrödinger equation is shown as below:-

$$\{ K^2 - \left| \mathbf{k}^{(j)} + \mathbf{g} \right|^2 \} C_g^{(j)} + \sum_{h \neq g} U_{g-h} C_h^{(j)} = 0 \qquad (3.2)$$

where $\mathcal{K}$ is the wavevector of the electron inside the specimen, $C^{(j)}$ is the plane wave amplitude for the j^{th} Bloch wave and U_{g-h} is the component of the inner potential. This expression illustrates how the crystal potential (the U terms) interferes with each one of the Bloch waves (their amplitudes: the C terms), which is known as the *dynamical coupling*.

In order to solve this electron wave equation, a large number of the eigenvectors and eigenvalues in matrix algebra are required. This mathematical approach is described in detail by De Graef.[8] It is worth mentioning that this Bloch wave method is time consuming and best suited for simulations of a small perfect crystal.

3.4.2 The multi-slice method

As suggested by its name, in the multi-slice method the crystal is divided into many thin slices, each of which meets the weak phase object approximation (WPOA). Hence the electron wave function can be expressed as the convolution between the transmission function (of the electrons travelling through the thin slices) and the propagator function (of the electrons propagating in the vacuum between these slices). This method is useful in both crystalline and nearly amorphous materials. By applying an efficient fast Fourier transform (FFT) routine, computing time can be reduced to an order of magnitude compared to the Bloch wave method. The details of the multi-slice method and the FFT routine have been described by Kirkland.[9] A simple schematic illustration of the multi-slice theorem is shown in Figure 3.4.

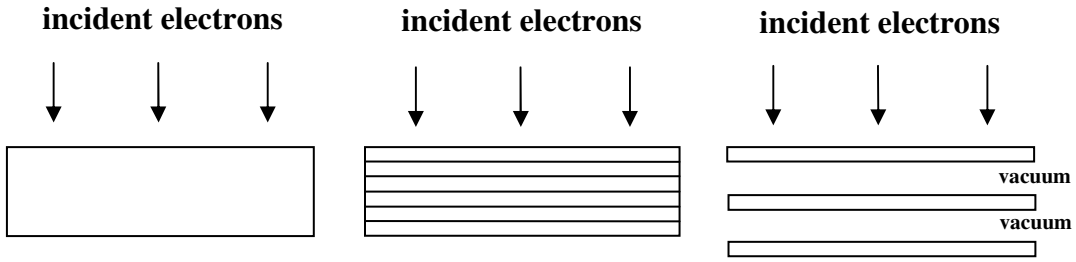

Figure 3.4 Schematic illustration of the multi-slice method. (a) Specimen, (b) the specimen divided into many thin slices and (c) each pair of the slice and the vacuum acts as a transmission step in the slice and a propagator within the vacuum.[9]

3.5 Software used in this project

A number of image simulation and image processing software programs have been used throughout the course of our studies, namely xHREM, CaRine, VESTA, DigitalMicrograph and ImageJ.

xHREM

For the STEM simulations presented in this project, a FFT-multislice simulation suite - xHREM (v3.5) developed by Dr. Ishizuka from HREM Research Inc. was used. Basically two steps are needed in a STEM simulation: (i) the input data for the scattering calculation are prepared by the "MultiGUI" routine in the simulation suite and (ii) after the multi-slice calculation, the STEM images can be generated using the "STEMimage" routine. It should be noted that the interaction between probe and specimen is calculated at each point for each slice. Details of this simulation suite can be found in references.[10,11] In this program the key parameters which need to be defined with some care are:-

(i) *Specimen parameters*, such as lattice parameters, space group, atomic coordinates and numbers of unit cells (thickness of specimen).

(ii) *Sampling size*, such as the scan step, the super-cell size and the slice thickness.

(iii) *Instrumental parameters*, such as condenser lens aperture size, C_s, defocus value and detector radius.

Other crystallographic and image processing software used throughout this research program are listed as follow:-

CaRIne

CaRIne Crystallography (v3.1) is a windows-based crystallographic software developed by Boudias and Monceau in 1989[12], which was mainly used as a reference resource for crystal structure simulation and analysis tasks, including stereographic projections, powder X-Ray diffraction, reciprocal lattices and (*hkl*) plane-spacing calculations. In this dissertation, CaRIne was used for generating 2D representations of (i) V, P, O atoms in specific V-P-O phases, (ii) Nb, P, O atoms in specific Nb-P-O phases and (iii) Fe, Mo, O atoms in particular Fe-Mo-O phases. In addition to this, simple calculations of structure factors, interplanar distances and interplanar angles between different lattice planes were performed using this software. Furthermore, theoretical powder XRD patterns and kinematical electron diffraction patterns can be generated via structure factor calculation for given structures. This can be used as a reliable reference for indentifying various V-P-O, Nb-P-O and Fe-Mo-O phases encountered in this study.

VESTA

VESTA (Visualization for Electronic and STructural Analysis) is a 3D visualization program for structural models, volumetric data and crystal morphologies which was developed by Momma and Izumi.[13] In this project, VESTA was used to

render 3D atomic models of V-P-O phases (*i.e.* $VOPO_4 \cdot 2H_2O$ and $VOHPO_4 \cdot 0.5H_2O$) described in Chapter 4.

DigitalMicrograph

DigitalMicrograph is a software package provided by Gatan Inc., which was used to acquire, process, analyze and present image and spectrum data in TEM and STEM.[14] It was also used to acquire Fourier Transforms (FTs) from digital HR-TEM and STEM images via a Fast Fourier Transform (FFT) function. The FFTs obtained were compared to electron diffraction patterns of a given structure in order to facilitate phase identification of materials. Additionally noise in HAADF-STEM images could be reduced using the low-pass filtering function in DigitalMicrograph.

ImageJ

ImageJ is a free of charge, java-based image processing program developed at the National Institute of Health. More details of ImageJ can be found at this link http://rsbweb.nih.gov/ij/index.html. In this study, ImageJ was used to generate line intensity profiles in simulated HAADF-STEM images of Nb-P-O materials.

3.6 Electron microscopy approaches employed in this project

A wide variety of electron microscopy techniques have been used throughout this project. SEM micrographs were obtained on three scanning electron microscopes: namely (i) a FEI XL30 ESEM equipped with a thermionic tungsten gun operating at 10 kV (at Lehigh University), (ii) an Hitachi S-4300LV SEM equipped with a Schottky field emission gun operating at 5 - 20 kV (at Lehigh University), and (iii) an Hitachi 326YO-N SEM operating at 20 kV (at Cardiff University)

TEM experiments such as BF-TEM imaging, SAED analysis and HR-TEM imaging were carried out using (i) a JEOL JEM-2000FX microscope equipped with a thermionic LaB_6 source operating at 200 kV and (ii) a JEOL JEM-2200FS microscope equipped with a Schottky field-emission source, CEOS C_s-corrector and an in-column energy filter operating at 200 kV.

STEM based techniques, such as BF-/HAADF-STEM and STEM-XEDS analysis were performed on a JEOL JEM-2200FS microscope equipped with a Schottky field-emission source and the CEOS C_s-corrector operating at 200 kV. This microscope is equipped with a Thermoelectron XEDS detector (loaded with the Noran System 6 software) having a 0.13 sr. collection solid angle.

XuM micrographs were taken on a FEI XL30 ESEM equipped with a tungsten filament. In the experiment, a large spot size, high current electron probe was used to generate the highest possible X-ray fluxes from the Pt foil target, which is a requirement for the XuM technique. Intact, non-sectioned V-P-O/SiO_2 spheres were glued individually to the tip of a carbon fiber/epoxy needle, and then were investigated using the XuM technique in order to reveal their internal structures by a combination of adsorption and phase contrast.

EFTEM experiments were performed on a JEOL JEM-2200FS microscope equipped with an integrated in-column Ω filter and a Schottky field emission gun (FEG) operating at 200 kV. It should be noted that the electron gun voltage needs to be increased a few kV (*i.e.* 1-2 kV) in an EFTEM experiment in order to keep the energy-loss electrons “on-axis”- a process which is termed illumination compensation.

3.7 Sample preparation for electron microscopy

Samples for investigation using scanning electron microscopy (SEM), transmission electron microscopy (TEM), or scanning transmission electron microscopy (STEM) were prepared as described below:-

SEM sample preparation: In this project most of the complex oxide materials are insulating in character, so a conductive coating is needed in order to reduce charging effects and to enhance the resolution of SEM images. The catalyst powders were mounted onto an aluminum SEM stub using carbon tape and sputtered with conductive materials, such as iridium or carbon, to form a 3-5 nm thick conductive layer on the sample in order to mitigate the effects of sample charging.

TEM/STEM sample preparation: In the 'wet-method' of preparation, samples were dispersed in high purity ethanol (99.7 vol%) using an agate pestle and mortar. A drop of the resulting suspension was then deposited onto a carbon supported 300-mesh TEM grid (either holey or lacey carbon) and allowed to dry. An alternative method (the so-called 'dry-method') is to grind the sample powders between two clean glass slides and then disperse them dry onto a carbon supported 300-mesh TEM grid (either holey or lacey carbon). Most of the TEM samples investigated using the JEOL JEM-2000FX microscope were prepared using the 'wet-method', which tend to give a very good dispersion of catalyst particles. The 'dry' method, on the other hand, was mainly used for preparing the TEM/STEM samples studied at high magnification in the JEOL JEM-2200FS instrument. This latter method can effectively reduce the effect of carbon contamination on the TEM grids, originating from the organic solvent, which can be a problem in Schottky source instruments.

3.8 Catalytic performance measurements (at Cardiff University)

3.8.1 Selective oxidation of *n*-butane to maleic anhydride over V-P-O catalysts

Reactions were carried out in a fixed bed micro-reactor containing V-P-O catalyst (200 mg), typically at 400 °C with a 2000 - 3000 h^{-1} gas hour space velocity (GHSV). The feedstock composition was determined to be 1.5 - 1.7 % *n*-butane/air by calibrated mass flow controllers. The products were fed *via* heated lines to an on-line gas chromatograph for analysis. The reactor comprised of a stainless steel tube (internal diameter (I.D.) 8 mm) with the catalyst bed held in place by plugs of quartz wool. A thermocouple was located in the center of the catalyst bed and temperature control was typically ±1°C. Carbon mass balances of ≥ 95 % were typically observed.

From the obtained data, *n*-butane conversion rate ($X_{but.}$) and selectivity to MA (S_{MA}), which were measured as percentages, can be calculated by the following equations:

$$X_{but.}\,(\%) = \frac{Moles\ of\ n{-}butane\ converted\ to\ all\ products \times 100}{Moles\ of\ n{-}butane\ fed\ into\ the\ reactor} \quad (3.3)$$

$$S_{MA}\,(\%) = \frac{Moles\ of\ n{-}butane\ converted\ to\ MA \times 100}{Moles\ of\ n{-}butane\ converted\ to\ all\ products} \quad (3.4)$$

The catalytic performance can also be expressed as the MA yield (Y_{MA}) given by the equation 3.5.

$$Y_{MA} = X_{but.} * S_{MA} \quad (3.5)$$

The specific activity, which is the *n*-butane conversion per unit surface area of V-P-O catalyst, was also used as a measure of catalytic performance.

3.8.2 Oxidative dehydrogenation of ethane to ethylene over Nb-P-O catalysts

The catalytic activity of Nb-P-O materials for the ethane oxidation was determined at atmospheric pressure at a reaction temperature of 500 ºC, using a fixed bed quartz tubular reactor (I.D. 35 mm, length- 500 mm). The feed consisted of a mixture of C_2H_6/O_2/He with a molar ratio of 3/1/6. The amount of Nb-P-O catalyst was varied from 1 to 10 g in order to study a range of contact times. The catalyst bed volume remained constant for all experiments by dilution with SiC when appropriate. The total flow rate was fixed in all cases between 15 and 30 ml min^{-1}. Two analyses at each reaction condition were carried out with a stabilization time of 60 minutes. Reactant and products were analyzed on-line by gas chromatography using two packed columns (2.5 m Molecular sieve 5 Å and 3 m Porapak Q). For comparative purposes, a blank run using 15 ml min^{-1} was also conducted at 500 ºC. An ethane conversion of less than 0.4 % was obtained for the blank test.

3.8.3 Selective oxidation of methanol to formaldehyde over Nb-P-O catalysts

Methanol oxidation reactions were carried out in quartz tubular reactor (I.D. 35 mm, length- 500 mm) containing 300 mg of Nb-P-O catalyst. The feedstock composition was determined by mass flow controllers to be a mixture of CH_3OH/O_2/He with a molar ratio of 5/10/85. The temperature of catalyst was varied from 300 to 500 °C at 50 ^oC intervals. Product analysis was carried out using a Varian V_A Star 3400 C_X Gas Chromatograph . Two columns were used in a series/bypass system: Carbosieve S-11 (3 Meters) for analysis of O_2, CO and a Proapak Q (1 meter) for the analysis of methanol, dimethyl ether, methyl formate, formaldehyde and CO_2. A thermal conductivity detector

(TCD) was used for the detection of O_2, CO_2 and CO_2, and a flame ionization detector (FID) was used for the detection of methanol, formaldehyde, methyl formate and dimethyl ether.

3.8.4 Selective oxidation of methanol to formaldehyde over Fe-Mo-O catalysts

Methanol oxidation reactions over Fe-Mo-O catalysts were carried out in a fixed-bed quartz tube reactor under atmosphere pressure. The feedstock composition was determined by mass flow controllers to be a mixture of CH_3OH/O_2/He with a molar ratio of 6/10/84. The temperature of reactor was controlled and measured by a thermocouple fixed in the center of the catalyst bed. The inlet and outlet lines were heated to prevent condensation of liquid methanol and products. The raw material and products were analysed by an on-line Varian Star 3400 CX gas chromatograph with a TCD and FID. Two in-parallel columns, one (Carbo-sieve) for O_2, CO and CO_2, and another (Propack Q) for CH_3OH, HCHO, CH_3OCH_3 and $HCOOCH_3$, were used to separate the reactor effluents.

3.9 Complementary characterization techniques (carried out at Cardiff University)

3.9.1 Surface area measurements

The surface area of a solid catalyst has a profound influence on its catalytic activity. It is imperative to determine the surface area of a given catalyst material when evaluating its performance. One of the most widely used surface area measurements is BET method, which was discovered by Brunauer, Emmett and Teller in 1938[15] and was further optimized by Ross and Olivier[16]. The surface area (S_{BET}) can be detected via the

volumetric measurement of the physical adsorption isotherm of a gas such as nitrogen. At the measurement temperature chosen, the equilibrium pressure of the adsorbate gas - p and its saturation pressure (typically at -196°C in this project) - p_0 are measured. A plot of $p/[V(p_0-p)]$ on the y-axis versus p/p_0 on the x-axis is made according to the BET equation

$$\frac{p}{V\times(p_0-p)}=\frac{1}{c\times V_m}+\frac{(c-1)}{c\times V_m}\left(\frac{p}{p_0}\right) \quad (3.6)$$

where c is a constant, V is the adsorbed gas volume and V_m is the monolayer adsorbed gas volume. The linearity p/p_0 of this BET equation is maintained between 0.05 and 0.35. V_m can be deduced from the slope and the y-intercept of the plot, which is then introduced into the equation 3.7 to determine the surface area S_{BET}.

$$S_{BET} = V_m N/M \quad (3.7)$$

where N is Avogadro's number and M is the molar volume of the adsorbate gas. In this project BET surface areas were measured by nitrogen adsorption at -196 °C on a Micromeritics Gemini instrument.

3.9.2 X-ray diffraction

X-ray diffraction (XRD) is one of the most important and widely used techniques for characterizing the crystal structure of a material. The structural analysis is performed based on the measured X-ray diffraction from a periodic crystal structure where a long-range order exists. This X-ray diffraction follows Bragg's Law,

$$n\lambda = 2d_{hkl}\sin\theta \quad (3.8)$$

In equation 3.8, n is an integer, λ is the wavelength of the incident X-ray, d_{hkl} is the spacing between the specific *hkl* planes and θ is the angle between the incident X-ray and

the scattering planes. Since λ is comparable to the interplanar spacing of most crystalline materials (*i.e.* V-P-O, Nb-P-O and Fe-Mo-O in this project) and the periodic lattice planes act as a diffraction grating for the incident X-rays. The formation of a set of diffracted beams from a given crystal lattice is similar to that encountered in electron diffraction in terms of the structure factor equation. The atomic form factor (also known as atomic scattering factor) is numerically different in X-ray diffraction as compared to electron diffraction, since X-rays are only scattered by the electron cloud surrounding the nucleus of an atom. By varying the angle 2θ (typically from 10 to 80° in our studies), the diffracted X-ray signal is collected for each angle, from which a continuous spectrum is generated showing X-ray intensities plotted against 2θ angular range. A detailed description of the XRD technique can be found in the book authored by Warren.[17]

In this project, XRD was mainly used for identifying the various phases and polymorphs present in V-P-O catalysts, Nb-P-O catalysts and Fe-Mo-O catalysts and determining the degree of crystallinity of such phases. In all cases, the possible presence of amorphous materials and trace amounts of other crystalline phases also needs to be considered. The acquisition of XRD patterns was performed using a PANalytical X'Pert Pro fitted with an X'Celerator detector and a CuK_α X-ray source ($\lambda = 1.54 \times 10^{-9}$ Å) operated at 40 kV and 40 mA. The identification of various phases was aided by use of the ICCD database and whenever necessary was compared with reported XRD spectra of standard phases.

3.9.3 X-ray photoelectron spectroscopy

X-ray photoelectron spectroscopy (XPS), also known as electron spectroscopy for chemical analysis (ESCA), is one of the most widely used techniques for quantitative surface analysis. Because of its shallow analysis depth (*i.e.* 1-10 nm), XPS can also provide essential information on the surface chemistry of a catalyst, such as the surface composition and oxidation state of surface atoms. In a typical XPS experiment (Figure 3.5), the specimen is illuminated with a monochromatic X-ray beam with an energy of typically few keV. This illumination gives rise to the ionization of surface atoms within the specimen by ejecting orbital electrons, which are also called photoelectrons. The kinetic energies (E_k) of these ejected photoelectrons are recorded by a spectrometer. In this process, part of the energy of the incident X-ray photons is transferred to the kinetic energy of emitted photoelectrons according to equation 3.9:-

$$h\nu = E_k + E_b + W \qquad (3.9)$$

where $h\nu$ is the energy of the incident X-ray photons, E_b is the binding energy of the emitted photoelectron and W is the work function of the material under investigation. This technique has been described in detail in a book authored by Barr.[18]

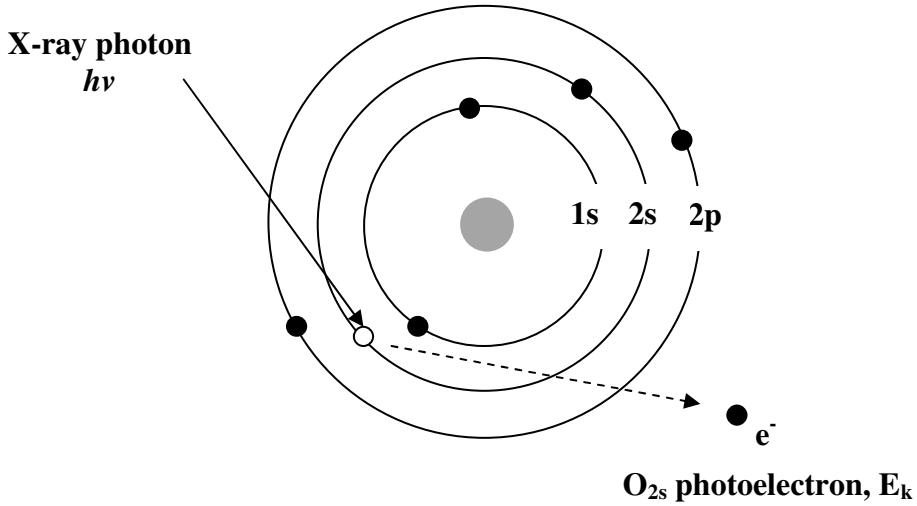

Figure 3.5 Schematic diagram showing the formation of a X-ray photoelectron from an O atom in an XPS experiment.[18]

In this project X-ray Photoelectron Spectroscopy (XPS) measurements were made on a Kratos Axis Ultra DLD, using monochromatised Al K_α radiation, and analyser pass energies of 160 eV (for survey scans) or 40 eV (for detailed scans). Samples were mounted using double-sided adhesive tape; binding energies are referenced to the C(1s) peak from adventitious carbonaceous contamination, assumed to have a binding energy of 284.7 eV. The XPS technique was used in the analyses of the V-P-O/SiO_2 particles and Nb-P-O materials studied in this project.

3.9.4 Laser Raman spectroscopy

Raman Spectroscopy is an optical technique which detects vibrational, rotational and other low-frequency movements in a molecule. When monochromatic light of frequency ν_0 impinges on a molecule, the incident photons can interact with the molecule. The molecule can be excited from the ground state to a virtual energy state, which then subsequently relaxes and emits a photon. Normally three different excitation and relaxation paths can occur (see Fig. 3.6):

(i) the re-emitted photon is at the same energy level with the incident photon ($v = v_0$, $\Delta v = 0$), which is called *Rayleigh* or *elastic* scattering;

(ii) the incident photon loses some of its energy to molecular vibrations giving rise to a lower energy re-emitted photon ($v < v_0$, $\Delta v < 0$), which corresponds to a *Stokes* line;

(iii) the incident photon gains some energy from molecular vibrations giving rise to a higher energy re-emitted photon ($v > v_0$, $\Delta v > 0$), which corresponds to an *anti-Stokes* line.

The latter two paths are known as Raman scattering, which are independent of the exciting light source and give rise to a characteristic Raman shift of the re-emitted photons. These characteristic Raman shifts can be used as finger-prints to identify different low-frequency movements (*i.e.* vibrational, rotational and stretching modes) occurring in a particular molecule. Because of the low efficiency of the Raman scattering process, the use of an intense excitation source, namely an Ar^+ laser is required.

Laser Raman spectroscopy (LRS) is a good technique for the investigation of complex oxide catalysts in this research program. It can be used to determine the presence of different phases via the detection of characteristic movements of a given oxide material. LRS is also a well-suited technique for the *in-situ* study of catalysts under reaction conditions and can provide details of surface structure and phase transformations. Additionally LRS can be used to detect and analyze surface chemisorbed species and reaction intermediates of a catalytic reaction, which can in some instances reveal the reaction mechanism. Further details of the Raman spectroscopy technique can be found in a book authored by Colthup *et al*.[19] In this project, Laser Raman spectroscopy was

used to identify the V-P-O and Fe-Mo-O phases. Laser Raman spectra were obtained on a Renishaw System 1000 Ramascope spectrograph fitted with a green Argon ion (Ar^+) laser (λ = 514.532 nm).

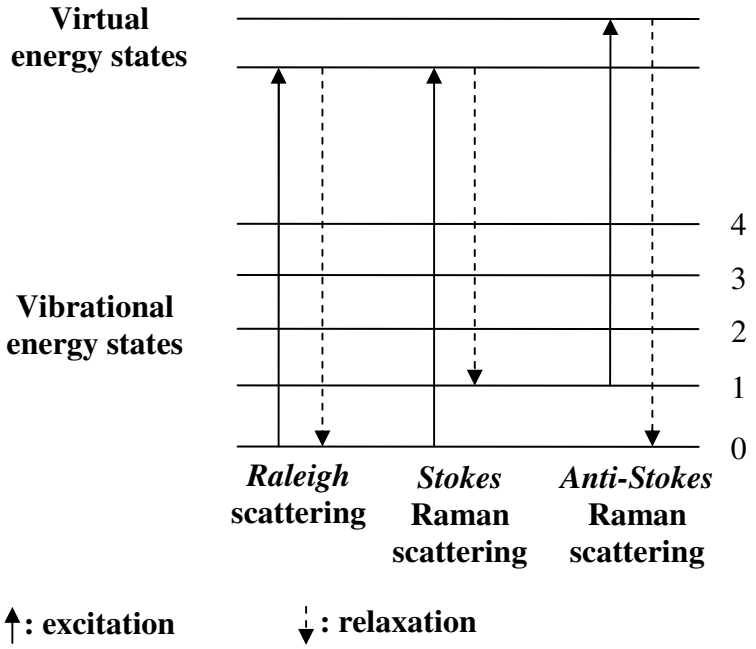

Figure 3.6 Energy level diagram summarizing a photon-molecule interaction showing three typical excitation and relaxation processes in Raman spectroscopy.[19]

3.10 References

1. S. C. Mayo, P. R. Miller, S. W. Wilkins, T. J. Davis, D. Gao, T. E. Gureyev, D. Paganin, D. J. Parry, A. Pogany, and A. W. Stevenson, "Quantitative X-ray projection microscopy: phase-contrast and multi-spectral imaging," *Journal of Microscopy-Oxford,* **207,** 79-96 (2002).

2. S. C. Mayo, T. J. Davis, T. E. Gureyev, P. R. Miller, D. Paganin, A. Pogany, A. W. Stevenson, and S. W. Wilkins, "X-ray phase-contrast microscopy and microtomography," *Optics Express,* **11,** 2289-2302 (2003).

3. D. B. Williams and C. B. Carter, Transmission electron microscopy: a textbook for materials science (Springer, 2nd Edition, 2009).

4. http://www.gatan.com/analysis/gif_tridiem865.php.

5. S. Jullian, R. Pantel, M. Juhel, L. F. T. Kwakman, and G. Vincent, "Determination of the spatial resolution function in energy filtered TEM and application to thin gate oxide measurements at 80 eV energy loss," *Microscopy and Microanalysis,* **10,** 578 (2004).

6. W. Zhou, "Nanostructural and chemical characterization of supported metal oxide catalysts by aberration corrected analytical electron microscopy," PhD Thesis, Lehigh University (2011).

7. S. Bernal, F. J. Botana, J. J. Calvino, C. López-Cartes, J. A. Pérez-Omil, and J. M. Rodríguez-Izquierdo, "The interpretation of HREM images of supported metal catalysts using image simulation: profile view images," *Ultramicroscopy,* **72,** 135-164 (1998).

8. M. De Graef, Introduction to conventional transmission electron microscopy (Cambridge University Press, 2003).

9. E. J. Kirkland, Advanced computing in electron microscopy (Plenum Press, 1998).

10. K. Ishizuka, "Prospects of atomic resolution imaging with an aberration-corrected STEM," *Journal of electron microscopy,* **50,** 291-305 (2001).

11. K. Ishizuka, "A practical approach for STEM image simulation based on the FFT multislice method," *Ultramicroscopy,* **90,** 71-83 (2002).

12. C. Boudias and D. Monceau, http://carine.crystallography.pagespro-orange.fr/index.html.

13. K. Momma and F. Izumi, "VESTA: a three-dimensional visualization system for electronic and structural analysis," *Journal of Applied Crystallography,* **41,** 653-658 (2008).

14. http://www.gatan.com/imaging/dig_micrograph.php.

15. S. Brunauer, P. H. Emmett, and E. Teller, "Adsorption of gases in multimolecular layers," *Journal of the American Chemical Society,* **60,** 309-319 (1938).

16. S. Ross and J. P. Olivier, On physical adsorption (Interscience Publishers, 1964).

17. B. E. Warren, X-ray diffraction (Dover Publications, Dover, 1990).

18. T. L. Barr, Modern ESCA: the principles and practice of x-ray photoelectron spectroscopy (CRC Press, 1994).

19. N. B. Colthup, L. H. Daly, and S. E. Wiberley, Introduction to infrared and Raman spectroscopy (Academic Press, 3rd Edition, 1990).

Chapter 4 Obtaining a better understanding of VPD method by adding alkanes during the alcohol reduction of $VOPO_4 \cdot 2H_2O$

4.1 Introduction

Several preparation methods for V-P-O catalysts have been developed and are now considered as standard, namely (i) the direct reduction of V_2O_5 by refluxing in an aqueous (acidic) medium, termed the *VPA route*,[1,2] (ii) the reduction of V_2O_5 in an organic medium, known as the *VPO route*,[2] and (iii) a more recent method based on the reduction of $VOPO_4 \cdot 2H_2O$ with an alcohol, termed the *VPD route*.[2,3] The VPD route was investigated initially by Horowitz *et al.* for short chain alcohols,[4]and Ellison *et al*.[5] for longer chain alcohols. Horowitz *et al*.[4] reported that a rosette-type morphology was typical for catalysts prepared via the VPD method when using 2-methyl-1-propanol and other primary alcohols as the reducing agent.

The use of secondary alcohols in the VPD route leads to discrete platelet type morphologies with much larger dimensions (2-4μm x 200 nm) than those prepared with primary alcohols, and tend to have much lower surface areas.[5] In the VPD case, catalysts having the rosette-type morphology, produced using primary alcohols, were found to be considerably more active than those displaying the platelet morphology due to the enhanced surface area.

Reaction of $VOPO_4 \cdot 2H_2O$ with 3-octanol produces the $VO(H_2PO_4)_2$ phase,[5] which is a completely different outcome to using primary and secondary alcohols. The $VO(H_2PO_4)_2$ material displays distinctive cuboidal particles about 10 μm in size and has a low surface area of *ca.* 2 m^2/g. The activity and selectivity of this $VO(H_2PO_4)_2$ phase

for MA production is negligible under the reaction conditions encountered during standard fixed bed operation.[6] Removal of $VO(H_2PO_4)_2$ from $VOHPO_4 \cdot 0.5H_2O$ by solvent extraction has been found to be beneficial whenever it was present as a minor impurity. Indeed most $VOHPO_4 \cdot 0.5H_2O$ preparations include boiling in water as a final step in order to remove water soluble impurities such as $VO(H_2PO_4)_2$. The reason for this intriguing primary/secondary/tertiary alcohol effect on the structure and morphology of VPD derived materials has yet to be fully determined and is considered to be due to some kind of steric effects of the alcohols as they interact with the laminar structure of $VOPO_4 \cdot 2H_2O$.

There have been numerous studies[7-10] concerned with catalyst preparation using the VPD method, however, the factors that influence the formation of $VOHPO_4 \cdot 0.5H_2O$ or $VO(H_2PO_4)_2$ from $VOPO_4 \cdot 2H_2O$ are still not well understood. In section 4.2, the addition of an alkane co-solvent during the reduction step of $VOPO_4 \cdot 2H_2O$ has been investigated, a variable which has not been considered in detail in any previous scientific publications and patents.

It is well known that the $VOPO_4 \cdot 2H_2O$ phase has a layer-type structure in which the VO_6 octahedra share their equatorial oxygen atoms with the PO_4 tetrahedra and each of the $VOPO_4$ sheets are connected by interlayer water molecules.[11] Hence the $VOPO_4 \cdot 2H_2O$ crystal is able, via water displacement, to accommodate organic molecules of various types between the layers, yielding a number of intercalation type compounds incorporating amine,[12] amide[13] and alcohol molecules.[14] Okuhara *et al.*[15] have reported the intercalation and subsequent exfoliation and fracture of $VOPO_4 \cdot 2H_2O$ crystals using primary and secondary alcohols. This was achieved via low temperature

heating in the alcohol followed by a subsequent reduction step in which the exfoliated $VOPO_4 \cdot 2H_2O$ sheets fracture to yield a $VOHPO_4 \cdot 0.5H_2O$ precursor which had a distinctive nano-sized (~ 340 x 35 nm) blocky morphology. In addition, the nanocrystalline $(VO)_2P_2O_7$ catalyst subsequently derived from this precursor was found to be highly active and selective for the oxidation *n*-butane to MA.[16] However limited studies have been performed on understanding the details of the phase transformation from $VOPO_4 \cdot 2H_2O$ to $VOHPO_4 \cdot 0.5H_2O$. O'Mahony *et al.*[17,18] tried to investigate the crystallization process of $VOHPO_4 \cdot 0.5H_2O$ in organic media using *in-situ* XRD, *ex-situ* XPS and *ex-situ* FIB studies. They proposed that rosette-type $VOHPO_4 \cdot 0.5H_2O$ is formed locally through the delamination and then the folding of platelet-type $VOPO_4 \cdot 2H_2O$, in which an intermediate monohydrate phase ($VOPO_4 \cdot H_2O$) is generated. It should be noted that this scenario is just a hypothesis for explaining the formation of rosette-type $VOHPO_4 \cdot 0.5H_2O$. It is well known that the $VOHPO_4 \cdot 0.5H_2O$ precursor and $(VO)_2P_2O_7$ activated catalysts have an epitaxial relationship, in which $[001]^{VOHPO_4 \cdot 0.5H_2O}$ // $[100]^{(VO)_2P_2O_7}$ and $[010]^{VOHPO_4 \cdot 0.5H_2O}$ // $[010]^{(VO)_2P_2O_7}$.[19] It is highly plausible that such an epitaxial relationship may be present between the $VOPO_4 \cdot 2H_2O$ and $VOHPO_4 \cdot 0.5H_2O$ phases.

To extend the study observed in section 4.2, in section 4.3 we investigate the effect the specific *order* in which the alkane and alcohol are added during the reduction of $VOPO_4 \cdot 2H_2O$ during the production of V-P-O materials. This systematic study of the VPD method has enabled us to better understand the preparation-performance relationship in the V-P-O catalyst system. In addition, in section 4.4 further details of the

important phase transformation process from the $VOPO_4 \cdot 2H_2O$ to the $VOHPO_4 \cdot 0.5H_2O$ structure will be unveiled using electron microscopy techniques.

4.2 Addition of alkanes during the alcohol reduction of $VOPO_4 \cdot 2H_2O$

4.2.1 Introduction

In the VPD route, the preparation of $VOHPO_4 \cdot 0.5H_2O$ is usually carried out via a two-step procedure, whereby $VOPO_4 \cdot 2H_2O$ is prepared by heating an aqueous solution of V_2O_5 and H_3PO_4 under reflux in the first step, then the $VOPO_4 \cdot 2H_2O$ is reduced, usually in an alcohol, to form the $VOHPO_4 \cdot 0.5H_2O$ precursor. When the reaction between V_2O_5, H_3PO_4 and a reducing agent is carried out in excess phosphoric acid, $VO(H_2PO_4)_2$ is found to be the major product.[20] This is perhaps unsurprising as a high P:V ratio in the starting material favours a product with a P:V ratio of 2. What is perhaps more surprising is the fact that $VOPO_4 \cdot 2H_2O$ with a fixed P:V ratio of 1 can be reduced with either 3-octanol[20] or an aldehyde or ketone[6] to give $VO(H_2PO_4)_2$.

In this study adding an alkane co-solvent during the reduction of $VOPO_4 \cdot 2H_2O$ in the VPD route has been studied, which has not been considered in detail in any previous scientific publications. Using an inert co-solvent it was found that the product of the preparation can be either $VOHPO_4 \cdot 0.5H_2O$ or $VO(H_2PO_4)_2$ depending on the reaction conditions. This enables a possible explanation for the formation of these two materials to be proposed.

4.2.2 Experimental

4.2.2.1 Catalyst preparation

Vanadium phosphate dihydrate ($VOPO_4 \cdot 2H_2O$) was prepared by the standard method described by Johnson *et al*.[3] V_2O_5 (10.0 g, Aldrich) and H_3PO_4 (60 ml, Aldrich) were refluxed in water (120 ml) under reflux conditions for 24 hours. The yellow solid was recovered by vacuum filtration, washed with cold water (100 ml) and acetone (100 ml) and dried in air for 24 h.

The $VOPO_4 \cdot 2H_2O$ was then reduced with alcohol (*i.e.* 1-octanol) in the presence of an alkane co-solvent (C_4-C_{16}). The synthesis was carried out by fixing the total volume of solvents whilst varying the alcohol/alkane ratio. The amount of $VOPO_4 \cdot 2H_2O$ was varied to keep a V:alcohol molar ratio of 1:50 while refluxing with a solvent mixture containing 0, 5, 15, 25, 50, 100, 125, 150, 160, 170 and 175 ml of alcohol and made up to a total volume of 175 ml with alkane (Table 4.1). The resulting solids were recovered by vacuum filtration and washed with alcohol (50 ml) and acetone (50 ml) and dried in air at 110°C for 24 h.

Table 4.1 Materials prepared by reacting $VOPO_4 \cdot 2H_2O$ with different amounts of 1-octanol and octane while keeping a V:ROH mole ratio of 1:50.

Material	$VOPO_4.2H_2O$ (g)	V:ROH[a]	1-Octanol (ml)	Octane (ml)
O2-15	0.3	1:50	15	160
O2-40	0.8	1:50	40	135
O2-50	1.0	1:50	50	125
O2-75	1.5	1:50	75	100
O2-100	2.0	1:50	100	75
O2-115	2.3	1:50	115	60
O2-125	2.5	1:50	125	50
O2-135	2.75	1:50	135	40
O2-160	3.2	1:50	160	15
O2-175	3.5	1:50	175	0

a: Vanadium to alcohol molar ratio.

4.2.2.2 Materials characterization

The materials were characterized using a combination of powder X-ray diffraction (XRD), BET surface area measurements, scanning electron microscopy (SEM) and transmission electron microscopy (TEM). Experimental details for these characterization methods have been described in Chapter 3, sub-sections 3.9.1, 3.9.2 and section 3.6, respectively.

4.2.3 Results and Discussion

Scanning electron microscopy (SEM) images (Fig. 4.1) confirm that the initial large flat plates of $VOPO_4 \cdot 2H_2O$ (Fig. 4.1, O2-15) progress to blocky, cubic $VO(H_2PO_4)_2$ (Fig. 4.1, O2-40, O2-50) as the amount of 1-octanol in the reaction mixture is increased. It can also be observed that as the mole fraction of alcohol in the solvent increases there is a shift in the resultant morphology of the $VOHPO_4 \cdot 0.5H_2O$ from platelets (Fig. 4.1, O2-75, O2-100, O2-115) to rosettes (Fig. 4.1, O2-125, O2-135, O2-160, O2-175). This progressive shift in morphology can also be observed in the XRD patterns (Fig. 4.2) with the platelet morphology producing an intense (001) reflection and rosettes characteristically having the (220) reflection as the dominant feature.[5,21] From these experiments it seems clear that the composition of the reduction solution has a major influence on which morphology/phase is formed.

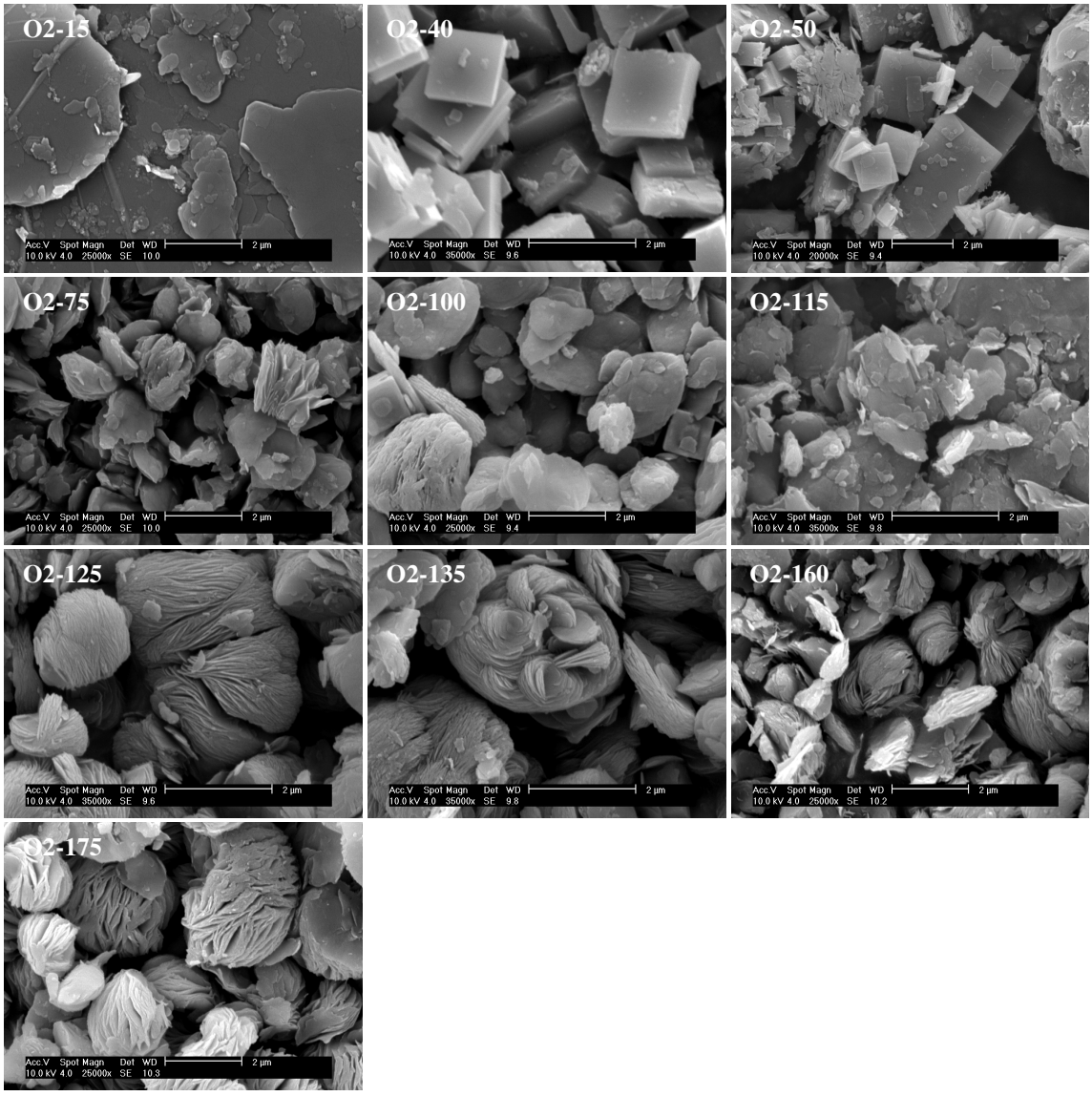

Figure 4.1 SEM micrographs of the materials prepared by reacting $VOPO_4 \cdot 2H_2O$ with different amounts of 1-octanol and octane while keeping the V: ROH mole ratio of 1:50.

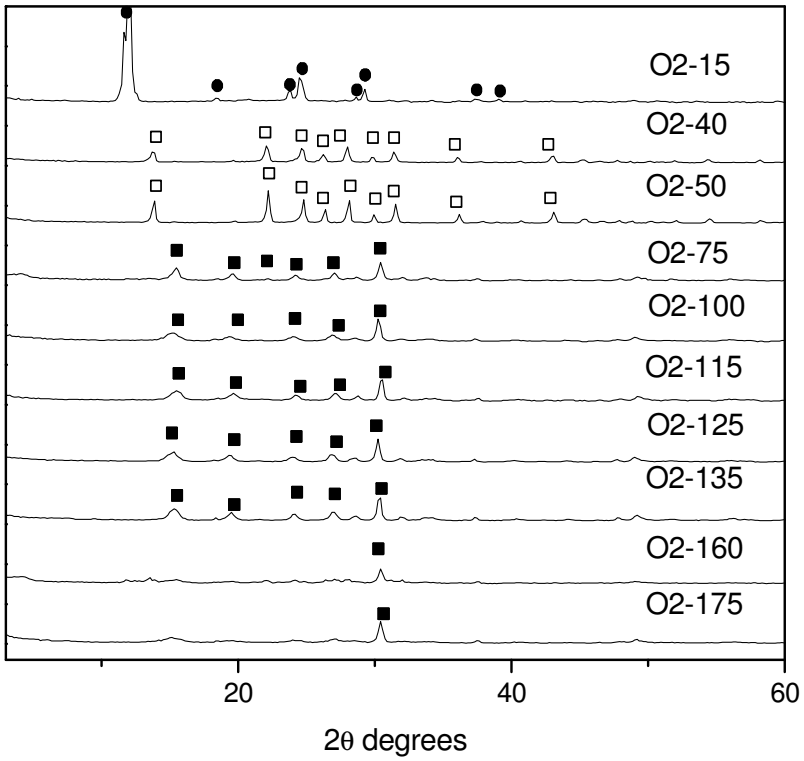

Figure 4.2 The XRD patterns of the materials prepared using different amounts of 1-octanol and octane as solvent with a V:ROH ratio of 1:50. Key: ■ = $VOHPO_4 \cdot 0.5H_2O$; □ = $VO(H_2PO_4)_2$; ● = $VOPO_4 \cdot 2H_2O$.

Detailed TEM studies were performed on the various crystallite morphologies noted in Figure 4.1 in order to carry out phase identification, measure crystallite dimensions, and characterize facet termination planes. Representative BF-TEM micrographs and selected area diffraction patterns (SADPs) obtained in this study are presented in Figure 4.3.

The starting dihydrate material consisted of square platelets (Fig. 4.3(a)) that were typically 5 μm in diameter and 0.2-1.0 μm in thickness. Selected area diffraction patterns (SADPs) obtained from the platelet normal direction (Fig. 4.3(b)) could be indexed to the [001] projection of the tetragonal $VOPO_4 \cdot 2H_2O$ phase (Fig. 4.3(c)). The

edge facets of the square platelets, each with a 90° intersection angle, correspond to alternating {110}-type planes around the [001] axis.

Characteristic square or rectangular block-type crystal morphologies (Fig. 4.3(d)) were produced when using high amounts of octane as a co-solvent (*i.e.* O2-40 and O2-50). The SADP from such a particle (Fig. 4.3(e)) matched to the [001] projection of tetragonal $VO(H_2PO_4)_2$ (Fig. 4.3(f)). These crystallites were typically about 1 μm x 1 μm x 2 μm in dimension and presented (001), (010) and (100) facet termination planes.

In the intermediate octane solvent range (*i.e.* O2-100 to O2-115) distinctive rhomboidal platelet crystals which had a tendency to stack together were noted (Fig. 4.3(g)). The lateral dimensions of the major and minor axes of these platelets were typically 2 μm x 1 μm and their thicknesses were in the 0.03-0.2 μm range. SADPs (Fig. 4.3(h)) from the platelet normal direction corresponded to the [001] projection of orthorhombic $VOHPO_4 \cdot 0.5H_2O$ (Fig. 4.3(i)). The edge facet termination planes of these angular platelets were {140} and $\{1\bar{4}0\}$-type.

Characteristic rosette type structures were observed (Fig. 4.3(j)) in samples with a low amount of octane as a co-solvent (*e.g.* O2-125 to O2-175). The rosettes were typically about 2 μm in diameter and consisted of a complex radial stack of platelets that were 0.03-0.2 μm in thickness. Occasionally some of these platelets would break off allowing us to collect SADPs from individual 'petals' of the rosette (Figs. 4.3(k)(l)). Analysis of such SADPs allowed us to confirm that they were $VOHPO_4 \cdot 0.5H_2O$ and exhibited [001] platelet normals.

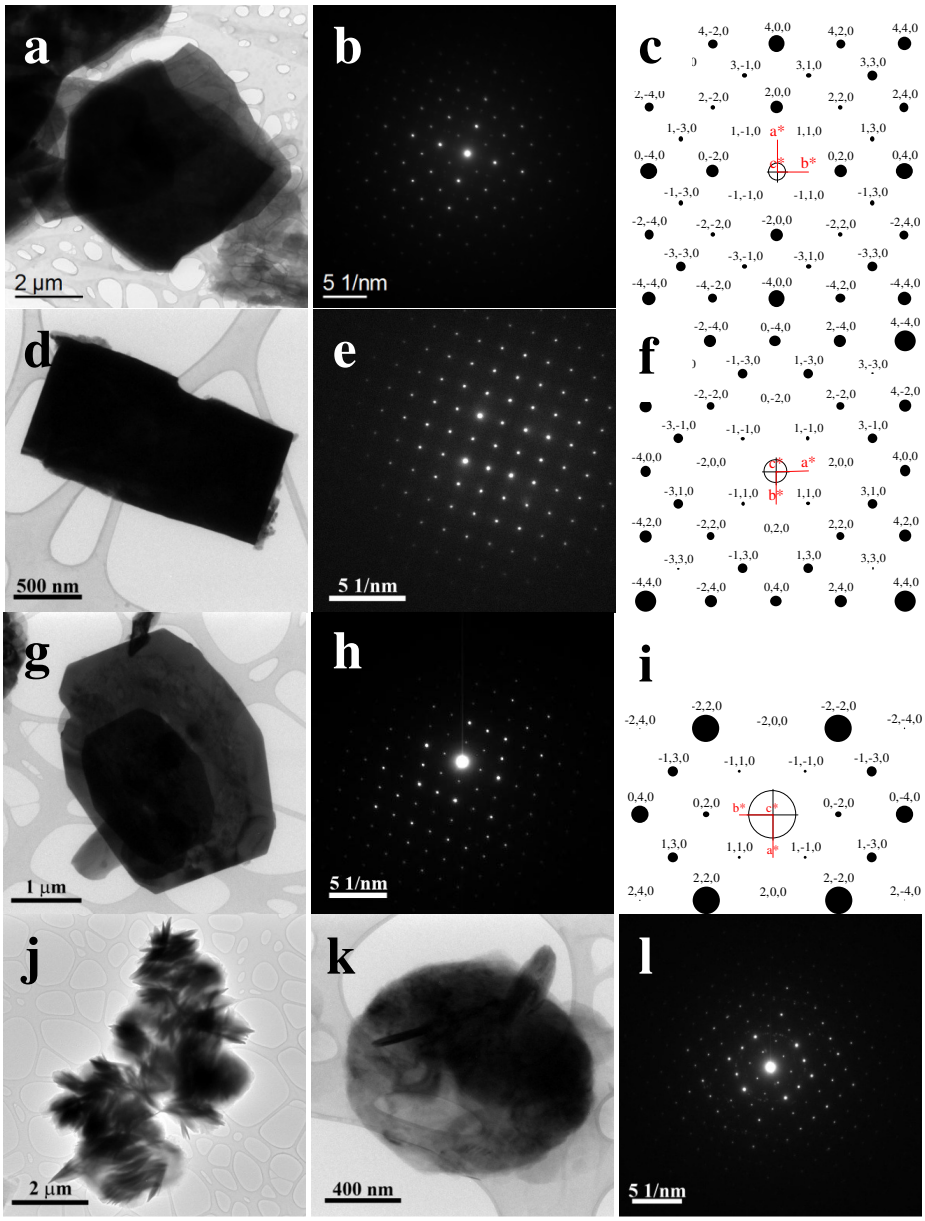

Figure 4.3 (a) BF-TEM micrograph, (b) experimental [001] SADP and (c) simulated and indexed [001] SADP from the cuboidal $VOPO_4 \cdot 2H_2O$ platelet. (d) BF-TEM micrograph, (e) experimental [001] SADP and, (f) simulated and indexed [001] SADP from the $VO(H_2PO_4)_2$ cuboid. (g) BF-TEM micrograph, (h) experimental [001] SADP and, (i) simulated and indexed [001] SADP from the rhomboidal platelet morphology of the $VOHPO_4 \cdot 0.5H_2O$. (j) BF-TEM micrograph of the rosette, (k) BF-TEM micrograph of one 'petal' from the rosette, and (l) experimental [001] SADP of the 'petal' in (k) corresponding to the [001] projection of $VOHPO_4 \cdot 0.5H_2O$.

The precise alcohol: alkane volume ratio seems to be a key factor influencing the vanadium phosphate formed from the starting dihydrate phase. If we assume that the

$VOHPO_4 \cdot 0.5H_2O$ and $VO(H_2PO_4)_2$ phase are synthesised through two different reaction pathways (Fig. 4.4), any changes in concentration of the alcohol could affect the reaction kinetics of the competing reactions and hence change the selectivity to a particular product. It was found during this study that $VOHPO_4 \cdot 0.5H_2O$ was only obtained with a high concentration of alcohol in the solvent mixture. It is proposed that the high concentration of alcohol results in a fast reaction rate between alcohol and $VOPO_4 \cdot 2H_2O$ and hence a faster reduction rate of V^{5+} to V^{4+}. Therefore, it is suggested that $VOHPO_4 \cdot 0.5H_2O$ is obtained when the V^{4+}: P ratio was kept at approximately 1:1 due to the fast reduction of V^{5+}. Conversely, it was found that $VO(H_2PO_4)_2$ was obtained with low concentrations of alcohol in the solvent mixture. The low concentration of alcohol results in a decreased reaction rate (between 1-octanol and $VOPO_4 \cdot 2H_2O$) and a correspondingly slower reduction rate of V^{5+} to V^{4+}. The slower reduction rate means that the V^{4+}: P ratio is 1: >>1 and the excess phosphorus favours the formation of $VO(H_2PO_4)_2$ which has a V: P ratio of 1:2. It can be concluded that the rate of reduction governs whether the V^{4+}: P ratio in solution is close to 1:1 or 1: >>1, which in turn is the key factor in determining which phase is formed. Two proposed scenarios of material formation are shown in Figure 4.4.

In this study, it has been discovered that by a relatively simple modification of the conventional VPD route, we can continuously and reproducibly go from the so-called E-phase ($(VO(PO_3)_2)$ blocky morphology - to the ($VOHPO_4 \cdot 0.5H_2O$) platelet morphology - to the ($VOHPO_4 \cdot 0.5H_2O$) rosette-type morphology. These crystal structure and morphological changes were shown to depend on the precise alcohol:alkane volume ratio in the reduction step.

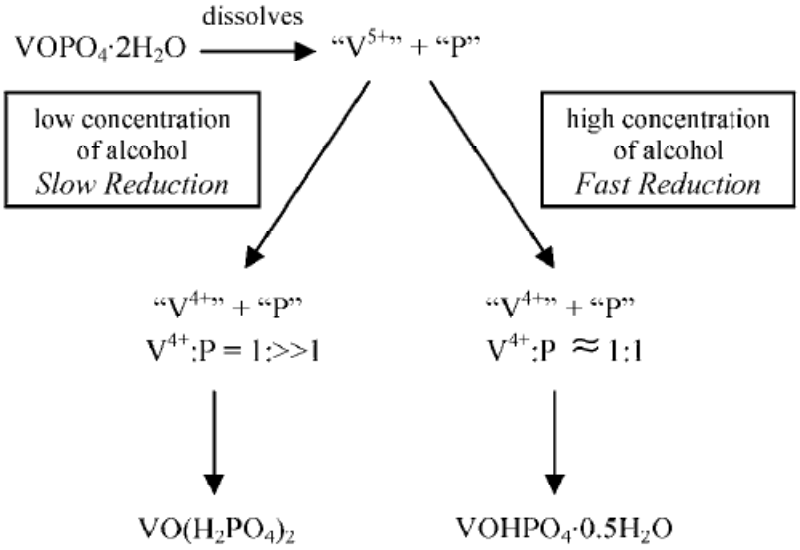

Figure 4.4 Proposed scenarios for the formation of $VO(H_2PO_4)_2$ and $VOHPO_4 \cdot 0.5H_2O$ from the reduction of $VOPO_4 \cdot 2H_2O$ with different alcohol/alkane mixtures.

4.3 Effect of the *order* of alcohol/alkane addition in the co-solvent reduction of $VOPO_4 \cdot 2H_2O$

4.3.1 Introduction

In the last section we have shown that the addition of an alkane co-solvent to the alcohol at the reduction stage in the VPD route can significantly influence the crystallinity and morphology of the resulting catalyst precursor. In this sub-section, vanadium phosphate catalysts have been prepared by reducing $VOPO_4 \cdot 2H_2O$ with *n*-octane and 1-butanol in an autoclave reactor. The specific *order* in which the alkane and alcohol are added during the reaction is shown to have a profound effect on the precursor morphology and eventual catalytic activity of the final $(VO)_2P_2O_7$ phase. Furthermore, through this study we have been able to elucidate the spatial orientation relationship between the $VOPO_4 \cdot 2H_2O$ and $VOHPO_4 \cdot 0.5H_2O$ crystalline phases. This information has

enabled us to propose a mechanism by which the important $VOPO_4 \cdot 2H_2O$ to $VOHPO_4 \cdot 0.5H_2O$ topotactic transformation occurs.

4.3.2 Experimental

4.3.2.1 Materials preparation

Preparation of $VOPO_4 \cdot 2H_2O$

V_2O_5 (10 g, Aldrich) and H_3PO_4 (60 ml, 85%, Aldrich) were refluxed in distilled water (120 ml) under reflux conditions for 24 h. The yellow solid was recovered immediately by vacuum filtration, washed with cold distilled water (100 ml) and acetone (100 ml) and dried in air at 110 °C for 24 h.

Reaction of $VOPO_4 \cdot 2H_2O$ with *n*-octane or (1-butanol) at 150°C. *(Route A and B)*

The $VOPO_4 \cdot 2H_2O$ (2 g) was reacted with 1-butanol (46 ml, route A) or *n*-octane (46 ml, route B) in an autoclave at 150 °C (autogeneous pressure) for 24 h. The resultant solid was recovered by vacuum filtration, and then washed with acetone (100 ml) and dried in air at 110 °C.

Reaction of $VOPO_4 \cdot 2H_2O$ with (1:1 1-butanol: *n*-octane mixture) *(Route C)*

The $VOPO_4 \cdot 2H_2O$ (2 g) was reacted with 1-butanol (23 ml) and *n*-octane (23 ml) in an autoclave at 150 °C (autogeneous pressure) for 24h. The resultant solid was recovered by vacuum filtration, and then washed and dried in air at 110 °C.

4.3.2.2 Catalyst testing

The oxidation of *n*-butane was carried out in a fixed bed micro-reactor with a standard mass of catalyst (0.2 g). The catalytic conditions for testing the activity of V-P-O catalysts have been described in sub-section 3.8.1.

4.3.2.3 Electron microscopy characterization

Scanning electron microscopy (SEM), bright field transmission electron microscopy (BF-TEM) and selected area electron diffraction (SAED) analyses were performed on these V-P-O materials. Experimental details for these characterization methods have been described in Chapter 3, section 3.6.

4.3.2.4 Complementary characterization techniques

A number of complementary techniques were used to structurally characterize the materials produced, including BET surface area measurements, powder X-ray diffraction (XRD) and Laser Raman spectroscopy as described in Chapter 3, sub-sections 3.9.1, 3.9.2 and 3.9.4, respectively.

4.3.3 Results

Characterization of the starting $VOPO_4 \cdot 2H_2O$ material

The standard $VOPO_4 \cdot 2H_2O$ (V^{5+}) material prepared using the VPD route typically consists of square platelets (Fig. 4.5(a)) that range from 4 - 60 μm in size and 0.2 - 1.0 μm in thickness and exhibit a layer-type structure (Fig. 4.5(b)). The surface area of such materials is typically about 1 m^2/g. Selected area electron diffraction (SAED) patterns obtained from the platelet normal direction (Fig. 4.5(d)) can be indexed to the [001] projection of the tetragonal $VOPO_4 \cdot 2H_2O$ phase (Fig. 4.5(e)).[11] The termination facets of the square platelets, each with a 90^o intersection angle, correspond to alternating {110}- type planes around the [001] axis of $VOPO_4 \cdot 2H_2O$ (Fig. 4.5(c)). The XRD patterns (Fig. 4.5(f)) of this material show that all the peaks can be assigned to

$VOPO_4 \cdot 2H_2O$ with the dominant reflection at 12.1˚ (*d*-spacing = 7.27 Å) corresponding to the (001) plane.

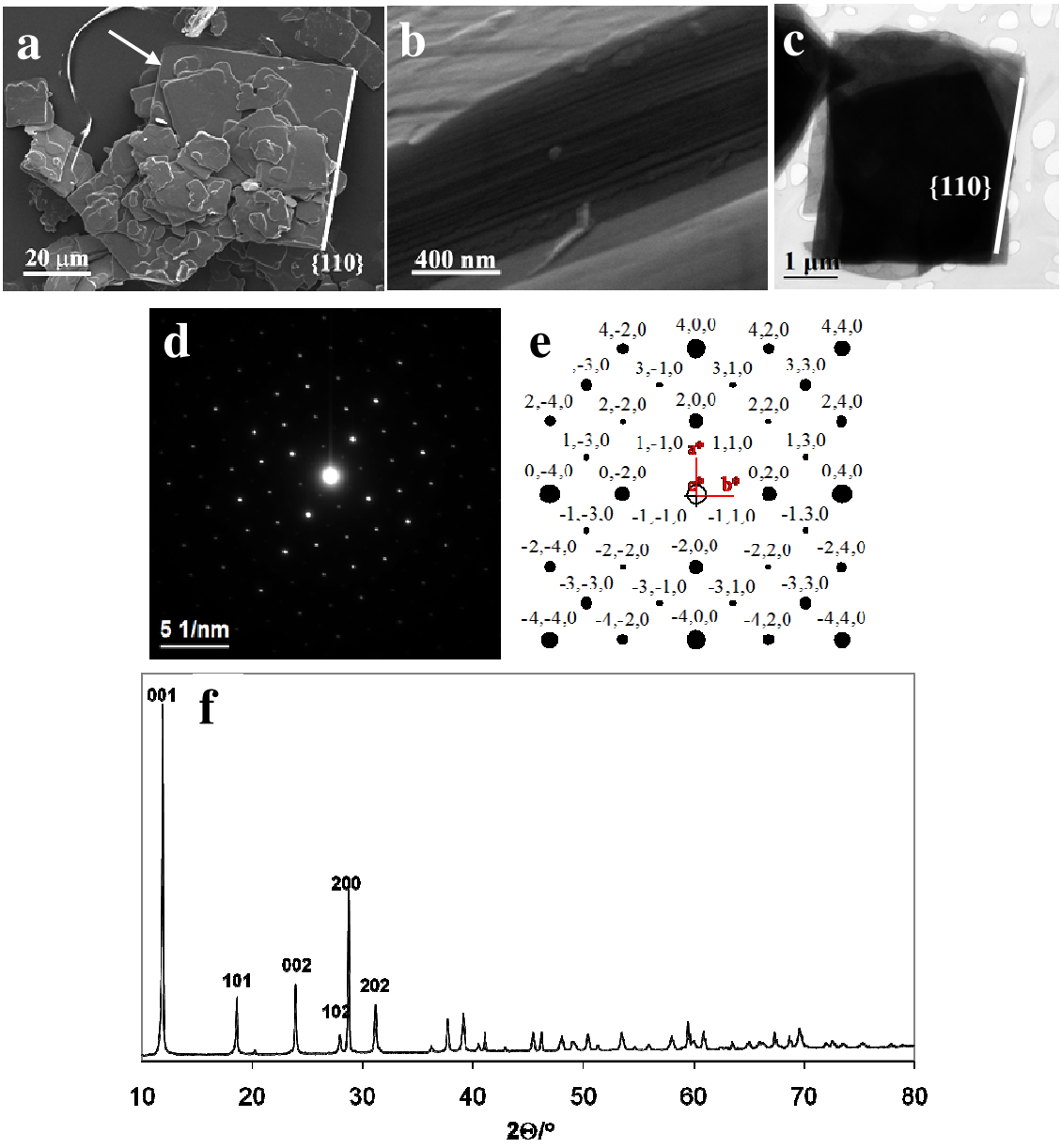

Figure 4.5 SEM micrographs of standard $VOPO_4 \cdot 2H_2O$ crystals showing (a) their square platelet morphology and (b) an edge-on view of their layer-type structure; (c) BF-TEM micrograph of a $VOPO_4 \cdot 2H_2O$ platelet showing {110}- type termination facets, (d) its corresponding SAED pattern which matches to the [001] projection of $VOPO_4 \cdot 2H_2O$ and (e) simulated and indexed SAED pattern in the [001] projection of $VOPO_4 \cdot 2H_2O$; (f) typical XRD pattern obtained from the $VOPO_4 \cdot 2H_2O$ material.

Starting from the standard square $VOPO_4 \cdot 2H_2O$ material, three different reaction protocols, denoted as routes A, B and C, were used to generate catalyst precursors $VOHPO_4 \cdot 0.5H_2O$ (V^{4+}) as shown in Figure 4.6. The primary difference between these routes is the order in which the 1-butanol/*n*-octane has been added to the $VOPO_4 \cdot 2H_2O$ slurry. In route A, 1-butanol was added first, followed by *n*-octane. In route B, the sequence is reversed *i.e. n*-octane was added first followed by 1-butanol. In the route C preparation, both *n*-octane and 1-butanl were added simultaneously to the $VOPO_4 \cdot 2H_2O$ slurry.

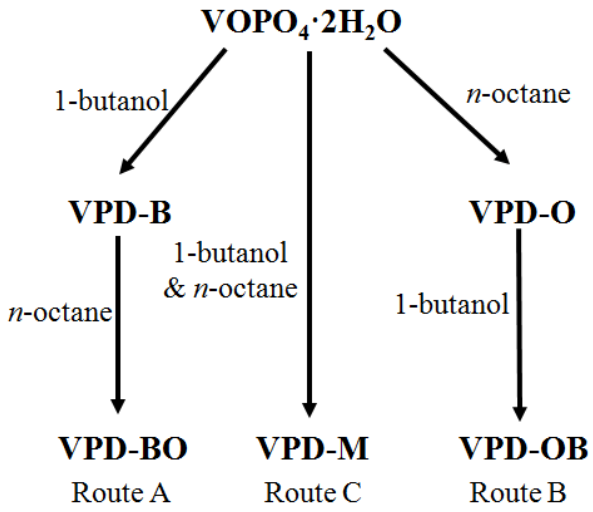

Figure 4.6 Schematic diagram summarizing the various combinations of alcohol and alkane addition during the dehydration of $VOPO_4 \cdot 2H_2O$ explored in this work.

XRD characterization of the $VOHPO_4 \cdot 0.5H_2O$ materials derived through Routes A, B and C

Figure 4.7(a) shows the XRD patterns of the final precursor materials (VPD-B, VPD-BO, VPD-OB and VPD-M) generated via routes A, B and C and the intermediate material (VPD-O) produced in route B, respectively. In each case for the four precursor materials, all the reflections can be indexed to $VOHPO_4 \cdot 0.5H_2O$. The predominant (220)

reflection in the XRD spectrum from sample VPD-B is characteristic of the rosette-type precursor morphology usually prepared by the standard VPD route using 1-butanol as the reducing agent. After refluxing with *n*-octane, precursor VPD-BO remained crystalline $VOHPO_4 \cdot 0.5H_2O$, as determined by XRD, showing a similar XRD pattern to that of material VPD-B, indicating that *n*-octane does not further alter the crystalline structure of $VOHPO_4 \cdot 0.5H_2O$. In route B when the starting $VOPO_4 \cdot 2H_2O$ material was mixed with *n*-octane to form the intermediate material VPD-O, it retained its $VOPO_4 \cdot 2H_2O$ crystalline structure as shown in Figure 4.7 (a, VPD-O) and Figure 4.7(b). The characteristic Raman shifts of $VOPO_4 \cdot 2H_2O$ (Fig. 4.7(b)) are found at 1033 cm^{-1} (V-O-P stretch), 990 cm^{-1} (V-O stretch) and 943 cm^{-1} (P-O stretch of PO_4 tetrahedra).[22,23] The subsequent reduction of sample VPD-O in 1-butanol generates a material whose dominant reflection in the $VOHPO_4 \cdot 0.5H_2O$ XRD pattern is no longer (220) but instead is (001). The high (001)/(220) peak ratio in the XRD spectrum of VPD-OB is typical of a platelet (as opposed to rosette) type morphology $VOHPO_4 \cdot 0.5H_2O$ material. This indicates that the $VOPO_4 \cdot 2H_2O$ material treated with *n*-octane (VPD-O) undergoes a different reduction process in route B compared to route A, where the $VOPO_4 \cdot 2H_2O$ material has already converted to $VOHPO_4 \cdot 0.5H_2O$ before it is refluxed with *n*-octane. For route C, the precursor material VPD-M, which was prepared by *co-addition* of *n*-octane and 1-butanol, exhibits an XRD pattern that bears some similarities to that of precursor VPD-OB but with a lower (001)/(220) peak ratio. This suggests that it adopts a structure which is intermediate between that of the classic rosette and platelet $VOHPO_4 \cdot 0.5H_2O$ morphologies.

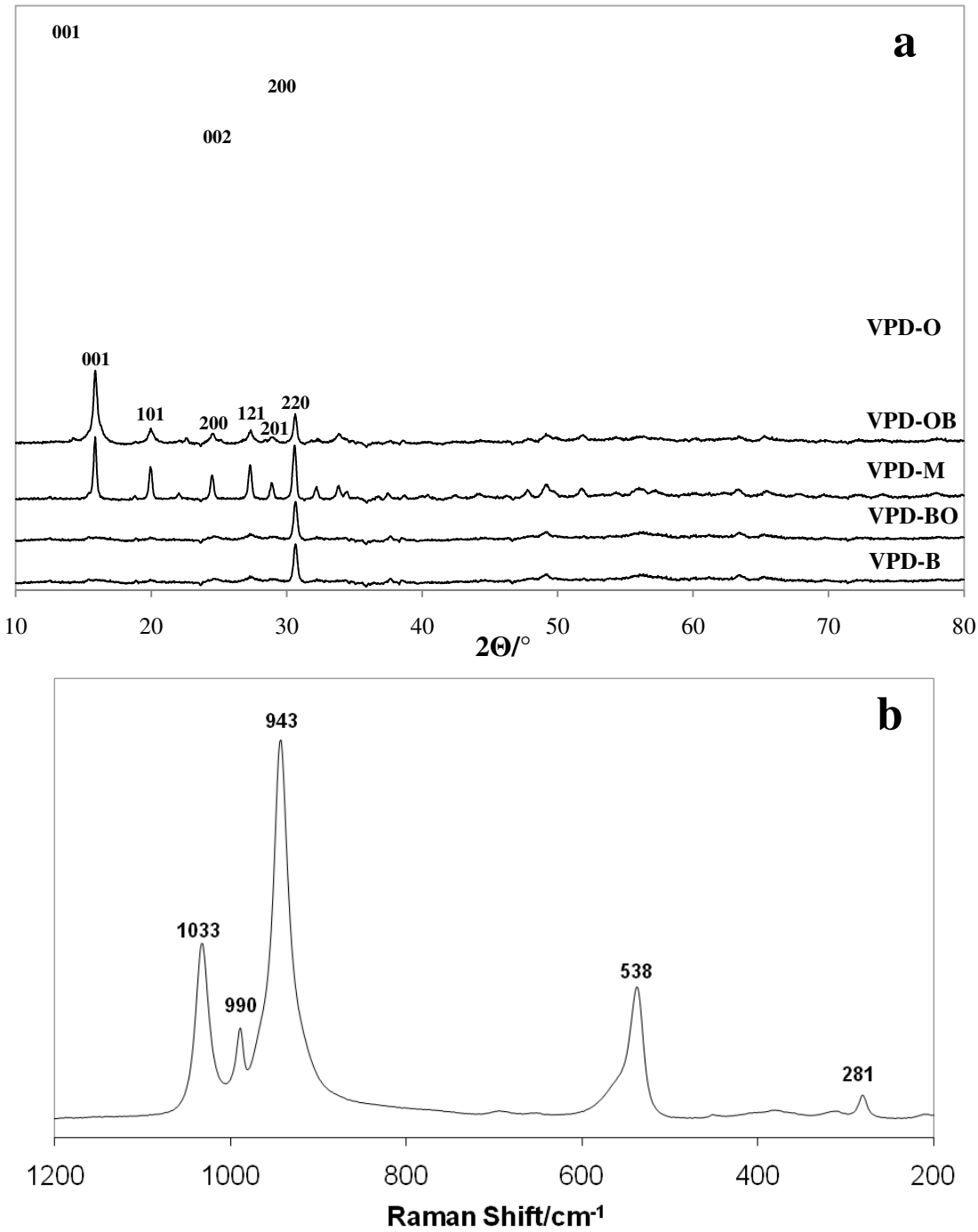

Figure 4.7 (a) Powder XRD patterns of intermediate material VPD-O and catalyst precursors VPD-B, VPD-BO, VPD-OB and VPD-M prepared by routes A, B and C, respectively. All the reflections in VPD-O can be indexed to $VOPO_4 \cdot 2H_2O$. All the reflections in VPD-B, VPD-BO, VPD-OB and VPD-M can be indexed to $VOHPO_4 \cdot 0.5H_2O$. (b) Laser Raman spectra of sample VPD-O showing main bands of $VOPO_4 \cdot 2H_2O$ at 1033 cm^{-1}, 990 cm^{-1} and 943 cm^{-1} corresponding to the $VOPO_4 \cdot 2H_2O$ phase.

Electron microscopy characterization of Route A materials

In the first step, the reaction of $VOPO_4 \cdot 2H_2O$ with 1-butanol in route A gave rise to a typical rosette-type agglomerate (VPD-B, Fig. 4.8(a)) in good agreement with the corresponding XRD pattern (Fig. 4.7, VPD-B). TEM and SAED analysis of a single 'petal' crystallite from one of the rosettes is shown in Figs. 4.8(b)(c). The 'petal' had (220) type termination facets and a normal direction which corresponded to the [001] projection of $VOHPO_4 \cdot 0.5H_2O$.[24], [25] The second step in the preparation procedure (*i.e.* the addition of *n*-octane) does not further change the crystal structure of the material. The VPD-BO sample is also the $VOHPO_4 \cdot 0.5H_2O$ phase (Fig. 4.8(f)) showing a similar rosette-type morphology (Fig. 4.8(d)) to that of VPO-B. Meanwhile the surface area (Table 4.2) decreases from $27 m^2/g$ for VPD-B to $18 m^2/g$ for VPD-BO after refluxing with *n*-octane, which could be correlated with the formation of a coarser rosette-type structure.

Table 4.2 Catalytic performance and surface area measurements of the various V-P-O materials for the oxidation of *n*-butane.

Catalyst precursor	Activated catalyst	Surface area (m^2/g)[a]		*n*-Butane Conversion (%)	Selectivity to maleic anhydride (%)	Specific activity[b]/ 10^{-5} mol/m^2/h
		Precursor	Catalyst			
VPD-B (Route A)	VPD-B-c	27	32	50	61	0.96
VPD-BO (Route A)	VPD-BO-c	18	27	50	58	1.09
VPD-OB (Route B)	VPD-OB-c	22	20	29	59	0.87
VPD-M (Route C)	VPD-M-c	17	24	47	55	1.09

[a]: All samples were degassed for an hour at 120 °C before BET analysis and were labelled according to Scheme 1.
[b]: Specific activity: moles maleic anhydride formed/g catalyst/h.
Reaction conditions: 400 °C, 1.7 % *n*-butane in air, GHSV = 2000 h^{-1}.

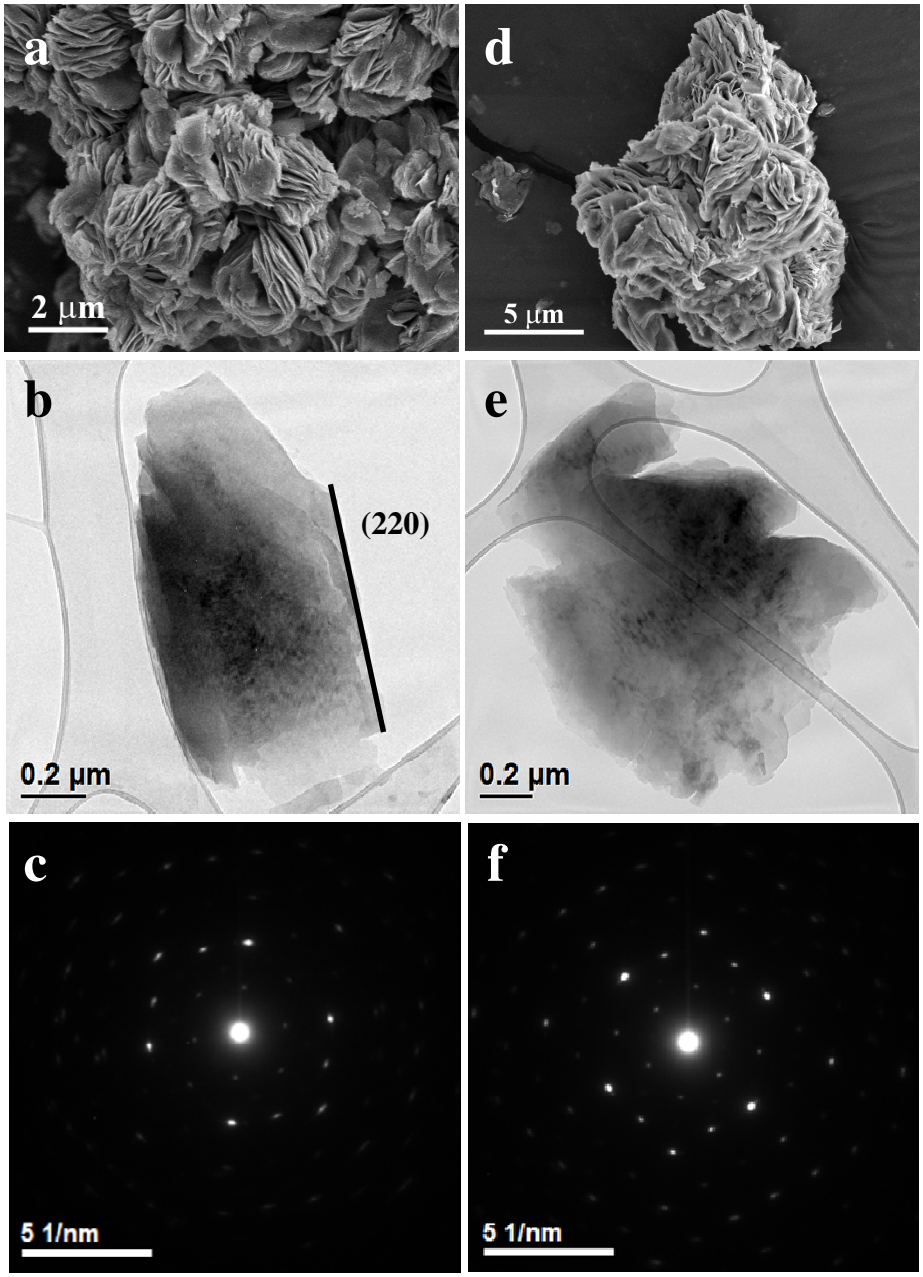

Figure 4.8 (a, b, c) VPD-B intermediate material: (a) SEM micrograph showing a characteristic rosette-type morphology; (b) BF-TEM micrograph showing a single 'petal' from the rosette agglomerate having (220)-type termination facets; and (c) SAED pattern from the 'petal' in (b) corresponding to the [001] projection of $VOHPO_4 \cdot 0.5H_2O$; (d, e, f) VPD-BO precursor material: (d) SEM micrograph showing a rosette-type morphology; (e) BF-TEM micrograph showing a single 'petal' from the rosette agglomerate; and (f) SAED pattern from the 'petal' in (e) corresponding to the [001] projection of $VOHPO_4 \cdot 0.5H_2O$.

Electron microscopy characterization of Route B materials

Refluxing $VOPO_4 \cdot 2H_2O$ with *n*-octane as the first step was found to change the morphology of the $VOPO_4 \cdot 2H_2O$ from square platelets (Fig. 4.5(a)) to octagonal platelets (Fig. 4.9(a)). These octagonal structures are typically 4-10 μm in size, and SAED analysis confirms them to be $VOPO_4 \cdot 2H_2O$ as evidenced by the [001] crystal projection shown in Figure 4.9(d). The termination facets of the octagonal platelet, each display a 45° intersection angle with adjoining facets, and correspond to alternating {100} and {110}- type planes (Fig. 4.9(c)). In addition, a small volume fraction of relatively large (~60 μm) flower-like octagonal platelets were also found in this VPD-O sample (Fig. 4.9(b)), which are believed to correspond to the largest square $VOPO_4 \cdot 2H_2O$ starting platelets (Fig. 4.5(a), arrowed) that are partway through a delaminating and etching process caused by progressive intercalation of the *n*-octane. It is known that α_I-$VOPO_4$ bears some structural similarities to $VOPO_4 \cdot 2H_2O$ when viewed along the [001] direction, but has a shorter interlayer spacing due to the absence of intercalated water molecules.[26,27] The delaminated edges in these occasionally found flower-type octagonal platelets (Fig. 4.9(b)), have probably lost their interlayer water molecules, and possibly locally converted to the α_I-$VOPO_4$ phase. However the α_I-$VOPO_4$ phase, if present, is there in such small quantities that it is below the detectibility limits of the XRD and Raman techniques.

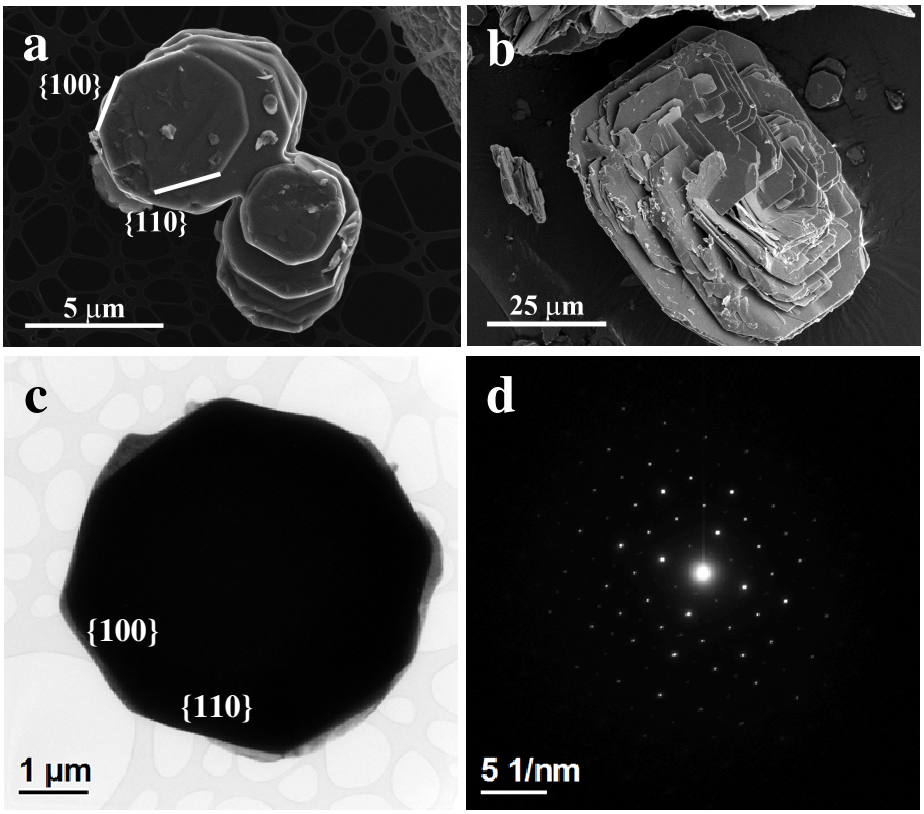

Figure 4.9 SEM micrographs of the intermediate VPD-O material (route B) showing (a) the major octagonal platelet morphology and (b) a minor octagonal flower-type morphology; (c) BF-TEM micrograph of sample VPD-O showing alternating {100} and {110} - edge facet termination planes of the octagonal platelets and (d) the corresponding SAED pattern for the particle in (c) which corresponds to [001] $VOPO_4 \cdot 2H_2O$.

The subsequent 2nd stage reflux with 1-butanol causes the reduction of the octagonal $VOPO_4 \cdot 2H_2O$ plates (V^{5+}) to the $VOHPO_4 \cdot 0.5H_2O$ (V^{4+}) phase. The XRD pattern in Figure 4.7 (VPD-OB) exhibits a dominant (001) $VOHPO_4 \cdot 0.5H_2O$ reflection as opposed to the (220), which is typical of plate-type V-P-O precursors. N_2 BET adsorption measurements (Table 4.2) reveals that the surface area of VPD-OB is 22 m^2/g. Unlike the rosette agglomerate morphology observed in Route A, nanoscale rhomboidal platelets (Figs. 4.10(a), (b)) are formed having a typical length of 400 - 600 nm and thickness of ~40 nm. The SAED pattern obtained from the platelet normal direction corresponds to the [001] $VOHPO_4 \cdot 0.5H_2O$ projection (Fig. 4.10(c)), which is consistent with the XRD

analysis (Fig. 4.7, VPD-OB). The edge termination facets exhibited by these rhomboidal platelets corresponded to the {140}-type planes.

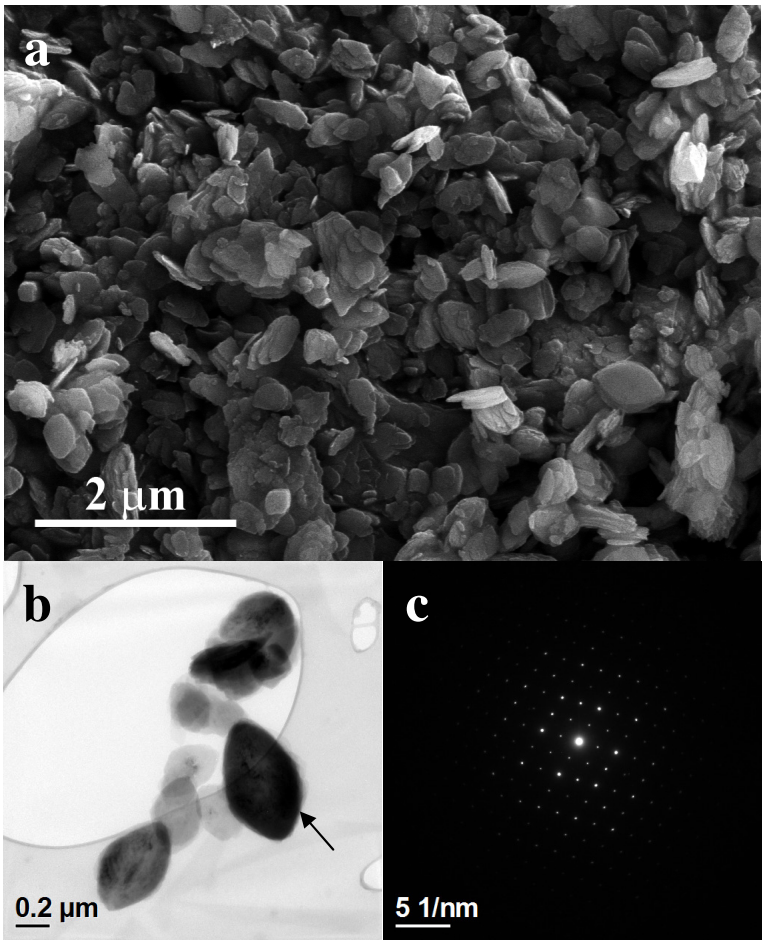

Figure 4.10 VPD-OB precursor material produced via Route B: (a) SEM micrograph showing nanoscale rhomboidal platelets; (b) BF-TEM micrograph of some nanoscale rhomboidal platelets showing edge termination facets corresponding to {140}-type $VOHPO_4 \cdot 0.5H_2O$ planes and (c) SAED pattern from the platelet arrowed in (b) which corresponds to the [001] projection of $VOHPO_4 \cdot 0.5H_2O$.

Clearly the formation of these nanoscale rhomboidal $VOHPO_4 \cdot 0.5H_2O$ platelets generated via route B is a consequence of a different transformation mechanism in comparison with Route A, where rosette formation is preferred.

Electron microscopy characterization of Route C material

When $VOPO_4 \cdot 2H_2O$ is reduced in a single step to $VOHPO_4 \cdot 0.5H_2O$ by refluxing with a mixture of *n*-octane and 1-butanol (route C), the morphology of the resulting material (VPD-M) exhibited structural characteristics that were somewhat intermediate between the route A VPD-B rosette-type agglomerates and the route B VPD-OB rhomboidal platelets. VPD-M showed what can be best described as loose rosette-type aggregations of angular rhomboidal platelets (Fig. 4.11(a)).

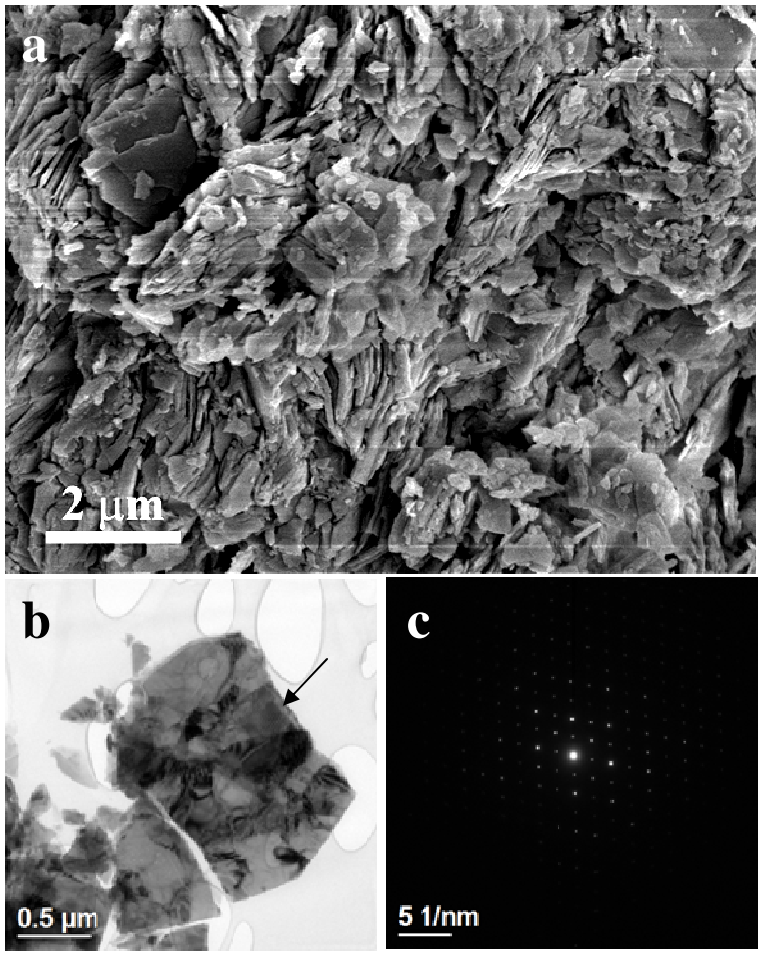

Figure 4.11 Precursor material VPD-M derived from route C: (a) SEM micrograph showing rosette-type aggregations of angular platelets; (b) BF-TEM micrograph of a typical angular plaetlet and (c) SAED pattern from the platelet arrowed in (b) which corresponds to [001] $VOHPO_4 \cdot 0.5H_2O$.

The BET surface area of VPD-M is only 17 m^2/g (Table 4.2) which is similar to that of the route B material. TEM analysis confirmed that these angular platelets are the $VOHPO_4 \cdot 0.5H_2O$ phase which exhibit the [001] projection as the platelet normal (Figs. 4.11(b), (c)), which is in good agreement with the corresponding XRD pattern (Fig. 4.7, VPD-M). Interestingly the (001)/(220) XRD peak ratio has an intermediate value (~1.11) between the highest peak ratio (~2.25) found in VPD-OB (route B) and the lowest ratio (~0.00) in VPD-BO (route A). This variation suggests the reduced exposure of (001) planes and increased exposure of (220) planes in VPD-M as compared to VPD-OB. The angular platelets in VPD-M when aggregated as shown in Fig. 4.11(a) could indeed result in a reduced exposure of (001) $VOHPO_4 \cdot 0.5H_2O$ planes and lead to lowering the (001)/(220) peak ratio.

Comparison of Route A, B and C materials as catalysts for *n*-butane oxidation

The V-P-O catalyst precursors derived from Routes A, B and C were activated and tested in a micro-reactor with 1.7 % *n*-butane/air feed at 400 °C. After 72 h, a steady state production of maleic anhydride was obtained. The catalytic performance data are summarized in Table 4.2 together with the surface areas of the activated catalysts. As expected, most catalysts display an increase in surface areas compared to their respective precursor materials after catalytic activation. Catalysts VPD-B-c, VPD-BO-c and VPD-M-c all show a similar activity and selectivity to MA, and exhibit comparable specific activity values. Surprisingly, catalyst VPD-OB-c (route B) obtained from the nanoscale rhomboidal catalyst precursor VPD-OB has the lowest specific activity for *n*-butane conversion at 29%, and is the only material that displays an decrease in surface area after activation.

The XRD patterns of all the activated catalysts are shown in Figure 4.12 and all the reflections in each of the patterns can be assigned to vanadyl pyrophosphate, $(VO)_2P_2O_7$. Catalysts VPD-B-c and VPD-BO-c display very similar XRD patterns having a dominant (024) reflection which is characteristic of rosette-type morphology catalysts. XRD patterns of catalyst VPD-OB-c have relatively broad (200) and (024) peaks indicative of a possible combination of the small primary particle size and the poorly crystalline active $(VO)_2P_2O_7$ phase in this sample. The gradually increasing (200)/(024) $(VO)_2P_2O_7$ peak ratios observed in Figure 4.12 (VPD-B-c ≈ VPD-BO-c < VPD-M-c < VPD-OB-c) show a similar trend to the (001)/(220) $VOHPO_4 \cdot 0.5H_2O$ peak ratios in Figure 4.7 (VPD-B ≈ VPD-BO < VPD-M < VPD-OB) confirming that a topotactic transformation from $VOHPO_4 \cdot 0.5H_2O$ to the $(VO)_2P_2O_7$ phase has occurred. Kiely *et al.* [19] have previously studied the structural details of this transformation in which $[001]^{VOHPO_4 \cdot 0.5H_2O}$ is parallel to $[100]^{(VO)_2P_2O_7}$ and $[010]^{VOHPO_4 \cdot 0.5H_2O}$ is parallel to $[010]^{(VO)_2P_2O_7}$.

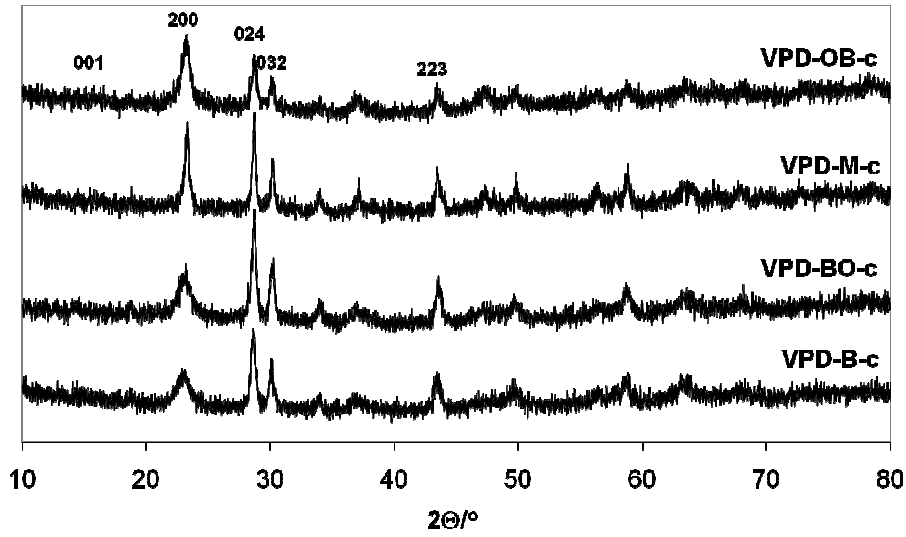

Figure 4.12 Powder XRD patterns of the activated catalysts VPD-BO-c (route A), VPD-B-c (intermediate step in route A), VPD-OB-c (final step in route B) and VPD-M-c (route C). All the reflections can be indexed to $(VO)_2P_2O_7$.

Figure 4.13 shows representative SEM micrographs (*column 1*), BF-TEM micrographs (*column 2*) and SAED patterns (*column 3*) obtained from the activated catalysts prepared via the three different routes. The morphology of catalyst produced in route A is very similar to that of the corresponding precursor, retaining its characteristic rosette-agglomerate morphology (Fig. 4.13(a)) as would be expected from the topotactic transformation of $VOHPO_4 \cdot 0.5H_2O$ to $(VO)_2P_2O_7$. SAED patterns from a catalyst "petal" (Figs. 4.13(b), (c)) can be indexed to the [100] projection of $(VO)_2P_2O_7$[28],[29] which is consistent with the XRD results presented in Figure 4.12- VPD-B-c. Catalyst VPD-OB-c (Fig. 4.13(d)) displays small crystallites whose size ranges from 50 to 400 nm. A similar morphology was also obtained by Imai *et al.*[16] through activating 340 nm x 35 nm starting $VOHPO_4 \cdot 0.5H_2O$ crystallites to form the $(VO)_2P_2O_7$. SAED patterns from a platelet type aggregate of such particles (Figs. 4.13(e)(f)) confirm them to be a collection of highly textured, but not perfectly aligned, $(VO)_2P_2O_7$ crystallites exhibiting a common [100] normal direction. A representative SEM micrograph of the VPD-M-c catalyst (Fig. 4.13(g)) also shows aggregations of many smaller particles. Figures 4.13(h) and (i) suggest that the small primary particles are $(VO)_2P_2O_7$ crystallites with an average size of ~200 nm. The corresponding polycrystalline ring SAED pattern from an agglomerate (Fig. 4.13(i)) show characteristic (200), (024), and (032) $(VO)_2P_2O_7$ reflections and indicate that the primary particles in these agglomerates are more randomly oriented with respect to each other as compared to the route B material.

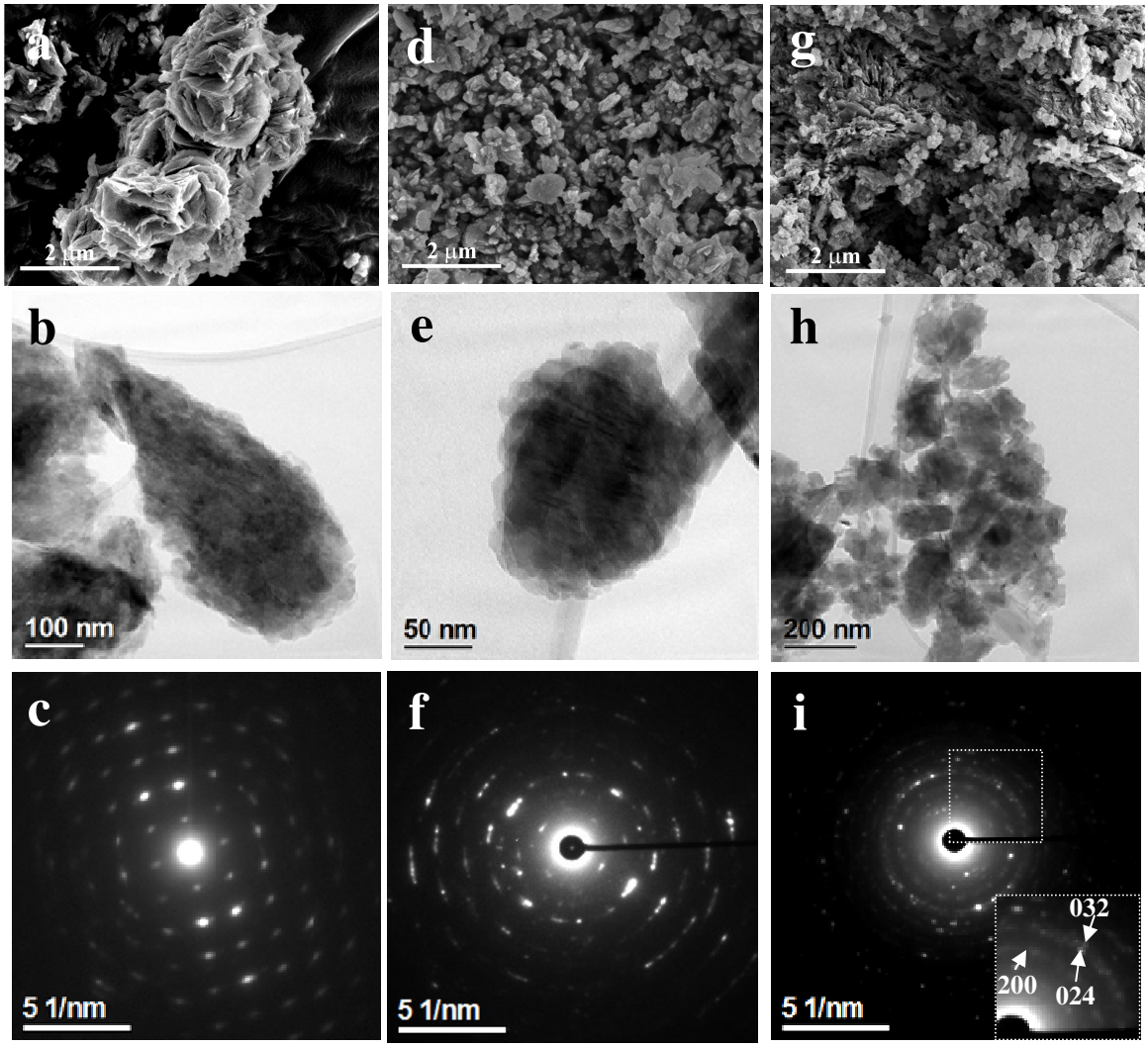

Figure 4.13 (a, b, c) Catalyst VPD-B-c (derived via routeA): (a) SEM micrograph showing a rosette-type agglomerate morphology; (b) BF-TEM micrograph showing a single 'petal' from a rosette and (c) the corresponding SAED pattern which can be assigned to the [100] projection of $(VO)_2P_2O_7$; (d, e, f) Catalyst VPD-OB-c (derived via route B): (d) SEM micrograph showing small agglomerates of particles; (e) BF-TEM micrograph showing an agglomerate of these particles and (f) the corresponding SAED pattern from the collection of particles shown in (e) which can be assigned to several superimposed [100] $(VO)_2P_2O_7$ patterns from particles having a relatively high degree of texture; (g, h, i) Catalyst VPD-M-c (derived via route C): (g) SEM micrograph showing almost random aggregations of small particles; (h) BF-TEM micrograph showing an aggreation of several small particles and (i) the corresponding SAED ring pattern which can be assigned to almost randomly oriented polycrystalline $(VO)_2P_2O_7$ (The inset shows an enlargement of a portion of the ring pattern delineated by the square box showing arcs corresponding to (200), (024) and (032) reflections of $(VO)_2P_2O_7$).

4.3.4 Discussion

The *order* in which the alcohol/alkane (*i.e.,* 1-butanol/*n*-octane) has been added during the co-solvent reduction of square $VOPO_4 \cdot 2H_2O$ platelets has a profound influence on the morphology of the $VOHPO_4 \cdot 0.5H_2O$ precursor generated. Here, we have shown via route A that without pre-exposure to *n*-octane, the product consists of typical rosette-type $VOHPO_4 \cdot 0.5H_2O$ agglomerates. Furthermore, *n*-octane added after the reduction with 1-butanol does not significantly change the morphology of the $VOHPO_4 \cdot 0.5H_2O$ material. By way of contrast, analysis of the route B preparation method, shows that pre-refluxing the square platelet $VOPO_4 \cdot 2H_2O$ with *n*-octane leads to the formation of partly delaminated octagonal $VOPO_4 \cdot 2H_2O$ platelets. Reduction of this intermediate material with 1-butanol forms distinctive nanoscale rhomboidal $VOHPO_4 \cdot 0.5H_2O$ platelets. Finally, using a mixture of *n*-octane and 1-butanol mixture (route C) reconstructs the square $VOPO_4 \cdot 2H_2O$ platelets into a rosette-type agglomerate of angular $VOHPO_4 \cdot 0.5H_2O$ platelets. All these morphological and structural alterations are summarized in Figure 4.14 and can be rationalized to some extent by the different actions of *n*-octane and 1-butanol on the $VOPO_4 \cdot 2H_2O$ crystallites. The *n*-octane predominantly etches the $VOPO_4 \cdot 2H_2O$ crystals altering their morphology, whereas the 1-butanol has a strong intercalation and exfoliation effect on $VOPO_4 \cdot 2H_2O$ and induces its reduction to $VOHPO_4 \cdot 0.5H_2O$.

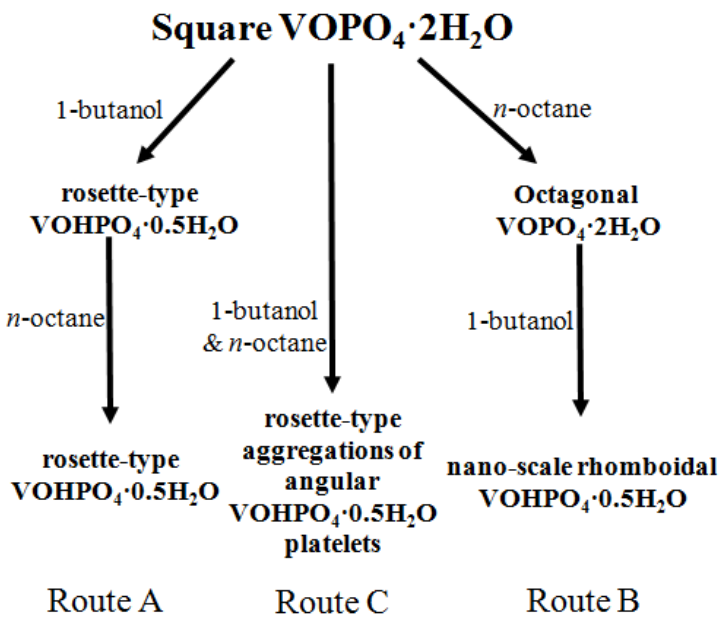

Figure 4.14 Summary of the morphological and structural features exhibited by this systematic set of samples.

In each case, these precursors, when activated under reaction conditions, convert to the active $(VO)_2P_2O_7$ phase and show good activity and selectivity to MA. The VPD-OB-c catalyst derived from the route B nanoscale rhomboidal precursor shows a lower specific activity possibly due to its poorer crystallinity and more limited exposure of the active (100) $(VO)_2P_2O_7$ plane.[22] The observed morphology of the VPD-OB-c catalyst also supports this notion as it shows small irregular, but strongly textured $(VO)_2P_2O_7$ particles, instead of the more sharply angular and better exposed crystallites normally found in fully activated rosette or platelet type catalyst.[16]

4.4 Understanding the topotactic transformation of the vanadyl (V) phosphate dihydrate to vanadyl (IV) hydrogen phosphate hemihydrate phase

It is well known that the catalytically active pyrophosphate phase, ($(VO)_2P_2O_7$), is obtained by activating a hemihydrate precursor ($VOHPO_4{\cdot}0.5H_2O$) under reaction

conditions. The details of the $VOHPO_4 \cdot 0.5H_2O$ to $(VO)_2P_2O_7$ topotactic structural transformation that occurs during this activation process have been solved previously by electron microscopy.[19] The VPD route used in this work for preparing the $VOHPO_4 \cdot 0.5H_2O$ precursor involves reacting V_2O_5 with H_3PO_4 to form the layered (V^{5+}) dihydrate phase ($VOPO_4 \cdot 2H_2O$), which is then subsequently reduced using an alcohol to form the $VOHPO_4 \cdot 0.5H_2O$ precursor (a V^{4+} phase). The structural details of this $VOPO_4 \cdot 2H_2O$ to $VOHPO_4 \cdot 0.5H_2O$ structural transformation are poorly documented and deserve some discussion here.

As shown in Figure 4.14, the morphological change to rosette type material occurring during the reduction of $VOPO_4 \cdot 2H_2O$ to $VOHPO_4 \cdot 0.5H_2O$ by 1-butanol (Fig. 4.14, route A) can be explained by the mechanism postulated by O'Mahony *et al.*[17] In their proposed scenario (Fig. 4.15), the layered $VOPO_4 \cdot 2H_2O$ material is delaminated by intercalation of the alcohol to form curled $VOPO_4 \cdot 2H_2O$ sheets due to the internal strain. The $VOHPO_4 \cdot 0.5H_2O$ phase is then nucleated at those curled sheet edges until eventually the whole sheet is transformed. The sheets remain connected to some extent during this process leading to the formation of rosette type agglomerates.

We have also demonstrated by simple experimentation that a shorter chain alcohol gives a stronger delaminating effect on the layered $VOPO_4 \cdot 2H_2O$ material as shown in Figure 4.16. After treatment with ethanol $VOPO_4 \cdot 2H_2O$ (Fig. 4.16(a)) shows a much greater degree of delamination at the crystallite edges as compared to the material treated with longer chain alcohols (*i.e.,* 1-butanol, Fig. 4.16(c)).

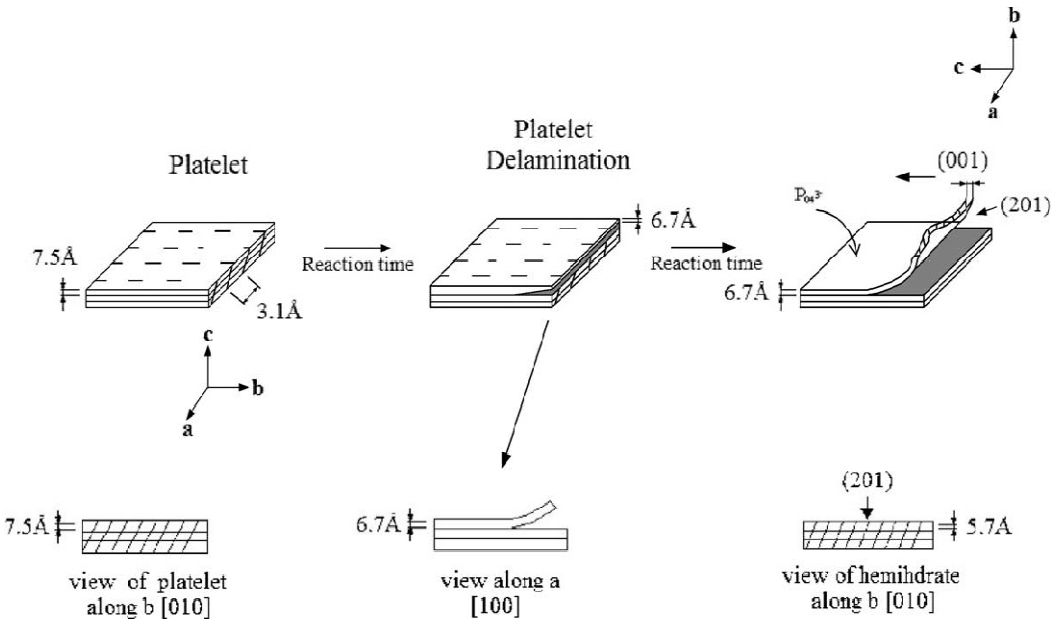

Figure 4.15 Schematic diagram of the crystallization process at early times for the transformation of platelet-type $VOPO_4 \cdot 2H_2O$ to rosette-type $VOHPO_4 \cdot 0.5H_2O$. [17]

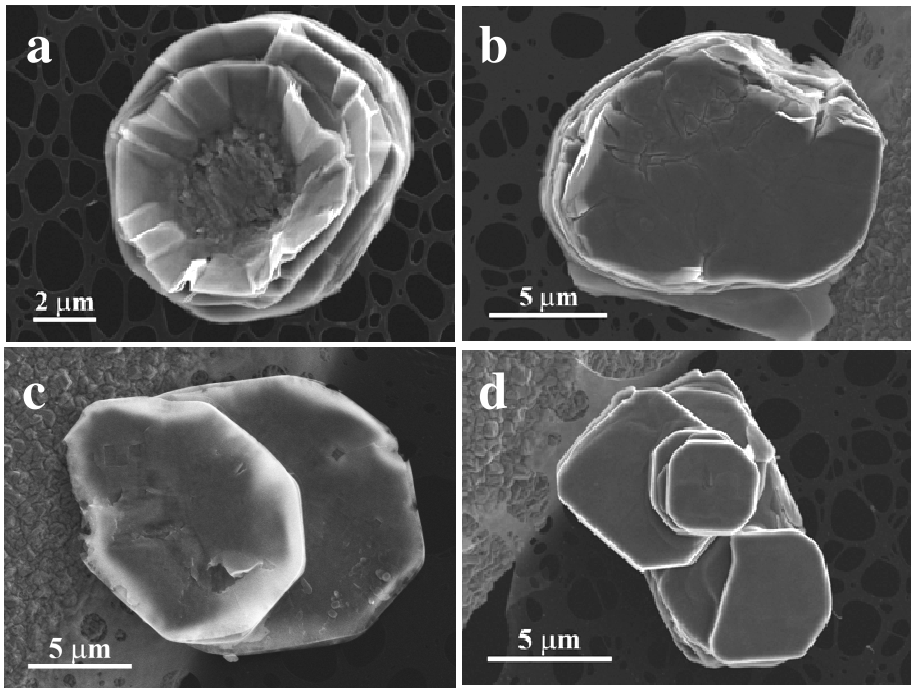

Figure 4.16 SEM micrographs of the same $VOPO_4 \cdot 2H_2O$ (VPD-O) material exposed to different alcohols: (a) C_2H_6O, (b) C_3H_8O, (c) $C_4H_{10}O$ and (d) $C_5H_{12}O$ for 1 min at room temperature showing progressively lower degrees of delamination to the crystallite edges with increasing chain length of the alcohol.

The square platelets of $VOPO_4 \cdot 2H_2O$ clearly tend to be reformed into rosette-type $VOHPO_4 \cdot 0.5H_2O$ agglomerates (Fig. 4.14, route A). In comparison, octagonal $VOPO_4 \cdot 2H_2O$, generated via route B, preferentially form nanoscale rhomboidal $VOHPO_4 \cdot 0.5H_2O$ platelets (Fig. 4.14, route B). In order to further understand this difference between routes A and B, both square and octagonal $VOPO_4 \cdot 2H_2O$ materials were exposed to 1-butanol at room temperature (Fig. 4.17). After 1 min treatment with 1-butanol both types of $VOPO_4 \cdot 2H_2O$ platelets show a slight delamination at their edges (Figs. 4.17(a)(c)). A closer look at the octagonal $VOPO_4 \cdot 2H_2O$ (VPD-B) platelet shows that it also exhibits small (~400 nm) fragments (arrowed in Fig. 4.17(b)) that have completely peeled away from the surface which are of a comparable scale to the resulting platelets of $VOHPO_4 \cdot 0.5H_2O$ precursor. The structural transformation in this latter case can be understood by invoking a similar initial mechanism to that proposed for the rosette-type $VOHPO_4 \cdot 0.5H_2O$ formation. However in this instance, the $VOPO_4 \cdot 2H_2O$ sheets are not only delaminated but also prone to fracture into smaller fragments, presumably because of structural defects introduced into the sheets. These fragments subsequently transform into the nanoscale rhomboidal $VOHPO_4 \cdot 0.5H_2O$ platelets. On the other hand, the standard square $VOPO_4 \cdot 2H_2O$ materials develop small square etch pits with {100}-type facet walls after 1 min exposure in 1-butanol (Fig. 4.17(c), (d)). With increasing exposure time to 1-butanol the original {110}-type edge termination facets of the $VOPO_4 \cdot 2H_2O$ crystal are gradually eroded and replaced with {100}-edge facets (Fig. 4.17(e)).

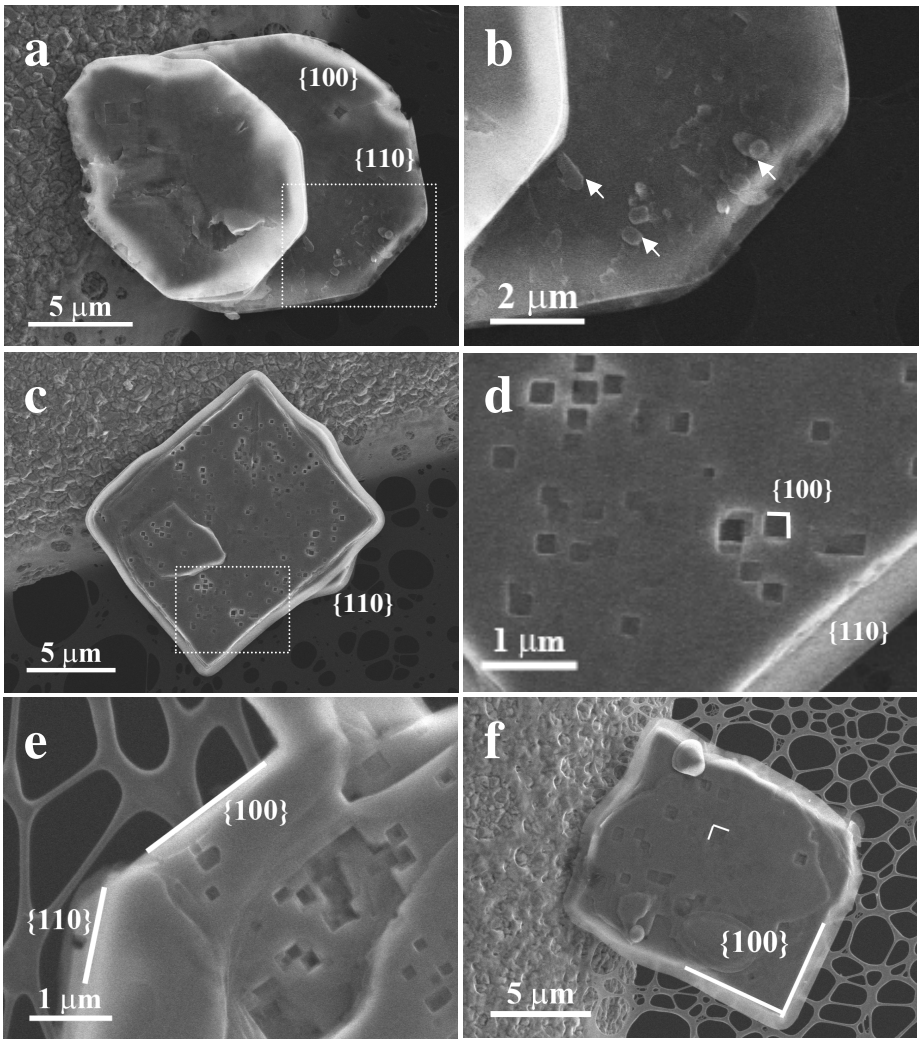

Figure 4.17 (a and b): SEM micrographs of octagonal $VOPO_4 \cdot 2H_2O$ platelets showing (a) slight delamination at their edges and (b) the generation of small (~400nm) dissociated surface fragments after 1 min exposure in 1-butanol; (c and d): SEM micrographs of square $VOPO_4 \cdot 2H_2O$ platelets after 1 min exposure in 1-butanol showing (c) slight delamination at their edges and (d) square etch pits with {100}- facet walls; (e and f): SEM micrographs of $VOPO_4 \cdot 2H_2O$ platelets showing (e) both {100}- and {110}- type termination facets after 20 min exposure in 1-butanol and (f) an occasionally found example having only {100}- type termination facets after 60 min exposure in 1-butanol.

After 60 min *n*-butanol exposure, $VOPO_4 \cdot 2H_2O$ platelets having only {100}-type edge termination facets and deep etch pits into their surface are observed (Fig. 4.17(f)). During the reduction reaction with *n*-butanol, the interlayer water molecules in $VOPO_4 \cdot 2H_2O$ need to escape from the structure. The deep penetrating {100}-type etch

pits observed in square platelets could open up convenient channels or vents along the <100> direction of the $VOPO_4 \cdot 2H_2O$ crystallite which facilitate the escape of the interlayer water molecules. In contrast, equivalent <100>-type channels are not opened up by *n*-butanol treatment of the octagonal $VOPO_4 \cdot 2H_2O$ platelets probably because of interference from the *n*-octane molecules introduced during the pre-treatment step. In this latter case, the need to release the trapped interlayer water molecules drives cracking and fracture of the platelets, resulting in the formation of fragments which break away from the structure.

It is well known that both the $VOPO_4 \cdot 2H_2O$ and $VOHPO_4 \cdot 0.5H_2O$ platelets exhibit a layer-type morphology having basal planes with [001] platelet normals as noted above (*i.e.,* $[001]^{VOPO_4 \cdot 2H_2O}$ remains oriented parallel to $[001]^{VOHPO_4 \cdot 0.5H_2O}$ during the transformation). The presence or absence of exposed {100}- type (*i.e.,* $(100)^{VOPO_4 \cdot 2H_2O}$ and $(010)^{VOPO_4 \cdot 2H_2O}$) facet planes and etch pits during the alcohol reduction/dehydration stage of the $VOPO_4 \cdot 2H_2O$ material seems to be very important in determining the morphology of the resulting $VOHPO_4 \cdot 0.5H_2O$ precursor (Fig. 4.14). When these specific (100) facet planes and etch pits are exposed, they can apparently be easily attacked by 1-butanol, resulting in a rosette type $VOHPO_4 \cdot 0.5H_2O$ morphology having (220) planes dominating the XRD patterns and consisting of crystalline 'petals' having (220) termination facets. Those {100}-type termination facets and etch pit edges in $VOPO_4 \cdot 2H_2O$ might be the nucleation sites for $VOHPO_4 \cdot 0.5H_2O$ formation and eventually epitaxial conversion into the (220) termination facets of $VOHPO_4 \cdot 0.5H_2O$. This proposed scenario is illustrated schematically in Figure 4.18, which is in good agreement with previous work by O'Mahony *et al.*[17]

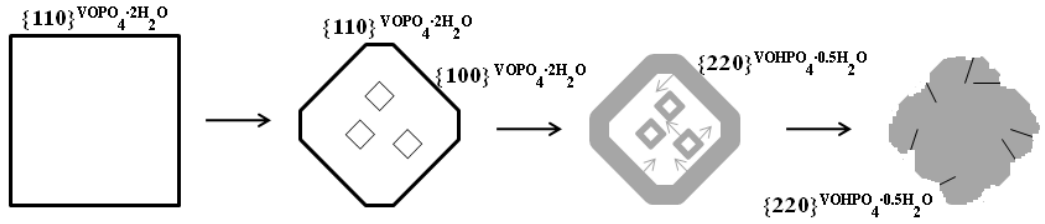

Figure 4.18 Schematic illustration of the transformation sequence from a square sheet of $VOPO_4 \cdot 2H_2O$ to rosette-type $VOHPO_4 \cdot 0.5H_2O$ during the reduction step involving 1-butanol (viewed along the [001] projection). (The gray area represents the $VOHPO_4 \cdot 0.5H_2O$ phase and the gray arrows show the growth directions of the $VOHPO_4 \cdot 0.5H_2O$ phase.)

In this study we have determined that {100}-type planes of $VOPO_4 \cdot 2H_2O$ can epitaxially transform to the (220) planes of $VOHPO_4 \cdot 0.5H_2O$. In addition, we know that the initial $[100]^{VOPO_4 \cdot 2H_2O}$ direction is parallel to the final $[110]^{VOHPO_4 \cdot 0.5H_2O}$ direction. Hence, the full orientation relationship that exists between the $VOPO_4 \cdot 2H_2O$ and $VOHPO_4 \cdot 0.5H_2O$ phases is: $[001]^{VOPO_4 \cdot 2H_2O}$ // $[001]^{VOHPO_4 \cdot 0.5H_2O}$ and $[100]^{VOPO_4 \cdot 2H_2O}$ // $[110]^{VOHPO_4 \cdot 0.5H_2O}$ as illustrated schematically in Figure 4.19. The $VOPO_4 \cdot 2H_2O$ structure is known to consist of non-connected VO_6 octahedra interlinked by PO_4 tetrahedra in each tetragonal '$VOPO_4$' layer.[11] These layers, which are stacked along the [001] direction, are connected by water molecules as shown in Figure 4.20(a). However, the sheets in the final $VOHPO_4 \cdot 0.5H_2O$ structure (Fig. 4.20(c)), are composed of pairs of face sharing VO_6 octahedra that are interlinked by PO_4 tetrahedra.[3,25,30] These layers are held along the [001] direction through the residual interlayer water molecules.

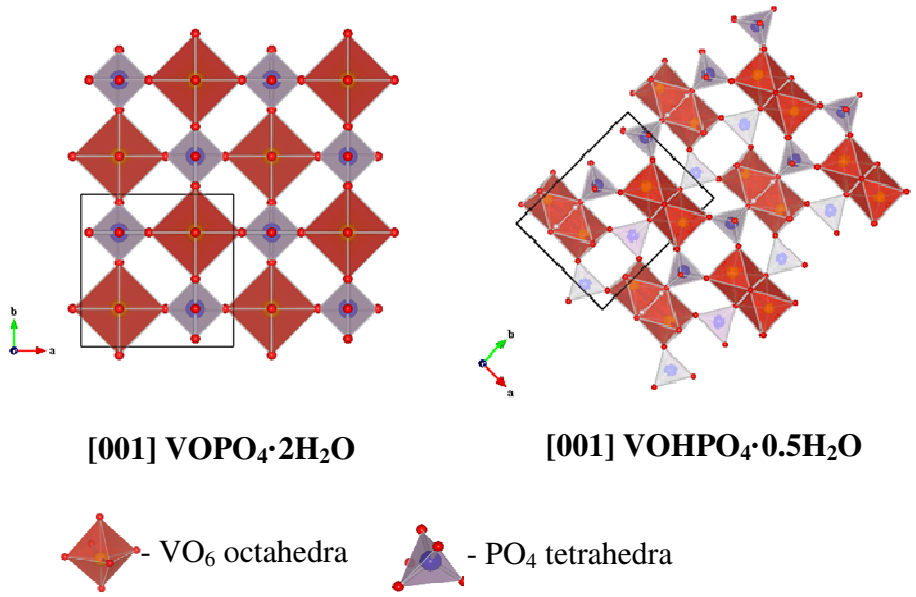

Figure 4.19 Atomic structure models of the $VOPO_4 \cdot 2H_2O$ (left) and $VOHPO_4 \cdot 0.5H_2O$ (right) phases oriented in such a way as to be faithful to the experimentally determined epitaxial orientation relationship: $[001]^{VOPO_4 \cdot 2H_2O}$ // $[001]^{VOHPO_4 \cdot 0.5H_2O}$ and $[100]^{VOPO_4 \cdot 2H_2O}$ // $[110]^{VOHPO_4 \cdot 0.5H_2O}$ (red spheres- O, blue spheres- P, yellow spheres- V; red octahedra- VO_6 octahedra, blue tetrahedra- PO_4 tetrahedra; H atoms are omitted for simplicity).

The transformation from $VOPO_4 \cdot 2H_2O$ to the $VOHPO_4 \cdot 0.5H_2O$ structure can be envisaged to occur in the following sequence of steps. Firstly, pairs of adjacent VO_6 octahedra shuffle towards one another in a co-ordinated fashion along the $[110]^{VOPO_4 \cdot 2H_2O}$ direction (as indicated by the arrows in Fig. 4.20(a)) and connect together such that they share a common edge. To facilitate this, two oxygen atoms are lost from one octahedral unit in the pair. This can also be viewed as one P-O-V bond being broken for every tetrahedral PO_4 group, leaving an unshared corner oxygen in the PO_4 tetrahedral unit. Meanwhile, one water molecule that is hydrogen bonded to each PO_4 group escapes from the structure giving rise to a transient $VOPO_4 \cdot H_2O$ monohydrate phase (Fig. 4.20(b)). Indeed, this transient monohydrate phase has previously been detected by O'Mahony *et al.*[17][18] during *in-situ* XRD and *ex-situ* XPS analysis of the dehydration of

$VOPO_4 \cdot 2H_2O$. Next the connected pairs of VO_6 octahedral units in the monohydrate structure re-orient to become face-sharing and yet another oxygen atom is lost from each octahedral pair (which then becomes incorporated into another escaping water molecule). Simultaneously, the V^{5+} cations within each of the VO_6 octahedral units must reduce to the V^{4+} valence state in order to ensure charge neutrality. The final result is that the $VOHPO_4 \cdot 0.5H_2O$ structure is topotactically generated which preferentially exposes the $(001)^{VOHPO_4 \cdot 0.5H_2O}$ basal plane.

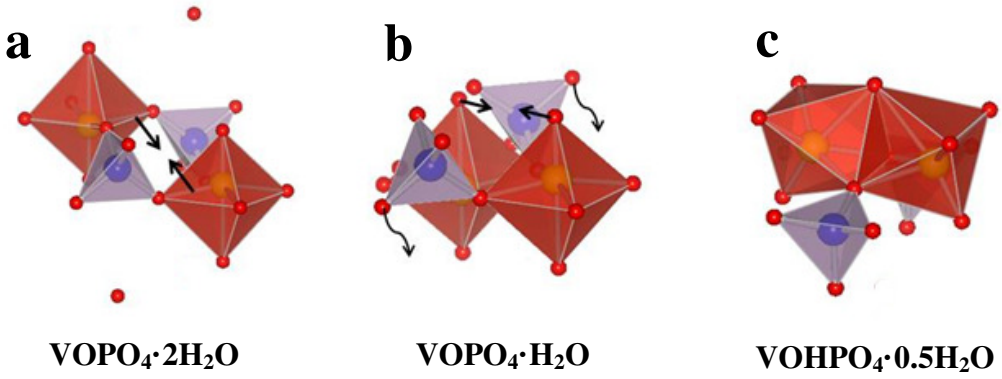

Figure 4.20 Structural models of the fundamental building blocks of the (a) $VOPO_4 \cdot 2H_2O$, (b) $VOPO_4 \cdot H_2O$ and (c) $VOHPO_4 \cdot 0.5H_2O$ structures. (red spheres- O, blue spheres- P, yellow spheres- V; red octahedra- VO_6 octahedra, blue tetrahedra- PO_4 tetrahedra; H atoms are omitted for simplicity). The diagram illustrates the proposed mechanism by which (i) unconnected neighbouring VO_6 octahedra units become edge sharing and (ii) edge shared VO_6 octahedra units become face sharing and PO_4 tetrahedral units re-orient during the topotactic $VOPO_4 \cdot 2H_2O$ to $VOHPO_4 \cdot 0.5H_2O$ transformation.

4.5 Summary and suggestions for future work

Using an inert co-solvent during the reduction step of $VOPO_4 \cdot 2H_2O$ in the VPD route, it was found that the product of the preparation can be either $VOHPO_4 \cdot 0.5H_2O$ or $VO(H_2PO_4)_2$ depending on the precise alcohol: alkane volume ratio. $VOHPO_4 \cdot 0.5H_2O$ is obtained when the V^{4+}: P ratio was kept at approximately 1:1 due to the fast reduction of

V^{5+}. When V^{4+}: P ratio is 1: >>1, the excess phosphorus favours the formation of $VO(H_2PO_4)_2$ which has a V: P ratio of 1:2. It can be concluded that the rate of reduction governs whether the V^{4+}: P ratio in solution is close to 1:1 or 1: >>1, which in turn is the key factor in determining which phase is formed.

The specific *order* in which the alkane and alcohol (*i.e. n*-octane and 1-butanol) are added to $VOPO_4 \cdot 2H_2O$ in the VPD process has a profound effect on the resultant precursor morphology and can influence the eventual activity of the final $(VO)_2P_2O_7$ catalyst. Here we have shown that without *n*-octane, the reduction product using 1-butanol is the rosette-type $VOHPO_4 \cdot 0.5H_2O$ agglomerate which is the typical precursor to the industrial V-P-O catalyst. The addition of *n*-octane after this reduction step does not significantly change the morphology of this precursor. In contrast, the addition of *n*-octane prior to the alcohol addition results in the formation of distinctive octagonal $VOPO_4 \cdot 2H_2O$ platelets, which are then subsequently reduced by 1-butanol to form nanoscale rhomboidal $VOHPO_4 \cdot 0.5H_2O$ platelets. On the other hand, co-addition of *n*-octane and 1-butanol can reduce and reform the square $VOPO_4 \cdot 2H_2O$ crystals into rosette-like aggregates of angular $VOHPO_4 \cdot 0.5H_2O$ platelets. Nearly all the catalysts produced show a good activity and selectivity to maleic anhydride, except for the pyrophosphate material generated from the nanoscale rhomboidal $VOHPO_4 \cdot 0.5H_2O$ platelets, which is probably due to their poorer crystallinity and more limited exposure of the active (100) $(VO)_2P_2O_7$ plane.

Additionally, through this study we have for the first time unequivocally identified the spatial orientation relationship between the $VOPO_4 \cdot 2H_2O$ and $VOHPO_4 \cdot 0.5H_2O$ crystalline phases, with $[001]^{VOPO_4 \cdot 2H_2O}$ // $[001]^{VOHPO_4 \cdot 0.5H_2O}$ and

$[100]^{VOPO_4\cdot 2H_2O}$ // $[110]^{VOHPO_4\cdot 0.5H_2O}$. This information has enabled us to propose a two-step mechanism by which the topotactic $VOPO_4\cdot 2H_2O$ to $VOHPO_4\cdot 0.5H_2O$ phase transformation occurs. This involves pairs of adjacent VO_6 octahedra in $VOPO_4\cdot 2H_2O$ becoming edge-sharing in the first step and then becoming face-sharing in the second step, losing interlayer water molecules at each stage, to eventually form $VOHPO_4\cdot 0.5H_2O$.

During the course of this research V-P-O materials were analyzed using SEM and conventional *ex-situ* TEM methods. Especially for studying the phase transformation of $VOPO_4\cdot 2H_2O$ into $VOHPO_4\cdot 0.5H_2O$, *ex-situ* SEM analysis was performed on the intermediate materials at different stages of the transformation process. Such intermediate materials prepared by mixing with alcohols at room temperature are not realistic intermediate materials, which should ideally be heated at 150 °C. If these realistic intermediate materials could be prepared and recovered from the refluxing slurry heated at 150 °C for SEM and even TEM analyses, it would provide additional information about the $VOPO_4\cdot 2H_2O$ to $VOHPO_4\cdot 0.5H_2O$ phase transformation. HR-TEM (low dose illumination conditions) could be used to analyze the rim region of the square etch pits to identify if the $VOHPO_4\cdot 0.5H_2O$ phase is formed topotactically from $VOPO_4\cdot 2H_2O$ in these areas (Figs. 4.18 and 4.20) and if there are any line or planar defects formed during this phase transformation. It would be even more helpful if we could use *in-situ* TEM for this particular experiment in order to prove or disprove our proposed transformation sequences under more realistic reaction conditions.

Our detailed study of the VPD route presented in this chapter was based on the use of primary alcohol (*e.g.* 1-octanol and 1-butanol) in the reduction step of

$VOPO_4 \cdot 2H_2O$. The primary product from this reaction are rosette-type $VOHPO_4 \cdot 0.5H_2O$ agglomerations. It is well known that secondary alcohols can also reduce $VOPO_4 \cdot 2H_2O$ to form platelet-type rhomboidal $VOHPO_4 \cdot 0.5H_2O$[5] and tertiary alcohols tend to preferably form blocky-type square $VO(H_2PO_4)_2$ crystallite.[5] Further analogous studies could be carried out in order to better understand the reaction mechanism of the VPD method when using secondary or tertiary alcohols. Using the same strategy as employed in this work, the addition of alkanes (*e.g. n*-octane) into secondary or tertiary alcohols during the reduction step of $VOPO_4 \cdot 2H_2O$ will probably change the structure and morphology of the resulting product. If the specific *order* in which the alkane and alcohol (*i.e.* secondary or tertiary) are added to $VOPO_4 \cdot 2H_2O$ is changed following the same strategy outlined in Figure 4.6. A more complete picture of the effect of each alcohol on the $VOPO_4 \cdot 2H_2O$ to rhomboidal $VOHPO_4 \cdot 0.5H_2O$ or square $VO(H_2PO_4)_2$ platelets could then be developed.

4.6 Acknowledgements

In section 4.2 the V-P-O catalyst syntheses, as well as the XRD and SEM experiments were performed by Dr. Umacaran Sithamparappillai, Dr. Nicholas F. Dummer and Dr. Jonathan K. Bartley in Prof. Graham J. Hutchings's group at Cardiff University. Their contributions are much appreciated.

In section 4.3 the V-P-O catalyst syntheses, BET surface area measurements, XRD experiments, Raman spectroscopy experiments and catalyst testing on the selective oxidation of *n*-butane to maleic anhydride were performed by Dr. Raja Al Otaibi, Mosaed Alhumaimess, Dr. Marco Conte, Dr. Nicholas F. Dummer and Dr. Jonathan K. Bartley in

Prof. Graham J. Hutchings's group at Cardiff University. Their various contributions to this work are much appreciated and gratefully acknowledged.

4.7 References

1. E. A. Lombardo, C. A. Sanchez, and L. M. Cornaglia, "The effect of preparation methods and activation strategies upon the catalytic behavior of the vanadium-phosphorus oxides," *Catalysis Today,* **15,** 407-418 (1992).

2. G. J. Hutchings, M. T. Sananes, S. Sajip, C. J. Kiely, A. Burrows, I. J. Ellison, and J. C. Volta, "Improved method of preparation of vanadium phosphate catalysts," *Catalysis Today,* **33,** 161-171 (1997).

3. J. W. Johnson, D. C. Johnston, A. J. Jacobson, and J. F. Brody, "Preparation and characterization of $VO(HPO_4)\cdot 0.5H_2O$ and its topotactic transformation to $(VO)_2P_2O_7$," *Journal of the American Chemical Society,* **106,** 8123-8128 (1984).

4. H. S. Horowitz, C. M. Blackstone, A. W. Sleight, and G. Teufer, "V-P-O catalysts for oxidation of butane to maleic-anhydride - Influence of $(VO)_2H_4P_2O_9$ precursor morphology on catalytic properties," *Applied Catalysis,* **38,** 193-210 (1988).

5. I. J. Ellison, G. J. Hutchings, M. T. Sananes, and J. C. Volta, "Control of the composition and morphology of vanadium phosphate catalyst precursors from alcohol treatment of $VOPO_4\cdot 2H_2O$," *Journal of the Chemical Society-Chemical Communications,* 1093-1094 (1994).

6. J. K. Bartley, C. Rhodes, C. J. Kiely, A. F. Carley, and G. J. Hutchings, " *n*-Butane oxidation using $VO(H_2PO_4)_2$ as catalyst derived from an aldehyde/ketone based preparation method," *Physical Chemistry Chemical Physics,* **2,** 4999-5006 (2000).

7. Y. Kamiya, S. Ueki, N. Hiyoshi, N. Yamamoto, and T. Okuhara, "Preparation of catalyst precursors for selective oxidation of *n*-butane by exfoliation-reduction of $VOPO_4\cdot 2H_2O$ in primary alcohol," *Catalysis Today,* **78,** 281-290 (2003).

8. L. Griesel, J. K. Bartley, R. P. K. Wells, and G. J. Hutchings, "Preparation of vanadium phosphate catalysts from $VOPO_4\cdot 2H_2O$: effect of $VOPO_4\cdot 2H_2O$ preparation on catalyst performance," *Journal of Molecular Catalysis A-Chemical,* **220,** 113-119 (2004).

9. Y. H. Taufiq-Yap, C. K. Goh, G. J. Hutchings, N. Dummer, and J. K. Bartley, "Effects of mechanochemical treatment to the vanadium phosphate catalysts derived from $VOPO_4\cdot 2H_2O$," *Journal of Molecular Catalysis A-Chemical,* **260,** 24-31 (2006).

10. H. Imai, Y. Kamiya, and T. Okuhara, "Synthesis of $(VO)_2P_2O_7$ catalysts via exfoliation-reduction of $VOPO_4\cdot 2H_2O$ in butanol in the presence of ethanol," *Research on Chemical Intermediates,* **34,** 669-677 (2008).

11. H. R. Tietze, "The crystal and molecular-structure of oxovanadium(v) ortho-phosphate dihydrate, $VOPO_4 \cdot 2H_2O$," *Australian Journal of Chemistry,* **34,** 2035-2038 (1981).

12. T. Yatabe, M. Nakano, and G. E. Matsubayashi, "Intercalation of substituted pyridine derivatives and bipyridine compounds into gel-V_2O_5 and $VOPO_4$ interlayer spaces and protonation of the guest molecules," *Journal of Materials Chemistry,* **8,** 699-703 (1998).

13. M. M. Lara, L. M. Real, A. J. Lopez, S. B. Gamez, and A. R. Garcia, "Interaction of amides with $VOAO_4 \cdot nH_2O$ (A=P, As)," *Materials Research Bulletin,* **21,** 13-22 (1986).

14. L. Benes, K. Melanova, V. Zima, J. Kalousova, and J. Votinsky, "Preparation and probable structure of layered complexes of vanadyl phosphate with 1-alkanols and 1,omega-alkanediols," *Inorganic chemistry,* **36,** 2850-2854 (1997).

15. N. Yamamoto, N. Hiyoshi, and T. Okuhara, "Thin-layered sheets of $VOHPO_4 \cdot 0.5H_2O$ prepared from $VOPO_4 \cdot 2H_2O$ by intercalation-exfoliation-reduction in alcohol," *Chemistry of Materials,* **14,** 3882-3888 (2002).

16. H. Imai, Y. Kamiya, and T. Okuhara, "Selective oxidation of *n*-butane over nanosized crystallites of $(VO)_2P_2O_7$ synthesized by an exfoliation-reduction process of $VOPO_4 \cdot 2H_2O$ in a mixture of 2-butanol and ethanol," *Journal of Catalysis,* **251,** 195-203 (2007).

17. L. O'Mahony, J. Henry, D. Sutton, T. Curtin, and B. K. Hodnett, "Crystallisation of $VOHPO_4 \cdot 0.5H_2O$," *Applied Catalysis A-General,* **253,** 409-416 (2003).

18. L. O'Mahony, T. Curtin, D. Zemlyanov, M. Mihov, and B. K. Hodnett, "Surface species during the crystallization of $VOHPO_4 \cdot 0.5H_2O$," *Journal of Catalysis,* **227,** 270-281 (2004).

19. C. J. Kiely, A. Burrows, G. J. Hutchings, K. E. Bere, J. C. Volta, A. Tuel, and M. Abon, "Structural transformation sequences occurring during the activation of vanadium phosphorus oxide catalysts," *Faraday Discussions,* **105,** 103-118 (1996).

20. N. H. Batis, H. Batis, A. Ghorbel, J. C. Vedrine, and J. C. Volta, "Synthesis and characterization of new VPO catalysts for partial n-Butane oxidation to maleic anhydride," *Journal of Catalysis,* **128,** 248-263 (1991).

21. M. T. Sananes, A. Tuel, G. J. Hutchings, and J. C. Volta, "Characterization of different precursors and activated vanadium phosphate catalysis by P_{31} NMR spin-echo mapping," *Journal of Catalysis,* **148,** 395-398 (1994).

22. V. V. Guliants, J. B. Benziger, S. Sundaresan, I. E. Wachs, J. M. Jehng, and J. E. Roberts, "The effect of the phase composition of model VPO catalysts for partial oxidation of n-butane," *Catalysis Today,* **28,** 275-295 (1996).

23. F. Ben Abdelouahab, R. Olier, N. Guilhaume, F. Lefebvre, and J. C. Volta, "A study by in situ laser Raman spectroscopy of VPO catalysts for *n*-butane oxidation to maleic anhydride I. Preparation and characterization of pure reference phases," *Journal of Catalysis,* **134,** 151-167 (1992).

24. C. J. Kiely, A. Burrows, S. Sajip, G. J. Hutchings, M. T. Sananes, A. Tuel, and J. C. Volta, "Characterisation of variations in vanadium phosphate catalyst microstructure with preparation route," *Journal of Catalysis,* **162,** 31-47 (1996).

25. M. E. Leonowicz, J. W. Johnson, J. F. Brody, H. F. Shannon, and J. M. Newsam, "Vanadyl hydrogenphosphate hydrates - $VO(HPO_4)\cdot 4H_2O$ and $VO(HPO_4)\cdot 0.5H_2O$," *Journal of Solid State Chemistry,* **56,** 370-378 (1985).

26. L. Benes, K. Melanova, M. Trchova, P. Capkova, and P. Matejka, "Water/ethanol displacement reactions in vanadyl phosphate," *European Journal of Inorganic Chemistry,* 2289-2294 (1999).

27. E. Bordes, P. Courtine, and G. Pannetie, "Crystallographic and thermal properties .1. Study of structural factors having an effect on formation of $VOPO_4$," *Annales De Chimie France,* **8,** 105-113 (1973).

28. P. T. Nguyen, R. D. Hoffman, and A. W. Sleight, "Structure of $(VO)_2P_2O_7$," *Materials Research Bulletin,* **30,** 1055-1063 (1995).

29. C. J. Kiely, S. Sajip, I. J. Ellison, M. T. Sananes, G. J. Hutchings, and J. C. Volta, "Electron-microscopy studies of vanadium phosphorus oxide catalysts derived from $VOPO_4\cdot 2H_2O$," *Catalysis Letters,* **33,** 357-368 (1995).

30. E. Bordes, P. Courtine, and J. W. Johnson, "On the topotactic dehydration of $VOHPO_4\cdot 0.5H_2O$ into vanadyl pyrophosphate," *Journal of Solid State Chemistry,* **55,** 270-279 (1984).

Chapter 5 Structural and Chemical Characterization of V-P-O Catalysts Synthesized by Some Novel Preparation Routes

Since the activated V-P-O catalyst is formed topotactically from the $VOHPO_4 \cdot 0.5H_2O$ precursor,[1-3] controlling the morphology of the precursor through the preparation route is an important parameter in generating a material which has a high catalytic performance. Commonly, V_2O_5 is used as the vanadium source and H_3PO_4 is used as the phosphorus source; a suitable reducing agent is then required to synthesize the $VOHPO_4 \cdot 0.5H_2O$ (V^{4+}) precursor phase. A number of different reducing agents and solvents have been tried in this respect.[4,5] In the earliest reported V-P-O catalyst preparation method (denoted as the VPA route) water was used as the solvent and hydrochloric acid was used as the reducing agent.[6,7] More recently, studies have concentrated on the use of alcohols as solvents and reducing agents, (*i.e.,* the VPO and VPD routes) as they tend to result in higher surface area catalysts.[6,8]

More recently, Okuhara *et al.*[4] have described the intercalation and subsequent exfoliation and fracture of $VOPO_4 \cdot 2H_2O$ crystals using primary and secondary alcohols. This was achieved via low temperature heat treatment in the alcohol followed by a subsequent reduction step in which the exfoliated $VOPO_4 \cdot 2H_2O$ sheets fracture to yield a $VOHPO_4 \cdot 0.5H_2O$ precursor which had a distinctive nano-sized (~ 340 x 35 nm) blocky morphology. More importantly, the nanocrystalline $(VO)_2P_2O_7$ catalyst subsequently derived from this precursor was found to be highly active and selective for the oxidation *n*-butane to MA.[9] In addition to this, a number of alternative synthesis routes have also

been explored. These include the formation of structured V-P-O materials which possess micro-, meso- and macro-porosity.[10-12]

Since the morphology of the vanadium phosphate precursors markedly affects the morphology and performance of the final catalysts, there is great interest in developing new preparation methods that can more precisely and reproducibly control the morphology of the initial precursor. Three new V-P-O preparation routes are investigated in this chapter; namely (i) the use of V-P-O 'seed' crystals in the VPD route (in order for controlling the morphology and structure of the V-P-O materials generated), (ii) the use of a di-block copolymer template in V-P-O production (in order for improving the crystallinity of the $VOHPO_4 \cdot 0.5H_2O$ precursor produced) and (iii) encapsulating fragile V-P-O catalysts with a mechanically resistant SiO_2 shell (in order for improving the mechanical resistance of the fragile rosette-type V-P-O catalysts).

5.1 Use of V-P-O 'seed' crystals in the VPD route

5.1.1 Introduction

The VPD method involves the reaction of V_2O_5 with H_3PO_4 using water as the solvent, which leads to the formation of the V^{5+} vanadium phosphate dihydrate $VOPO_4 \cdot 2H_2O$ phase. This is subsequently reduced in a second stage using an alcohol as the reducing agent to form the $VOHPO_4 \cdot 0.5H_2O$ precursor. This route was covered in some details in the previous chapter. Here we present an investigation of the addition of crystalline seeds in the preparation of vanadium phosphates during the VPD type alcohol reduction of $VOPO_4 \cdot 2H_2O$ and we demonstrate that this seeding strategy can have a dramatic influence on the morphology and structure of the precursor materials.

5.1.2 Experimental

5.1.2.1 V-P-O material preparation

$VOPO_4 \cdot 2H_2O$ was prepared by refluxing V_2O_5 (5.0 g, Aldrich) and H_3PO_4 (30 ml, 85%, Aldrich) in water (120 ml) for 24 h. The yellow solid produced was recovered immediately by vacuum filtration, washed with water (100 ml) and acetone (100 ml) and dried in air (110 °C, 24 h).

The transformation of the dihydrate phase to $VOHPO_4 \cdot 0.5H_2O$ or $VO(H_2PO_4)_2$ using alcohol was achieved as follows: $VOPO_4 \cdot 2H_2O$ (2 g) was refluxed in 1-octanol or 2-methyl-1-propanol (100 ml) for 24h to produce the hemihydrate phase with a rosette morphology. The use of 2-butanol (50ml) generated the discrete hemihydrate platelet morphology, whereas 3-octanol (100 ml) formed the $VO(H_2PO_4)_2$ phase. Seeding experiments with $VOHPO_4 \cdot 0.5H_2O$ (either in rosette and platelet morphologies) or with $VO(H_2PO_4)_2$ were carried out using the following procedure: $VOPO_4 \cdot 2H_2O$ (2 g) was refluxed in the presence of the seed precursor material (0.05 g) in alcohol (100 ml) for 24h. The resultant solids were recovered by vacuum filtration, and then washed with acetone (100 ml) and dried in air at 110 °C for 24h.

5.1.2.2 Catalyst testing

Reactions were carried out in a fixed bed micro-reactor (8 mm I.D.) containing a standard 0.2g of catalyst, at 400°C with a GHSV of 3000 h^{-1}. The catalytic conditions for testing the activity for *n*-butane oxidation over V-P-O catalysts have been described in sub-section 3.8.1.

5.1.2.3 Electron microscopy characterization

Scanning electron microscopy (SEM), bright field transmission electron microscopy (BF-TEM) and selected area electron diffraction (SAED) analyses were performed on these V-P-O materials. Experimental details for these characterization methods have been described in Chapter 3, section 3.6.

5.1.2.4 Complementary characterization techniques

BET surface area measurements and powder X-ray diffraction (XRD) were performed as described in Chapter 3, sub-sections 3.9.1 and 3.9.2, respectively.

5.1.3 Results and Discussion

5.1.3.1 Preparation and characterization of the standard seed 'precursor' materials

A set of standard vanadium phosphate materials were prepared via the VPD methodology *i.e.* reduction of dihydrate ($VOPO_4 \cdot 2H_2O$) with an alcohol at elevated temperatures as follows; 1-octanol (120 °C), 2-butanol (98 °C) and 3-octanol (174 °C). They each respectively yielded a different form of V-P-O material and these were subsequently used as precursor materials for seeding experiments. The 1-octanol gave hemihydrate ($VOHPO_4 \cdot 0.5H_2O$) with a rosette morphology (Table 5.1 entry 1, and Fig. 5.1(a)), whereas, 2-octanol gave discrete rhomboidal platelets (Table 5.1 entry 2, and Fig. 5.1(b)). The octagonal blocky $VO(H_2PO_4)_2$ morphology was obtained from 3-octanol (Table 5.1 entry 3 and Fig. 5.1(c)).

Table 5.1 Preparative conditions and BET surface areas of the V-P-O seed precursor materials.

Entry	Sample name	Preparation method[a]	T (°C)	Yield (g)	BET (m^2/g)
1	rosette seed **(a)**	1-octanol (100ml)	120	2	33
2	platelet seed **(b)**	2-butanol (50ml)	98[b]	1.60	9
3	$VO(H_2PO_4)_2$ seed **(c)**	3-octanol (100ml)	174[b]	1.15	2

[a]: all with 2 g $VOPO_4 \cdot 2H_2O$.
[b]: reflux temperature.

As shown in Figure 5.1, the preferential exposure of the {220} and the {001}-type planes in the rosette and platelet hemihydrate materials is consistent with previous studies.[6] The exposure of these preferred crystallographic planes can be correlated to the crystal morphology generated by the interaction of the primary or secondary alcohols with the intercalated water in these layer structures. However, as yet there does not seem to be a complete mechanistic explanation as to how the rosettes are formed via the VPD route. One of the possible mechanisms was discussed in Chapter 4.3, Figure 4.15. The characteristic difference in peak intensities in XRD patterns obtained from materials prepared by VPO and VPD methods most likely has its origin in differences in (i) agglomerate texture (*i.e.* simple stacked plates as opposed to spherulitic structures) and (ii) the differing degrees of crystallinity. The crystallisation of $VOHPO_4 \cdot 0.5H_2O$ from V_2O_5 and H_3PO_4 has been studied in detail by O'Mahony *et al.* using time resolved X-ray diffraction.[13] They found that starting from $VOPO_4 \cdot 2H_2O$, a $VOPO_4 \cdot H_2O$ intermediate phase was formed initially (< 30 min), which was subsequently consumed as the $VOHPO_4 \cdot 0.5H_2O$ started to form. Sequential FIB section and SEM microscopy performed by these researchers showed rosette structures gradually forming from delaminated plates as the reaction proceeded.

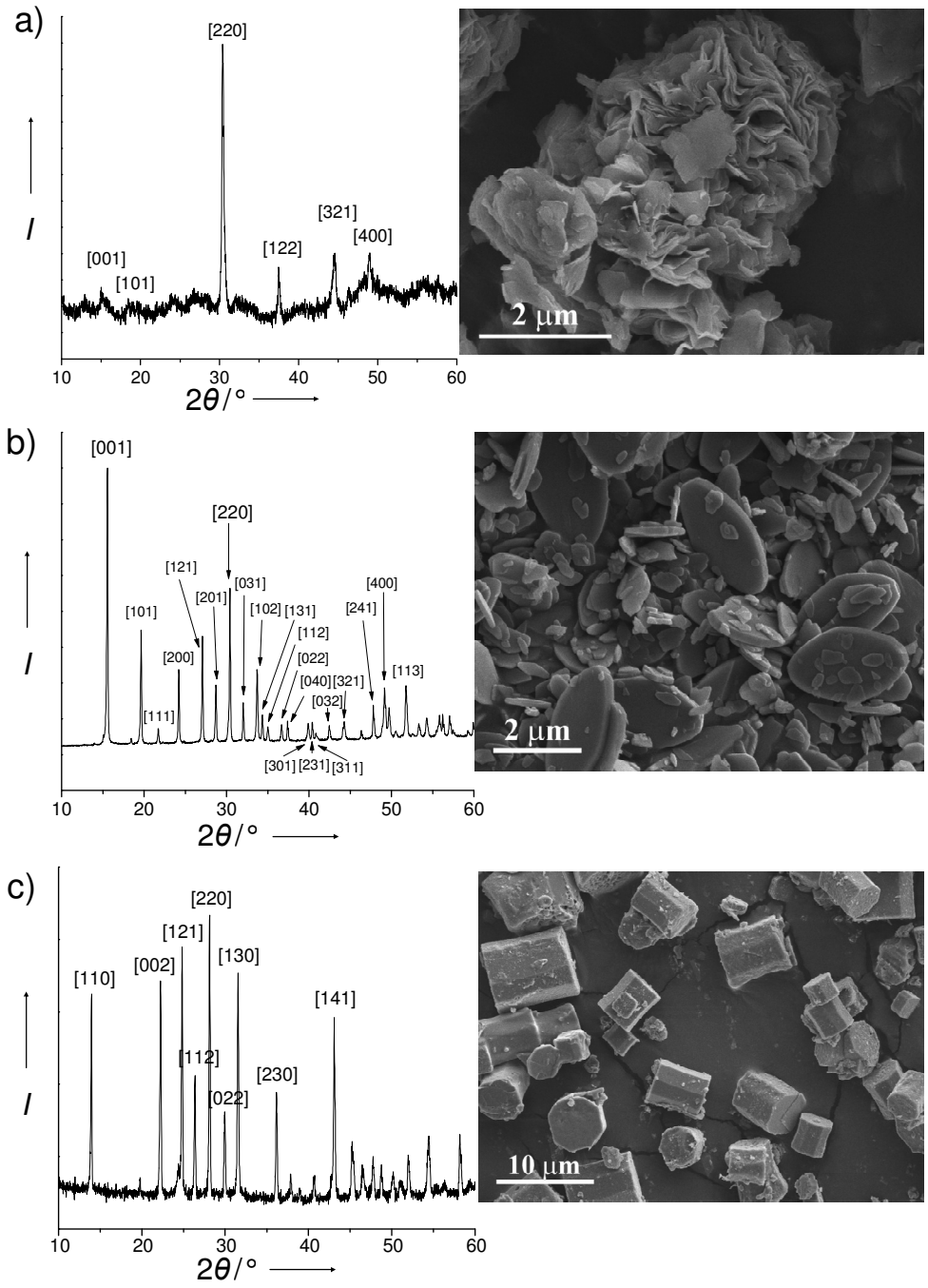

Figure 5.1 Powder XRD patterns and SEM micrographs of V-P-O materials recovered from standard VPD reaction with; (a) 1-octanol ($VOHPO_4 \cdot 0.5H_2O$ rosette), (b) 2-butanol ($VOHPO_4 \cdot 0.5H_2O$ platelet) and (c) 3-octanol ($VO(H_2PO_4)_2$).

The corresponding TEM analysis of these materials is presented in Figure 5.2. The rosette type precursor (Figs. 5.2(a)(b)) consists of agglomerates of $VOHPO_4 \cdot 0.5H_2O$ platelets each having [001] platelet normals. The discrete rhomboidal platelets of $VOHPO_4 \cdot 0.5H_2O$ (Fig. 5.2(c)) produced using 2-butanol also showed characteristic [001] normals, while the edge facets were **{**140**}-**type. The $VO(H_2PO_4)_2$ seed material (Figs. 5.2(d)(e)) formed using 3-octanol exhibits an octagonal cross-section when viewed along [001] direction with {110} and {010}-type side termination facets. These three standard materials have been used in small quantities as sacrificial materials in subsequent experiments as discussed later.

Butane oxidation was investigated over these three standard 'seed precursor' samples using standard reaction conditions (400 °C, space velocity 3000 h^{-1}). The catalytic performances were found to be comparable to previously reported literature examples.[13] For the standard 1-octanol reduced hemihydrate having the rosette type structure, butane conversion was found to be 70% with a selectivity to MA of 71% (specific activity 1.9 x 10^{-5} $mol_{MA}/m^2 \cdot h$). The discrete platelet morphology V-P-O, formed using 2-butanol, gave a conversion of 30% with a MA selectivity of 57 % (0.9 x 10^{-5} $mol_{MA}/m^2 \cdot h$). In direct contrast, the $VO(H_2PO_4)_2$ sample, prepared using 3-octanol, gave a low butane conversion of only 3% and no MA was detected.

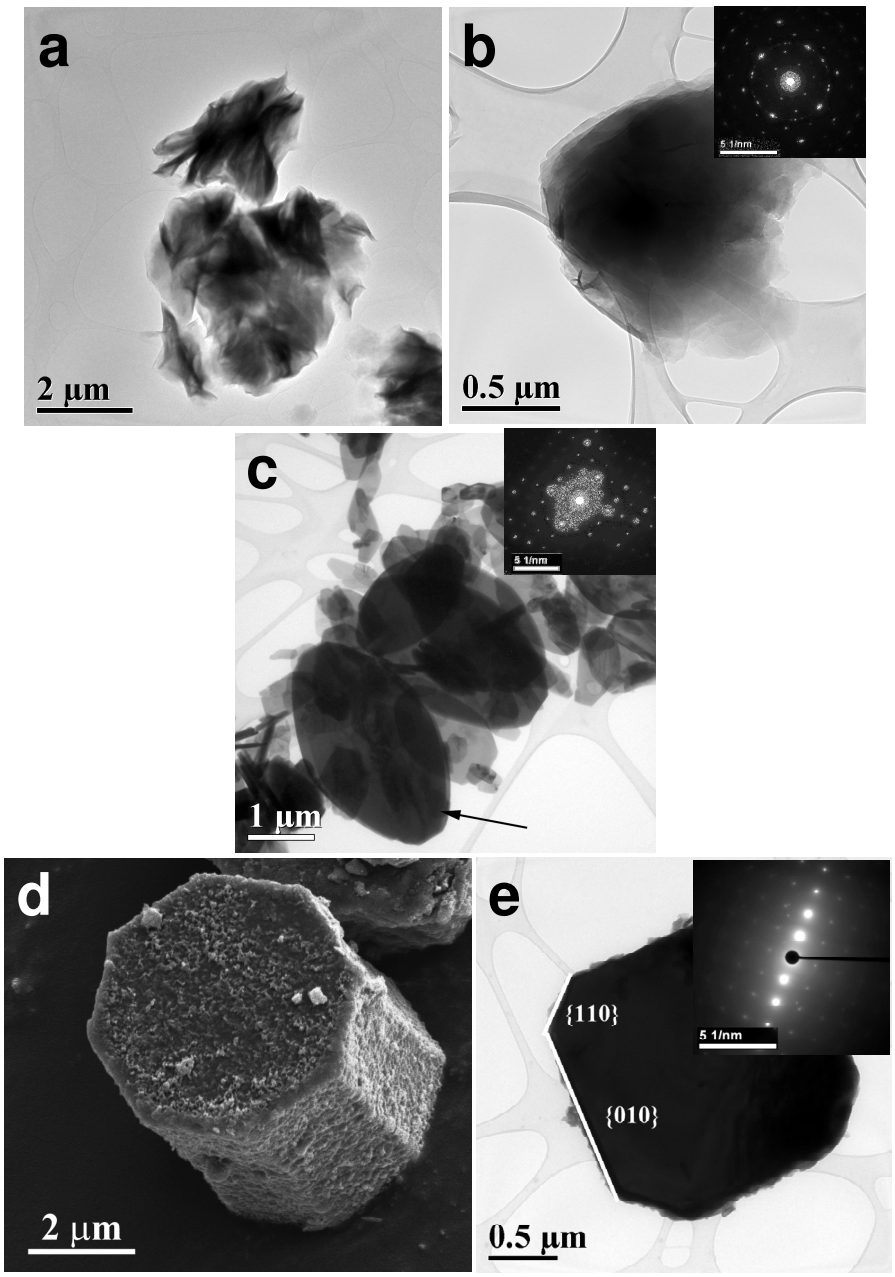

Figure 5.2 BF-TEM micrographs of (a) the rosette seed precursor and (b) an individual "petal" from a rosette (the inset SADP corresponds to [001] $VOHPO_4 \cdot 0.5H_2O$.); (c) the platelet seed (the inset SADP from the arrowed platelet corresponds to [001] $VOHPO_4 \cdot 0.5H_2O$.); (d) Higher magnification SEM micrograph of $VO(H_2PO_4)_2$ seed precursor and (e) BF-TEM micrograph of the $VO(H_2PO_4)_2$ seed precursor showing an octagonal section with {110} and {010}-type termination facets (inset SADP corresponds to [001] ($VO(H_2PO_4)_2$).

5.1.3.2 The influence of reduction temperature and the addition of V-P-O seed precursor to VPD preparations employing 1-octanol.

Heating $VOPO_4 \cdot 2H_2O$ in 1-octanol produces a high yield of $VOHPO_4 \cdot 0.5H_2O$, provided that the reducing agent was kept at temperatures below 160 °C, despite the boiling point of 1-octanol being 185 °C. Typically such reactions are conducted under reflux conditions of the alcohol used. The XRD and SEM data (Fig. 5.1(a)) indicate that the material recovered is $VOHPO_4 \cdot 0.5H_2O$ having a typical rosette morphology. Interestingly, when this same reaction is performed at a temperature in excess of 160 °C, only very minor amounts of the hemihydrate phase is formed. Apparently the expected hemihydrate structure consisting of layered V-P-O sheets is unable to form at these higher temperatures. XRD analysis of the minor amounts of the material that are produced indicate that it is largely amorphous, with only one, very minor (220) reflection present. Fascinatingly, the addition of a small amount of rosette-type $VOHPO_4 \cdot 0.5H_2O$ (0.05 g) to the reaction mixture before increasing the reflux temperature to 185 °C, resulted in a high yield of hemihydrate at the higher temperatures (Fig. 5.3). It is thought that the minor amount of hemihydrate material added to the reaction mixture serves to create seed crystallites, which may act as preferential nucleation sites, thereby lowering the energy of subsequent hemihydrate formation. This is illustrated in Figure 5.3 where the yield of hemihydrate product is monitored as a function of time-on-line for reactions conducted in the presence of 1-octanol with and without a V-P-O 'seed'. The rapid hemihydrate formation process, therefore, overcomes the competing reaction; namely the formation of the blue/black V^{4+} solute. We note that the hemihydrate material can be

recovered in almost complete yield after 24 h refluxing at 185 °C in the presence of the seeding material.

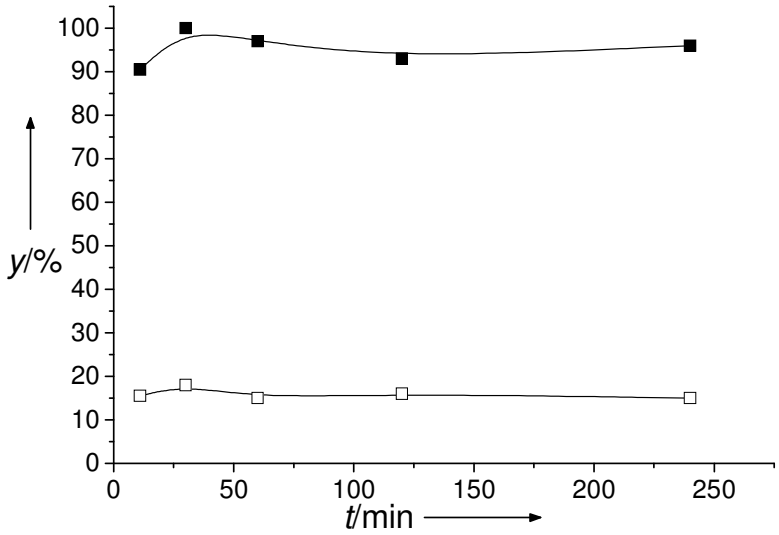

Figure 5.3 Yield of V-P-O material from reaction at reflux temperature (185 °C) of 1-octanol; (closed squares) with 0.05g of rosette seed precursor added and (open squares) with no seed material added.

To test the hypothesis that the addition of a minor amount of hemihydrate material (which we term the 'seed precursor') to the reaction mixture serves to create nucleation or seeding sites, a small amount of the VPD rosette material (shown in Figs. 5.1(a) and 5.2(a)) was refluxed on its own for 2 h at 185℃ in 1-octanol. Not all the $VOHPO_4 \cdot 0.5H_2O$ dissolved in this time and the residual material was recovered and dried. It can be seen from the SEM and TEM micrographs presented in Figure 5.4 (a)(b) respectively, that some of the petals of the rosette which were originally about 2μm in lateral size have fragmented to produce much smaller platelets that are only about 0.1-0.2μm in dimension. Electron diffraction confirmed these entities to be poorly crystalline $VOHPO_4 \cdot 0.5H_2O$, and it is thought that these smaller platelet fragments serve as the 'seed' crystallites and act as a template for subsequent $VOHPO_4 \cdot 0.5H_2O$ growth.

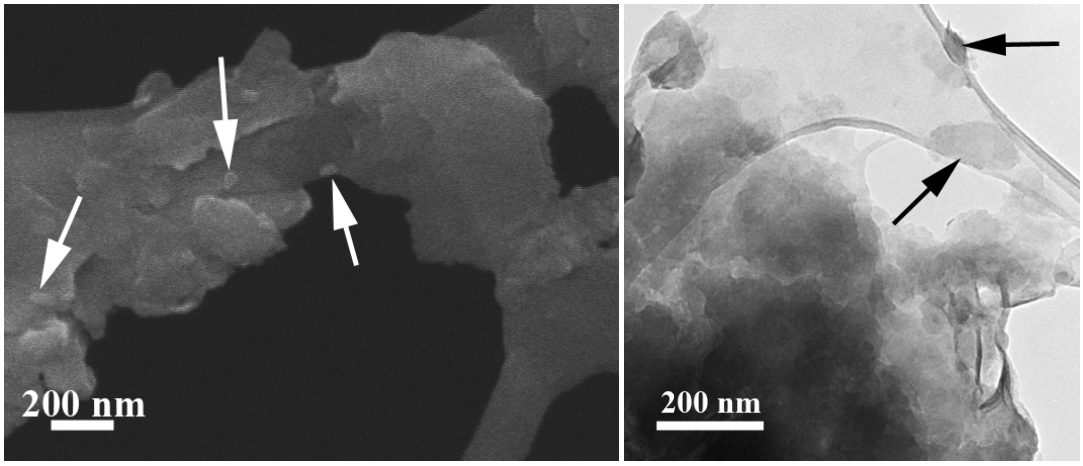

Figure 5.4 (a) High resolution SEM and (b) BF-TEM micrographs of a disintegrated "petal" from a recovered rosette-type seed precursor that was refluxed in 1-octanol for 2h at 185°C. Some residual [001] $VOHPO_4 \cdot 0.5H_2O$ fragments (arrowed) remain which can act as seeding templates.

This discovery is highly significant for two reasons. Firstly, this is the first report of the use of a seed to direct the formation of V-P-O materials. Secondly, we will demonstrate in the following sections that addition of small amounts of different morphology V-P-O seeding precursor material leads to dramatic morphological changes in the resulting material.

The morphology of the V-P-O seed precursor used can be observed by XRD, SEM and TEM analysis to affect the morphology of the recovered hemihydrate material. When a rosette-type seed precursor was used, the hemihydrates recovered consisted of rosettes which were radially more open-spaced than its starting seed precursor morphology (denoted sample A, see Fig. 5.5(a) and Fig. 5.6(a)). A single "petal" crystallite from one of the rosettes in sample A can be assigned by SAED analysis to be the [001] projection of $VOHPO_4 \cdot 0.5H_2O$ (Fig. 5.6(b)). This is also corroborated by the XRD measurements presented in Figure 5.5 where the XRD pattern is comparable to that

of a standard VPD reaction in 1-octanol, which produces a hemihydrate with rosette morphology where the (220) reflection is dominant.

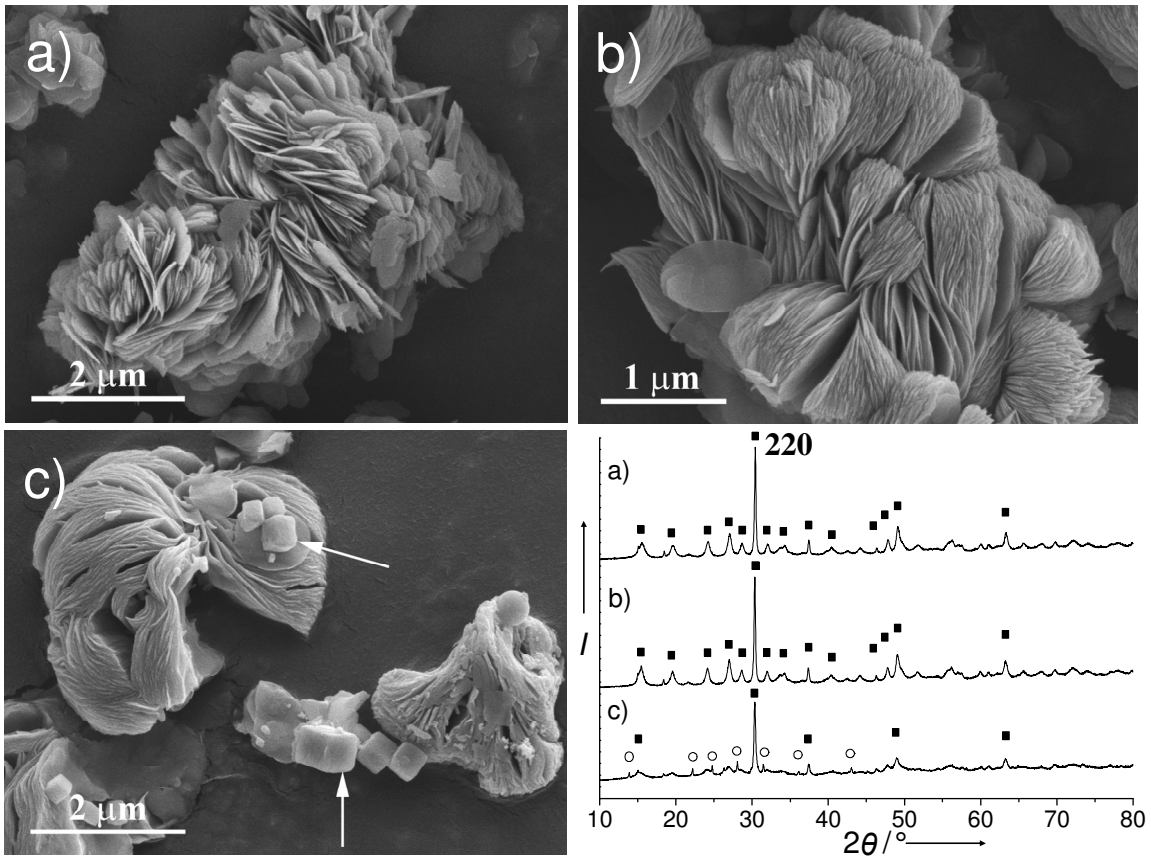

Figure 5.5 SEM micrographs and powder XRD patterns of the recovered material from seeding reactions; (a) with a rosette hemihydrate seed precursor, (b) with a platelet hemihydrate seed precursor and (c) with $VO(H_2PO_4)_2$ seed precursor. (■) = $VOHPO_4 \cdot 0.5H_2O$ and (□) = $VO(H_2PO_4)_2$.

The platelet-type hemihydrate or $VO(H_2PO_4)_2$ seed precursors are expected to undergo a similar process to that described above, whereby the seed precursors are exfoliated by the alcohol at the reaction temperature and then fracture to produce much smaller seed fragments. Morphological variations are apparent in Figure 5.5(b) and Figure 5.6(c), whereby, the use of a platelet-type hemihydrate seed precursor yields an aggregated hemihydrate product (labeled sample B) consisting of a mixture of closely

spaced rosettes and platelets. Interestingly, the resulting hemihydrate from the addition of a $VO(H_2PO_4)_2$ seed precursor (denoted sample C, Fig. 5.5(c)), has a dominant reflection at (220) with the other reflections indexed as the (110), (002), (121) and (112) reflections of the $VO(H_2PO_4)_2$ phase. SEM and TEM analyses presented in Figures 5.5(c) and 5.6(d) indicate that, in addition to closely-spaced hemihydrate rosettes, a minor blocky phase is present at a volume fraction of about 5 vol%. This minor phase was confirmed by selected area electron diffraction (SAED) analysis to be $VO(H_2PO_4)_2$ with (100), (100) and (001) termination facets (Fig. 5.6 (d)). The $VO(H_2PO_4)_2$ crystallites now have a more cuboidal morphology (arrowed in Figs. 5.5(c) and 5.6(d)) as compared to the octagonal shaped starting $VO(H_2PO_4)_2$ seed precursors (Fig. 5.2(d)). There is potential for the $VO(H_2PO_4)_2$ seed structure to persist in the reaction mixture during nucleation, yet it appears to have re-crystallized or transformed into another morphology in this instance.

The use of seeds also influences the surface areas of the hemihydrates that are formed. Without seeding, a typical preparation with 1-octanol leads to a surface area of $33 m^2/g$. With rosette seeds the area increases to 38 m^2/g, but use of the other seeds leads to a decrease in overall surface area. These observations are consistent with the electron microscopy results described previously.

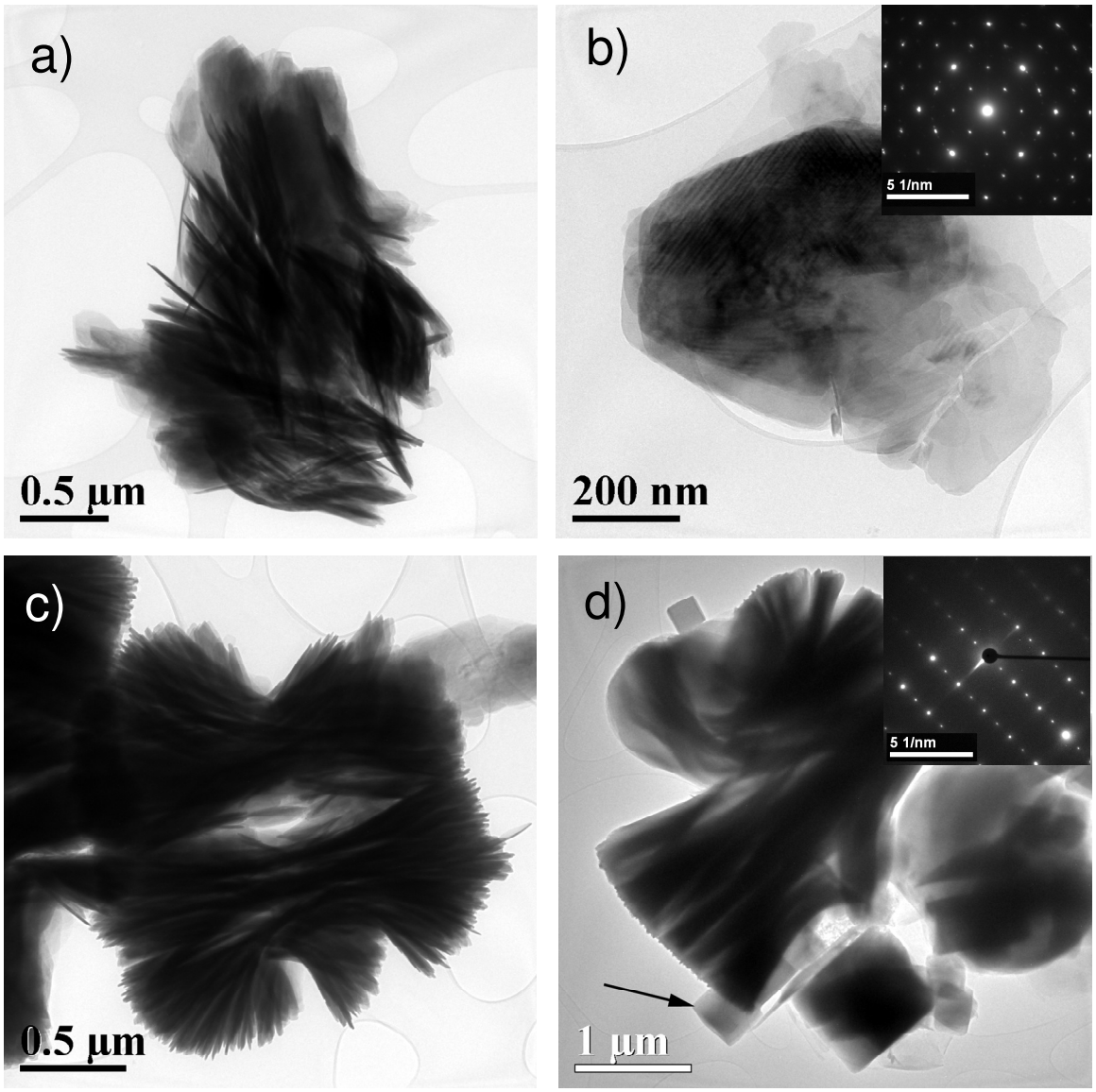

Figure 5.6 BF-TEM micrographs of (a) sample A showing rosettes; (b) an individual rosette "petal" from sample A (inset SADP corresponds to [001] $VOHPO_4 \cdot 0.5H_2O$); (c) sample B showing close-spaced rosettes and (d) sample C showing close-spaced rosettes and cuboidal particles (inset SADP from arrowed particle corresponds to [010] $(VO(H_2PO_4)_2)$.

5.1.3.3 Effect of alcohol on vanadium phosphate precursor morphology when using the seeded VPD route.

The use of the V-P-O seed precursors in the VPD type preparation utilizing other alcohols, *i.e.* 2-methyl-1-propanol, 2-butanol and 3-octanol, has also been investigated.

These particular solvents were chosen because of their efficacy in influencing the morphology of the resulting V-P-O material during a standard un-seeded VPD preparation.

Reaction of $VOPO_4 \cdot 2H_2O$ with 2-methyl-1-propanol

Using seed precursors with different $VOHPO_4 \cdot 0.5H_2O$ morphologies, that is, platelets and rosettes, and 2-methyl-1-propanol as the solvent and reducing agent, altered the final morphology of the recovered material as illustrated in Figure 5.7. Irrespective of whether a hemihydrate platelet or rosette seed precursor was used, the resulting materials both consist of similar hemihydrate plates agglomerated in a characteristic rosette-like morphology.

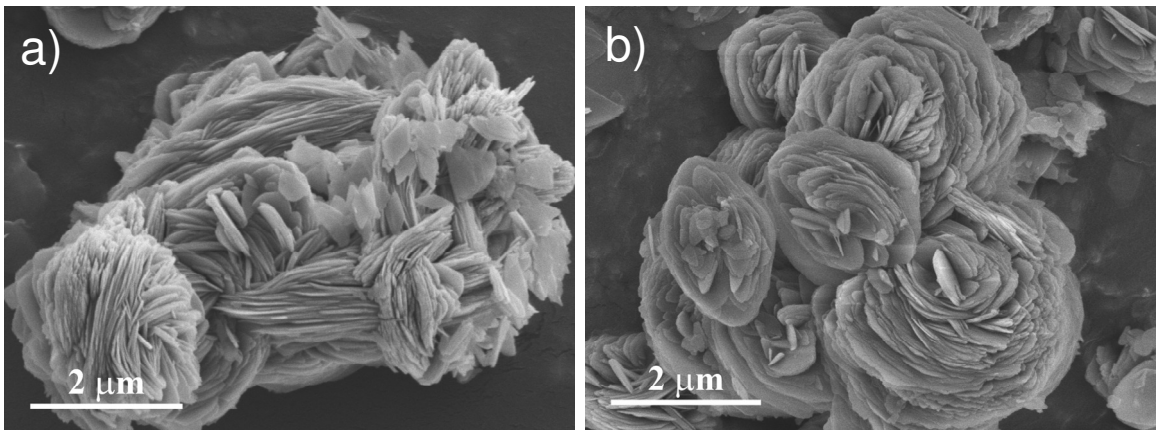

Figure 5.7 SEM micrographs of the materials recovered from the reactions seeded with (a) platelet precursor or (b) rosette precursor respectively in 2-methyl-1-propanol.

The BET surface area of the resulting hemihydrate materials differs from the seeds produced via standard preparation methods. More specifically, the material formed with platelet seeds shows an increase in BET surface area to 14 m^2/g as compared to the 9 m^2/g exhibited by the original platelet seed precursor materials. Conversely, the product of the rosette seeding experiment shows a decrease of BET surface area to 17 m^2/g from the 33 m^2/g displayed by the original rosette-type seed precursor. XRD analyses (Fig. 5.8)

of these products are in agreement with the SEM and BET results, showing less intense (220) reflections and more intense (001) reflections as compared to the rosette seed precursor (Fig. 5.1(a)). Catalytic evaluation was carried out on these materials resulting in specific activities of 2.3 and 2.0×10^{-5} $mol_{MA}/m^2 \cdot h$ respectively, for the platelet and rosette seeded experiments.

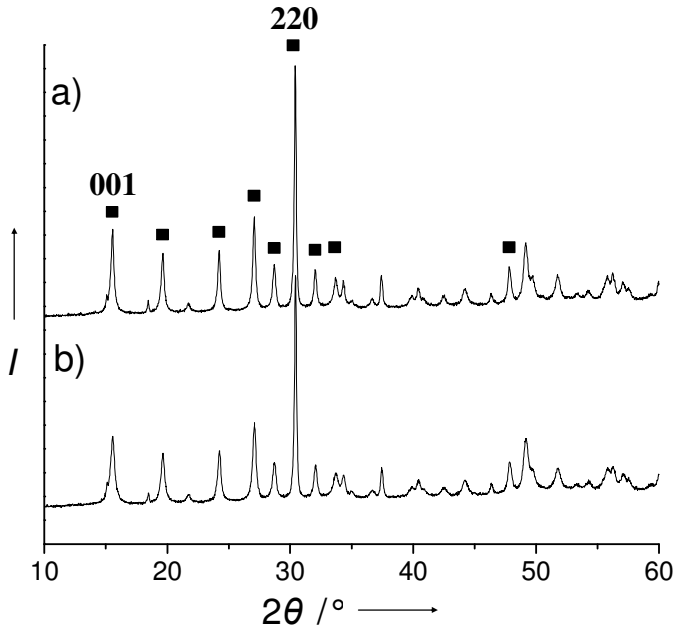

Figure 5.8 Powder XRD patterns of recovered materials produced from seeded reactions using 2-methy-1-propanol; (a) with platelet seed precursor and (b) with rosette seed precursor in the VPD route. ■ = $VOHPO_4 \cdot 0.5H_2O$.

Reaction of $VOPO_4 \cdot 2H_2O$ with 2-butanol

When 2-butanol is used in a standard un-seeded VPD preparation, the resulting hemihydrate consists of platelets with a rhomboidal appearance. The XRD pattern from such material was similar to that shown in Figure 5.1(b) and termed the platelet seed precursor; the reflections are sharp and the material is highly crystalline. This is in contrast to the XRD pattern generated from a rosette type hemihydrate material, which exhibits the characteristic broad, singular (220) reflection (Fig. 5.1(a)).

The use of a platelet seed precursor in the presence of 2-butanol, led to a hemihydrate material consisting of highly crystalline rhomboidal platelets (Figs. 5.9(a) and 5.10(a)). XRD analysis of the resultant materials (Fig. 5.9) exhibits a switch in the relative intensity of the (001) and (220) reflections as compared to the seed precursor material shown in Figure 5.1(b). This switch is indicative of a gradual progression towards a rosette-type structure. Indeed, this is exemplified in the material recovered where a rosette seed precursor was used, which shows rosette type aggregations formed from platelets (Figs. 5.9(b) and 5.10(b)). The BET surface areas for these recovered materials are 8 and 13 m^2/g for the platelet and rosette seeded reactions, respectively. Catalytic evaluation of these materials gave specific activities of 2.7 x 10^{-5} and 1.6 x 10^{-5} mol_{MA} m^{-2} h^{-1}, respectively.

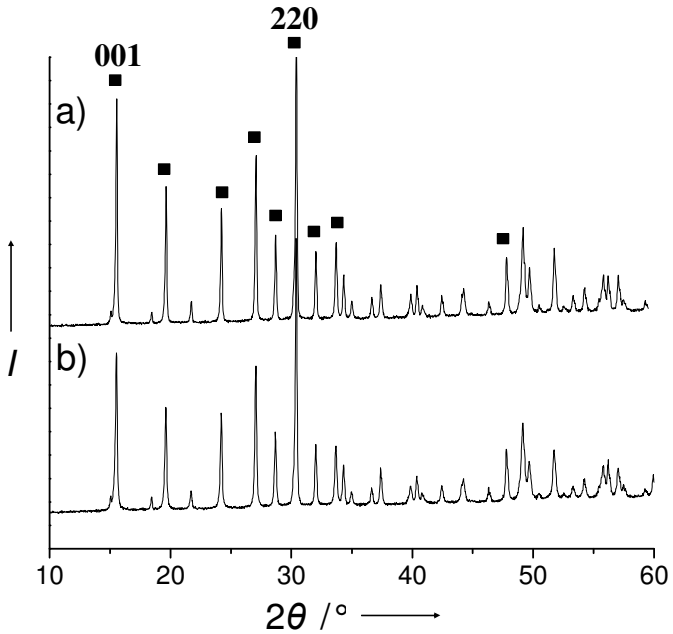

Figure 5.9 XRD patterns of material recovered from seeded reaction using 2-butanol; (a) with platelet seed precursor and (b) with rosette seed precursor in the VPD route. ■ = $VOHPO_4 \cdot 0.5H_2O$.

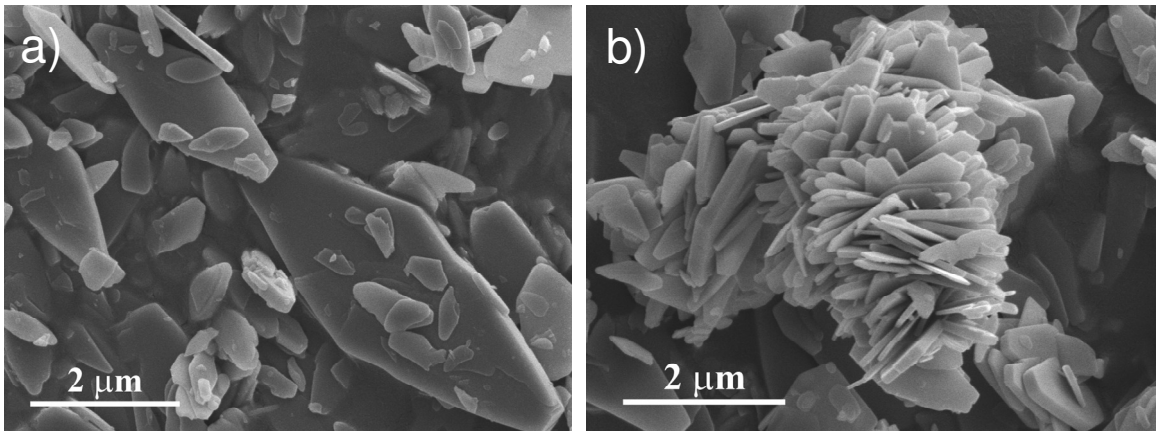

Figure 5.10 SEM micrographs of the material recovered from the (a) platelet and (b) rosette hemihydrate precursor seeded VPD type reactions in 2-butanol.

Reaction of $VOPO_4 \cdot 2H_2O$ with 3-Octanol

At 174 °C, the reflux temperature of 3-octanol, the dihydrate $VOPO_4 \cdot 2H_2O$ reacts to form $VO(H_2PO_4)_2$.[14] The powder XRD pattern and SEM micrograph of this material are shown in Figure 5.1(c). However, the use of rosette type V-P-O seed in this reaction results in a mixed phase material (Figs. 5.11(b) and 5.12(b)). The expected product $VO(H_2PO_4)_2$ is now the minor phase and a hemihydrate (platelet-type) phase is the major component, as determined by XRD (Fig. 5.11(b)). Interestingly, the material recovered after the use of a platelet seed precursor, showed only $VOHPO_4 \cdot 0.5H_2O$ in the XRD pattern (Fig. 5.11(a)). In order to clarify this finding, the sample was also investigated by TEM, which gave results in full agreement with that of the XRD results. From SEM (Fig. 5.12) both samples can be seen to consist of agglomerations of platelets. The crystallinity of the samples was also observed to increase markedly when compared to the un-seeded material produced by reactions carried out in 1-octanol. The XRD patterns of these samples share this characteristic with that of the standard hemihydrate exhibiting a platelet morphology. However, as noted previously the dominant reflection in the XRD pattern is now the (220) reflection, instead of the (001) reflection, because plate

agglomerations cause an effective reduction in the fraction of $VOHPO_4 \cdot 0.5H_2O$ (001) planes that are exposed and accessible. In both cases the BET surface area was approximately 4 m^2/g, which is comparable to that of $VO(H_2PO_4)_2$ which has a surface area of 2 m^2/g.

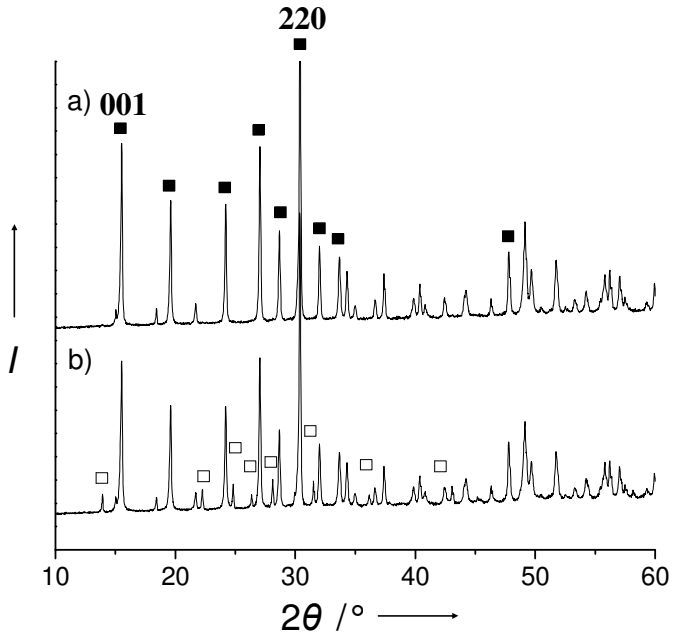

Figure 5.11 Powder XRD patterns of material from reactions seeded with (a) platelets and (b) rosettes respectively using 3-octanol. ■ = $VOHPO_4 \cdot 0.5H_2O$, □ = $VO(H_2PO_4)_2$

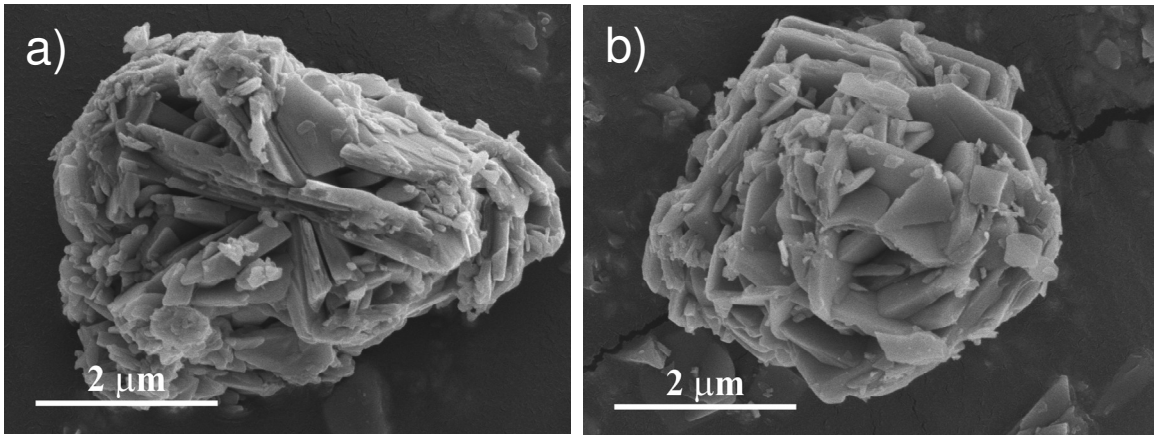

Figure 5.12 SEM micrographs of material recovered from the reactions seeded with (a) platelet and (b) rosette type seed precursors respectively in 3-octanol.

n-Butane oxidation experiments conducted using these materials indicate that despite the low surface area of these precursors, they still perform reasonably well. In particular, the sample recovered from a platelet seeded reaction, having a specific activity of 4.5 x 10^{-5} $mol_{MA}/m^2 \cdot h$ is significantly higher than that of a standard VPD rosette material (*ca*. 1.9 x 10^{-5} $mol_{MA}/m^2 \cdot h$). The presence of minor quantities of the $VO(H_2PO_4)_2$ phase in the rosette seeded sample concurs with the lower measured specific activity as compared to the former material. The enhanced specific activity of this mixed phase material is of interest since the presence of $VO(H_2PO_4)_2$ typically leads to lower activity.

5.1.4 Summary for the use of V-P-O 'seed' crystals in the VPD route

The use of small amounts of vanadium phosphate materials as sacrificial seed precursors during the reaction of $VOPO_4 \cdot 2H_2O$ with alcohols (*i.e.* 1-octanol, 2-methyl-1-propanol, 2-butanol or 3-octanol) has been shown to be effective not only in altering the morphology of the product, but it can also induce certain phase transformations. The use of a seed in these preparations shows that the rate of material formation can be increased. In the case of reactions involving 1-octanol, the seed overcomes a barrier to hemihydrate formation, which would usually prevent the hemihydrate material crystallizing and aggregating at reflux temperatures. This seeding method has proved beneficial in the formation of catalyst precursors for the selective oxidation of *n*-butane to MA. Material formed from a reaction in 3-octanol, seeded with a hemihydrate with platelet morphology, has a high specific activity of 4.5 x 10^{-5} $mol_{MA}/m^2 \cdot h$. This compares favourably to the

$VO(H_2PO_4)_2$ material produced from the standard reaction in 3-octanol, which was shown to have negligible activity.

5.2 Use of a di-block copolymer template in V-P-O production

5.2.1 Introduction

2-poly(styrene-alt-maleic acid) (PSMA) has been investigated as a structure directing agent for a wide range of applications and has been shown to have a variety of different effects depending on the material synthesized. The morphology of PbS particles has been shown to be dependent on the relative amounts of PSMA and cetyltrimethylammonium bromide (CTAB) added into the preparation mixture.[15] This is proposed to be a result of the structure directing agents preferentially interacting with particular crystal faces of the PbS leading to kinetic control over growth in the [111] and [100] directions. Using the PSMA-CTAB mixture, star-like PbS particles with six symmetrical, perpendicular arms were formed, but cubic and spherical particles could also be produced if CTAB concentrations were increased.

Diblock copolymers can also be used to promote the crystallisation of particular phases, a feature that has been studied for a range of diverse applications, from medicine to improving the strength of cement. Yu *et al.* showed that PSMA could have an application in preventing urolithiasis.[16] During the formation of CaO_X the addition of the copolymer was found to promote the growth of the tetragonal phase, which is easily expelled from the body, over the monoclinic phase which is difficult for the body to expel and hence, forms kidney stones.

During the preparation of heterogeneous catalysts, preferentially exposing the active plane or preferentially forming the active phase can lead to an increase in selectivity and/or activity. In this section, we show that a diblock copolymer, PSMA, can dramatically influence the crystallinity and morphology of a vanadium phosphate (V-P-O) catalyst precursor.

5.2.2 Experimental

5.2.2.1 Materials preparation

To prepare the standard vanadium phosphate presursor V_2O_5 (5.9 g, Strem) and H_3PO_4 (8.25 g, 85%, Aldrich) were added to isobutanol (2-methyl-1-propanol, 125 ml, Aldrich) and the mixture was heated under reflux conditions for 16 h. The resultant pale blue solid was recovered by vacuum filtration, and washed with alcohol (100 ml) and acetone (100 ml), then dried in air at 110 ºC. This material was denoted P0.

For the copolymer modified materials V_2O_5 and H_3PO_4 were reacted in isobutanol with a small amount of Na-PSMA. In a typical preparation, PSMA (sodium salt solution, 13%, Aldrich) was added dropwise to a solution of H_3PO_4 in 15 - 20 ml isobutanol under vigorous stirring until a homogeneous solution was formed. The remainder of isobutanol and V_2O_5 were then added and the reaction mixture was heated under reflux conditions for 16-18 h. The resultant pale blue solid was recovered by vacuum filtration and dried at 110 ºC. Three samples were prepared with different PSMA to V_2O_5 weight ratios of 1:260 (denoted P260), 1:130 (denoted P130) and 1:65 (denoted P65). The precursors P0, P260, P130 and P65 were activated at 400 ºC *in-situ* in a flow of 1.7% butane in air (150

h for P0, 20 h for P260, P130 and P65, respectively) to give their respective catalysts, denoted C0, C260, C130 and C65 as shown in Table 5.2.

Table 5.2 Materials prepared by adding different amounts of PSMA.

PSMA: V_2O_5 weight ratio	Precursor #	Catalyst #
0	P0	C0
1: 260	P260	C260
1: 130	P130	C130
1: 65	P65	C65

5.2.2.2 Catalyst testing

The catalytic conditions for testing the activity for *n*-butane oxidation over V-P-O catalysts have been described in sub-section 3.8.1.

5.2.2.3 Electron microscopy characterization

Scanning electron microscopy (SEM), bright field transmission electron microscopy (BF-TEM) and selected area electron diffraction (SAED) analyses were performed. Experimental details for these characterization methods have been described in Chapter 3, section 3.6.

5.2.2.4 Complementary characterization techniques

BET surface area measurements and powder X-ray diffraction (XRD) were carried out as described in Chapter 3, sub-sections 3.9.1 and 3.9.2, respectively.

5.2.3 Results and Discussion

All of the precursor materials were shown by XRD to be the $VOHPO_4 \cdot 0.5H_2O$ phase (Fig. 5.13). However, a distinct change in morphology can be observed with increasing PSMA concentration. The standard precursor, P0, has the (220) as the most intense reflection. This decreases with increasing PSMA addition, while the (001) peak

increases until it is the most intense reflection (Table 5.3). The different patterns with different relative intensities of the (001) and (220) reflections have been previously shown to be characteristic of two distinct morphologies of $VOHPO_4 \cdot 0.5H_2O$. The pattern with the (220) reflection as the dominant feature is typical of rosette-like structures, whereas the pattern with the (001) reflection as the dominant feature is typical of rhomboidal platelet structures. The XRD patterns also show that the precursors prepared with PSMA were more crystalline compared with the material prepared using standard procedures, and that the degree of crystallinity improved with increasing PSMA content. The BET surface area of the samples decreases with increasing PSMA addition (Table 5.3). This is in keeping with a shift in morphology from rosettes to rhomboidal platelets, with rosettes typically being higher surface area.[8]

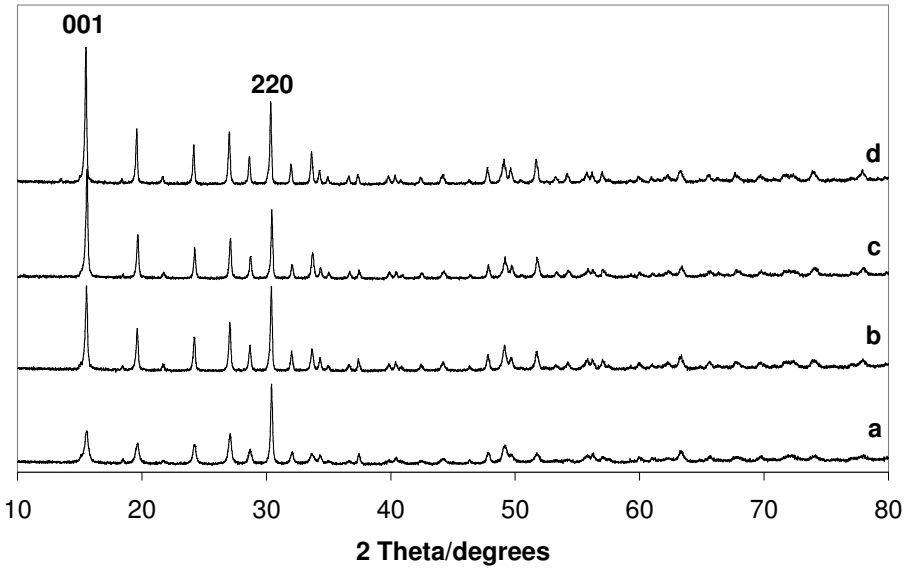

Figure 5.13 Powder XRD patterns of: (a) P0; (b) P260; (c) P130 and (d) P65. All reflections can be assigned to $VOHPO_4 \cdot 0.5H_2O$.

Table 5.3 Relative intensities of the (001) and (220) reflections for the $VOHPO_4 \cdot 0.5H_2O$ precursors calculated from the XRD patterns shown in Figure 5.13 and BET surface area measurements before and after catalyst testing.

Sample	Relative Intensity (001)/(220)	Surface Area (m^2g^{-1}) precursor	catalyst
P65	1.60	10	11
P130	1.53	13	15
P260	1.01	19	21
P0	0.47	10	12

The electron microscopy results correlate well with the XRD data. SEM analyses of the precursors show that they are a mixture of characteristic rosette-like agglomerates of angular platelets together with isolated rhomboidal crystallites (Fig. 5.14).

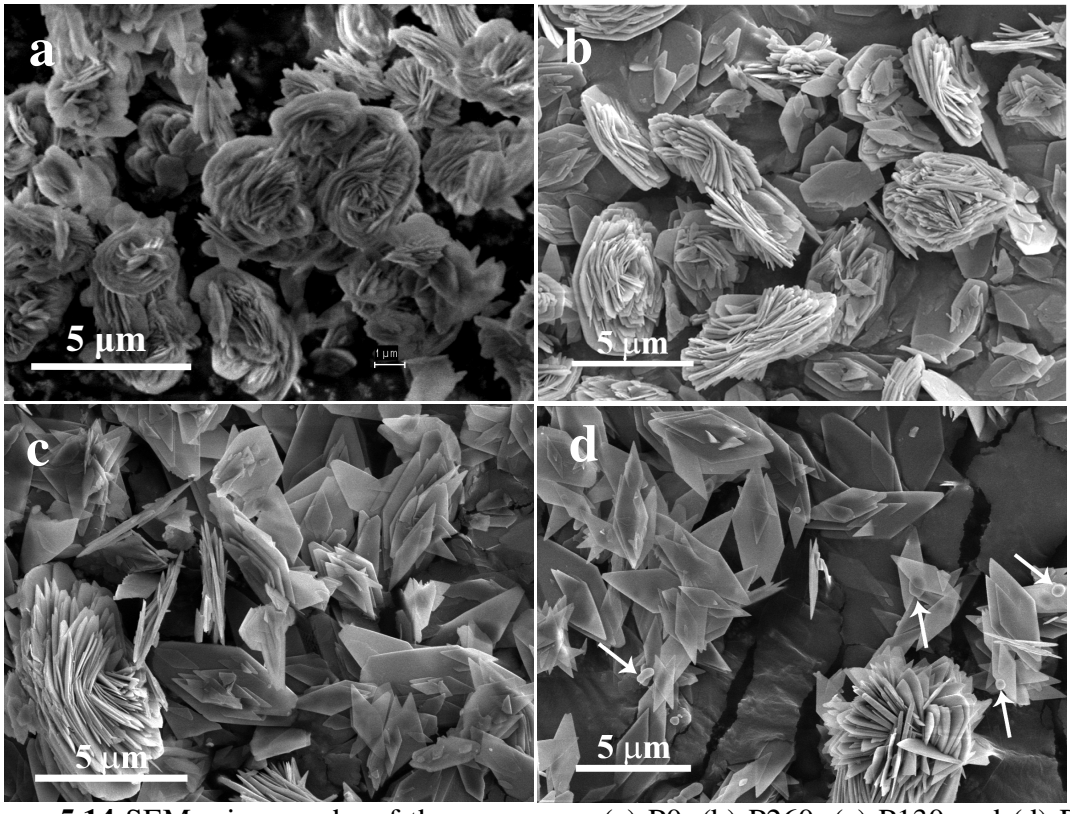

Figure 5.14 SEM micrographs of the precursors (a) P0, (b) P260, (c) P130 and (d) P65 (spherical particles are arrowed).

From the micrographs it can be seen that as the amount of PSMA in the preparation was increased the number of rosette-like agglomerates decreased and the proportion of rhomboidal platelets increased, in good agreement with the change in intensity of the (220) and (001) reflections observed in the XRD patterns (Fig. 5.13, Table 5.2). For the material prepared with the highest PSMA concentration (P65) there are also a number of small spherical particles with size ranging 0.1 - 1 μm which are highlighted by arrows (Fig. 5.14(d)).

TEM analyses of the rhomboidal platelets are shown in Figure 5.15. It can be seen that the crystallites develop more defined morphologies as the amount of PSMA is increased. This is in keeping with the proposed mechanisms for how the diblock copolymer acts as a structure directing agent. PSMA consists of two separate monomers as shown below:-

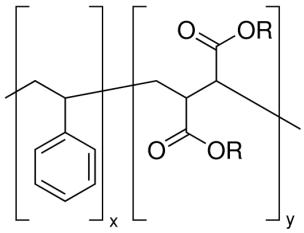

R = H or Na

The styrene group is present to aid solubilization of the polymer in the solvent, whereas the maleic acid group is present to interact with the inorganic material interfaces and crystal planes, giving rise to the structure directing properties. This has been proposed to be due to a specific orientated adsorption of the copolymer onto particular crystal planes, preventing growth in that direction, while promoting crystal growth in the perpendicular planes.[15,16]

In this study the PSMA seems to promote the formation of the rhomboidal platelets as the number of rosette agglomerations decreases with increasing copolymer concentration. For the material prepared in the absence of PSMA the crystals have rough, ill-defined edges leading to hexagonal particles. When a small amount of the copolymer is added (P260) the hexagonal crystallites become more regular, with well defined edges. The angle between the two long, straight pairs of terminating facets at the platelet edge (Fig. 5.15(b)) have a characteristic value of 143-144°. These correspond to the (140) and ($1\bar{4}0$) facet planes of the $VOHPO_4 \cdot 0.5H_2O$ phase. The angle between the flat tip and the platelet edge (140) facet plane is around 72°, which means this tip corresponds to (100) facet planes of $VOHPO_4 \cdot 0.5H_2O$. The aspect ratio (AR, length/width) of sample P260 is around 1.78. As the amount of PSMA is gradually increased (P130) the AR increases to around 2.49 (Fig. 5.15(c)) while the (100) facet plane becomes jagged. At the highest concentration (P65) the (100) facet plane disappears and the AR has reached its upper limit at around 3.0 in most of the particles giving four sided, rhombic crystallites (Fig 5.15(d)). It is apparent that PSMA can promote the grain growth along the {140}-type planes of $VOHPO_4 \cdot 0.5H_2O$.

Selected area diffraction patterns (SADPs) obtained from these platelets (Fig. 5.15(a-d)) indicated that they were all [001] oriented $VOHPO_4 \cdot 0.5H_2O$ platelets (one example is shown in Fig. 5.15(d1)), however, the spherical particles observed at high PSMA concentration were found to be $VO(H_2PO_4)_2$ (Fig. 5.15(d2)). $VO(H_2PO_4)_2$ is often found as an unwanted impurity phase in the preparation of $VOHPO_4 \cdot 0.5H_2O$, although it can be removed through washing as it is water soluble.[17] It has been previously reported

that the production of $VO(H_2PO_4)_2$ is unavoidable due to the reaction with aldehyde formed during the reduction of V_2O_5 with alcohol.[18,19]

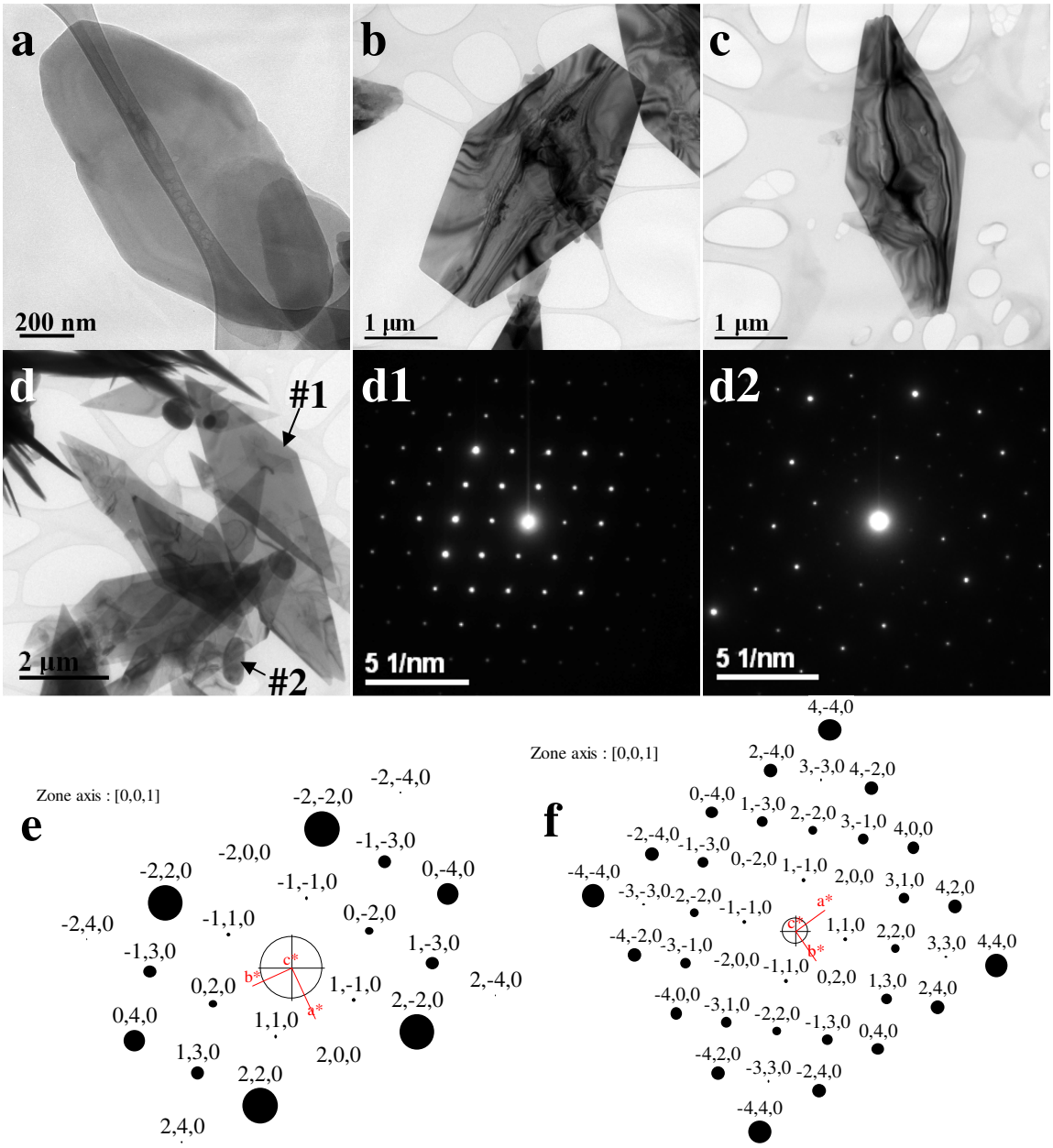

Figure 5.15 BF-TEM micrographs of the precursors (a) P0, (b) P260 (AR: 1.78), (c) P130 (AR: 2.49) and (d) P65 (AR: 3.00); SADPs from (d1) rhombic platelet (#1 in d) – [001] $VOHPO_4 \cdot 0.5H_2O$ and (d2) sphere (#2 in d) – [001] $(VO(H_2PO_4)_2)$; Simulated and indexed SADPs of (e) the [001] projection of $VOHPO_4 \cdot 0.5H_2O$ and (f) the [001] projection of $(VO(H_2PO_4)_2)$.

However, in this study $VO(H_2PO_4)_2$ was only observed with high amounts of PSMA. This could be an indication that there is an optimum quantity of PSMA required to form the highly crystalline $VOHPO_4 \cdot 0.5H_2O$ platelets. It is also interesting to note that the $VO(H_2PO_4)_2$ crystallites formed are spherical rather than their usual cubic morphology.[18,19] The formation of spherical particles is common when an excess of the copolymer structure directing agent is added to a preparation and is thought to be a result of the diblock copolymer forming a very strong interaction between the polymer and the crystallizing $VO(H_2PO_4)_2$ which effectively suppresses the crystal growth.[20]

When these precursor materials were tested as catalysts for *n*-butane oxidation they were found to activate in a very short period of time compared to the standard vanadium phosphate materials (Fig. 5.16). Typically, the performance of a standard catalyst gradually increases as the $VOHPO_4 \cdot 0.5H_2O$ precursor is gradually transformed *in-situ* to the active catalyst ($(VO)_2P_2O_7$ plus some additional V^{5+} phases) over a period several days before it equilibrates and reaches a steady state performance (Fig. 5.16(a)).[3] The materials prepared with PSMA became active much more quickly and reached a steady state performance in a matter of hours (Fig. 5.16(b)). This fast activation is attributed to the high degree of crystallinity facilitating the removal of water from the $VOHPO_4 \cdot 0.5H_2O$ lattice during the dehydration step.

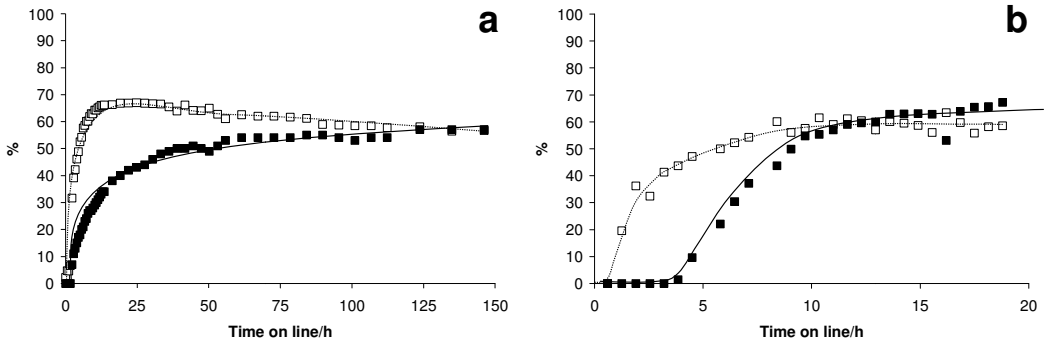

Figure 5.16 Butane oxidation over: (a) P0 – steady state performance is reached after >100 h on line; (b) P65 – steady state performance is reached after >15 h on line. ■ maleic anhydride selectivity; □ conversion. 1.5% butane in air, 400 ºC, 3000 h^{-1} GHSV.

The transformation of the active catalyst has been well studied previously and found to be topotactic.[1-3] The characterization of the catalyst after activation confirmed this is the case for the samples prepared using PSMA as can be seen from SEM (Fig. 5.17) and TEM (Fig. 5.18) micrographs. The SEM micrographs of catalysts C130 (Fig. 5.17(a)) and C65 (Fig. 5.17(b)) show the same morphological features observed in precursor materials P130 (Fig. 5.14(c)) and P65 (Fig. 5.14(d)). The activated catalysts consist of a mixture of rhomboidal platelets and rosette-like agglomerates of platelets. The minority spherical particles were found to persist in catalyst C65 which are highlighted by arrows in Figure 5.17(b).

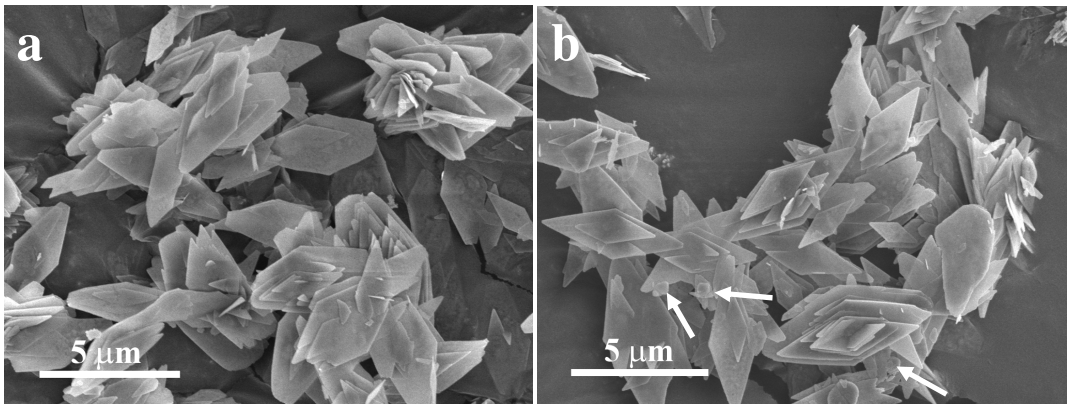

Figure 5.17 SEM micrographs of the catalysts: (a) C130 and (b) C65.

In the BF-TEM micrographs of catalysts C130 and C65 (Figs. 5.18(a)(b)), both are found to retain their rhomboidal morphologies after activation and have the similar microstructures, namely interior oblong crystallites and serrated rims (Figs. 5.18(c-f)). Inset SADPs taken from the platelet normal indicate that they are [100] orientated $(VO)_2P_2O_7$ phase. The angles between the long straight pairs of terminating facets at the platelet edge have a characteristic value of 143-144° as in the precursors, confirming that an *in-situ* topotactic transformation has indeed occurred.

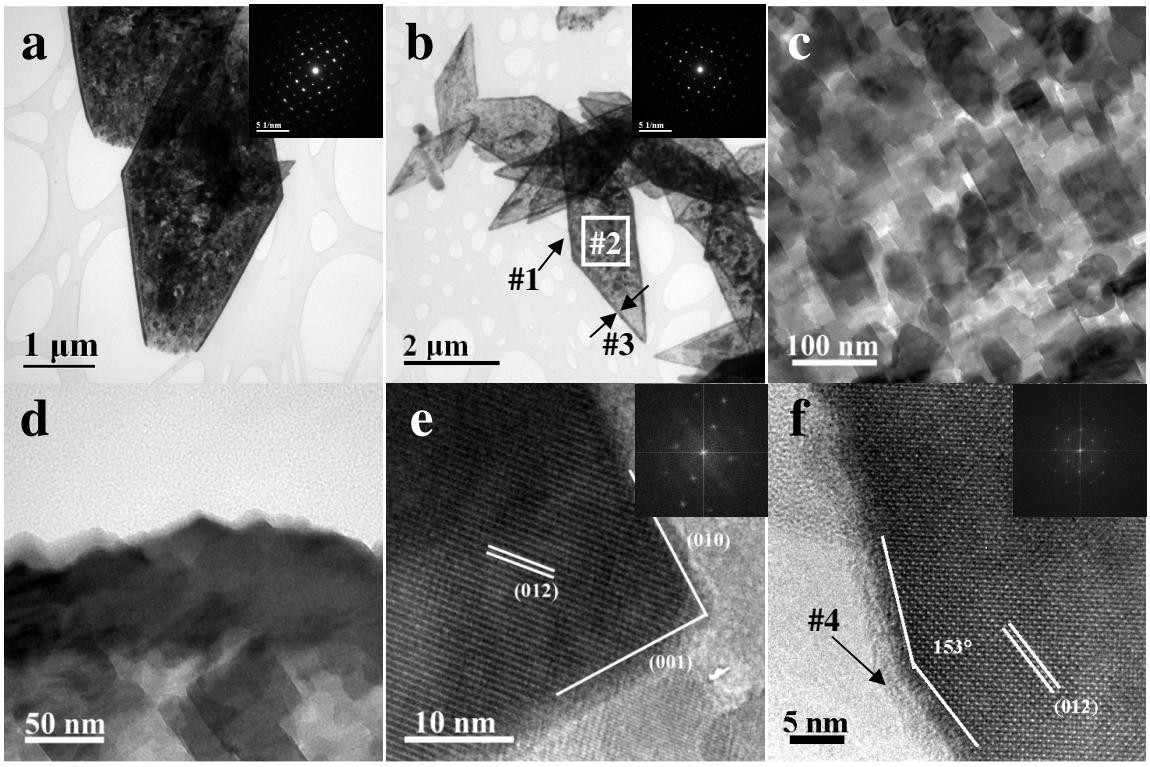

Figure 5.18 BF-TEM micrographs of (a) activated catalyst C130 {inset SADP from rhomboidal platelet corresponds to [100] $(VO)_2P_2O_7$}; (b) activated catalyst C65 {inset SADP from rhombic platelet #1 - [100] $(VO)_2P_2O_7$}; higher magnification BF TEM micrographs of (c) the interior (#2 in b) and (d) rim region (#3 in b) of rhombic platelet (#1 in b); low pass filtered HREM micrographs of (e) small oblong crystallites from area #2 in b showing the [100] projection of $(VO)_2P_2O_7$ with (010) and (001) facet terminations and (f) the serrated rim region (#3 in b) showing characteristic (012) and $(0\bar{1}7)$ facet planes with an intersection angle at around 153° and the disordered overlayer (#4).

The $(VO)_2P_2O_7$ formed from this transformation is much more crystalline for the materials prepared using the copolymer structure directing agent than for the standard material. This can be seen by the sharpening of the (200) reflection in the XRD patterns (Fig. 5.19), however, from the TEM studies (Fig. 5.18) it can be clearly seen that, although the interior of the platelets is crystalline, an thin amorphous rim forms around the edge of the platelet. This is in keeping with our previous observations that the active site for *n*-butane oxidation is an amorphous overlayer on a crystalline or amorphous bulk support.[21,22]

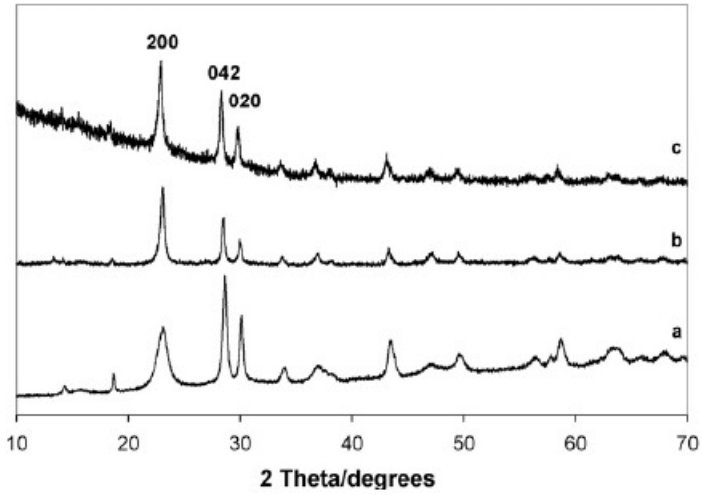

Figure 5.19 Powder XRD patterns of (a) C0, (b) C130 and (c) C65 catalysts. All reflections can be assigned to $(VO)_2P_2O_7$.

5.2.4 Summary for the use of a di-block copolymer template in V-P-O production

Using a diblock copolymer as a template in the preparation of a vanadium phosphate catalyst has been shown to influence the morphology of the synthesized material and also the performance of the activated catalyst. Samples prepared using this methodology were much more crystalline than those prepared using standard methodologies which is attributed to the copolymer template acting as a structure director. It is thought that the template can interact with the (001) $VOHPO_4 \cdot 0.5H_2O$ plane

preventing growth in this direction. This leads to very regular rhomboidal crystals, rather than the lozenge shaped crystals obtained from standard preparations.

For these catalysts the increased crystallinity and morphological changes gives rise to a much faster *in-situ* transformation of the precursor to the active catalyst, resulting in a stable steady state performance being reached in a matter of hours as compared to days for the standard catalyst. During the activation of the precursor material there are two processes occurring; the dehydration of $VOHPO_4 \cdot 0.5H_2O$ to form $(VO)_2P_2O_7$ together with a disordering of the surface of the catalyst. The high crystallinity of the precursors prepared using a diblock copolymer template aids the dehydration step, which increases the speed of the activation process before the amorphous surface forms to give the final catalyst after 4 h.

This methodology, although demonstrated here for vanadium phosphate catalysts, could potentially also be applied to a number of mixed oxide or metal phosphate catalyst preparations to produce more crystalline, uniform catalysts.

5.3 V-P-O/SiO_2 core-shell materials for use in fluidized bed reactors

5.3.1 Introduction

Improvements in catalyst activity and specificity have been sought through supporting various V-P-O precursors on higher surface area materials. Silicon carbide,[23] oxides[24,25] and micro-porous solids[26] have been used as supports which have purported to show improved heat transfer, increased mechanical strength and higher surface area to volume ratio of the active V-P-O component. The use of high surface area silica gels[27] and fumed silica[28] supports has led to diverse results under the reported reaction

conditions. Typically, during the preparation of these V-P-O materials $VOPO_4$ phases are more prevalent, which effectively increases the V^{5+}/V^{4+} ratio in the catalyst. When compared to the unsupported $(VO)_2P_2O_7$, the MA selectivity is subsequently impaired for these supported types of materials. However, Bueno *et al.*[27] reported that the use of fumed silica increases the specific activity by five times for a 15 % VPO/SiO_2 sample over the un-supported V-P-O (1.5 % Bu 17.5 % O_2, 1200 h^{-1} GHSV, 380 °C). Conversely, deposition of silica on the surface of $(VO)_2P_2O_7$ resulted in deactivation of the catalyst as reported by Inumaru *et al.*[29] The activity was partially regained through subsequent fracturing of the silica layer and was correlated to specific selective planes. The benefits of improved heat transfer are well suited to the typical fixed-bed operation. However, this mode of operation necessitates the use of an *n*-butane feed which is heavily diluted (*ca.* 1.5% butane in air). To overcome this feed composition drawback and the potential problem of hot-spots; fluidized-bed reactors have been employed.[30] However, the V-P-O catalyst requires an improved attrition resistance for longevity in this kind of mechanically dynamic environment.[31]

DuPont has developed a specialized form of V-P-O catalyst for this fluidized bed process, which is the subject of the current investigation. This DuPont catalyst consists of a V-P-O core (*ca.* 150 μm) surrounded by a porous silica shell (*ca.* 2 μm) to improve its attrition resistance in a circulating fluidized bed reactor. The specific intended application of this catalyst was for the manufacture of a monomer used in LYCRA®; namely tetrahydrofuran (THF) (Fig. 5.20) which could be formed through the catalytic hydrogenation of maleic acid from maleic anhydride. The plant capacity for THF was 100 MMlb/year. The reactor for maleic anhydride production consisted of separate

oxidation and reduction chambers as shown in Figure 5.21.[32] The catalyst was circulated through the reactor with alternate lattice oxygen regeneration, followed by the catalyzed conversion of *n*-butane to maleic anhydride. In this reactor system the V-P-O/SiO_2 catalyst charges were envisaged to have up to two years of continuous service in the circulating fluidized bed reactor (CFBR).

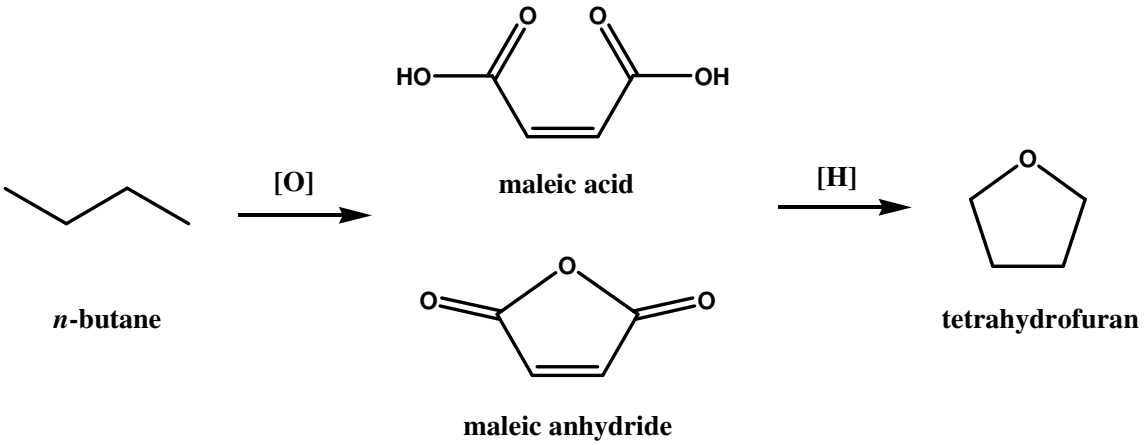

Figure 5.20 The DuPont two-step production of tetrahydrofuran via a maleic acid intermediate.

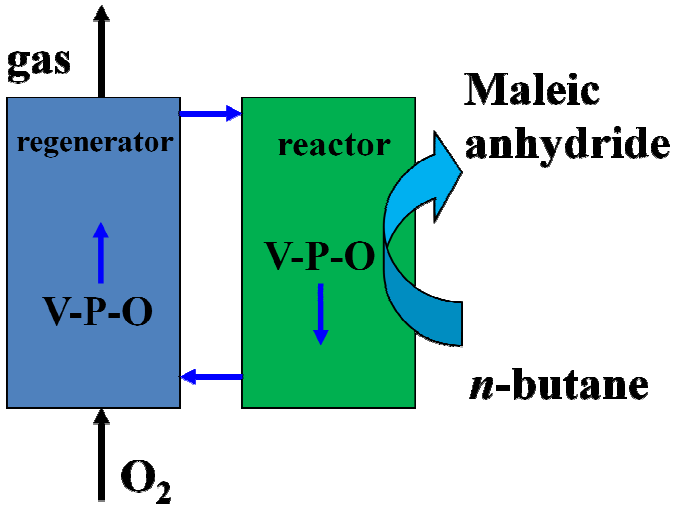

Figure 5.21 Schematic diagram of the industrial circulating fluidized bed reactor showing the reactor (reducing environment) on the right and regenerator (oxidizing environment) on the left. V-P-O materials are used to catalyze the selective oxidation of *n*-butane to maleic anhydride in the reactor and are re-oxidized in the regenerator.

Several research centers worldwide have received samples of this V-P-O/SiO_2 material for analysis, with the eventual aim of combining the extensive body of results generated, in an effort to understand further the functionality of this V-P-O catalyst. We present here our attempts to evaluate comprehensively the catalyst in precursor, freshly activated and equilibrated states. This has been achieved through *n*-butane oxidation at various temperatures and feedstock flow rates. Several conventional characterization techniques (*i.e.* BET, XRD, SEM, TEM, XPS) have been employed to study the catalyst structure and composition in detail at the various stages of its lifetime. In addition, we have used a novel X-ray ultramicroscopy (XuM) technique[33] within an SEM environment to obtain information on the internal structure of individual core-shell V-P-O/SiO_2 particles without the need for physical sectioning.

5.3.2 Experimental

5.3.2.1 V-P-O materials preparation

The V-P-O precursor was prepared on a commercial scale in an organic medium with *iso*-butanol and benzyl alcohol. This was followed by micronization to 1-2 μm, then spray-dried with polysilicic acid to form a porous silica shell; containing up to 10 % silica. The catalyst precursor ($VOHPO_4 \cdot 0.5H_2O$) was then calcined at 390 °C in the regenerator zone of the demonstration reactor, to form the active catalyst {$(VO)_2P_2O_7$}. Additionally, a sample of the equilibrated catalyst was investigated which had been used for >2 years on-line in an industrial circulating reactor and supplied for investigation. Hereafter, these samples are referred to as the precursor, freshly activated and equilibrated materials. The nominal silica content for the materials is 9 % for the

precursor, and 5 - 20 % for the equilibrated sample, although this is subject to some variability.

5.3.2.2 Catalyst testing

The catalytic conditions for testing the activity for *n*-butane oxidation over V-P-O materials have been described in sub-section 3.8.1.

5.3.2.3 Electron microcopy characterization

A range of electron microscopy techniques were used to characterize the V-P-O/SiO_2 materials structurally in the precursor, freshly activated and equilibrated states. Scanning electron microscopy (SEM), bright field transmission electron microscopy (BF-TEM) and selected area electron diffraction (SAED) analyses were carried out as described in Chapter 3, section 3.6.

X-ray ultra-Microscopy (XuM) analyses were performed in an FEI XL30 ESEM equipped with a Gatan XuM system. Each V-P-O/SiO_2 sphere was individually glued to the tip of a carbon fiber/epoxy needle, and carbon coated, for XuM analysis. XuM utilizes the X-rays generated in an SEM when the electron beam is focused onto a Pt foil target. This essentially provides a point source of X-rays which can then pass through a nearby sample, an un-sectioned V-P-O/SiO_2 sphere in this case, and generate a projection image on an X-ray sensitive CCD camera. The resultant X-ray image contains both absorption and phase contrast information, the latter of which provides edge enhancement for boundaries, cracks and micropores as well as a contrast mechanism for low density materials. In addition, the XuM allows the possibility of collecting tomographic data which can provide a 3D visualization of the shape and relative distribution of inclusions

and micropores within the volume of material under analysis. The tungsten filament XL30 ESEM was used in the large spot size, high current regime in order to generate the high X-ray fluxes required for the XuM technique.

5.3.2.4 Complementary characterization techniques

Surface area measurements, XRD and XPS experiments were performed as described in Chapter 3, sub-sections 3.9.1, 3.9.2 and 3.9.3, respectively.

5.3.3 Results and Discussion

5.3.3.1 Catalytic performance

The BET surface area was determined to be $25m^2/g$, $33m^2/g$ and $11m^2/g$ for the precursor, calcined and equilibrated catalyst materials, respectively. The catalysts were evaluated in a fixed bed micro-reactor operating under different *n*-butane feedstock flow-rates and reaction temperatures. The V-P-O/SiO_2 materials were used as-received and were typically comprised of particles 20-150μm in diameter. Firstly the precursor was activated *in-situ* (Fig. 5.22) and the reaction product analysis was performed on-line. During this activation period, both conversion and MA selectivity improve in a fashion similar to that previously reported for standard hemihydrate precursors.[8] The approximate 72 h activation period was also found to be consistent with values noted for standard V-P-O catalysts. At 400 °C and a GHSV of 3029 h^{-1} the selectivity to MA was *ca.* 58 % at a conversion of *ca.* 80 %.

The equilibrated catalyst showed a marked loss in activity and selectivity towards MA production. More specifically, at 37 % conversion the catalyst was able to achieve only 22% selectivity to MA. In order to better understand how this decrease in

performance happened after two years on line, a wide variety of techniques (*i.e.* XRD, SEM, TEM, XuM, XPS) have been performed on the precursor, freshly activated and equilibrated materials.

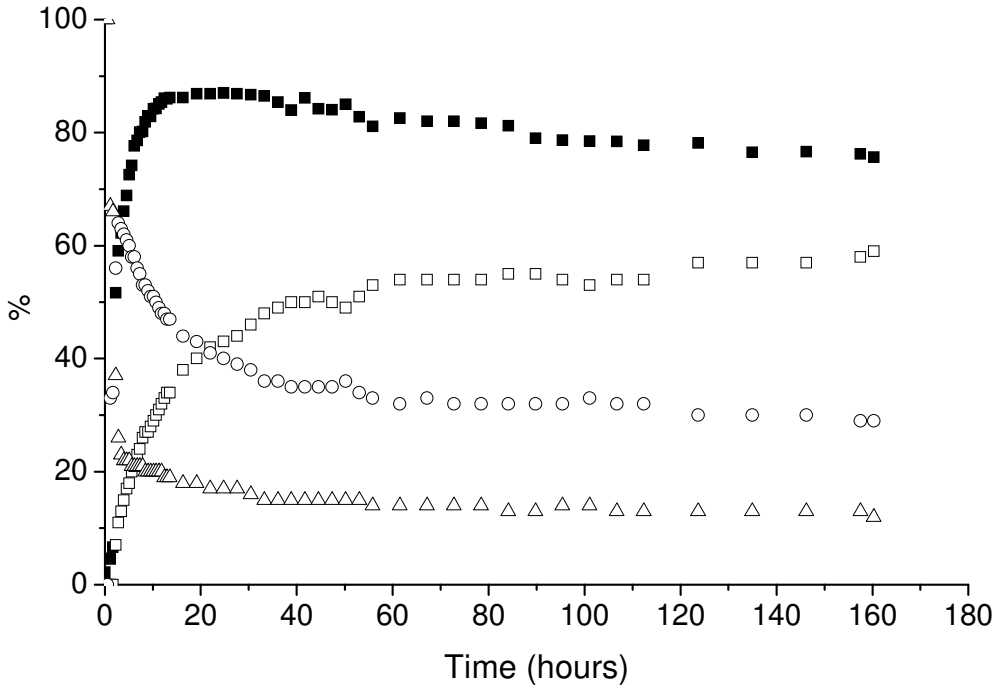

Figure 5.22 Time-on-line selectivity and butane conversion data over the V-P-O/SiO_2 precursor (S.A. 25 m^2/g). Butane conversion = ■. Selectivity; □ = MA, ○ = CO_2 and Δ = CO.

5.3.3.2 Catalyst characterization

Powder X-ray diffraction

The powder XRD patterns of the precursor, freshly activated and equilibrated catalysts are shown in Figure 5.23. For the precursor material all the reflections present can be assigned to the hemihydrate ($VOHPO_4 \cdot 0.5H_2O$) phase. The freshly activated catalyst shows peaks consistent with the vanadyl pyrophosphate ($(VO)_2P_2O_7$) phase. In comparison, the XRD pattern from the equilibrated catalyst shows that it is not a single

phase material. In addition to the majority $(VO)_2P_2O_7$ phase, significant amounts of β-$VOPO_4$ were found.

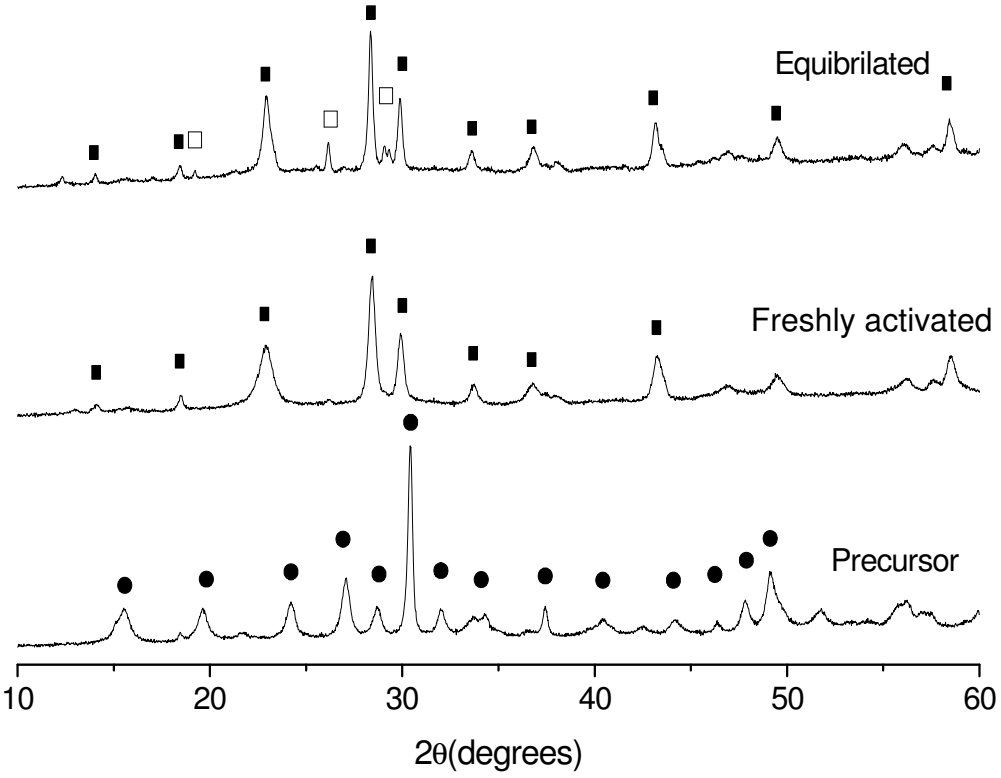

Figure 5.23 Powder XRD of the precursor, freshly activated and equilibrated V-P-O/SiO_2 materials; ■ $(VO)_2P_2O_7$, □ = β-$VOPO_4$, • $VOHPO_4 \cdot 0.5H_2O$.

Scanning Electron Microscopy (SEM)

Figure 5.24 shows a montage of SEM and XuM micrographs from the precursor (column 1), freshly activated (column 2) and equilibrated (column 3) V-P-O/SiO_2 materials. Shown in Figure 5.24; Row 1 are a series of low magnification SEM micrographs in which the general spherical morphology of the three materials can be seen. For the precursor and freshly activated materials the particle diameters were both found be in the 20-150μm size range, whereas for the equilibrated material this has reduced significantly to a size range of 20-100μm presumably due to extended exposure to the

mechanically abrasive environment of the fluidized bed reactor. The form of the SiO_2 shell encapsulating the V-P-O material also exhibits a definite evolution during the course of the material lifetime as shown by the higher magnification SEM micrographs presented in Figure 5.24, row 2. In the precursor material the amorphous shell is highly porous and contains multiple fissures. The SiO_2 shell in the freshly activated catalyst still has a rough, porous texture and shows some evidence of additional surface debris. Both the precursor and freshly activated catalyst also show evidence of gross surface protrusions or 'blisters.' In stark contrast, the equilibrated catalyst, which has suffered exposed to a severely abrasive environment in the circulating catalyst reactor, shows much smoother and rounder silica shells in which numerous angular crystalline VPO fragments, about 100-200nm in size, are embedded. In each case it was possible to find particles which had fractured to reveal the interior microstructure as shown in Figure 5.24, row 3. In addition to showing the complicated structure of the internal crystalline V-P-O material, such fractured particles also show evidence of internal porosity. If these pores or bubbles are just below the surface region they can give rise to the characteristic external 'blisters' or protrusions noted on the outer surface of the particle. The fracture surfaces also expose the SiO_2/V-P-O interface region as shown in Figure 5.24, row 4. In the equilibrated catalyst, the SiO_2 layer is dense and a definite V-P-O/SiO_2 interface is visible. In direct contrast, the silica layer in both the precursor and freshly activated materials is porous and the SiO_2/V-P-O interface is more diffuse and ill-defined.

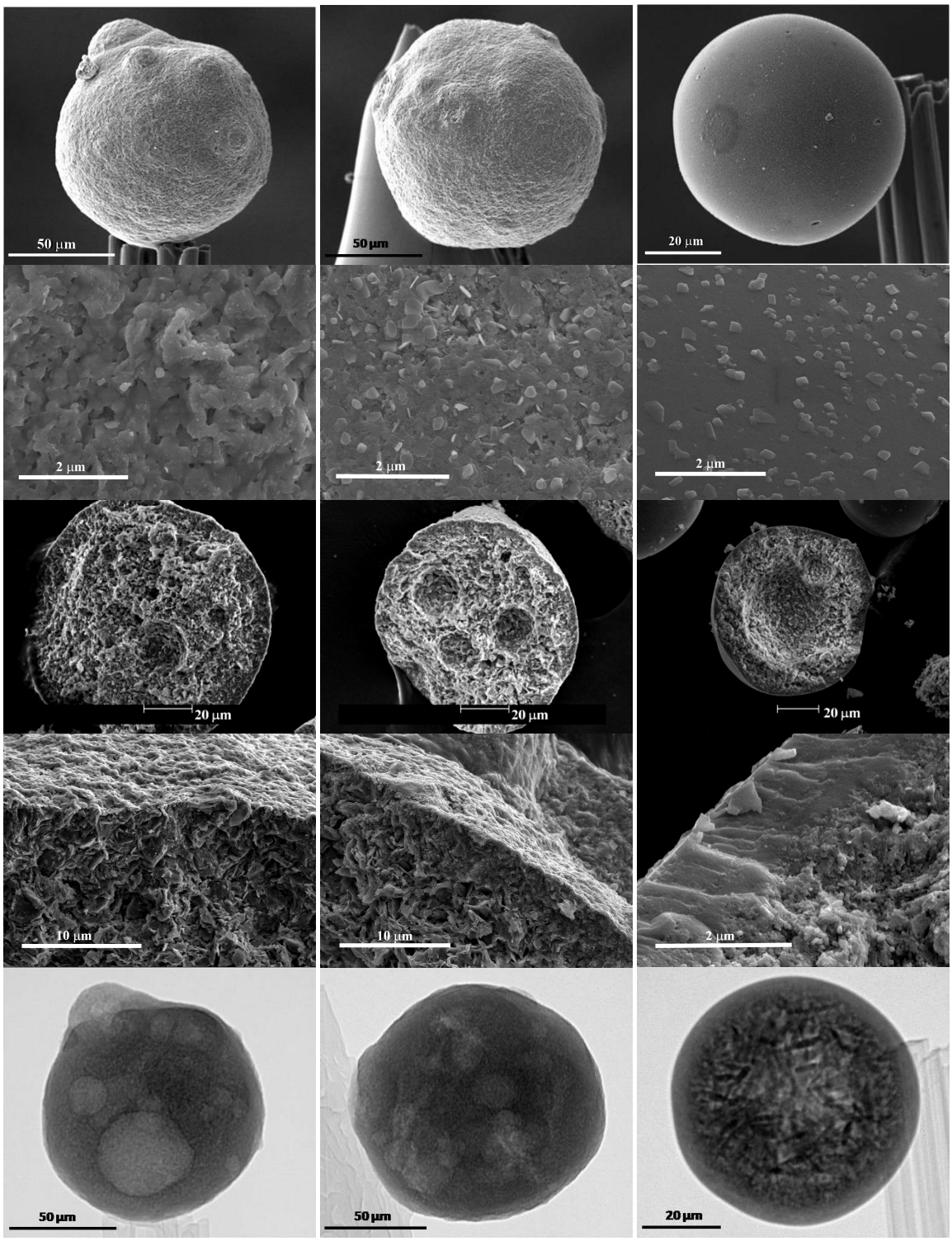

Figure 5.24 SEM (*rows 1-4*) and XuM *(row 5)* micrographs of the precursor material *(column 1),* freshly activated catalyst *(column 2)* and 2-year equilibrated catalysts *(column 3).*

X-ray Ultramicroscopy (XuM)

To examine the interior of these composite particles, without sectioning or damaging the particles, we have for the first time employed X-ray projection microscopy within an SEM environment (Fig. 5.24; row 5) to examine catalyst materials. Internal porosity, associated with the surface blisters are frequently seen in the precursor and freshly activated catalyst by X-ray phase contrast (Fig. 5.24; row 5; columns 1 & 2).

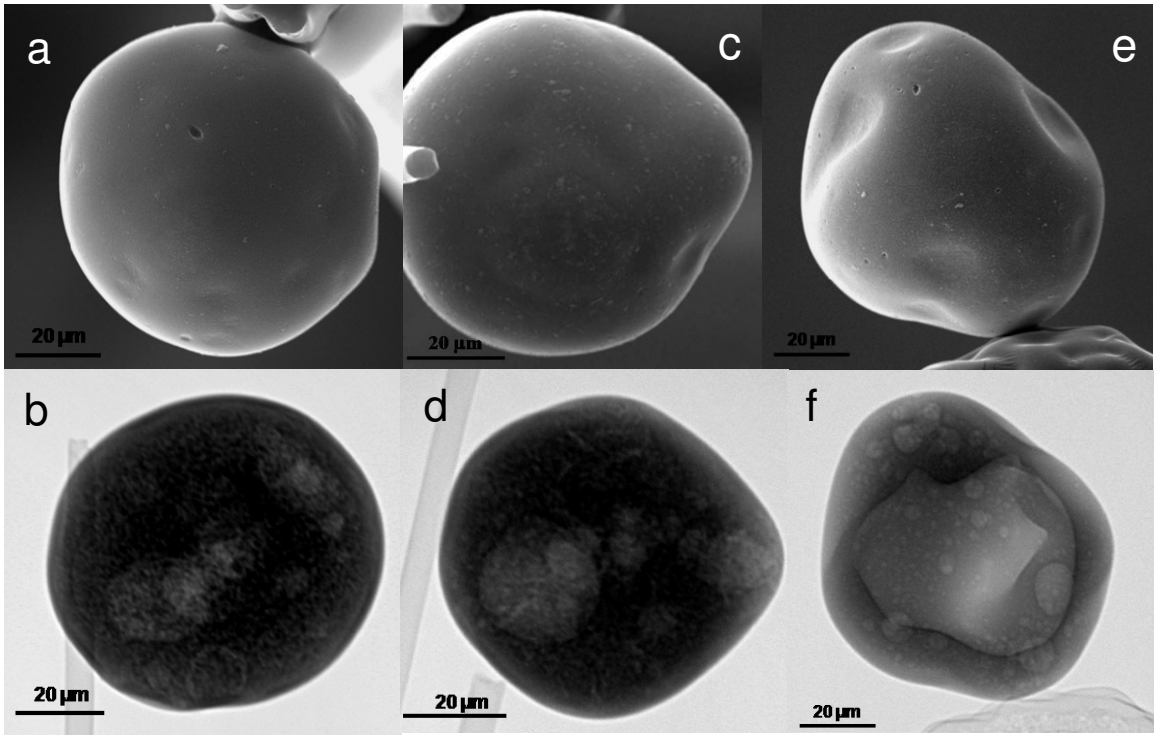

Figure 5.25 SEM (*row 1*) and corresponding XuM (*row 2*) micrographs of three particles from the 2-year equilibrated catalyst showing the presence of significant internal porosity.

The interior V-P-O crystallites are most clearly imaged by X-ray absorption contrast in the equilibrated catalyst (Fig. 5.24; row 5; column 3). This particular image also shows a clearly delineated 2-5µm thick SiO_2 shell, whereas the SiO_2/V-P-O interface is less well defined in the precursor and freshly activated materials. In fact, XuM analysis of the equilibrated V-P-O/SiO_2 material (Figs. 5.25(b)(d)), showed that the internal

porosity arising from the blistering or trapped gas in the precursor shell can still be retained even after extended use. Furthermore, about 5% of the particles in the equilibrated material are hollow having completely lost their internal V-P-O material (Fig. 5.25(f)), while still retaining an almost spherical external morphology (Fig. 5.25(e)). Such degraded particles are also likely to be catalytically inactive.

Transmission Electron Microscopy (TEM)

Crushing the V-P-O/SiO_2 particles and dispersing them on a holey carbon grid allowed us to examine their contents in more detail within the TEM. A montage of BF-TEM micrographs, selected area diffraction patterns (SADPs) and simulated electron diffraction patterns from the precursor, freshly activated and equilibrated catalysts are presented in Fig. 5.26. The precursor material (shown in Fig. 5.26(a)) consists of irregular platelets ranging between 100 nm and 3μm in size. Each platelet was found to be single crystalline and SADPs obtained along platelet normal direction were consistent with the [001] projection of $VOHPO_4 \cdot 0.5H_2O$. Figure 5.26(b) shows the typical V-P-O morphology found in the freshly activated catalyst. Each 'platelet' is composed of an agglomerate many tiny crystallites that are typically ~40 x 40 nm in size. SADP's from individual platelets show them to be a collection of highly textured, bur not perfectly oriented, $(VO)_2P_2O_7$ crystallites exhibiting a common [100] direction normal to the platelet. This suggests that the starting single crystals of $VOHPO_4 \cdot 0.5H_2O$ topotactically transform into platelets of roughly the same dimension which are composed of an ordered textured mosaic of $(VO)_2P_2O_7$ nanocrystals. In the 2-year used V-P-O/SiO_2 materials (Fig. 5.26(c)-(e)), three distinct types of V-P-O material were found. The first and most abundant morphology (shown in Fig. 5.26(c)), is an identical $(VO)_2P_2O_7$ structure to that

described for the freshly activated materials in Figure 5.26(b). The other minority phases identified by SAED analysis were β-$VOPO_4$ crystallites (Fig. 5.26(d)) having an irregularly shaped morphology and angular δ-$VOPO_4$ platelets (Fig. 5.26(e)) with an angularly shaped morphology.

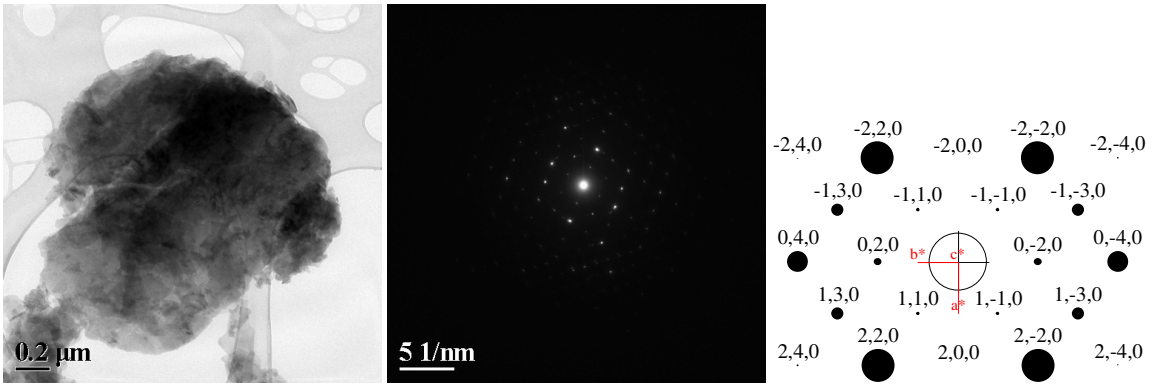

(a)

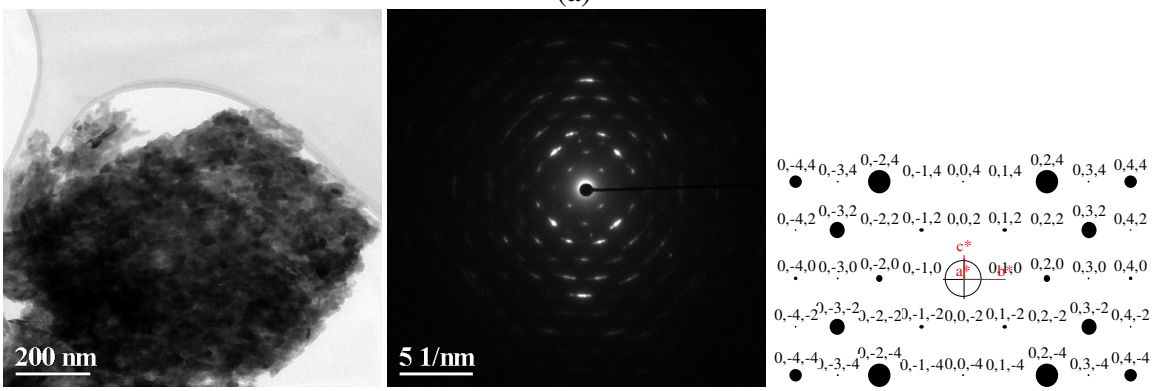

(b)

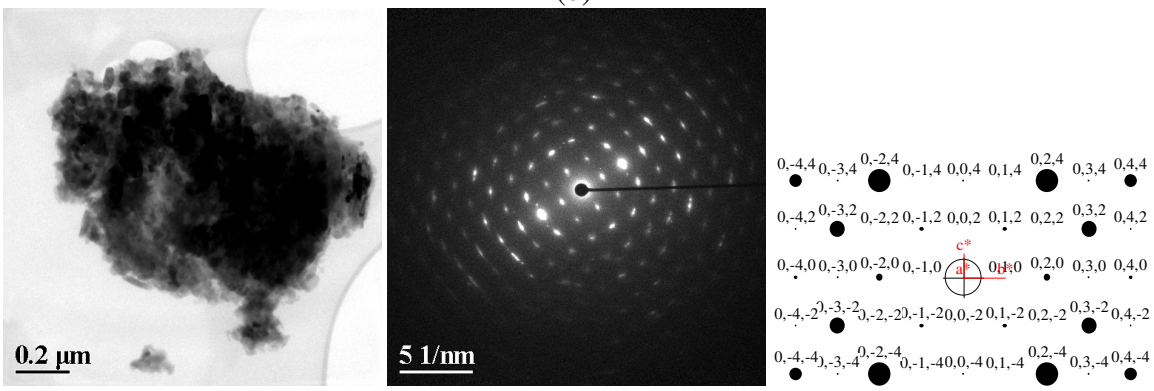

(c)

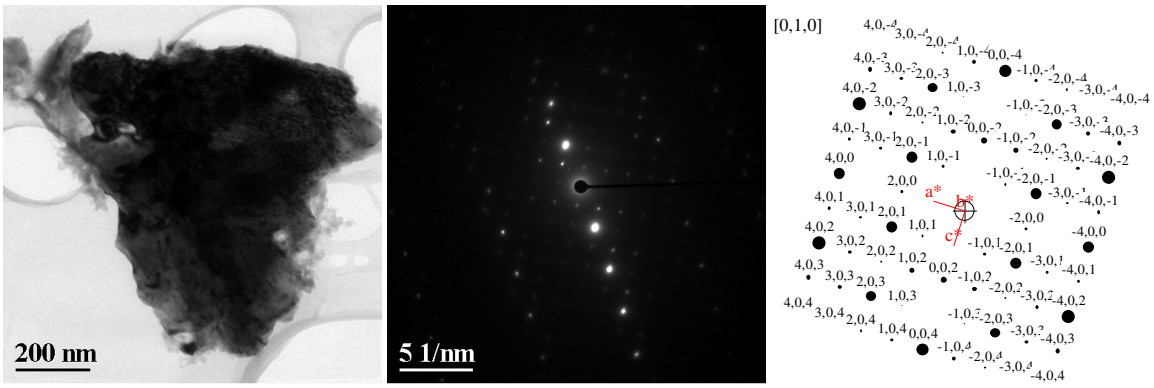

(d)

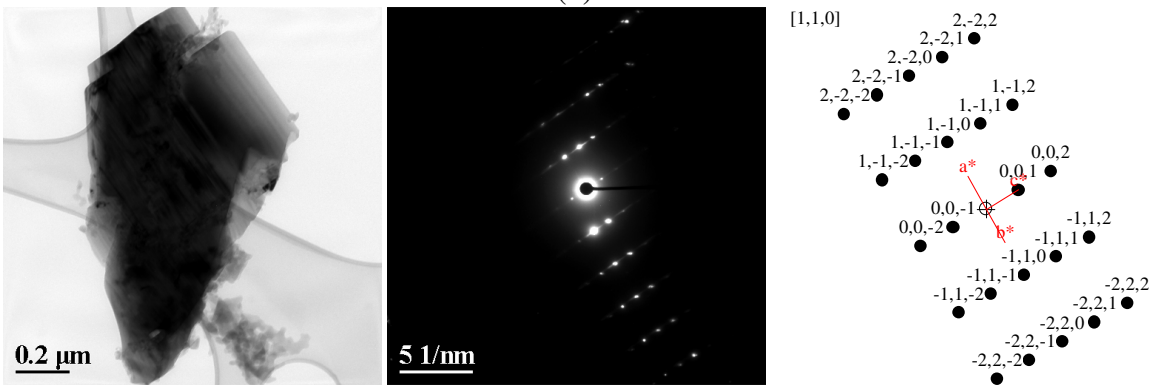

(e)

Figure 5.26 BF-TEM micrographs (*colunm 1*), SADP's (*column 2*) and simulated & indexed SADPs (*column 3*) of (a) a [001] $VOHPO_4 \cdot 0.5H_2O$ phase platelet in the precursor material; (b) a [100] $(VO)_2P_2O_7$ platelet in calcined catalysts. The 2 year equilibrated particles showed the co-existence of (c) [100] $(VO)_2P_2O_7$, (d) [010] β-$VOPO_4$ and (e) [110] δ-$VOPO_4$ phases.

X-Ray Photoelectron Spectroscopy (XPS)

XPS analysis (Table 1) of the precursor, freshly activated catalyst and equilibrated material showed several additional interesting features. Even though the materials were examined in an uncrushed state for XPS analysis, all showed significant amounts of surface V and P (Table 5.4). For the precursor and freshly activated materials these signals probably originate from two sources: namely V and P atomically dispersed within the SiO_2 shell and internal V-P-O exposed from occasional cracked or broken spheres. For the equilibrated materials, as shown by SEM, there were additional fragments of V-P-O material embedded in the smooth SiO_2 shell which contribute to the V(2p) and P(2p)

XPS signals; the P(2p) binding energies observed for the 3 catalysts are very consistent at 133.9 +/- 0.1 eV. It is expected that any SiO_2 spheres which fractured during extended use could spill their V-P-O contents, the ground up fragments of which could subsequently become embedded in the surface regions of the SiO_2 shells. An additional point worth noting from Table 5.4 is that the used materials showed significant traces of surface Fe, a contaminant which probably arises from attrition of the walls of the stainless steel reactor vessel during extended use. This Fe contamination has also been shown in work conducted on the same equilibrated material at another institution which is part of the VPO workshop.[34] The higher proportion of V^{5+} species in the surface of the equilibrated catalyst, is consistent with the presence of some $VOPO_4$ phases, in addition to $(VO)_2P_2O_7$. This is in a good agreement with the XRD and TEM observations of β- and δ-$VOPO_4$ are present in the equilibrated V-P-O/SiO_2 sample.

Table 5.4 Surface composition of the three samples as determined from XPS analysis.

Sample	Atom %					
	O	**Si**	**V**	**P**	**Fe**	**N**
Precursor	72.4	22.0	1.9	3.7	0	0
Freshly activated	71.8	7.7	7.9	12.7	0	0
Equilibrated	64.1	8.7	5.3	15.5	3.5	2.8

5.3.3.3 Possible reasons for the decrease in catalytic performance with time on line

The equilibrated catalyst showed a marked loss in activity and selectivity towards MA production. More specifically, at 37 % conversion the catalyst was able to achieve only 22% selectivity to MA. From the structural characterization data obtained on the

equilibrated material it is clear that this decrease in performance is due to the development of V^{5+} phases. It has been well documented that the presence of such V^{5+} phases can result in a lower activity.[35,36] In fact, the equilibrated catalyst remains relatively active despite the significant surface smoothing and obvious reduction in the size and number density of pores in the SiO_2 shell (Fig. 5.24). High resolution SEM micrographs (Fig. 5.24, row 2) also show that discrete shards of V-P-O material are embedded into the SiO_2 surface, which may explain, in part, why a relatively efficient performance level is retained even after 2 years of intensive service in the CFBR. However, for operation in the CFBR environment the transport of oxygen through the protective shell may be impeded by the increased density of the silica, resulting in some measurable loss of catalyst efficiency. Additionally, the presence of iron (3.5 atom%) in the sample may affect the product selectivity, if not the activity. Zazhigalov *et al.*[37] reported such a phenomenon with a V_2O_5-H_3PO_4-$CoCl_2$ catalyst, where the inclusion of Fe from apparent equipment corrosion lowered MA selectivity. Additionally Sananes-Schulz *et al.*[38] previously reported that the addition of an iron dopant (at 1 %) led to increased volume fraction of $VOPO_4$ domains during activation. This resulted in lower crystallinity of the pyro-phosphate catalyst and subsequently degraded catalytic performance.

5.3.4 Summary for V-P-O/SiO_2 core-shell materials for use in fluidized bed reactors

Reaction evaluation and novel characterization techniques have allowed us to study in great detail the DuPont V-P-O/SiO_2 industrial catalyst. *n*-Butane oxidation has

shown similarities to standard literature examples under fixed-bed operation in terms of the specific activity. From this initial study we have been able to identify several structural aspects of the 2-year equilibrated catalyst which have contributed to its markedly decreased activity. In particular, the microstructural analysis shows that during use the silica layer becomes more pronounced and dense leading to loss in the overall activity on a weight basis. However, on the basis of surface area the specific activity is largely retained, indicating that, once the required microstructure is established, it is the surface area of the catalysts that largely controls the overall effectiveness of the material as a catalyst. Furthermore, we show that X-ray ultra-Microscopy can be a very incisive technique in revealing the internal structures of such composite catalyst particles.

5.4 Overall conclusions and suggestions for future work

In this chapter, three different novel routes for preparing V-P-O catalysts have been explored; namely (i) the use of V-P-O 'seed' crystals in the VPD route, (ii) the use of a di-block copolymer template in V-P-O production and (iii) the encapsulation of fragile V-P-O catalysts with a mechanically resistant SiO_2 shell. These new methods have all shown some specific advantages over the conventional VPA, VPO or VPD methods.

In the seeding experiments, $VOHPO_4 \cdot 0.5H_2O$ was prepared from $VOPO_4 \cdot 2H_2O$ using 1- and 3-octanol, 2-butanol and 2-methyl-1-propanol, respectively, as both solvent and reducing agent. With 1-octanol the reaction temperature was found to be crucial in obtaining a high yield of the precursor phase, and at temperatures ≥160 °C a solution, containing V^{4+} ions formed in preference to $VOHPO_4 \cdot 0.5H_2O$. However, $VOHPO_4 \cdot 0.5H_2O$ formation can be achieved above 160°C by carrying out the reduction

process in the presence of a small amount of V-P-O material which effectively acts as a templating seed. The use of this seeding concept is shown to have a dramatic effect on altering the morphology of the final activated catalyst and on inducing certain phase transformations. Specifically when 3-octanol is used, $VO(H_2PO_4)_2$ is solely generated, except in the presence of a V-P-O seed where significant amounts of $VOHPO_4 \cdot 0.5H_2O$ can also be formed. This material shows a high specific activity of 4.5×10^{-5} $mol_{MA}/m^2 \cdot h$ which is much better than the negligible activity exhibited by the $VO(H_2PO_4)_2$ material generated from the un-seeded reaction in 3-octanol. Our findings show that both the phase composition and morphology of vanadium phosphates can be influenced by the use of seeds during the preparation process.

A diblock copolymer has been shown to be an effective template in the preparation of a vanadium phosphate catalyst. It can influence the morphology as well as the crystallinity of the synthesized material and hence improve the performance of the activated catalyst. The templated V-P-O precursor materials are more crystalline as compared with those prepared using standard methodologies. This can be attributable to the possibility that the copolymer template acts as a structure director, which can promote the grain growth along the {140}-type planes of $VOHPO_4 \cdot 0.5H_2O$ resulting in the formation of rhombic crystallites. Due to the increased crystallinity and morphological changes, these templated V-P-O materials give rise to a much faster *in-situ* precursor-to-catalyst transformation. Two processes are believed to occur during the activation of the precursor material, namely (i) the dehydration of $VOHPO_4 \cdot 0.5H_2O$ to form $(VO)_2P_2O_7$ and (ii) a disordering of the surface of the catalyst, the former step of which benefits from

the high crystallinity of the templated V-P-O precursors resulting in a significantly increased speed of the activation process.

Putting a protective silica shell around the V-P-O core material shows a great advantage in protecting V-P-O materials from being fractured in a circulating fluidized bed reactor (CFBR). The V-P-O/SiO_2 industrial catalyst exhibited a reasonable initial catalytic performance, however after more than two years on line a huge degradation in the performance was observed. Three DuPont V-P-O/SiO_2 industrial catalysts, namely (i) the catalyst precursor, (ii) the calcined precursor and (iii) equilibrated material (2 years on-line), were studied by a wide variety of characterization techniques (*e.g.* XRD, SEM, TEM and XPS) and a novel X-ray ultraMicroscopy (XuM) technique. From this initial study we have been able to identify several structural aspects of the 2-year equilibrated catalyst which have contributed to its markedly decreased activity. These include (i) presence of V^{5+} (*e.g.* β-$VOPO_4$) phases which are not active phases for *n*-butane oxidation, (ii) silica shell surface smoothing and decrease in porosity and (iii) loss of V-P-O material from within the shells (~5% of all particles) and destruction of particles.

In the seeding method, the V-P-O sacrificial seed is effective in altering the morphology of the product and inducing certain phase transformations. The precise mechanism for this seeding effect is not well understood. A set of intermediate materials collected during the seeding experiment (*i.e.* after 0.5h, 4h, 12h and 24h of refluxing) could be recovered and studied by electron microscopy techniques in order to follow the evolution of the seeding effect. In addition only the E-phase ($VO(H_2PO_4)_2$) was investigated and found to transform with the assistance of appropriate V-P-O seeds in this work. Further studies could be designed in order to exploit the seeding effect to minimize

the amounts of other undesired V-P-O polymorphs (*e.g.* α-$VOPO_4$ and β-$VOPO_4$) in the preparation.

In the copolymer template method, although the activation time required to convert the precursor material to the active catalyst was decreased significantly, the activity and selectivity to MA was similar to that of V-P-O catalysts prepared using standard methods. It is well known that V-P-O catalysts prepared by either VPA, VPO or VPD route have a similar specific activity, although they usually show different activities and selectivities. This implies that the surface structure of the activated catalysts generated from standard preparation routes are very similar.[8] It is apparent that the ability to prepare a high-surface area V-P-O catalyst can improve its activity and selectivity to MA production. The previous chapter has shown that the alkane treatment of $VOPO_4 \cdot 2H_2O$ before the alcohol reduction could create nano scale rhomboidal $VOHPO_4 \cdot 0.5H_2O$ platelets having a poor crystallinity. If the copolymer template is added together with the alcohol in the reduction step, a nano scale $VOHPO_4 \cdot 0.5H_2O$ material with a high crystallinity might be expected, which could exhibit a fast activation and have a better specific activity.

In the method involving the encapsulation of fragile V-P-O catalysts within a mechanically resistant SiO_2 shell, the outer SiO_2 shell was found to be intact for the initial few days, but became densified over a longer time period which prevented the reactant gas and the products transferring through the shell, resulting in a pronounced decrease of the catalytic performance. So a more mechanically resistant porous shell needs to be developed, which could firstly maintain intact after a long time of mechanic abrasion and secondly is not detrimental to the catalytic activity of V-P-O catalysts. Some

of the potential candidates could be SiC, Si_3N_4 and BN, which are known to be hard ceramic materials.[39] As heat-conductive ceramics, when used as supports for V-P-O catalysts, they did not show detrimental effects to the catalytic activity of V-P-O catalysts.[23] These properties present in SiC, Si_3N_4 and BN meet the requirements as a support of the fragile V-P-O catalyst that is used in a CFBR.

5.5 Acknowledgements

In section 5.1 the V-P-O catalyst syntheses, XRD experiments, BET surface area measurement and catalyst testing on the selective oxidation of *n*-butane to maleic anhydride were performed by Dr. Raja Al Otaibi, Dr. Jonathan K. Bartley and Dr. Nicholas F. Dummer in Prof. Graham J. Hutchings's group at Cardiff University. Their various contributions to this work are all gratefully appreciated and acknowledged.

In section 5.2 the V-P-O catalyst syntheses, BET surface area measurement, XRD experiments and catalyst testing on the selective oxidation of *n*-butane to maleic anhydride were performed by Dr. Zhongjie Lin, Dr. Nicholas F. Dummer and Dr. Jonathan K. Bartley in Prof. Graham J. Hutchings's group at Cardiff University. Their various contributions to this work are all gratefully appreciated and acknowledged.

In section 5.3 the V-P-O/SiO_2 catalysts were supplied by DuPont. BET surface area measurement, XRD experiments and catalyst testing on the selective oxidation of *n*-butane to maleic anhydride were performed by Dr. Nicholas F. Dummer and Dr. Jonathan K. Bartley in Prof. Graham J. Hutchings's group at Cardiff University. XuM experiments were performed in collaboration with Dr. Carol Kiely at Lehigh University. XPS experiments were carried out by Dr. Albert F. Carley in Prof. Graham J. Hutchings's

group at Cardiff University. Their various contributions to this work are all gratefully appreciated and acknowledged.

5.6 References

1. E. Bordes, P. Courtine, and J. W. Johnson, "On the topotactic dehydration of $VOHPO_4 \cdot 0.5H_2O$ into vanadyl pyrophosphate," *Journal of Solid State Chemistry,* **55,** 270-279 (1984).

2. J. W. Johnson, D. C. Johnston, A. J. Jacobson, and J. F. Brody, "Preparation and characterization of $VO(HPO_4) \cdot 0.5H_2O$ and its topotactic transformation to $(VO)_2P_2O_7$," *Journal of the American Chemical Society,* **106,** 8123-8128 (1984).

3. C. J. Kiely, A. Burrows, G. J. Hutchings, K. E. Bere, J. C. Volta, A. Tuel, and M. Abon, "Structural transformation sequences occurring during the activation of vanadium phosphorus oxide catalysts," *Faraday Discussions,* **105,** 103-118 (1996).

4. N. Yamamoto, N. Hiyoshi, and T. Okuhara, "Thin-layered sheets of $VOHPO_4 \cdot 0.5H_2O$ prepared from $VOPO_4 \cdot 2H_2O$ by intercalation-exfoliation-reduction in alcohol," *Chemistry of Materials,* **14,** 3882-3888 (2002).

5. Y. Kamiya, S. Ueki, N. Hiyoshi, N. Yamamoto, and T. Okuhara, "Preparation of catalyst precursors for selective oxidation of *n*-butane by exfoliation-reduction of $VOPO_4 \cdot 2H_2O$ in primary alcohol," *Catalysis Today,* **78,** 281-290 (2003).

6. G. J. Hutchings, M. T. Sananes, S. Sajip, C. J. Kiely, A. Burrows, I. J. Ellison, and J. C. Volta, "Improved method of preparation of vanadium phosphate catalysts," *Catalysis Today,* **33,** 161-171 (1997).

7. E. A. Lombardo, C. A. Sanchez, and L. M. Cornaglia, "The effect of preparation methods and activation strategies upon the catalytic behavior of the vanadium-phosphorus oxides," *Catalysis Today,* **15,** 407-418 (1992).

8. C. J. Kiely, A. Burrows, S. Sajip, G. J. Hutchings, M. T. Sananes, A. Tuel, and J. C. Volta, "Characterisation of variations in vanadium phosphate catalyst microstructure with preparation route," *Journal of Catalysis,* **162,** 31-47 (1996).

9. H. Imai, Y. Kamiya, and T. Okuhara, "Selective oxidation of *n*-butane over nanosized crystallites of $(VO)_2P_2O_7$ synthesized by an exfoliation-reduction process of $VOPO_4 \cdot 2H_2O$ in a mixture of 2-butanol and ethanol," *Journal of Catalysis,* **251,** 195-203 (2007).

10. M. Carreon, V. Guliants, F. Pierelli, and F. Cavani, "Ordered mesostructured mixed metal oxides: microporous VPO phases for n-butane oxidation to maleic anhydride," *Catalysis Letters,* **92,** 11-16 (2004).

11. M. Carreon and V. Guliants, "Macroporous vanadium phosphorus oxide phases displaying three-dimensional arrays of spherical voids," *Chemistry of Materials,* **14,** 2670-2675 (2002).

12. M. Carreon and V. Guliants, "Mesostructured vanadium-phosphorus-oxide phases," *Microporous and Mesoporous Materials,* **55,** 297-304 (2002).

13. L. O'Mahony, J. Henry, D. Sutton, T. Curtin, and B. K. Hodnett, "Crystallisation of $VOHPO_4 \cdot 0.5H_2O$," *Applied Catalysis A-General,* **253,** 409-416 (2003).

14. I. J. Ellison, G. J. Hutchings, M. T. Sananes, and J. C. Volta, "Control of the composition and morphology of vanadium phosphate catalyst precursors from alcohol treatment of $VOPO_4 \cdot 2H_2O$," *Journal of the Chemical Society-Chemical Communications,* 1093-1094 (1994).

15. X. Zhao, J. Yu, and B. Cheng, "Morphology control of lead sulfide particles in mixed systems of poly-(styrene-alt-maleic acid) and cetyltrimethylammonium bromide," *Materials Chemistry and Physics,* **101,** 379-382 (2007).

16. J. G. Yu, H. Guo, and B. Cheng, "Shape evolution of $SrCO_3$ particles in the presence of poly-(styrene-alt-maleic acid)," *Journal of Solid State Chemistry,* **179,** 800-803 (2006).

17. J. K. Bartley, C. Rhodes, C. J. Kiely, A. F. Carley, and G. J. Hutchings, " *n*-Butane oxidation using $VO(H_2PO_4)_2$ as catalyst derived from an aldehyde/ketone based preparation method," *Physical Chemistry Chemical Physics,* **2,** 4999-5006 (2000).

18. J. K. Bartley, R. P. K. Wells, and G. J. Hutchings, "The unexpected role of aldehydes and ketones in the standard preparation method for vanadium phosphate catalysts," *Journal of Catalysis,* **195,** 423-427 (2000).

19. J. K. Bartley, C. J. Kiely, R. P. K. Wells, and G. J. Hutchings, "Vanadium(V) phosphate prepared using solvent-free method," *Catalysis Letters,* **72,** 99-105 (2001).

20. H. Colfen and L. M. Qi, "A systematic examination of the morphogenesis of calcium carbonate in the presence of a double-hydrophilic block copolymer," *Chemistry-a European Journal,* **7,** 106-116 (2001).

21. G. J. Hutchings, A. Desmartinchomel, R. Olier, and J. C. Volta, "Role of the product in the transformation of a catalyst to its active state," *Nature,* **368,** 41-45 (1994).

22. G. J. Hutchings, J. K. Bartley, J. M. Webster, J. A. Lopez-Sanchez, D. J. Gilbert, C. J. Kiely, A. F. Carley, S. M. Howdle, S. Sajip, S. Caldarelli, C. Rhodes, J. C. Volta, and M. Poliakoff, "Amorphous vanadium phosphate catalysts from supercritical antisolvent precipitation," *Journal of Catalysis,* **197,** 232-235 (2001).

23. M. J. Ledoux, C. Crouzet, C. Pham-Huu, V. Turines, K. Kourtakis, P. L. Mills, and J. J. Lerou, "High-yield butane to maleic anhydride direct oxidation on vanadyl pyrophosphate supported on heat-conductive materials: beta-SiC, Si_3N_4, and BN," *Journal of Catalysis,* **203,** 495-508 (2001).

24. R. A. Overbeek, A. R. C. J. Pekelharing, A. J. vanDillen, and J. W. Geus, "Preparation, characterization and testing of newly developed silica-supported V-P-O catalysts," *Applied Catalysis A-General,* **135,** 231-248 (1996).

25. R. A. Overbeek, P. A. Warringa, M. J. D. Crombag, L. M. Visser, A. J. vanDillen, and J. W. Geus, "Preparation, characterization and testing of newly developed titania supported V-P-O catalysts," *Applied Catalysis A-General,* **135,** 209-230 (1996).

26. W. Nie, X. Wang, W. Ji, Q. Yan, C. Yi, and C. Au, "A study on VPO specimen supported on aluminum-containing MCM-41 for partial oxidation of n-butane to MA," *Catalysis Letters,* **76,** 201-206 (2001).

27. J. M. C. Bueno, G. K. Bethke, M. C. Kung, and H. H. Kung, "Supported VPO catalysts for selective oxidation of butane III: Effect of preparation procedure and SiO_2 support," *Catalysis Today,* **43,** 101-110 (1998).

28. C. Y. Xiao, X. Chen, Z. Y. Wang, W. J. Ji, Y. Chen, and C. T. Au, "The novel and highly selective fumed silica-supported VPO for partial oxidation of *n*-butane to maleic anhydride," *Catalysis Today,* **93-5,** 223-228 (2004).

29. K. Inumaru, T. Okuhara, and M. Misono, "Active crystal-face of vanadyl pyrophosphate for catalytic-oxidation of *n*-butane to maleic-anhydride," *Chemistry Letters,* 1955-1958 (1992).

30. E. Bordes and R. M. Contractor, "Adaptation of the microscopic properties of redox catalysts to the type of gas-solid reactor," *Topics in Catalysis,* **3,** 365-375 (1996).

31. R. M. Contractor, H. E. Bergna, H. S. Horowitz, C. M. Blackstone, B. Malone, C. C. Torardi, B. Griffiths, U. Chowdhry, and A. W. Sleight, "Butane oxidation to maleic anhydride over vanadium phosphate catalysts," *Catalysis Today,* **1,** 49-58 (1987).

32. R. M. Contractor and A. W. Sleight, "Selective oxidation in riser reactor," *Catalysis Today,* **3,** 175-184 (1988).

33. S. C. Mayo, P. R. Miller, S. W. Wilkins, T. J. Davis, D. Gao, T. E. Gureyev, D. Paganin, D. J. Parry, A. Pogany, and A. W. Stevenson, "Quantitative X-ray projection microscopy: phase-contrast and multi-spectral imaging," *Journal of Microscopy-Oxford,* **207,** 79-96 (2002).

34. L. Perez-Moreno, S. Irusta, J. Soler, J. Herguido, and M. Menendez, "Effect of the use in circulating fluidized bed on the performance of a VPO catalyst: Characterization and transient studies," *Chemical Engineering Journal,* **147,** 330-335 (2009).

35. M. Abon, K. E. Béré, and P. Delichère, "Nature of active oxygen in the n-butane selective oxidation over well-defined V-P-O catalysts: an oxygen isotopic labelling study," *Catalysis Today,* **33,** 15-23 (1997).

36. T. Shimoda, T. Okuhara, and M. Misono, "Preparation of vanadium-phosphorus mixed-oxide (P/V=1) catalysts and their application to oxidation of butane to maleic-anhydride," *Bulletin of the Chemical Society of Japan,* **58,** 2163-2171 (1985).

37. V. A. Zazhigalov, V. M. Belousov, G. A. Komashko, A. I. Pyatnitskaya, T. A. Kriger, O. Y. Polotnyuk, and Y. I. Sorokin, "Effect of iron additions on the properties of vanadium-phosphorus catalysts for the oxidation," *Journal of Applied Chemistry of the USSR,* **60,** 865-869 (1987).

38. M. T. SananesSchulz, A. Tuel, G. J. Hutchings, and J. C. Volta, "The V^{4+}/V^{5+} balance as a criterion of selection of vanadium phosphorus oxide catalysts for n-butane oxidation to maleic anhydride: A proposal to explain the role of Co and Fe dopants," *Journal of Catalysis,* **166,** 388-392 (1997).

39. J. H. Zhao, L. C. Stearns, M. P. Harmer, H. M. Chan, G. A. Miller, and R. F. Cook, "Mechanical-behavior of alumina silicon-carbide nanocomposites," *Journal of the American Ceramic Society,* **76,** 503-510 (1993).

Chapter 6 Nanostructural and Chemical Characterization of Niobium Phosphate (Nb-P-O) Oxidative Dehydrogenation Catalysts

6.1 Introduction

6.1.1 Oxidative dehydrogenation of ethane to ethylene

Ethylene (C_2H_4) is commercially produced by an energy intensive process which involves the steam cracking of hydrocarbons (*e.g.* naphtha and ethane (C_2H_6)).[1] The oxidative dehydrogenation (ODH) of ethane to ethylene (eqn. 6.1) is a much more energy efficient and cost effective process than traditional steam cracking technologies.

$$C_2H_6 + O \rightarrow C_2H_4 + H_2O \quad (6.1)$$

Before this ODH process can be considered as a viable alternative to steam cracking, catalysts producing high ethylene yields need to be developed.

Recently the development of new catalysts for the ODH of ethane has been attracting increased attention from academic researchers. In some cases higher yields to ethylene than those obtained by the traditional steam cracking have been achieved.[2] However, the ODH process has not yet been adopted by the ethylene manufacturers and no commercial plants have been built using this approach, which is most likely because of the familiarity and trust in the traditional steam cracking process. Hence in order to apply catalytic ODH for ethylene production, the preparation and identification of improved catalysts is necessary.

The majority of catalysts used for the ODH are metal oxide materials. The most successfully exploited complex oxide catalysts are vanadium phosphate (V-P-O) materials, which are used commercially for the selective oxidation of *n*-butane to maleic

anhydride.[3,4] The role of phosphorus in the *n*-butane oxidation process is crucial, as well as for the ODH of alkane. The addition of phosphorus into molybdenum oxide based catalysts shows an improved performance for the ODH of ethane to ethylene.[5] A similar positive effect was also observed in vanadium oxide based catalysts for the ODH of propane to propylene.[6] A number of metal phosphate catalysts have been studied by Matsuura and Kimura[7] for the ODH of propane to propylene. They reported that $NbOPO_4$ was active and relatively selective towards propylene. Niobium phosphate is in fact a close relative of these two catalysts, namely niobium oxide (a solid acid)[8] and vanadium phosphate (an oxidation catalyst)[4]. Against this background, it is surprising that niobium phosphates have not been more widely investigated as catalysts, especially considering the importance of Nb and P for the ODH of ethane and propane. Furthermore, niobium phosphates have a range of properties and structures that are considered desirable for selective oxidation catalysts. In the present work we have addressed some of these deficiencies and have studied a series of niobium phosphate components. Their relative activities for the selective oxidative dehydrogenation of ethane to ethylene have been determined, and comparisons made with two standard niobium oxide phases.

6.1.2 Selective oxidation of methanol to formaldehyde

Formaldehyde ($H_2C=O$), as the simplest aldehyde, is a colorless gas at room temperature with a pungent odor. It has a melting point of -92°C and a boiling point of -21°C. Because of its high chemical reactivity, formaldehyde, as one of the most important chemical building blocks, and is used to produce numerous chemical products, such as thermosetting resins, oil-soluble resins and adhesives.[9]

A historical review by Chauvel *et al*.[10] noted that in 1859 Alexander M Butlerov first reported the preparation of formaldehyde. This was followed by then in August by W. Von Hoffman (1868), who the first time, produced formaldehyde by passing methanol vapor and air over a heated platinum spiral. Since the 19th century, formaldehyde has been produced commercially and its early uses included application as a disinfectant and an embalming agent.

The first industrial catalysts for producing formaldehyde involved methanol dehydrogenation over a copper gauze. These were later replaced by silver catalysts, due to the higher yield achieved, and their greater resistance to poisoning.[11] In the 1950's, the selective oxidation of methanol over a Fe-Mo oxide catalyst was designed as an alternative process.[10] Historically the silver process and the Fe-Mo oxide process each account for approximately 50% of the total production of formalin (*i.e.* an aqueous solution of formaldehyde).[9-11] However, recently the Fe-Mo oxide process has been preferred over the silver process.[10] The chemical reactions pertinent to each of these processes are shown below,[11]

The Fe-Mo oxide process:

$$2CH_3OH + O \rightarrow 2CH_2O + 2H_2O \quad (6.2)$$

The silver process:

$$2CH_3OH + O \rightarrow 2CH_2O + 2H_2O \quad (6.3)$$

$$CH_3OH \rightarrow CH_2O + H_2 \quad (6.4)$$

Both chemical reactions (eqns. 6.3 and 6.4) are found to occur in the silver process to produce formaldehyde, whereas only methanol oxidation (eqn. 6.2) is found to happen in the Fe-Mo oxide process. In the silver process the reaction is carried out under

methanol rich conditions at atmospheric pressure and a reaction temperature between 560 and 600 °C. Typically a conversion rate of 65-75% with a selectivity as high as 89% can be achieved. In the Fe-Mo oxide process, on the other hand, the reaction is carried out in an excess of air, and the reaction temperature is kept below 400 °C to ensure a high conversion rate and a thermally stable catalyst. The typical conversion rate can be as high as 99% with a selectivity as high as 95% for this latter method. The Fe-Mo oxide process has several advantages over the silver process,[12] namely (i) higher yield, (ii) higher resistance to poisoning, (iii) longer lifetime of catalyst and (iv) lower operating temperature.

In this chapter, besides performing an evaluation of Nb-P-O's catalytic performance for the ODH of ethane to ethylene, the same set of Nb-P-O catalysts will be studied for the selective oxidation of methanol to formaldehyde in order to extend its potential range of applications. In addition the activity of the Nb-P-O catalysts can be probed using methanol oxidation as a model reaction. Since the products formed can be easily related to the acidity/basicity and redox properties of the catalyst. In particular, the formation of formaldehyde has previously been related to the redox behavior, whereas the formation of dimethyl ether relates to the acid character.[13] By studying the methanol oxidation on Nb-P-O materials we should gain a better understanding of the catalytic nature of niobium phosphate materials.

6.2 Experimental

6.2.1 Catalyst preparation

The nomenclature adopted for identifying the niobium phosphate (NbP-series) catalysts produced in this study is summarized in Table 6.1. A $Nb_2P_4O_{15}$ catalyst, designated as NbP-1, was prepared using a method similar to that described previously.[14] Niobium (V) chloride (10 mmol or 2.7017 g) was added to distilled water (50 mL) and phosphoric acid and left to stir for 30 minutes. Aqueous ammonia was then added until the pH reached 2.6 and remained constant. The precipitate was recovered by filtration and washed with distilled water. Hydroxylamine (6 mmol, 0.18 mL), water (10 mL) and phosphoric acid (8 mmol, 0.46 mL) were then added to the precipitate and the resulting suspension was kept at pH 3.88 for 30 minutes using aqueous ammonia. The resulting gel was placed in a Teflon-lined stainless steel autoclave and heated at 65 °C under autogeneous pressure for 48 hours. The resulting solid was filtered, washed and dried at 110 °C for 15 hours and then calcined at 500 °C.

Catalyst NbP-2 ($NbOPO_4$) was prepared by refluxing niobium(V) chloride (Aldrich, 99.9%, 16.91 g dissolved in 50mL of distilled water) and ortho-phosphoric acid (Aldrich, 99.99%, 30mL in 120mL of distilled water) for 24 hours. Ortho-phosphoric acid was added with continuous stirring. The P:Nb ratio chosen was 8:1. The temperature of the mixture was then 130 °C and to induce reaction. The resulting solid was filtered and washed with distilled water and dried at 110°C for 16 h, before being ground with a pestle and mortar and calcined in air at 500 °C for 3 h.

Catalyst NbP-3 (nominally $Nb_{1.91}P_{2.82}O_{12}$) was prepared from the niobium phosphate material (NbP-2) by reduction in hydrogen at 500 ^{o}C for 3 h.

Catalyst NbO-1 (orthorhombic Nb_2O_5) was prepared from niobium(V) chloride (Aldrich, 99.9%, 16.91g) which was dissolved in distilled water with continuous stirring. Sodium carbonate (Aldrich, 99.99%, 53.00 g in 250 mL of distilled water, 2 M) was added drop-wise to the aqueous niobium chloride solution until a precipitate was formed. The resulting solid was then filtered and dried in an oven at 110°C for 16 h, before being calcined in static air at 500 °C for 3 h.

Catalyst NbO-2 (monoclinic Nb_2O_5) was synthesized from a niobium(V) chloride (Aldrich, 99.9%, 16.91g in 50mL of distilled water, 0.25 M) which was heated to 80 °C with continuous stirring. Urea (30.03g in 250mL of distilled water, 2 M) was then added drop-wise and stirred for 3 hours. The resulting solid was filtered and dried in an oven at 110 °C for 16 h, before being calcined at 500 °C for 3 h in static air.

Table 6.1 Nomenclature of the niobium phosphate and niobium oxide materials studied.

Unused catalysts	Used catalysts for ethane oxidative dehydrogenation	Used catalysts for methanol oxidation
NbP-1	NbP-1E	NbP-1M
NbP-2	NbP-2E	NbP-2M
NbP-3	NbP-3E	NbP-3M
NbO-1	NbO-1E	N.A.
NbO-2	NbO-2E	N.A.

6.2.2 Catalyst testing

The catalytic conditions for testing the activity for ethane oxidation over Nb-P-O catalysts have been described in sub-section 3.8.2. The condition for methanol oxidation reaction over Nb-P-O catalysts are described in sub-section 3.8.3.

6.2.3 Electron microscopy characterization

Scanning electron microscopy (SEM), bright field transmission electron microscopy (BF-TEM), selected area electron diffraction (SAED) analyses and high resolution transmission electron microscopy (HR-TEM) were all performed on these materials. Experimental details for these characterization methods have been described in Chapter 3, section 3.6.

6.2.4 Complementary characterization techniques

Surface area measurements, XRD and XPS experiments were performed as described in Chapter 3, sub-sections 3.9.1, 3.9.2 and 3.9.3, respectively. All crystalline phases were identified by matching the experimental patterns to those in the ICCD PDF database.

6.3 Unused niobium phosphate materials

The BET catalyst surface areas and crystalline phases identified by XRD are summarized in Table 6.2. The XRD pattern of the NbO-1 catalyst was confirmed to be characteristic of orthorhombic Nb_2O_5, whilst the NbO-2 sample presented the diffraction peaks expected from the monoclinic Nb_2O_5 phase. These standard niobium oxide phases (NbO-1 and NbO-2), prepared from precipitation using sodium carbonate and urea respectively, had surface areas of 7 m^2/g and 8 m^2/g, respectively.

The different preparation methods employed for making catalysts containing both niobium and phosphorus, resulted in the formation of three different crystalline phases as determined from XRD analysis (Table 6.2). The NbP-1 catalyst was mainly comprised of a crystalline cubic $Nb_2P_4O_{15}$ phase (ICCD: 00-035-0020), whilst NbP-2 was consistent

with tetragonal $NbOPO_4$, a niobium oxyphosphate phase (ICCD: 04-009-1784). The BET surface areas of catalysts NbP-1 and NbP-2 were very similar at 7-8 m^2g^{-1}. The NbP-3 catalyst was prepared from NbP-2 by a reduction treatment with hydrogen at 500 ^oC for 3h. The crystalline phase of NbP-3 as determined by XRD analysis was characteristic of orthorhombic $Nb_{1.91}P_{2.82}O_{12}$ (ICCD: 04-009-2580) with a trace of second as yet un-identified phase which will be described later. The surface area of NbP-3 was slightly higher than that of the other phosphorus-containing catalysts at 12 m^2g^{-1}. Interestingly based only on the crystalline phases assigned from XRD, our results imply that the NbP-3 material ($Nb_{1.91}P_{2.82}O_{12}$) prepared from NbP-2 ($NbOPO_4$) shows an increase of the P:Nb ratio to 1.48:1 from 1:1. However, it should be noted that this increase only takes into account crystalline phases identified in XRD and additional disordered material present might not be detected by the XRD technique. The crystallographic information for all three Nb-P-O phases observed is summarized in Table 6.3.

Table 6.2 Physico-chemical properties of the catalysts in this study. (XRD and BET experiments performed by Dr. Matthew Davies at Cardiff University.)

Unused catalysts[a]	**Crystalline phases by XRD**	**BET surface area/m^2g^{-1}**
NbP-1	Cubic $Nb_2P_4O_{15}$	8
NbP-2	Tetragonal $NbOPO_4$	7
NbP-3	Orthorhombic $Nb_{1.91}P_{2.82}O_{12}$	12
NbO-1	Orthorhombic Nb_2O_5	11
NbO-2	Monoclinic Nb_2O_5	9

[a] NbP catalysts contain Nb, P and O; NbO catalysts contain only niobium and oxygen.

Table 6.3 Crystallographic information of the Nb-P-O phases studied in this project.

Nb-P-O phases	**Space group**	**a,b,c (Å)**	**α, β, γ (°)**
Cubic $Nb_2P_4O_{15}$ [a]	Pa-3 (205)	a=b=c=24.199	α=β=γ=90°
Tetragonal $NbOPO_4$ [b]	P4/nmm (129)	a=b=6.4043, c=4.1217	α=β=γ=90°
Orthorhombic $Nb_{1.91}P_{2.82}O_{12}$ [c]	Pn*a (62A)	A=8.7520, b=12.0900, C=8.6740	α=β=γ=90°

[a]: ICCD PDF# 00-035-0020, [b]: ICCD PDF# 04-009-1784 and [c]: ICCD PDF# 04-009-2580.

SEM micrographs of the unused NbP-1 catalyst are presented in Figure 6.1. The material exhibited a distinctive open pore morphology with micro-pore dimensions of 10 - 20 μm and a wall thickness of 0.5 - 1 μm.

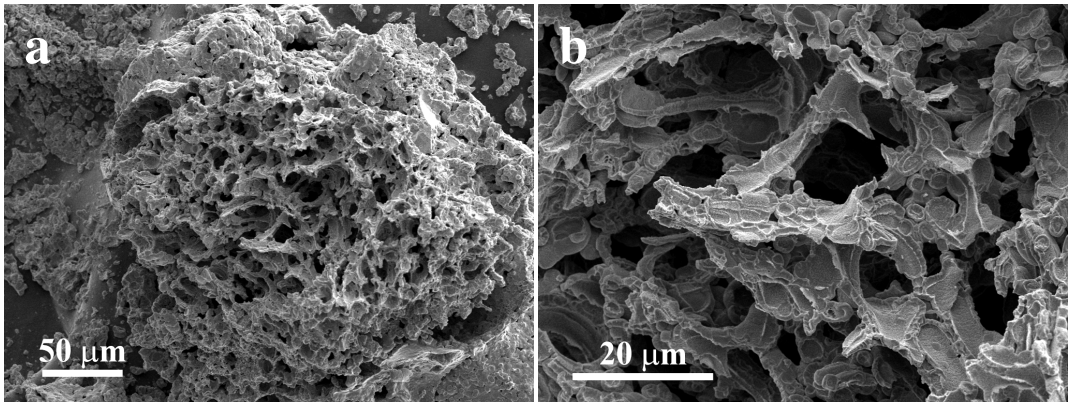

Figure 6.1 SEM micrographs of the NbP-1 material showing (a) micro-porous structure and (b) wall thickness of 0.5 - 1 μm.

SEM micrographs of the unused NbP-2 catalyst are shown in Figure 6.2. Macroscopic layered plate-like structures up to 100 μm in size (Fig. 6.2(a)) were observed, which were comprised of fused agglomerates of much smaller (100 - 200 nm) particles (Fig. 6.2(b)). Detailed TEM and electron diffraction studies confirmed that these small particles were tetragonal $NbOPO_4$ crystals exhibiting the [001] direction as the particle normal (Figs. 6.3(a)-(c)), which is in good agreement with the XRD data.

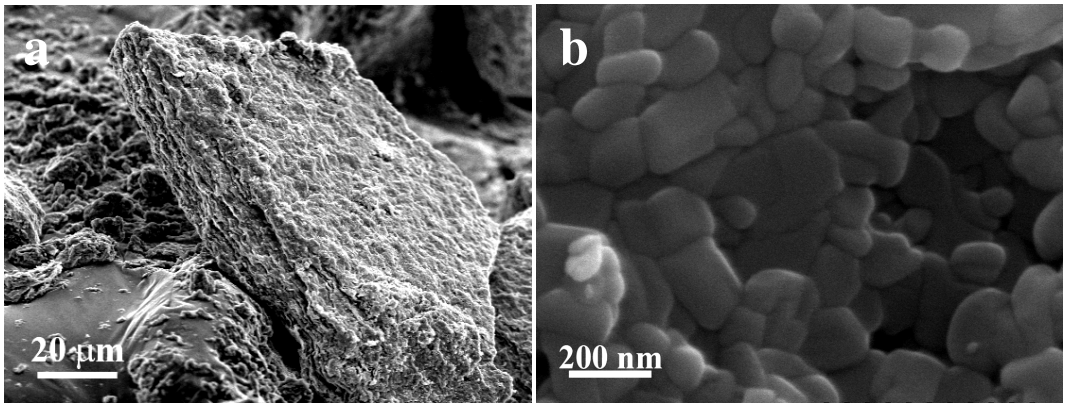

Figure 6.2 SEM micrographs of unused NbP-2 material showing (a) bulk layered platelets comprised of (b) fused agglomerates of much smaller particles.

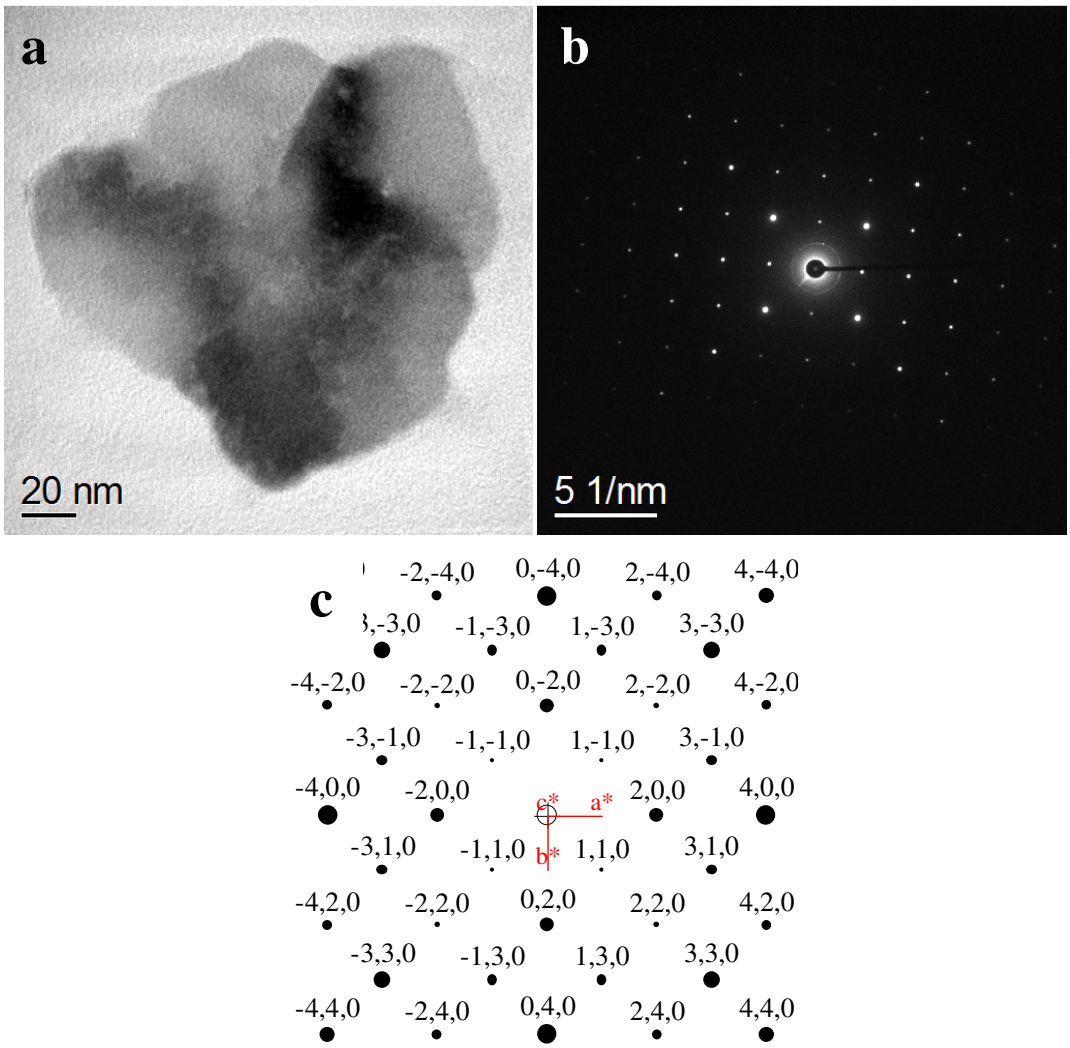

Figure 6.3 (a) BF-TEM micrograph of an isolated small particle in the unused NbP-2 catalyst, (b) the corresponding SADP which matches to the [001] projection of tetragonal $NbOPO_4$ and (c) simulated and indexed SADP from the [001] $NbOPO_4$.

SEM micrographs of the fresh NbP-3 catalyst are displayed in Figure 6.4. Two distinct morphologies were observed, namely stacks of highly regular oblong platelets (Fig. 6.4(a)) and more random agglomerates of irregularly shaped platelets (Fig. 6.4(b)). TEM and SAED analysis of the particles with the regular oblong morphology (Figs. 6.5(a)(b)(f)) show them to be crystals which have fully transformed to the orthorhombic $Nb_{1.91}P_{2.82}O_{12}$ phase. These $Nb_{1.91}P_{2.82}O_{12}$ platelets exhibit a characteristic [100] platelet

normal with (022) and ($02\bar{2}$) edge termination facets. The theoretical intersection angle of these two facets is around 90.4 °, which is consistent with the experimentally measured angle. The irregularly shaped platelets (Figs. 6.5(c)(d)) were much more difficult to structurally assign. SADP's obtained from these irregular platelets show an overlap of several crystalline patterns (Fig. 6.5(e)). The diffraction patterns in Figure 6.5(e) can be divided into at least seven overlapping single crystal patterns, each with a small rotation angle, which show similar spacing's and angles to a typical SADP taken from the [001] projection of $NbOPO_4$. Our best interpretation is that these arise from tetragonal $NbOPO_4$ platelets, the major phase of the NbP-2 starting material, which have only partially transformed to the $Nb_{1.91}P_{2.82}O_{12}$ phase. This interpretation is also corroborated by the presence of characteristic 3.2 nm spacing moiré fringes (Fig. 6.5(d)), which are indicative of the co-existence of different overlapping crystal structures along the incident beam direction within these platelets.

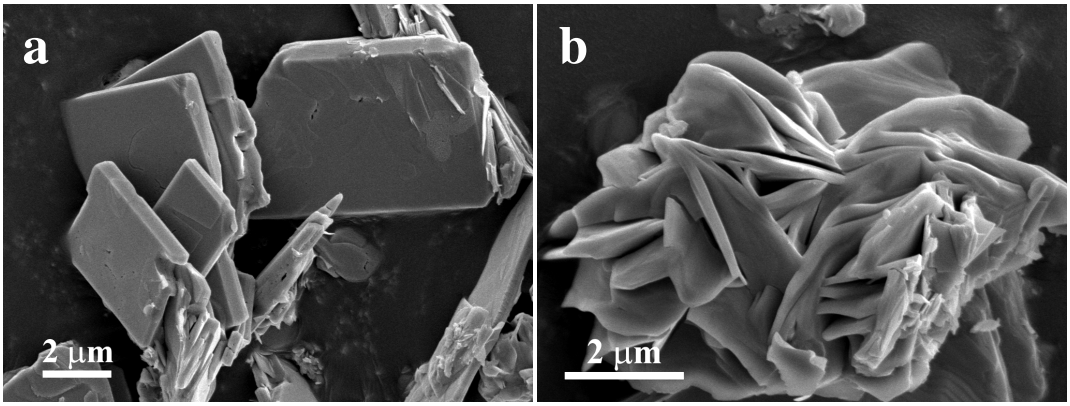

Figure 6.4 SEM micrographs of the unused NbP-3 material showing two distinct morphologies: (a) stacks of regular oblong platelets and (b) randomly packed agglomerates of irregularly shaped platelets.

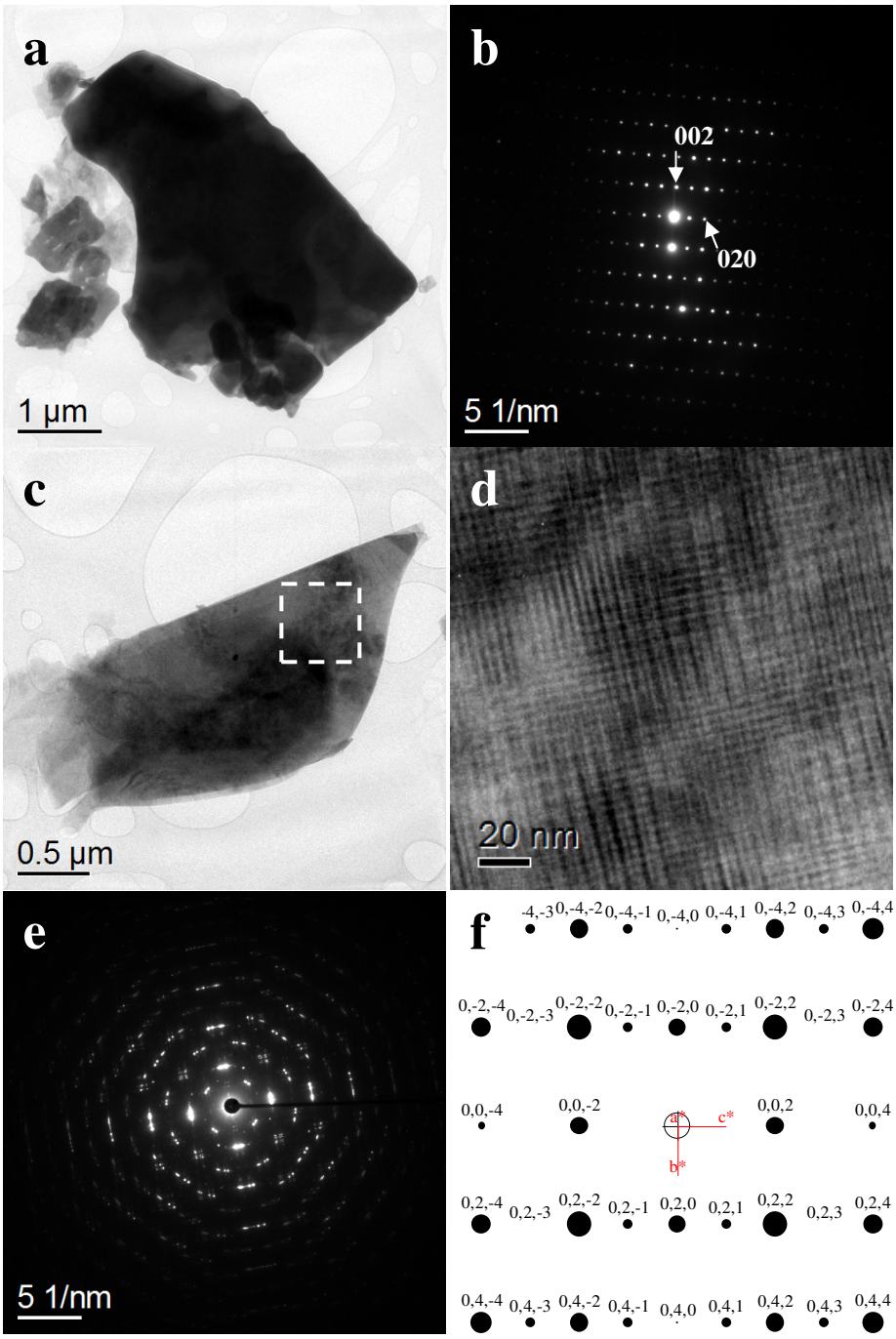

Figure 6.5 (a) BF-TEM micrograph of an oblong platelet from the unused NbP-3 material and (b) its corresponding SADP which can be assigned to the [100] projection of orthorhombic $Nb_{1.91}P_{2.82}O_{12}$; (c) BF-TEM micrograph of an irregularly shaped platelet; (d) the enlargement of a portion of the irregular platelet in (c) delineated by the square box showing moiré fringes; (e) complex overlapping SADP's from the irregular platelet indicating that it may be a partially transformed tetragonal $NbOPO_4$ crystal; (f) simulated and indexed SADP from the [001] projection of orthorhombic $Nb_{1.91}P_{2.82}O_{12}$.

6.4 Niobium phosphate materials used for catalyzing the oxidative dehydrogenation (ODH) of ethane to ethylene

The niobium oxide and niobium phosphate catalysts as described in Table 6.2 were used for the oxidative dehydrogenation of ethane to ethylene. Ethylene, carbon monoxide and carbon dioxide are the only reaction products detected, and experimental carbon mass balances for all the catalysts tested were 100 ± 3 %. The ethane ODH performance of the Nb-P-O series of catalysts is significantly better than the niobium oxide catalysts (Fig. 6.6). In contrast to the modest *ca*. 15% ethylene selectivity at 5% conversion for the Nb-O catalysts, the Nb-P-O catalysts exhibit ethylene selectivities in the range of 78-95% at 5% conversion. Amongst all the Nb-P-O catalysts, the NbP-3 catalyst is the most selective to ethylene, followed by NbP-2 and then NbP-1. The order of selectivity to ethylene at 5% ethane conversion for these Nb-P-O materials showed the following trend:-

NbP-3E (95%) > NbP-2E (85%) > NbP-1E (78%)

Extrapolation of the ethylene selectivities to zero conversion for samples NbP-1E and NbP-2E gives values of *ca.* 85% and 95%, respectively. These values suggest that although the selectivity to ethylene is high, carbon oxides are still being formed as primary products, albeit at low levels. The extrapolation to zero conversion for the NbP-3 catalyst gives a very promising result, since a 100% ethylene selectivity is predicted, which implies that ethylene is the only primary reaction product.

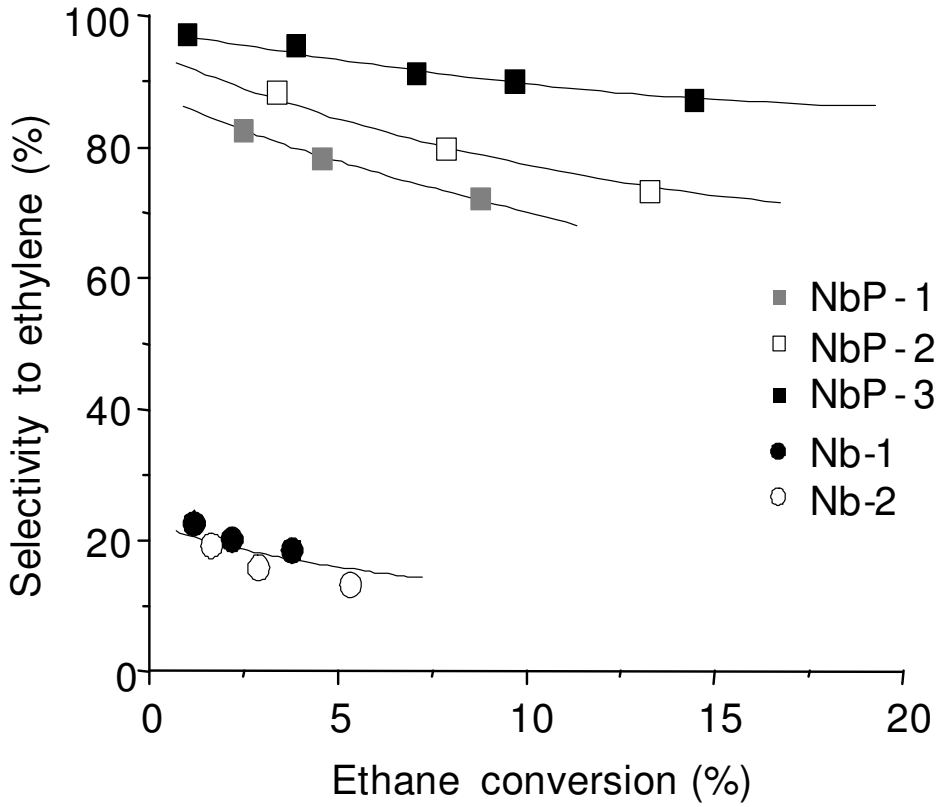

Figure 6.6 Evolution of the selectivity to ethylene with the ethane conversion at 500ºC for NbP-series and NbO-series materials in this study (Reaction conditions: $C_2/O_2/He$ = 30/10/60, T=500 ºC, different contact times.)

It is clear that the niobium-phosphorus oxide based materials are far superior catalysts when compared to the niobium oxides, hence we have concentrated our detailed structural characterization studies on the niobium phosphate catalysts. There was no change in the XRD pattern for the NbP-1 catalyst after use (NbP-1E) implying that the cubic $Nb_2P_4O_{15}$ phase was retained. However some evidence of particle sintering and a reduction in the overall degree of porosity were noted as shown in Figure 6.7, which can be explained by the exposure to high temperature (500 ºC) during the catalytic reaction.

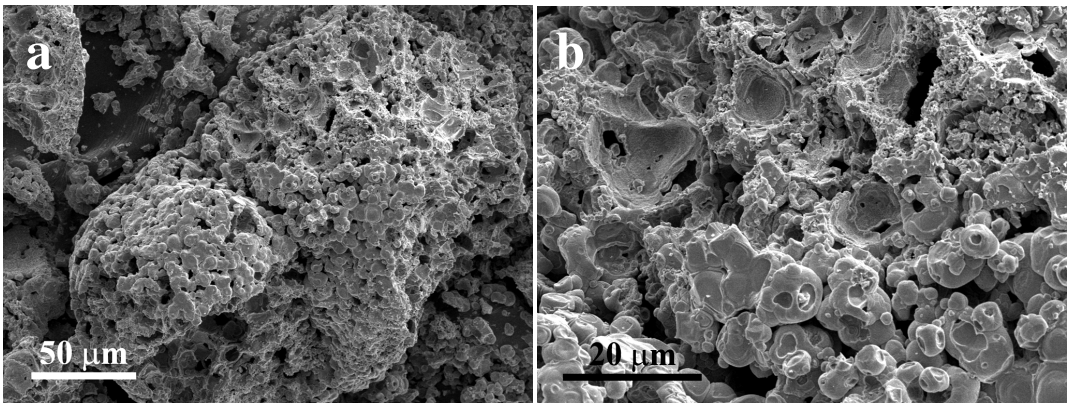

Figure 6.7 SEM micrographs of the NbP-1E material showing (a) a reduction in overall degree of porosity and (b) particle sintering.

Figure 6.8 shows representative BF-TEM images of the NbP-1E material. This catalyst is comprised of three typical morphologies, namely smaller particles (Figs. 6.8(a)(c)), angular crystalline $Nb_{1.91}P_{2.82}O_{12}$ platelets (Fig. 6.8(d)) and microporous particles (Fig. 6.8(e)). This assignation is supported by the accompanying SAED ring patterns showing a combination of three different diffraction features. The smaller particles are the predominant morphology, which produce a SAED ring pattern consistent with the cubic $Nb_2P_4O_{15}$ structure, which was the main phase detected by XRD. Characteristic higher order diffraction rings- (521), (630) and (933) from the cubic $Nb_2P_4O_{15}$ phase are clearly visible in the SAED ring pattern (#3, #4 and #5 respectively in Fig. 6.8(b)). The angular crystalline platelets (Fig. 6.8(d), ~5 vol. %) displayed SADP's consistent with the [100] projection of the $Nb_{1.91}P_{2.82}O_{12}$ phase (Fig. 6.8(d)). The rings labelled #1 and #2 in Figure 6.8(b) correspond to (011) and (111) planes of this $Nb_{1.91}P_{2.82}O_{12}$ phase. The microporous particles (Figs. 6.8(e)(f), ~ 5 vol. %), on the other hand, were proven by SAED analysis to be amorphous in character as they showed only a typical diffuse scatter ring pattern.

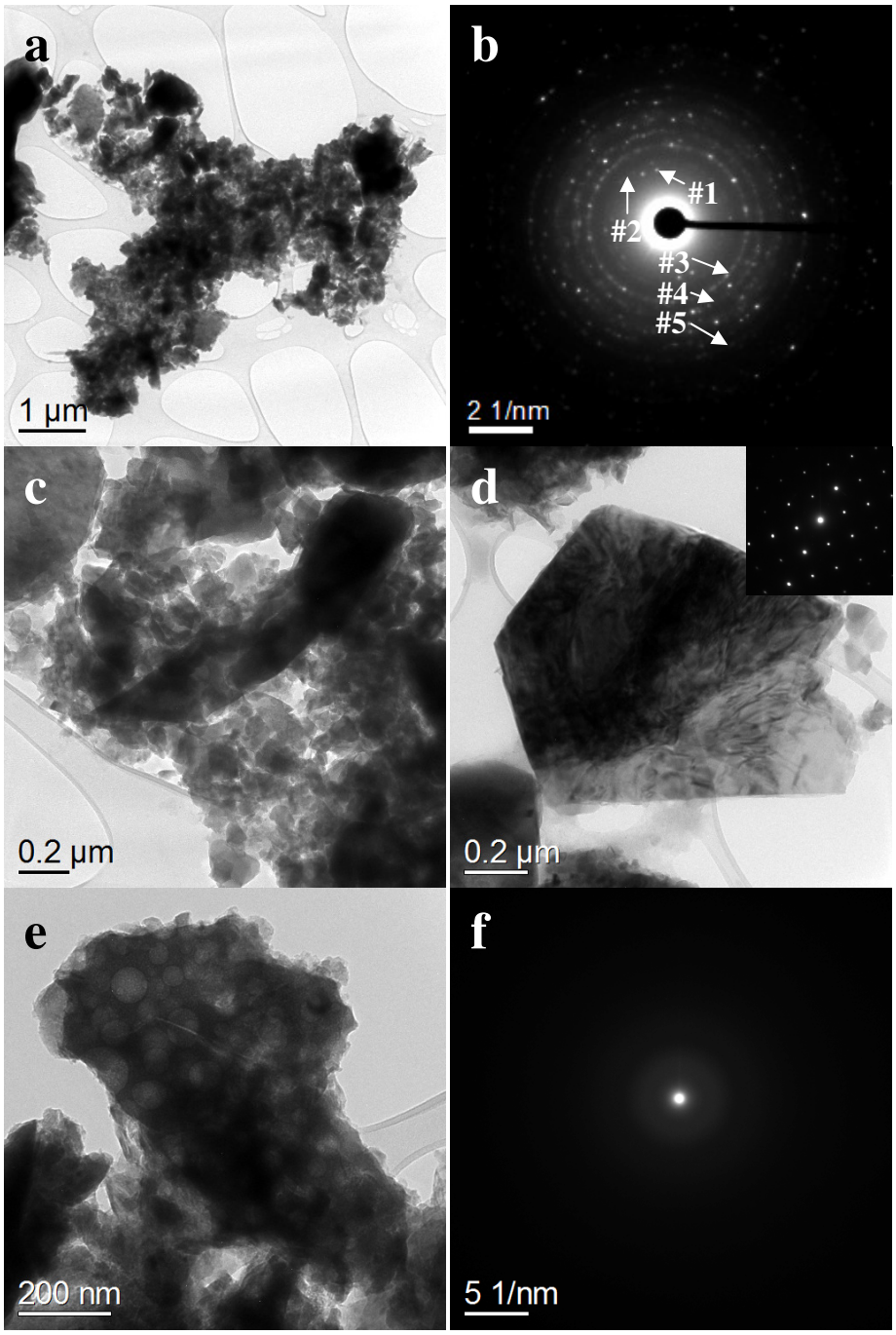

Figure 6.8 BF-TEM micrographs of the NbP-1E catalyst showing (a) a combination of three different morphologies with (c) smaller particles of $Nb_2P_4O_{15}$ (major morphology); (d) angular orthorhombic $Nb_{1.91}P_{2.82}O_{12}$ platelets (inset, SADP corresponds to [100] $Nb_{1.91}P_{2.82}O_{12}$); and (e) an amorphous microporous morphology; (b) is the corresponding SAED ring pattern from the agglomerate in (a) which can be assigned to a combination of $Nb_{1.91}P_{2.82}O_{12}$ (minor phase, rings #1 and #2) and cubic $Nb_2P_4O_{15}$ (major phase, the remainder of the rings, ring #3 - (521), ring #4 - (630) and ring #5 - (933)); (f) the

corresponding SADP from the microporous materials in (e) showing an amorphous morphology.

Catalysts NbP-2E and NbP-3E produced the highest yields of ethylene among the five materials tested, and they are inter-related by the fact that NbP-3 was prepared directly from NbP-2 by a thermal reduction treatment in hydrogen. The morphology of the used NbP-2E sample is very similar to that of the NbP-2 fresh catalyst, showing macroscopic layered plate-like structures up to 100 μm in size (Fig. 6.9(a)), which are comprised of fused agglomerates of much smaller (100 - 200 nm) particles (Fig. 6.9(b)).

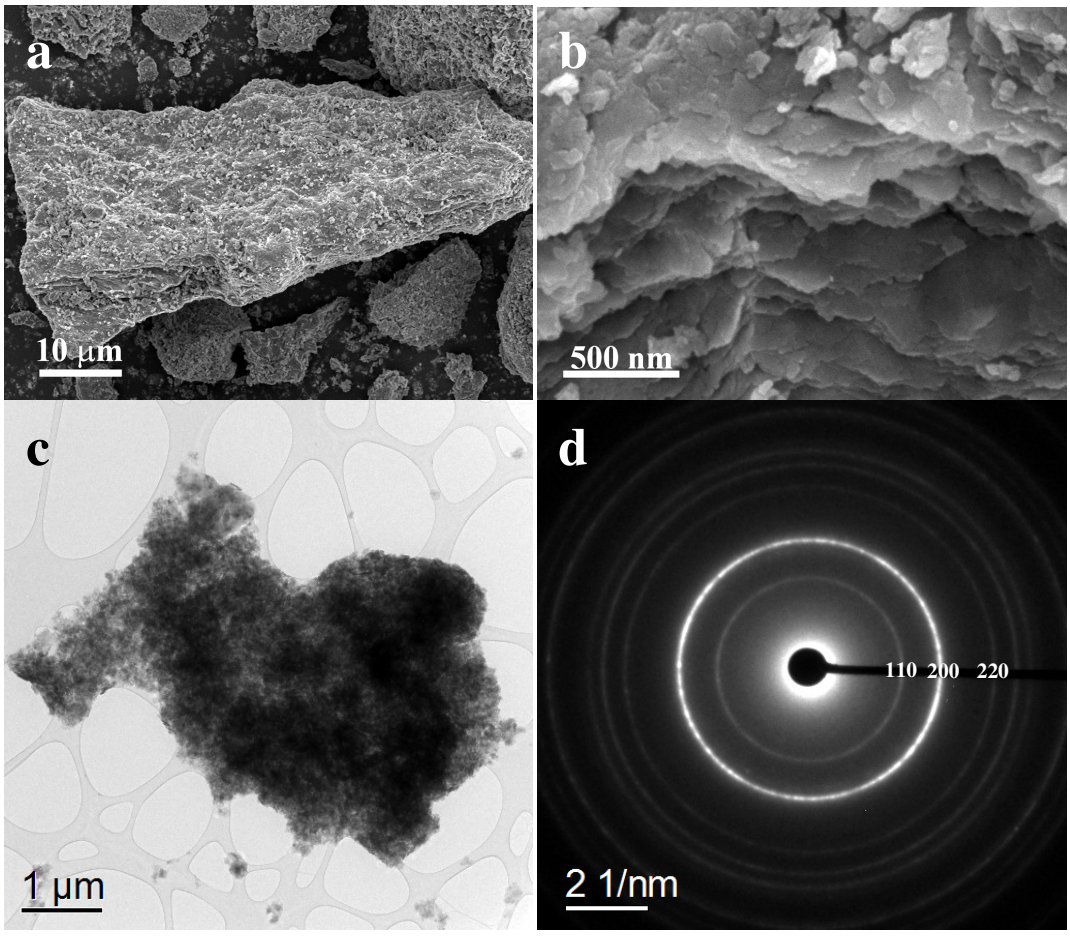

Figure 6.9 SEM micrographs of the NbP-2E material after use as a catalyst for the oxidative dehydrogenation of ethane showing (a) layered plate-like structures and (b) fused agglomerates of much smaller (100 - 200 nm) particles; (c) BF-TEM micrograph of NbP-2E catalysts showing an agglomerate of random particles and (d) its corresponding SAED ring pattern corresponding to tetragonal $NbOPO_4$.

More detailed TEM and SAED studies confirm that these small particles are tetragonal $NbOPO_4$ crystals (Figs. 6.9(c)(d)) exhibiting characteristic (110), (200) and (220) rings in the SAED ring pattern, which is consistent with the XRD data. Obviously, the ethane oxidation reaction did not change the structure or alter the crystallography of the NbP-2 catalyst.

SEM images of the NbP-3E catalyst are illustrated in Figure 6.10(a)(b). Two distinct morphologies were present, with the major one being the large oblong platelets as observed in the unused NbP-3 sample (Fig. 6.10(a)), which constitute a large proportion of the catalyst. The agglomerates of irregular platelets present in the unused NbP-3 sample were no longer present in the NbP-3E catalyst after use. Instead they had transformed into agglomerates of much smaller (100 - 200 nm) particles (Fig. 6.10(b)). TEM and electron diffraction analysis of the oblong platelets (Figs. 6.10(c)(e)) confirm that they retain the $Nb_{1.91}P_{2.82}O_{12}$ crystalline structure as identified in the unused NbP-3 catalyst. It was also possible to determine the crystal structure of the smaller particles (Figs. 6.10(e)(f)) using high resolution transmission electron microscopy. HR-TEM micrographs obtained from individual particles exhibited sets of (002) and (020) lattice planes with an intersection angle of 90° which corresponds to the [100] projection of orthorhombic $Nb_{1.91}P_{2.82}O_{12}$, and hence confirms that the small crystals have the same crystal structure as the larger oblong platelets. It is worth mentioning that all the niobium phosphate materials studied so far are not very stable under conventional levels of electron beam irradiation, and that they could form internal pores or even be amorphized within the span of a couple of seconds. Hence in all Nb-P-O TEM experiments described

above were performed using low dose illumination conditions in order to minimize beam damage artifacts.

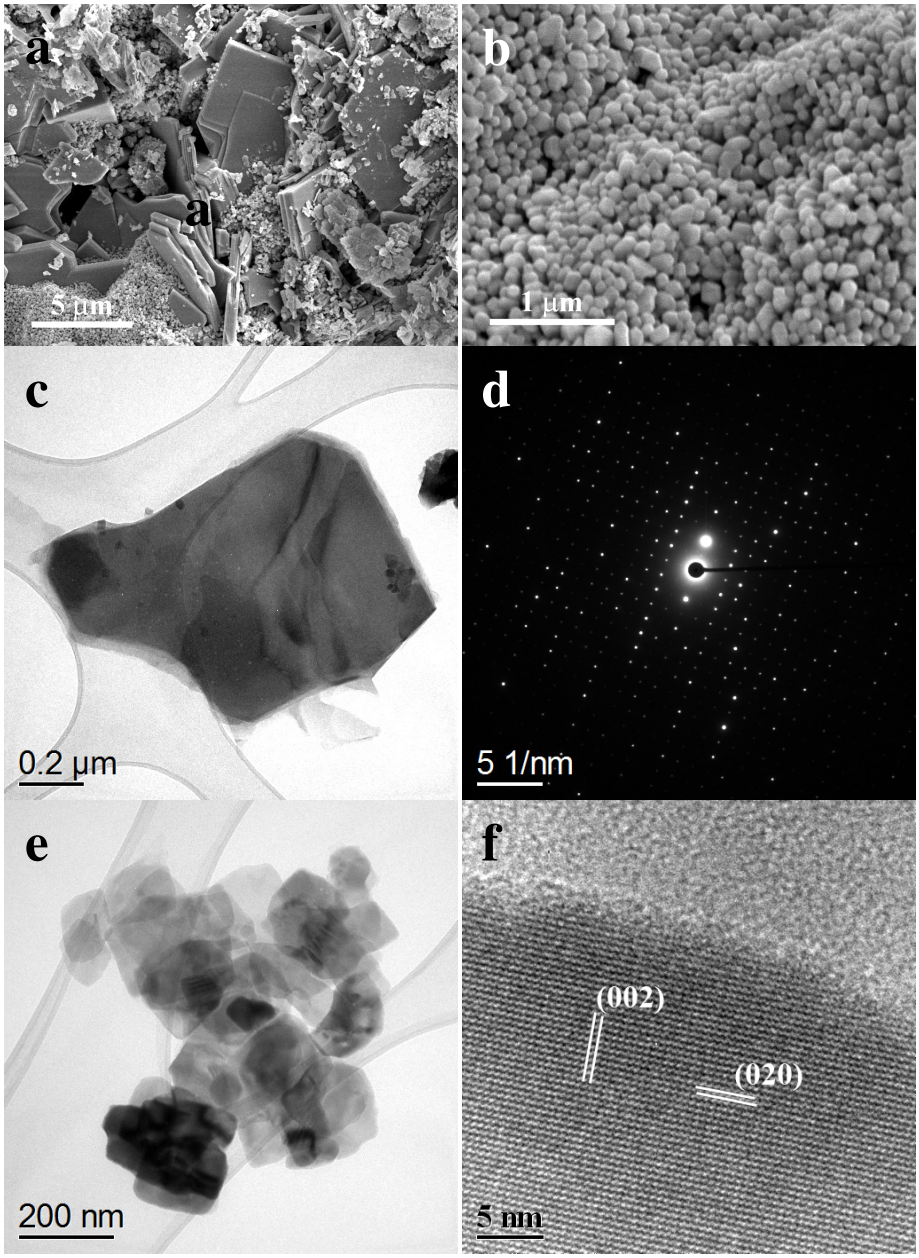

Figure 6.10 SEM micrographs of NbP-3E showing two different morphologies: (a) stacked agglomerates of oblong platelets, and (b) agglomerates of much smaller irregular and rounded particles; (c) BF-TEM micrograph of an oblong platelet in the NbP-3E material and (d) its corresponding SADP which matches well to the [100] projection of $Nb_{1.91}P_{2.82}O_{12}$; (e) BF-TEM and (f) HR-TEM micrographs of the smaller particles. The latter image (f) shows (002) and (020) lattice planes intersecting at 90° consistent with the [100] projection of orthorhombic $Nb_{1.91}P_{2.82}O_{12}$.

6.5 Correlations of catalytic performance and microstructure of Nb-P-O catalysts for the ODH of ethane to ethylene

As noted in Figure 6.6 the catalytic performance of all the NbP catalysts were significantly better than those of the niobium oxide catalysts, and hence all of the niobium phosphate phases identified in this study are potentially active for the ODH of ethane to ethylene. The best catalytic performance was exhibited by sample NbP-3, which implies that the $Nb_{1.91}P_{2.82}O_{12}$ crystalline phase is the most effective bulk structure for ethane selective oxidation by a niobium phosphate catalyst.

Niobium has been reported as an important component of some of the best ethane ODH catalysts, and it is often present with other essential components. In the present work it has been demonstrated that pure Nb_2O_5 can activate ethane and oxidize it to ethylene when relatively low space velocities and higher reaction temperatures were employed, but the selectivity to ethylene was relatively low. Ethane activation is not due to a homogeneous gas phase process as the conversion values determined from the blank experiments under the same conditions were negligible. Nb_2O_5 is not an oxide that is particularly reducible, since the reduction of Nb_2O_5 with hydrogen can only be initiated around 800 ºC.[35] However, catalyst reducibility may be expected to be important for this reaction, as the ODH of ethane to ethylene proceeds mainly by a redox mechanism utilising lattice oxygen.[2,15] As in other studies, it has been observed that the addition of another component, in this case phosphorus, to the niobium oxide significantly enhances the catalyst performance. The explanation for the beneficial effect of phosphorous in this reaction is not straightforward. The addition of phosphorus modifies the catalyst structure, as clearly evidenced by our electron microscopy and XRD studies, but it also modifies

the acidic and redox characteristics of the niobium oxide. For example, niobium (V) oxides have an acid strength, H_0 value of $\leq$ -5.6, whereas niobium phosphate has a higher acid strength (H_0 up to -8.2).[16] The increased acidity of the phosphates could potentially have an important influence on catalytic performance. For example, the acidity of the support used to produce supported vanadium oxide catalysts is an important factor for the selective oxidation of ethane to ethylene. Indeed, increasing the acidity of the support has previously been found to be beneficial for ethylene formation.[15] It should be noted however that electron microscopy techniques are not able to identify the acidic and redox characteristics of the catalyst materials. In this study our best efforts have been made to explain the structure-performance relationships present in the Nb-P-O catalyst system for the oxidative dehydrogenation of ethane ethylene through variation in crystal structures and morphologies. Further investigations and comments concerning the acidic and redox characteristics of Nb-P-O materials will be described in the section 6.7.

In order to investigate the surface composition of the catalysts, samples NbP-1, NbP-2 and NbP-3 were also analysed using XPS. Figure 6.11 shows the Nb(3d) spectra observed for these catalysts, both fresh and after use for ethane ODH. The O(1s) and P(2p) spectra did not show any significant differences and hence are not presented. Quantified data, namely the P/Nb and O/(P+Nb) surface atom ratios, are compared with the bulk values obtained from XRD/TEM analysis in Table 6.4. The Nb(3d) spectra are complex, and we see evidence for at least three different spectral components across the dataset. Moreover, and in contrast to the XRD and TEM results, the XPS spectra show changes after ethane ODH, especially for sample NbP-2. Interestingly, the Nb(3d) spectrum from used NbP-2E is almost identical to that from used NbP-1E, although the

spectra from the corresponding fresh materials (Fig. 6.11) are quite different. If we consider the Nb($3d_{5/2}$) spectrum from fresh NbP-1, it is tempting to assign the two equally intense and overlapping components to Nb^{5+} and Nb^{4+} species, although the magnitude of the binding energies (208.6 eV and 207.5 eV respectively) are approximately 1 eV higher than expected for the corresponding species in simple Nb oxides.[17,18] This effect has also been observed in phosphorous containing $Sn_xNbTiP_3O_{12}$ compounds[19] and ascribed to the presence of highly ionic Nb^{x+} species, although final state effects cannot be excluded. After use, the relative concentration of Nb^{5+} in the NbP-1 catalyst increases somewhat.

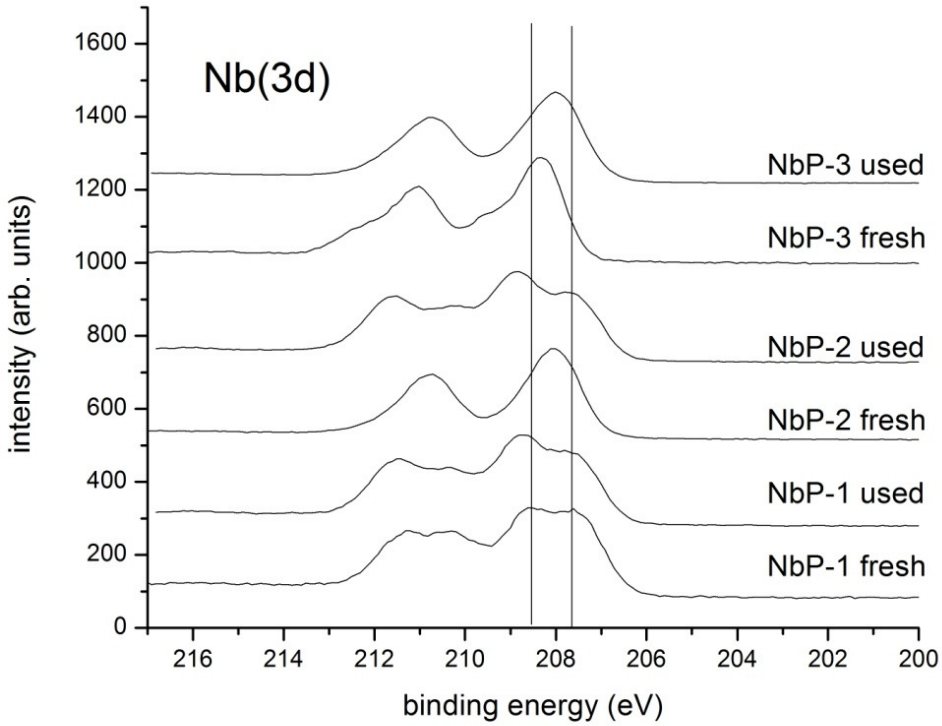

Figure 6.11 Nb(3d) X-ray photoelectron spectra for the catalysts NbP-1, NbP-2 and NbP-3, both before and after use for ethane ODH.

Table 6.4 Surface atom P/Nb and O/(P+Nb) ratios derived from XPS measurements compared with the corresponding bulk ratios based on the phases identified by XRD and TEM.

Catalyst	Surface atom ratios		Bulk elemental ratios	
	P/Nb	O/(P+Nb)	P/Nb	O/(P+Nb)
NbP-1 fresh	1.6	2.7	2.0	2.5
NbP-1E used	1.7	2.8		
NbP-2 fresh	1.3	2.6	1.0	2.0
NbP-2E used	1.6	2.8		
NbP-3 fresh	2.5	3.0	1.5	2.5
NbP-3E used	1.5	3.0		

The surface P/Nb molar ratios for the fresh NbP-1 and NbP-2 catalysts agree reasonably well with the expected bulk stoichiometries (Table 6.3); after use for ethane ODH, the NbP-2E sample exhibits a small increase in P content. For the NbP-3 material, however, we observe a major enrichment in phosphorous on the surface of the fresh catalyst (prepared by hydrogen reduction of NbP-2), which decreases after use to a level more typical of the other two catalysts, NbP-1 and NbP-2, and in very good agreement with the bulk composition. The change in surface ratio is most likely related to the change of the catalyst structure and morphology during use. As discussed previously the fresh catalyst had two plate-like morphologies of partially transformed tetragonal $NbOPO_4$ and a $Nb_{1.91}P_{2.82}O_{12}$ phase. However, after use the $NbOPO_4$ component was transformed completely to agglomerates of small particles of $Nb_{1.91}P_{2.82}O_{12}$.

Since we are unable to analyze the catalysts by XPS under reaction conditions, comparing the used materials might be expected to provide a better correlation with catalytic behavior. The most selective catalyst (NbP-3) exhibits only a single Nb($3d_{5/2}$) component, in contrast to the very similar Nb(3d) spectra for NbP-1 and NbP-2, where two clear Nb species are observed.

It is not possible to directly reconcile some of the features observed by XPS with structural data obtained from electron microscopy and XRD. This is not surprising since XPS is a highly surface sensitive technique, while electron microscopy and XRD are techniques probing bulk structure. The different surface states of Nb identified from XPS could be associated with the metal in different oxidation states. Niobium does not exist in both the 4+ and 5+ oxidation states in the bulk phosphate-phases, and hence there could be very thin regions confined to the surface layers of the catalysts that differ in structure from the bulk phases. This could be partially supported by the HR-TEM micrograph shown in Figure 6.10(f) in which a ~2 nm thick amorphous overlayer was observed on the surface of the used NbP-3E catalyst, which could possibly constitue the active surface layer. It should be noted however that some fraction of the amorphous overlayer could also be caused by electron beam damage artifacts, since the Nb-P-O materials are not stable under the electron beam.

6.6 Niobium phosphate materials for catalyzing the selective oxidation of methanol to formaldehyde

From sections 6.4 and 6.5 detailing the ethane ODH, it has been shown that niobium phosphate catalysts have a high selectivity to ethylene formation. In this section, attempts will be made to evaluate the catalytic performance of niobium phosphate catalysts in the selective oxidation of methanol to formaldehyde (eqn. 6.2) and compare it with that of the industrial iron molybdate catalyst. The aim of this work is to examine whether or not Nb-P-O materials can selectively generate formaldehyde while still maintaining a high conversion rate. In addition, comments on the acidic and redox

characteristics of the Nb-P-O materials can be made based on the results from the methanol oxidation experiments.

All the Nb-P-O samples studied here are labeled as shown in Table 6.1. The catalytic testing shows that the catalyst denoted as NbP-1M has the highest activity of all the niobium phosphate catalysts tested, with 90% conversion at 300^{o}C (Fig. 6.13(a), NbP-1M) which rivals the performance of the industrial iron molybdate catalysts (Fig. 6.12). However due to its high activity, the selectivity to formaldehyde is only 26% at 300 ^{o}C (Fig. 6.13(b), NbP-1M). The only by-product produced during the reaction is CO_2 with a high selectivity of 74% at 300^{o}C.

The NbP-2M catalyst shows an intermediate activity when compared with other niobium phosphate catalysts tested. At 500^{o}C, a 72% conversion was reached (Fig. 6.13(a), NbP-2M). Comparing NbP-2M with the industrial iron molybdate catalyst, at 300^{o}C where iron molybdate produces almost 100% methanol conversion (Fig. 6.12), NbP-2M has a much lower activity, with only 11% conversion (Fig. 6.13(a), NbP-2M). In terms of selectivity at 300^{o}C, iron molybdate has a very high formaldehyde selectivity of 95% (Fig. 6.12), while the NbP-2M catalyst produces a relatively lower formaldehyde selectivity of 75%, which is to be expected when the conversion level is so low (Fig. 6.13(b), NbP-2M). Along with formaldehyde, dimethyl ether (DME), CO and CO_2 are formed using the NbP-2M catalyst, with around 26% selectivity to DME at 300 ^{o}C (Fig. 6.13(b), NbP-2M).

The NbP-3M catalyst shows a similar activity when compared with NbP-2M, with 70% conversion reached at 500^{o}C (Fig. 6.13(a), NbP-3M). At 300^{o}C, a 20% conversion level is reached with 75% selectivity to formaldehyde, which, in common with NbP-2M,

is a relatively low activity compared to the near 100% conversion shown by iron molybdate at this temperature (Fig. 6.12 and Fig. 6.13(a), NbP-3M). As well as formaldehyde, other oxidation products produced over NbP-3M during the reaction are, DME, CO, and CO_2. At higher temperatures, a substantial amount of DME is produced with ~40% selectivity 400 ^{o}C. At 400 ^{o}C, the order of the formaldehyde yield for the niobium phosphate catalysts is:

NbP-2M > NbP-3M > NbP-1M.

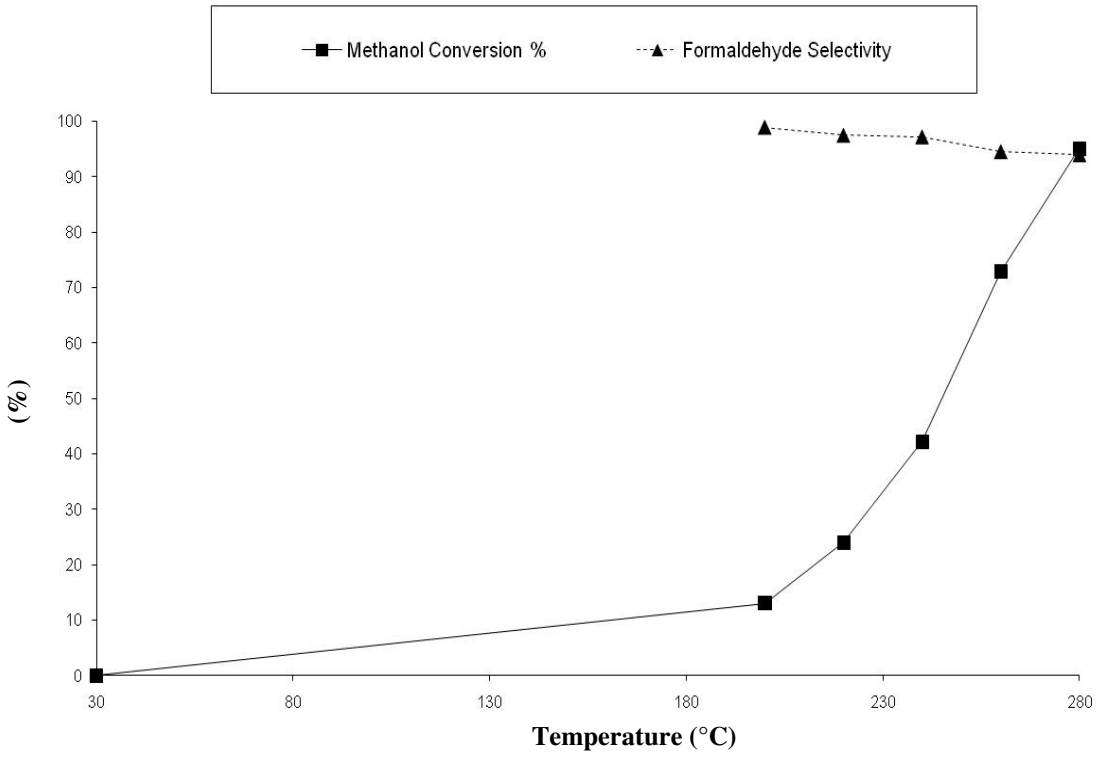

Figure 6.12 Methanol oxidation on an industrial iron molybdate catalyst showing methanol conversion and formaldehyde selectivity at different temperatures.

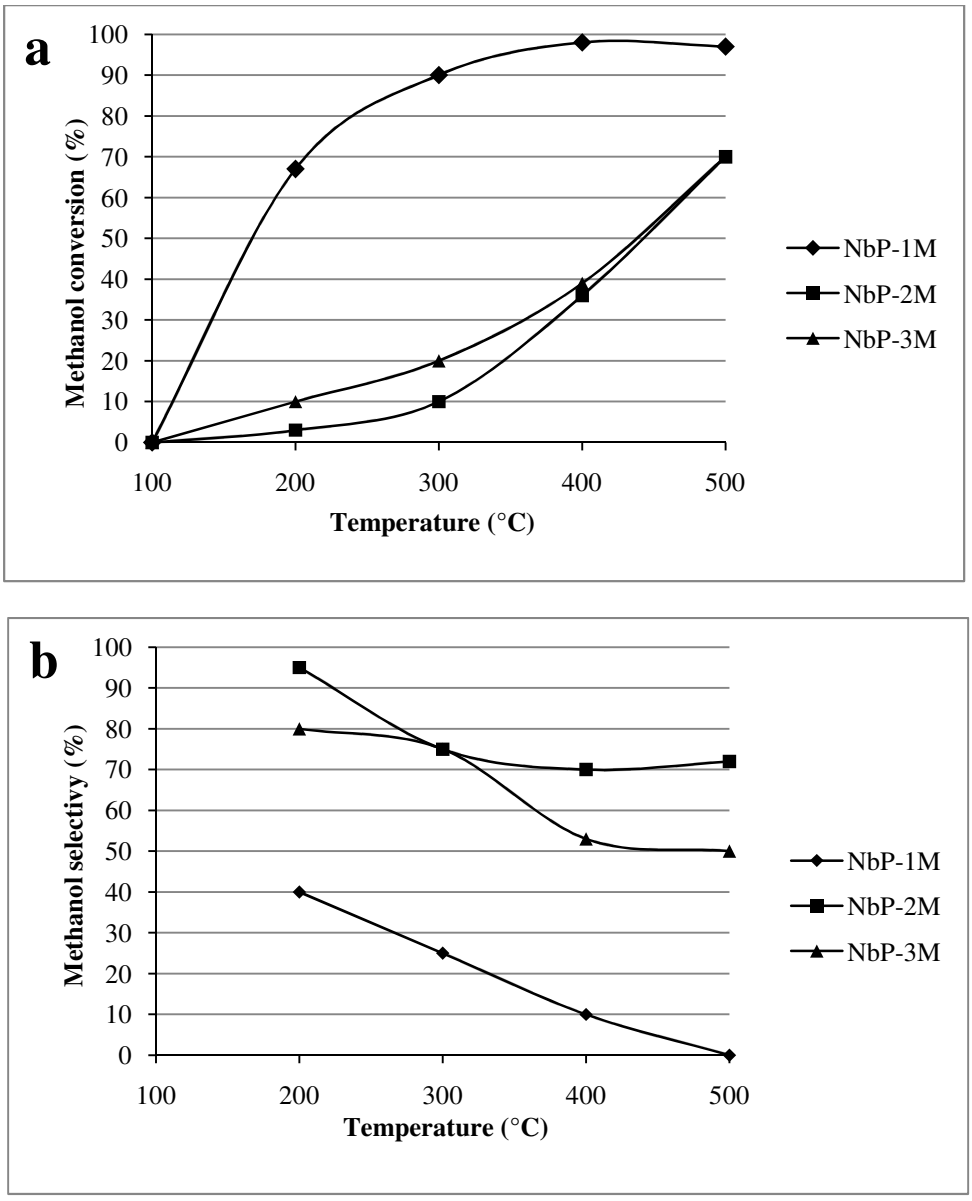

Figure 6.13 (a) Conversion of methanol over niobium phosphate catalysts prepared via three different methods, and (b) formaldehyde selectivity from methanol oxidation over niobium phosphate catalysts prepared using different methods. (Symbols: ◆ NbP-1M; ■ NbP-2M; ▲ NbP-3M.)

In order to further understand the structure-performance relationships of Nb-P-O catalysts for the selective oxidation of methanol to formaldehyde, detailed structural characterization studies using a combination of techniques have been carried out on the Nb-P-O materials after use in the methanol oxidation. XRD analysis suggested that there

is no structural change in the NbP-1M catalyst compared with fresh NbP-1 material, implying that the cubic $Nb_2P_4O_{15}$ phase is retained. SEM micrographs of NbP-1M after use are shown in Figure 6.14. Some evidence of particle sintering and a reduction in the overall degree of porosity were observed, which is similar to the morphology noted in Figure 6.1 for NbP-1E. The porous structure was retained after use, indicating that the cubic $Nb_2P_4O_{15}$ phase is relatively robust during the chemical reaction.

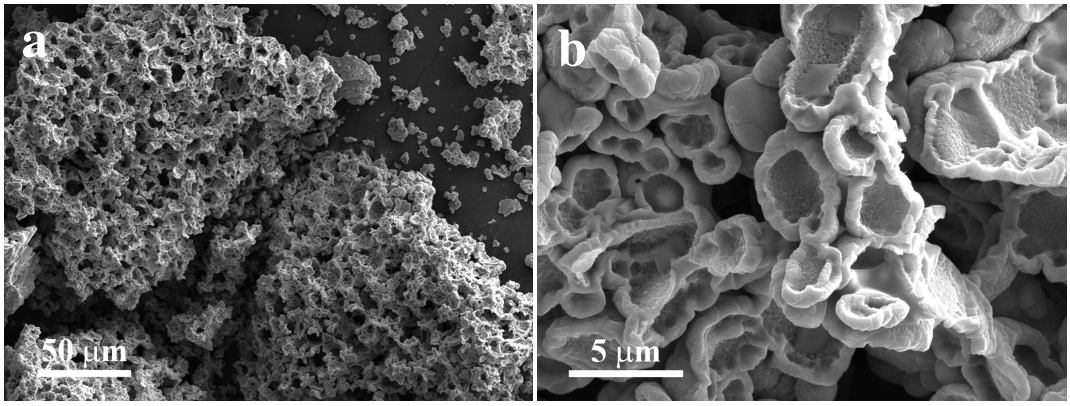

Figure 6.14 SEM micrographs of the NbP-1M material showing (a) micro-porous structure and (b) sintered particles.

The NbP-2M material, which was the best catalyst among all three Nb-P-O catalysts for methanol oxidation, shows a plate-like morphology composed of stacks of thin angular platelets with thicknesses ranging 10 - 20 nm and lateral dimensions of 0.2 - 2 μm as shown in Figure 6.15(a)(b). An SADP taken normal to one of the angular platelets confirms that it is the tetragonal $NbOPO_4$ phase viewed along the [001] projection (Fig. 6.15(d)), which agrees with the XRD data. Bend contours and moiré fringes are also observed in the BF-TEM micrograph, the latter of which indicates that they are composed of distorted and slightly misoriented stacks of thin angular $NbOPO_4$ platelets (Fig. 6.15(c)). In contrast to the NbP-2E sample which retained its morphology and structure after the ethane oxidative dehydrogenation reaction, the fused agglomerates

found in unused NbP-2 material had apparently transformed into larger angular platelets in the NbP-2M catalyst after methanol oxidation. These angular $NbOPO_4$ platelets in NbP-2M are not as beam sensitive as the other Nb-P-O materials described so far which gave us the opportunity to apply more advanced electron microscopy techniques (*i.e.*, HR-TEM and HAADF-STEM) on them using our state-of-the-art aberration corrected JEOL 2200FS (S)TEM.

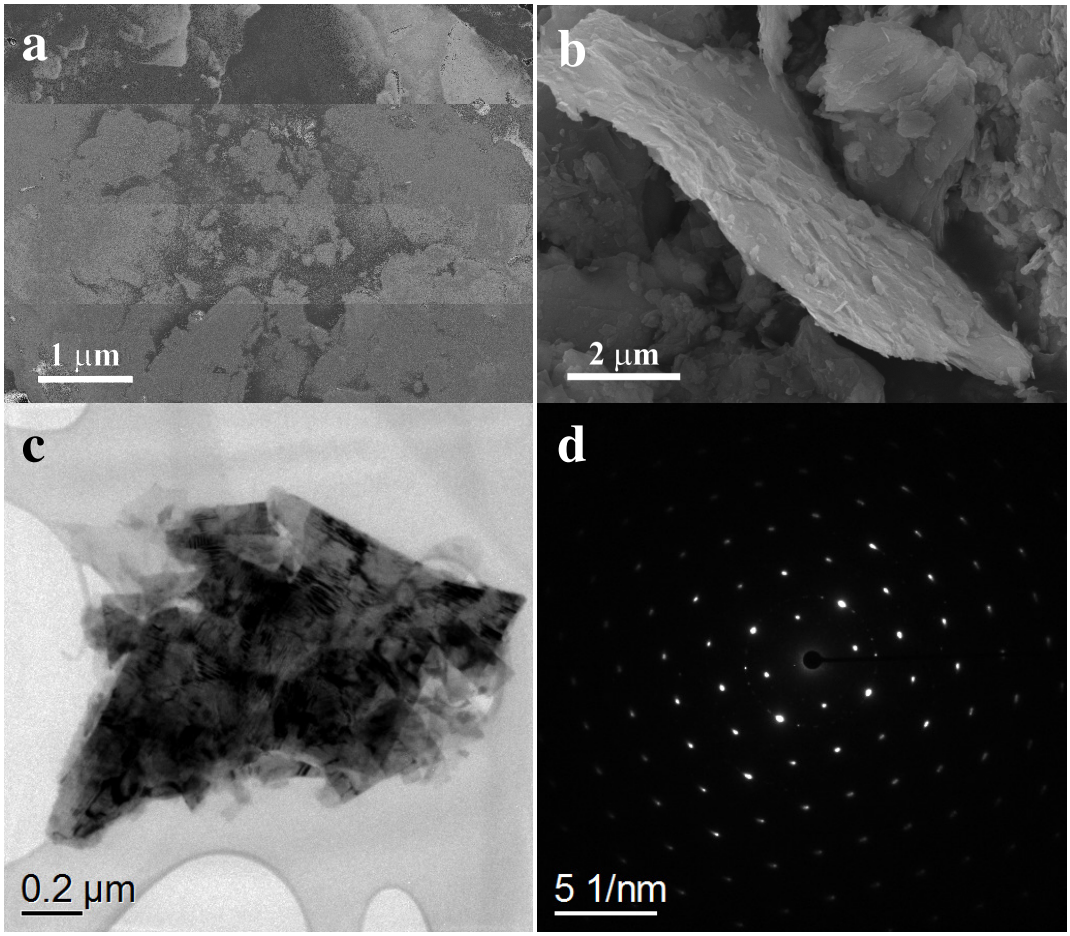

Figure 6.15 (a, b) SEM micrographs of the NbP-2M materials showing (a) stacks of angular platelets (b) with a platelet thickness of 10 - 20 nm; (c) BF-TEM micrograph of the NbP-2M material showing angular platelets with moiré fringes and bend contours and (d) the corresponding SADP taken from the platelet normal which matches to the [001] projection of tetragonal $NbOPO_4$.

Figure 6.16 (a) and (b) respectively shows HR-TEM and HAADF-STEM micrographs of a typical angular platelet in NbP-2M. Both the (110) and (200) planes with spacings of 4.53 Å and 3.20 Å and an interplanar angle of 90° can be resolved. This is consistent with the tetragonal $NbOPO_4$ phase identified from XRD and SAED analysis. The termination facets of the platelet are the {100}-type planes as observed in both HR-TEM and HAADF-STEM micrographs (Fig. 6.16(a)(b)). There is an amorphous overlayer observed on the edge (Fig. 6.16(b)) which could be attributable to the possible active surface layer and/or the beam damage artefacts. The higher magnification [001] projection of the platelet using the HAADF-STEM technique (Fig. 6.16(c)) shows an alternating bright/faint intensity of neighboring atomic columns. The brighter atomic columns have a nearest lateral spacing of ~ 4.53 Å. When compared with the model tetragonal $NbOPO_4$ structure along the [001] direction (Fig. 6.16(c), top right), it is clear that these brighter atomic columns should correspond to the Nb (Z = 41) columns, while the fainter atomic columns may correspond to P (Z = 14) columns. In this image, the intensity of O atoms are below the detection limit. In order to justify this interpretation, a detailed analysis of the HAADF-STEM micrograph (Fig. 6.16(c)(d1)(d2)) has been performed. If a line intensity profile is drawn along the 1-1' direction, a weak intensity bump is observed midways between the two intense Nb peaks. When another line profile is drawn along the 2-2' direction, such a weak intensity feature is absent. This implies that some lighter elements are detected between two Nb columns along the 1-1' direction using HAADF imaging. Considering the spacing between the smaller peaks (~ 4.53 Å) and the spacing between the weak peak and its closest Nb column (~ 3.20 Å), and comparing the image with the inset crystal model in Figure 6.16(c), we can further

conclude that P (Z = 14) atomic columns in the $NbOPO_4$ [001] projection are detectable using HAADF-STEM. Since only one weak peak is observed between two intense Nb peaks, this indicates that O columns are not really detectable in this experiment. In order to confirm this argument, an [001] $NbOPO_4$ HAADF-STEM image simulation has been carried out using the xHREM simulation suite (v3.5, HREM research inc.) as shown in Figure 6.17. According to the experimental conditions employed, the key input parameters of the HAADF-STEM simulation are as follows:-

Accelerating voltage: 200 kV,

Condenser lens aperture radius: 25 mrad,

Third order C_s: 0.001 mm,

Defocus: 0 Å,

Fifth order C_s: 3.2 mm,

Dark field detector inner radius: 110 mrad,

Dark field detector outer radius: 300 mrad.

A pair of two $NbOPO_4$ models was loaded for simulation using the identical parameters as noted above: (i) the [001] projection of $NbOPO_4$ and (ii) the [001] projection of $NbOPO_4$ only without P atoms included in the structure. Figure 6.17(a) is the simulated HAADF-STEM images of the [001] projection of $NbOPO_4$ which is in good agreement with the experimental image showing periodic brighter atomic columns (Nb) and weaker intervening P atomic columns. If a line intensity profile is drawn along the 3-3' direction, the simulated image intensity profile also matches reasonably well with the experimental intensity profile along the 1-1' direction in Figure 6.16(c). The intensity ratio between Nb atomic column and P atomic columns in the simulated image

(Nb/P ≈ 8.23) is not far from the ratio obtained from the experimental image (Nb/P ≈ 12.0). It is well known that the intensity ratio in HAADF-STEM images is dependent upon many parameters, such as the sample thickness and defocus values, which could cause the small difference in the Nb/P intensity ratio from that predicted by image simulations.[20,21] In addition, the P atoms in the Nb-P-O could be sublimated during exposure to the electron beam, which may result in a higher Nb/P ratio in the experimental image.[22] Hence the simulated Nb/P intensity ratio (Fig. 6.17(b)) shows a reasonable agreement with the experimental Nb/P intensity ratio taken from Figure 6.16(d1). In order to rule out the possibility that the electron probe tail might give rise to these intensity artifacts which may look like P atomic columns in the structure (Fig. 6.16(a)), in Figure 6.17(c) a HAADF-STEM image of $NbOPO_4$ structure only without the P atoms was simulated using the same parameters as these used for generating Fig. 6.16(a). It shows only the brighter atomic columns (Fig. 6.17(c)), which correspond to the Nb columns. When a line intensity profile is drawn along the 4-4' direction, the small intensity peaks noted in Figure 6.16(b) disappear, which confirms that these weak peaks observed in the experimental HAADF image are not an imaging artifact of the probe shape but a real structural feature. By combining the above experimental images and simulated results we can confidently conclude that P atomic columns can be detected in the [001] projection of $NbOPO_4$ which represents the first report of imaging P atomic columns in Nb-P-O materials.

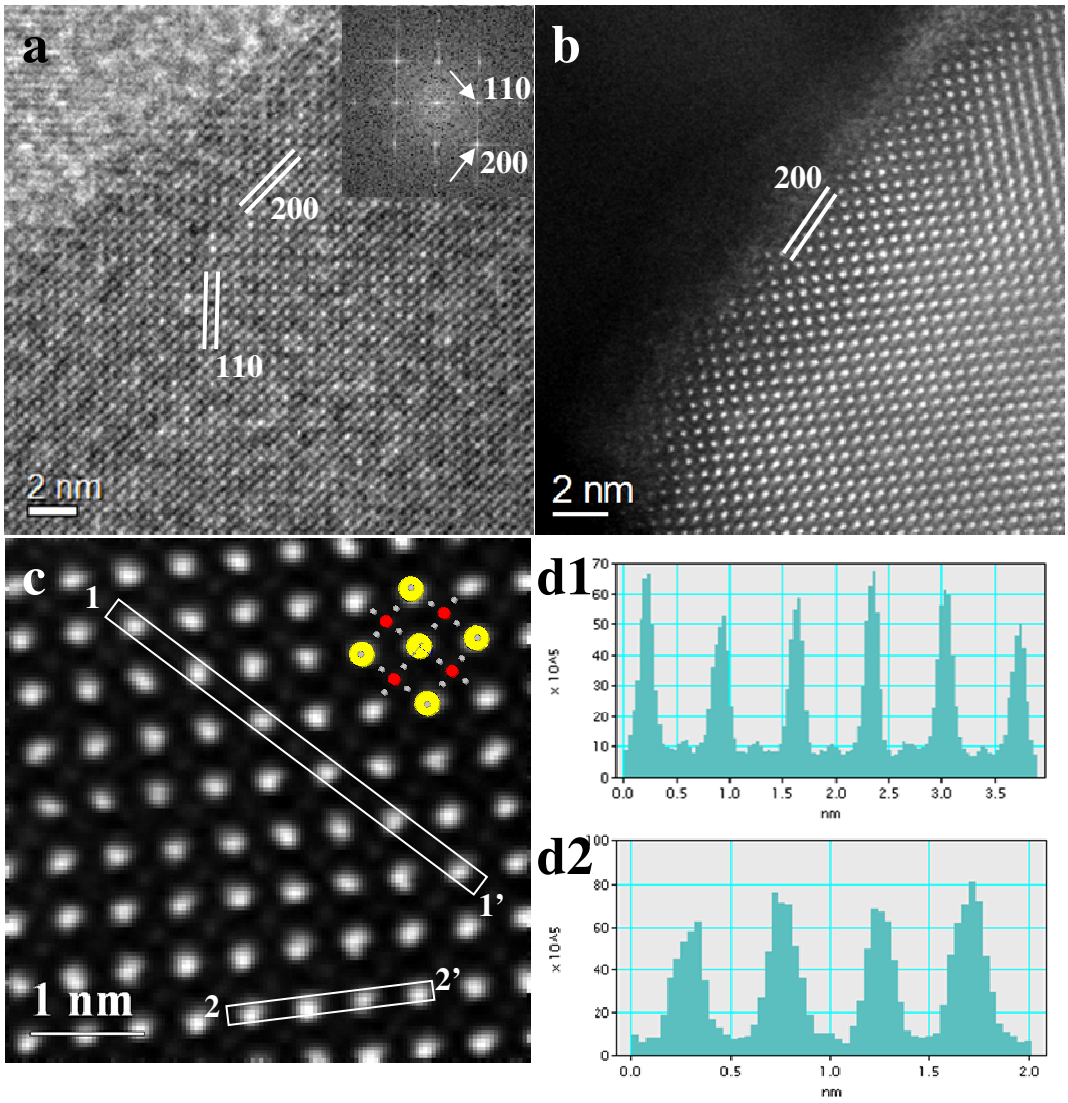

Figure 6.16 (a) HR-TEM and (b) HAADF-STEM (low pass filtered) micrographs of NbP-2M showing (110) and (200) planes in the [001] projection of tetragonal $NbOPO_4$; (c) a higher magnification HAADF-STEM image showing periodic brighter Nb atomic columns and fainter P atomic columns (top right, yellow spheres respresent Nb atoms, red spheres represent P atoms and grey spheres represent O atoms); (d1, d2) the line intensity profiles taken along 1-1' and 2-2' (The measured peak intensity ratio determined by ImageJ between Nb and P along 1-1' direction is ~ 12).

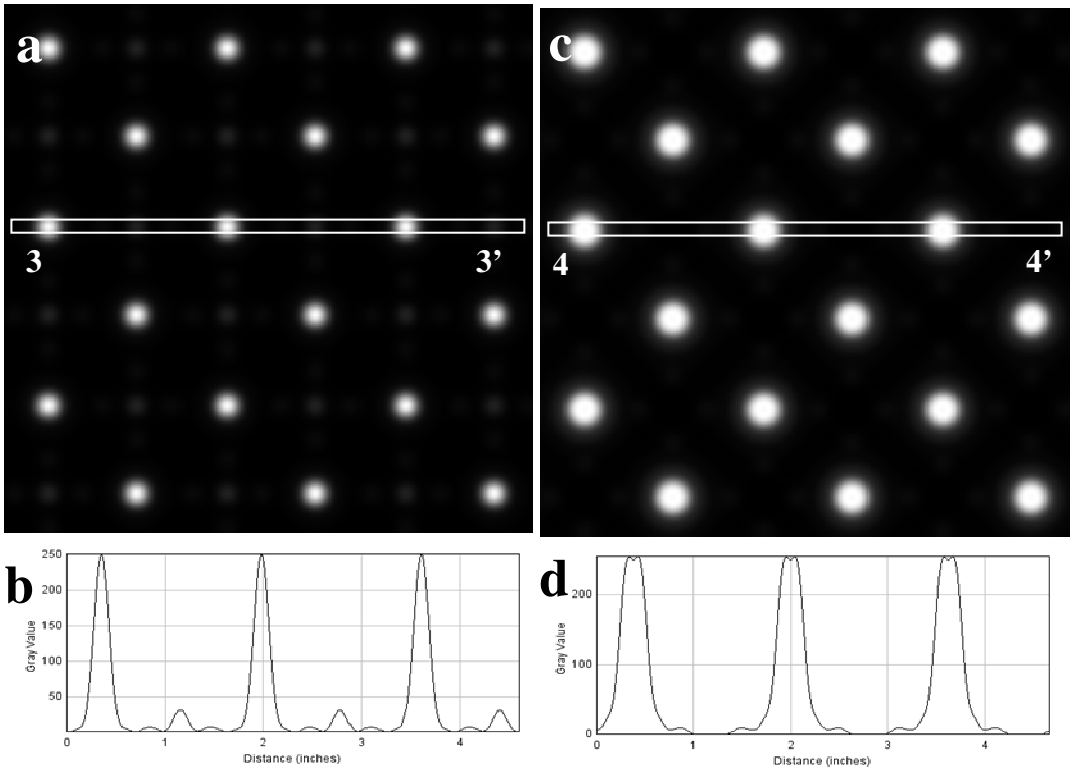

Figure 6.17 Simulated HAADF-STEM images of (a) the [001] projection of tetragonal $NbOPO_4$ (10 unit cells in c axis, 0 nm defocus, 200 kV) and (c) the [001] projection of tetragonal $NbOPO_4$ without P atoms included (10 unit cells in c axis, 0 nm defocus, 200 kV); Line intensity profile taken from (b) 3-3' showing Nb/ P intensity ratio at 255/ 31 ≈ 8.23 and (d) 4-4' showing no weak intensity bumps between the two intense Nb peaks (Line intensity profile was obtained using ImageJ (v1.44p) software).

In direct contrast to the NbP-2M material, the hydrogen reduced NbP-3M sample exhibited two distinct morphologies after methanol oxidation (Fig. 6.18(a)(b)). This is a similar result to which was found for the NbP-3E catalyst in the ODH of ethane to ethylene. The major morphology observed in the NbP-3 sample is composed of large oblong platelets (Fig. 6.18(a)), which has a lateral dimension of 5-10 μm. The agglomerates of irregular platelets present in the NbP-3 sample are no longer present in the catalyst after the reaction. Instead they have transformed into agglomerates of much smaller (100 - 200 nm) particles (Fig. 6.18(b)).

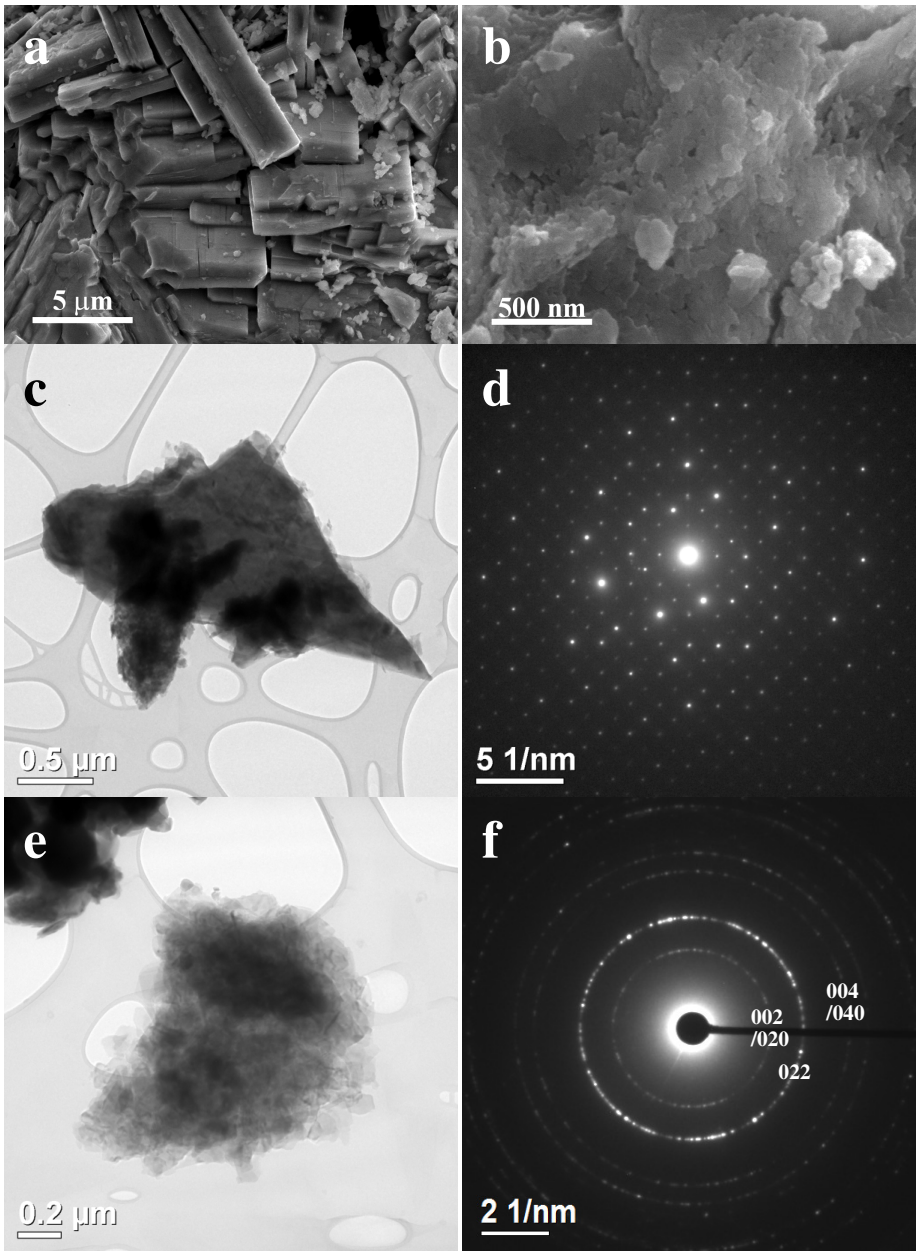

Figure 6.18 SEM micrographs of NbP-3M showing two different morphologies: (a) stacked agglomerates of oblong platelets, and (b) agglomerates of much smaller irregular particles; (c) BF-TEM micrograph of a fragment of an oblong platelet in the NbP-3M material and (d) its corresponding SADP which matches well to the [100] projection of $Nb_{1.91}P_{2.82}O_{12}$; (e) BF-TEM micrograph of an agglomerate of smaller particles and (f) the corresponding SAED ring pattern of the agglomerate in (e) which can also be assigned to $Nb_{1.91}P_{2.82}O_{12}$ with typical (002)/(020), (022) and (004)/(040) planes labeled.

BF imaging and electron diffraction analysis of the oblong platelets (Figs. 6.18(c)(d)) confirmed that they retained the $Nb_{1.91}P_{2.82}O_{12}$ crystalline structure as found in the unused NbP-3 material. It was also possible to determine the crystal structure of the smaller particles (Figs. 6.18(e)(f)) using the SAED technique. A polycrystalline ring pattern can be formed by selecting a large number of particles using a larger SAED aperture. Since the orthorhombic $Nb_{1.91}P_{2.82}O_{12}$ phase has similar lattice parameters in the [100] projection with b = 8.6848 Å and c = 8.7452 Å, in the SAED ring pattern both (002) and (020) rings tend to appear as one single ring. As shown in Figure 6.17(f), SAED ring patterns obtained from an agglomerate of smaller particles exhibits typical (002)/(020), (022) and (004)/(040) planes of orthorhombic $Nb_{1.91}P_{2.82}O_{12}$ phase, which indicates that the smaller crystals have the same structure as the larger oblong platelets.

6.7 Correlations of structure and catalytic performance for the Nb-P-O catalysts

We have demonstrated that all of the niobium phosphate phases are potentially active for the selective oxidation of methanol to formaldehyde. The best catalytic performance at 400 °C was exhibited by sample NbP-2M, followed by NbP-3M and then NbP-1M. This sequence of catalytic performance is different from the trend observed in the ODH of ethane to ethylene, in which the $Nb_{1.91}P_{2.82}O_{12}$ crystalline phase is the most effective catalyst. In the present case, the $NbOPO_4$ phase appears to be a more desirable structure for the selective oxidation of methanol to formaldehyde.

The catalytic activity of Nb-P-O catalysts can be understood using the selective oxidation of methanol as a model reaction. The reaction products from methanol oxidation are related to the acidity/basicity and redox properties of the catalyst. In

particular, the formation of formaldehyde can be related to redox behavior, whereas the formation of dimethyl ether (DME) can be related to acid character.[40] Data for the oxidation of methanol over the three niobium phosphate catalysts at 50% conversion rate are shown in Table 6.5. The distribution of products obtained at iso-methanol conversion was different for the NbP-1, NbP-2 and NbP-3 catalysts. The NbP-1 catalyst is found to have an intermediate selectivity towards formaldehyde (68%) with no selectivity for dimethyl ether (0%). These results indicate that the NbP-1 catalyst activity was dominated by redox sites on the catalyst. The NbP-2 catalyst shows a high formaldehyde selectivity (75%) with some selectivity towards dimethyl ether (25%), which indicates that the NbP-2 has strong redox characteristics, with some acid character. In contrast, the NbP-3 catalyst exhibits the lowest formaldehyde selectivity (52%) with the highest dimethyl ether selectivity (38%), which not only implies that NbP-3 has appreciable redox behavior, but that it also has a greater degree of acid character.

In consideration of the catalyst testing results in the ODH of ethane to ethylene, the NbP-1 catalyst is found to have the lowest selectivity for ethylene (78%). The NbP-2 catalyst shows an intermediate ethylene selectivity at 85%. The NbP-3 catalyst, as the most selective ethane oxidation catalyst, exhibits a high ethylene selectivity at 95%. The above results indicate that the catalyst efficiency for both the ODH of ethane and the methanol oxidation are determined by a combined balancing effect of catalyst redox behavior and acid character. The NbP-1 material, which only has limited redox ability, is an inefficient catalyst for both chemical reactions. As found in many selective oxidation reactions, the redox ability is important for ethane oxidation,[1,15] and the increased catalyst acidity is important for achieving the ethylene selectivity.[15] Therefore the NbP-3

catalyst has both of these properties to a certain extent, which gives rise to the high ethylene selectivity and the promising catalytic performance observed. In contrast the NbP-1 has a negligible acid character, which imparts on it the lowest ethylene selectivity. The oxidation of methanol, on the other hand, mainly depends on the redox characteristics of the catalyst.[23] The NbP-2 material with its greater redox ability can give rise to a high selectivity to formaldehyde.

Table 6.5 Product distribution at iso-conversion for methanol oxidation over the series of niobium phosphate catalysts.

Catalyst	Conversion/%	Selectivity/%			
		H_2CO	CH_3OCH_3	CO	CO_2
NbP-1	50	68	0	0	32
NbP-2	50	75	25	0	0
NbP-3	50	52	38	5	5

Electron microscopy was able to reveal the morphological and structural transformations of these three Nb-P-O catalysts in both the ethane ODH at 500°C and the methanol oxidation at 400 °C. In the ODH reaction, the porous NbP-1 catalyst (cubic $Nb_2P_4O_{15}$) transformed into the porous NbP-1catalyst (still cubic $Nb_2P_4O_{15}$) with a more sintered morphology. The layer-type NbP-2 composed of small particles (tetragonal $NbOPO_4$) maintained its morphology and structure after reaction, generating a layer-type NbP-2E containing small particles in each layer (still tetragonal $NbOPO_4$). After reduction in H_2 at 500 °C, the layer-type NbP-2 (tetragonal $NbOPO_4$) was reduced to a mixture of two materials in NbP-3, namely (i) oblong $Nb_{1.91}P_{2.82}O_{12}$ platelets and (ii) "partially transformed" irregularly shaped $NbOPO_4$ platelets. After the ODH reaction, this mixture of Nb-P-O materials were transformed into the same orthorhombic $Nb_{1.91}P_{2.82}O_{12}$ phase with two different morphologies (NbP-3E), *i.e.* (i) oblong

$Nb_{1.91}P_{2.82}O_{12}$ platelets and (ii) agglomerates of smaller irregular $Nb_{1.91}P_{2.82}O_{12}$ particles. The oblong $Nb_{1.91}P_{2.82}O_{12}$ platelets were found to persist after the reaction giving rise to the same morphological and structural material. These "partially transformed" irregularly shaped $NbOPO_4$ platelets, however, were reformed into the small $Nb_{1.91}P_{2.82}O_{12}$ particles.

In the oxidation of methanol to formaldehyde, analogous morphological and structural changes were observed in these Nb-P-O materials. The porous $Nb_2P_4O_{15}$ materials (cubic $Nb_2P_4O_{15}$) with some sintering features were retained in the NbP-1M catalyst, similar to that found in NbP-1E. Whereas the NbP-2M catalyst is composed of stacks of angular platelets, which is different from what has been observed in the unused NbP-2 and used NbP-2E materials. The tetragonal $NbOPO_4$ phase was maintained in this transformation. For the NbP-3M catalysts, similar changes as noted in the transformation from NbP-2 to NbP-2E were observed. The oblong $Nb_{1.91}P_{2.82}O_{12}$ platelets persisted, and the "partially transformed" irregularly shaped $NbOPO_4$ platelets were transformed into the small $Nb_{1.91}P_{2.82}O_{12}$ particles.

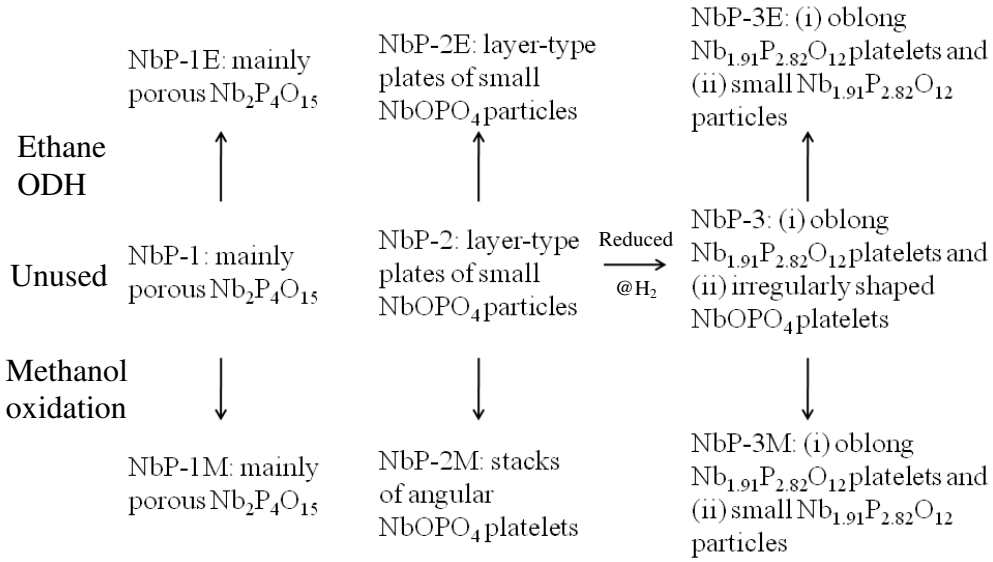

Figure 6.19 Schematic diagram of the morphological and structural changes observed in NbP-1, NbP-2 and NbP-3 catalysts before and after the reaction.

Figure 6.19 shows a schematic diagram concisely summarizing the morphological and structural changes observed in NbP-1, NbP-2 and NbP-3 catalysts before and after the reaction (*i.e.* the ethane ODH and the methanol oxidation, respectively).

6.8 Conclusions and suggestions for future work

In this chapter, we have shown that all three of the niobium phosphate phases generated are potentially good candidates for both the ODH of ethane to ethylene and the selective oxidation of methanol to formaldehyde. Sample NbP-3E was found to have the best catalytic performance for the ODH of ethane to ethylene, which indicates that the $Nb_{1.91}P_{2.82}O_{12}$ phase is the most effective bulk structure for this reaction amongst the niobium phosphate catalysts studied. On the other hand, sample NbP-2M was found to exhibit the best catalytic performance for the selective oxidation of methanol to formaldehyde, followed by NbP-3M and NbP-1M, which means that the $NbOPO_4$ phase is a more efficient structure for methanol oxidation. This difference in catalytic performance for either the ODH or the methanol oxidation can be explained by a stronger acidity exhibited by the NbP-3E catalyst (good for the ODH) and a higher redox ability inherent to the NbP-2M material (good for methanol oxidation). In addition, the morphological and structural modifications occurring during the preparation and the catalytic reactions have been investigated using electron microscopy, which were correlated with their catalytic performance.

It should be noted that the Nb-P-O catalysts described in this chapter were studied before and after catalytic reactions. To truly understand a complex oxide catalyst of this type, it is important to study (i) the phase transformations that occur during activation

under reaction conditions and (ii) to determine the active phase. Prior studies on related V-P-O materials show that the precursor material ($VOHPO_4 \cdot 0.5H_2O$) takes many tens of hours under reaction conditions to topotactically transform into the active phase {$(VO)_2P_2O_7$} via transitional structures (*e.g.,* δ-$VOPO_4$ & some disordered phases) under reaction conditions. Similarly the Nb-P-O catalyst might be expected to experience a comparable set of phase transformations and surface structure reconstructions during activation under reaction conditions.[24] *In-situ* XRD analysis would be very useful for determining the catalyst structure and polymorphs as a function of reaction time-on-line. However, such analysis is usually complicated by the co-existence of several crystalline polymorphs and possible amorphous phases. Electron diffraction patterns taken from individual micron-size crystallites in the TEM, however, can produce additional more spatially resolved crystallographic information. TEM could also be a valuable tool for clarifying some of the phase transformations that occur during Nb-P-O catalyst activation (especially for the NbP-2 catalyst) by examining a sequence of samples activated for different times-on-stream (*e.g.,* 0.1h, 8h, 24h and 40h).

It is also worth mentioning that the TEM analysis performed in this study is conventional TEM, or so-called *ex-situ* TEM. In the sample transfer step from the reactor to the microscope, the material would be exposed to air, which may introduce hydration or oxidation effects to the specimen. Furthermore oxide samples when electron irradiated in the TEM column, can undergo local heating in vacuum and knock-on damage which may induce reduction effects on these complex oxides. These hydration, oxidation and reduction effects may substantially change the material's microstructure, especially in the particle near-surface regions. An alternative TEM method that could be employed to

study such transformations would be anaerobic-transfer TEM [25,26]. First the Nb-P-O materials are placed on the grid on a specially designed holder (*e.g.* an HHST4004 environmental cell single tilt heating holder supplied by Gatan, Inc.). After being heated in a benchtop reactor under realistic reaction conditions (*e.g.* temperature and reaction gases) for a couple of hours, the grid with the partially activated Nb-P-O material is retracted into the protective cell, filled with an inert gas to avoid exposure of the materials to air and then retaining the Nb-P-O surface structure. Then the Nb-P-O catalysts can be transferred under anaerobic conditions into a conventional TEM for subsequent analysis. In addition the TEM instruments employed in this project are operating at 200 kV, which cause electron beam induced damage to the Nb-P-O materials. Since the JEOL JEM-ARM200F (which can operate in the 60 - 200 kV range) will be available at Lehigh University starting 2012, it is worth investigating these beam sensitive Nb-P-O materials at a lower voltage condition (*e.g.* 60 kV) in order to minimize beam damage effects.

Ideally we would like to utilize an *in-situ* environmental TEM to study these Nb-P-O catalysts 'real-time' under realistic reaction conditions [27]. An S/TEM fitted with an environmental cell (ECELL) system could in principle be used to perform real-time observations of bulk phase transformations and surface structure modifications of Nb-P-O materials under reaction conditions. However it should also be noted that in the ECELL, electrons may interact with reaction gas to produce a plasma, which is not an entirely realistic reaction atmosphere. Another point to consider is that a gas pressure of a few torr is required in the ECELL, which can cause incident electrons to be scattered by reactant gas molecules, effectively reducing the imaging resolution of the microscope.

It is known that most catalytic reactions occur at specific active sites on the catalyst surface. In order to understand the Nb-P-O catalyst behavior, it is important to thoroughly explore its surface structure and composition. A variety of additional techniques can be utilized to explore catalyst surface structure changes in the reaction.

An *in-situ* spectroscopy system can distinguish between different Nb-P-O phases on the surface by identifying different Nb=O bond vibrations in Raman spectra.[28] Active sites, reaction kinetics and reaction mechanism can also in principle be investigated [29]. A possible strategy for determining the reaction mechanism is as follows: by using transient isotopic $^{16}O_2$-$^{18}O_2$ switching experiments, the role of gaseous O_2 and lattice oxygen during the ODH of ethane to ethylene can be determined, which could correspond to Mars-van-Krevelen mechanism only if the lattice oxygen is incorporated into the products.

In-situ XPS would be another useful technique for investigating the surface composition under reaction conditions. By using three differential pumping stages, it is plausible to achieve a mbar pressure range in the sample cell while still being able to obtain XPS spectra with good signal-to-noise ratio. More details about the *in-situ* XPS system can be found in reference [30]. In V-P-O, the surface P/V ratio and V^{4+}/V^{5+} ratio are often considered as important factors to control for tuning the catalytic performance [31]. Extending this finding to Nb-P-O catalysts, the P/Nb ratio on the surface will be monitored, as well as the various oxidation states of Nb. By comparing these two ratio parameters in active catalysts to those in inactive catalysts, optimum values may be found, which could help in the design of even more active catalysts.

6.9 Acknowledgements

The Nb-P-O catalyst syntheses, XRD experiments, BET surface area measurement and catalyst testing on the ODH of ethane to ethylene were performed by Dr. Matthew Davies in Prof. Taylor's group at Cardiff University. The catalyst testing on the selective oxidation of methanol to formaldehyde was performed by Gareth Whiting in Prof. Taylor's group at Cardiff University. The catalyst design experiments were performed by Dr. Matthew Davies in Cardiff University and Dr. Benjamin Solsona in Universitat de Valencia. Their various contributions to this work are all gratefully acknowledged.

6.10 References

1. H. H. Kung, "Oxidative dehydrogenation of light (C2 to C4) alkanes," *Advances in Catalysis,* **40,** 1-38 (1994).

2. F. Cavani, N. Ballarini, and A. Cericola, "Oxidative dehydrogenation of ethane and propane: How far from commercial implementation?" *Catalysis Today,* **127,** 113-131 (2007).

3. C. J. Kiely, A. Burrows, S. Sajip, G. J. Hutchings, M. T. Sananes, A. Tuel, and J. C. Volta, "Characterisation of variations in vanadium phosphate catalyst microstructure with preparation route," *Journal of Catalysis,* **162,** 31-47 (1996).

4. G. J. Hutchings, "Vanadium phosphate: a new look at the active components of catalysts for the oxidation of butane to maleic anhydride," *Journal of Materials Chemistry,* **14,** 3385-3395 (2004).

5. N. Haddad, E. Bordes-Richard, and A. Barama, "MoO_x-based catalysts for the oxidative dehydrogenation (ODH) of ethane to ethylene: Influence of vanadium and phosphorus on physicochemical and catalytic properties," *Catalysis Today,* **142,** 215-219 (2009).

6. R. P. Singh, M. A. Bañares, and G. Deo, "Effect of phosphorous modifier on V_2O_5/TiO_2 catalyst: ODH of propane," *Journal of Catalysis,* **233,** 388-398 (2005).

7. I. Matsuura and N. Kimura, "Oxidation and ammoxidation of propane over tetragonal type $M^{5+}OPO_4$ catalysts," in *Studies in Surface Science and Catalysis*, V. Cortés Corberán and S. Vic Bellón, ed., 271-279 (Elsevier, 1994).

8. K. Tanabe, "Catalytic application of niobium compounds," *Catalysis Today,* **78,** 65-77 (2003).

9. M. Bohnet, Ullmann's encyclopedia of industrial chemistry (Wiley-VCH, 6th Edition, 2003).

10. A. R. Chauvel, P. R. Courty, R. Maux, and C. Petitpas, "Select best formaldehyde catalyst," *Hydrocarbon Processing,* **52,** 179-184 (1973).

11. J. J. McKetta and W. A. Cunningham, Encyclopedia of chemical processing and design (M. Dekker, 1976).

12. N. Pernicone, "MoO_3-$Fe_2(MoO_4)_3$ catalysts for methanol oxidation," *Journal of the Less Common Metals,* **36,** 289-297 (1974).

13. M. Badlani and I. Wachs, "Methanol: a "smart" chemical probe molecule," *Catalysis Letters,* **75,** 137-149 (2001).

14. N. K. Mal and M. Fujiwara, "Synthesis of hexagonal and cubic super-microporous niobium phosphates with anion exchange capacity and catalytic properties," *Chemical Communications,* 2702-2703 (2002).

15. T. Blasco and J. M. L. Nieto, "Oxidative dyhydrogenation of short chain alkanes on supported vanadium oxide catalysts," *Applied Catalysis A: General,* **157,** 117-142 (1997).

16. Q. Sun, A. Auroux, and J. Shen, "Surface acidity of niobium phosphate and steam reforming of dimethoxymethane over $CuZnO/Al_2O_3$-NbP complex catalysts," *Journal of Catalysis,* **244,** 1-9 (2006).

17. N. Alov, "Determination of the states of oxidation of metals in thin oxide films by X-ray photoelectron spectroscopy," *Journal of Analytical Chemistry,* **60,** 431-435 (2005).

18. S. Martínez-Méndez, Y. Henríquez, O. Domínguez, L. D'Ornelas, and H. Krentzien, "Catalytic properties of silica supported titanium, vanadium and niobium oxide nanoparticles towards the oxidation of saturated and unsaturated hydrocarbons," *Journal of Molecular Catalysis A: Chemical,* **252,** 226-234 (2006).

19. J. Marco, J. Ramón Gancedo, and F. J. Berry, "The oxidation states of titanium and niobium in compounds of composition $Sn_xNbTiP_3O_{12}$ ($0 < x < 0.50$) : an XPS study," *Polyhedron,* **16,** 2957-2961 (1997).

20. D. O. Klenov and S. Stemmer, "Contributions to the contrast in experimental high-angle annular dark-field images," *Ultramicroscopy,* **106,** 889-901 (2006).

21. K. Ishizuka, "Prospects of atomic resolution imaging with an aberration-corrected STEM," *Journal of electron microscopy,* **50,** 291-305 (2001).

22. W. D. Pyrz, D. A. Blom, T. Vogt, and D. J. Buttrey, "Direct imaging of the MoVTeNbO M1 phase using an aberration-corrected high-resolution scanning transmission electron microscope," *Angewandte Chemie-International Edition,* **47,** 2788-2791 (2008).

23. N. Pernicone, F. Lazzerin, G. Liberti, and G. Lanzavecchia, "On the mechanism of CH_3OH oxidation to CH_2O over $MoO_3/Fe_2(MoO_4)_3$ catalyst," *Journal of Catalysis,* **14,** 293-302 (1969).

24. C. J. Kiely, A. Burrows, G. J. Hutchings, K. E. Bere, J. C. Volta, A. Tuel, and M. Abon, "Structural transformation sequences occurring during the activation of vanadium phosphorus oxide catalysts," *Faraday Discussions,* **105,** 103-118 (1996).

25. L. F. Allard, G. A. Panjabi, S. N. Salvi, and B. C. Gates, "Imaging of nearly uniform Os5C clusters dispersed on MgO powder," *Nano Letters,* **2,** 381-384 (2002).

26. C. E. Kliewer, G. Kiss, and G. J. DeMartin, "Ex situ transmission electron microscopy: A fixed-bed reactor approach," *Microscopy and Microanalysis,* **12,** 135-144 (2006).

27. P. L. Gai and J. J. Calvino, "Electron microscopy in the catalysis of alkane oxidation, environmental control, and alternative energy sources," *Annual Review of Materials Research,* **35,** 465-504 (2005).

28. V. V. Guliants, S. A. Holmes, J. B. Benziger, P. Heaney, D. Yates, and I. E. Wachs, "In situ studies of atomic, nano- and macroscale order during $VOHPO_4 \cdot 0.5H_2O$ transformation to $(VO)_2P_2O_7$," *Journal of Molecular Catalysis A-Chemical,* **172,** 265-276 (2001).

29. C. Zhao and I. E. Wachs, "An Operando Raman, IR, and TPSR spectroscopic investigation of the selective oxidation of propylene to acrolein over a model supported vanadium oxide monolayer catalyst," *Journal of Physical Chemistry C,* **112,** 11363-11372 (2008).

30. F. Senf, F. Eggenstein, U. Flechsig, R. Follath, S. Hartlaub, H. Lammert, T. Noll, J. S. Schmidt, G. Reichardt, O. Schwarzkopf, M. Weiss, T. Zeschke, and W. Gudat, "Performance of the first undulator beamline U49-1-SGM at BESSY II," *Nuclear Instruments & Methods in Physics Research Section A-Accelerators Spectrometers Detectors and Associated Equipment,* **467,** 474-478 (2001).

31. E. Kleimenov, H. Bluhm, M. Havecker, A. Knop-Gericke, A. Pestryakov, D. Teschner, J. A. Lopez-Sanchez, J. K. Bartley, G. J. Hutchings, and R. Schlogl, "XPS investigations of VPO catalysts under reaction conditions," *Surface Science,* **575,** 181-188 (2005).

Chapter 7 Nanostructural and chemical characterization of iron molybdate (Fe-Mo-O) nanorod catalysts by Analytical Electron Microscopy

7.1 Introduction

In 1931 iron molybdate (Fe-Mo-O) was reported to be active and selective for the oxidation of methanol to formaldehyde,[1] and began to be employed as the preferred industrial catalyst for methanol oxidation in 1950's. The commercial Fe-Mo-O catalyst consists of two crystalline phases, namely $Fe_2(MoO_4)_3$ and MoO_3.[2,3] It has been suggested that the catalyst must contain both $Fe_2(MoO_4)_3$ and excess MoO_3 in order to maintain good catalytic activity, selectivity and achieve a long lifetime.[3] A more detailed literature review of the Fe-Mo-O catalysts for the oxidation of methanol to formaldehyde has been presented in Chapter 1, section 1.4.

In this work, a novel hydrothermal synthesis and impregnation technique were used to prepare iron molybdate nanorod catalysts that were subsequently assessed for the oxidation of methanol to formaldehyde. A wide variety of techniques including BET, XRD, Raman spectroscopy, SEM and TEM have been used to characterize the physical structure and chemical composition of the synthesized materials. The effects of varying the Mo/Fe atomic ratio and the calcination time on the structure, composition and catalytic performance of these Fe-Mo-O nanorod catalysts have been systemically investigated.

7.2 Experimental

7.2.1 Catalyst preparation and testing

Preparation of MoO_3 nanorods

MoO_3 nanorods were synthesized as reported in literature.[4] In a typical preparation procedure, 7.2 g of MoO_3 powder (Sigma Aldrich) and 55 ml of 30% H_2O_2 (Sigma Aldrich) aqueous solution were added into a 100 ml beaker and reacted under stirring at 30 ^oC to form the transparent orange-green peroxomolybdic acid solution. Then the solution was diluted with 2 mol/L nitric acid solution to keep its pH value between 0 and 1. The diluted peroxomolybdic acid solution was then transferred into a Teflon-lined stainless steel autoclave until it was 60-80% full. The autoclave was then sealed and maintained at 170-180^oC for 40 - 50 h in an electric oven. After cooling down to room temperature in ambient surroundings, the MoO_3 nanorods were collected and then filtered, washed and dried.

Preparation of $Fe_2(MoO_4)_3/MoO_3$ nanorod catalysts

The $Fe_2(MoO_4)_3/MoO_3$ materials were produced by impregnating an aqueous solution of iron nitrate onto the MoO_3 nanorods and then carrying out an appropriate heating process. The detailed preparation procedure is described as follows:- An appropriate amount of $Fe(NO_3)_3 \cdot 9H_2O$ aqueous solution was used according to the expected atomic ratio of Mo/Fe (6:1 to 1.6:1) in the final $Fe_2(MoO_4)_3/MoO_3$ catalyst. This was used to impregnate the desired amount of MoO_3 nanorod powder. The mixture obtained was kept at ambient temperature for 2h, and then dried at 60 ^oC under vacuum conditions overnight. Finally the material was calcined in air at the desired temperature

(*e.g.* between 400 °C and 500 °C) for a range of time periods. Two systematic sets of Fe-Mo-O catalysts were prepared, namely (i) an atomic ratio series and (ii) a calcination time series as summarized in Table 7.1.

Table 7.1 Fe-Mo-O samples produced in this project.

Atomic ratio series[a]		**Calcination time series**[b]	
Sample	Mo:Fe atomic ratio	Sample	Calcination time
FeMoO-ar1	6:1	FeMoO-ct1	3h
FeMoO-ar2	3.6:1	FeMoO-ct2	6h
FeMoO-ar3	2.2:1	FeMoO-ct3	12h
FeMoO-ar4	1.6:1	FeMoO-ct4	18h
		FeMoO-ct5	48h

[a]: Preparation conditions: calcination temperature = 500 °C, calcination time = 2h.
[b]: Preparation conditions: Mo:Fe atomic ratios = 2.2:1, calcination temperature = 400 °C.

Catalyst testing

The methanol oxidation experiments were carried out in a fixed-bed quartz tube reactor under atmospheric pressure as described in detail in sub-section 3.8.4.

7.2.2 Electron microscopy characterization

Scanning electron microscopy (SEM), bright field transmission electron microscopy (BF-TEM), selected area electron diffraction (SAED), high resolution transmission electron microscopy (HR-TEM), energy filtered transmission electron microscopy (EFTEM) and X-ray Energy-dispersive spectroscopy (XEDS) experiments were performed in this particular study. Experimental details for these characterization methods have been described in Chapter 3, section 3.6.

7.2.3 Complementary characterization techniques

Surface area measurements, XRD and Raman spectroscopy experiments were performed as described in Chapter 3, sub-sections 3.9.1, 3.9.2 and 3.9.4, respectively.

Crystalline phases were identified by matching the experimental patterns to the ICCD PDF database.

7.3 Results

7.3.1 Structural characterization of the bare MoO_3 nanorod support material

As shown in Figure 7.1, the as-synthesized uniform MoO_3 nanorods preferentially grow along the [010] direction (Fig. 7.1(c)(d)). The typical dimensions of these rectangular nanorods are 50 - 100 nm in thickness, 100 - 200 nm in width, and 8 - 10 μm in length (Figs. 7.1(a)(b)). SADP's taken from the nanorod are found to be the [100] projection of α-MoO_3 having the {001}-type termination facets and an [010] preferred growth direction. An XRD pattern from an as-synthesized MoO_3 nanorod sample is presented in Figure 7.1(e), which can be indexed to α-MoO_3 (PDF# 04-008-4311), in good agreement with the electron microscopy analysis. The intensities of the (200), (400) and (600) reflections are much stronger than those of the (110) and (021) peaks for MoO_3 nanorods, consistent with them having a strongly preferred [010] growth direction and {001}-type termination facets. The BET surface area of these as-synthesized MoO_3 nanorods was found to be 12.6 m^2/g.

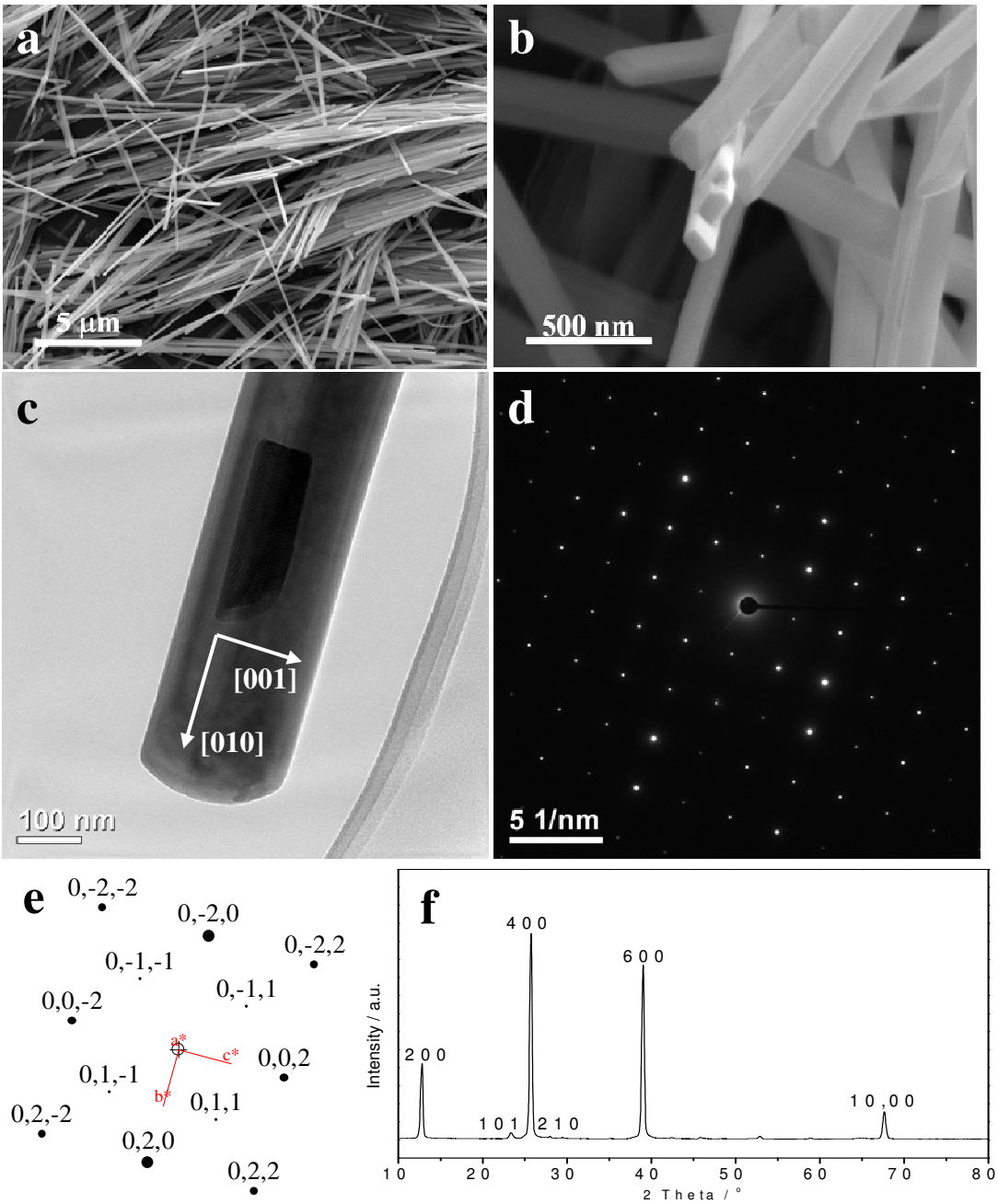

Figure 7.1 SEM micrographs of MoO_3 nanorods showing (a) a typical length of 8-10 µm and (b) a rectangular shape in cross section with a thickness of 50 - 100 nm and a width of 100 - 200 nm; (c) BF-TEM micrograph and (d) SADP of a nanorod with an [010] growth direction and {001}-type termination facets. The SADP corresponds to the [100] projection of MoO_3 (PDF# 04-008-4311); (e) the simulated and indexed SADP of the [100] projection of MoO_3 (PDF# 04-008-4311) and (f) An XRD pattern of the as-synthesized MoO_3 nanorods showing typical reflections of the α-MoO_3 phase (PDF# 04-008-4311).

7.3.2 Effect of changing Mo/Fe atomic ratio on the physical structure, chemical composition and catalytic performance of Fe-Mo-O catalysts

The catalytic performance of the systematic set of Fe-Mo-O nanorod materials with different Mo/Fe atomic ratios, as well as the pure MoO_3 nanorod material, for the oxidation methanol to formaldehyde are shown in Figure 7.2. The bare MoO_3 nanorod catalyst exhibits a lower formaldehyde yield within the 220 - 300 ^oC temperature range as compared with that of all the Fe-Mo-O nanorod materials produced. Within the 220 - 280 ^oC reaction temperature range, decreasing the Mo/Fe atomic ratio from 6:1 to 2.2:1 results in an increase of the formaldehyde yield. However decreasing the Mo/Fe atomic ratio further to 1.6:1 results in a decrease of the formaldehyde yield. Amongst all the catalysts tested, the one with Mo/Fe=2.2:1 shows the best catalytic performance in this 220 - 280 ^oC temperature range. As the reaction temperature is further increased up to 300 ^oC, the formaldehyde yield over the FeMoO-ar3 catalyst decreases slightly and all Fe-Mo-O catalysts showed a similar efficacy. This is probably because more CO is formed on the FeMoO-ar3 catalyst as compared with the other catalysts.

The BET surface areas of Fe-Mo-O nanorod catalysts generated with different Mo/Fe atomic ratios are listed in Table 7.2. In comparison with the bare MoO_3 nanorods (12.6 m^2/g), the surface areas of $Fe_2(MoO_4)_3/MoO_3$ materials are all lower, and lie between 5.2 and 7.7 m^2/g. The XRD patterns observed from these Fe-Mo-O nanorod catalysts (calcined at 500^oC for 2h) are shown in Figure 7.3. As the Mo/Fe atomic ratios decrease from 6:1 to 1.6:1 (*i.e.* corresponding to gradually increasing the amount of Fe in the preparation), the characteristic diffraction peaks of the $Fe_2(MoO_4)_3$ phase gradually intensify, whereas the intensity of the MoO_3 reflections progressively weakens. No

diffraction peaks corresponding to the crystalline Fe_2O_3 hematite phase were found in any of the catalyst samples.

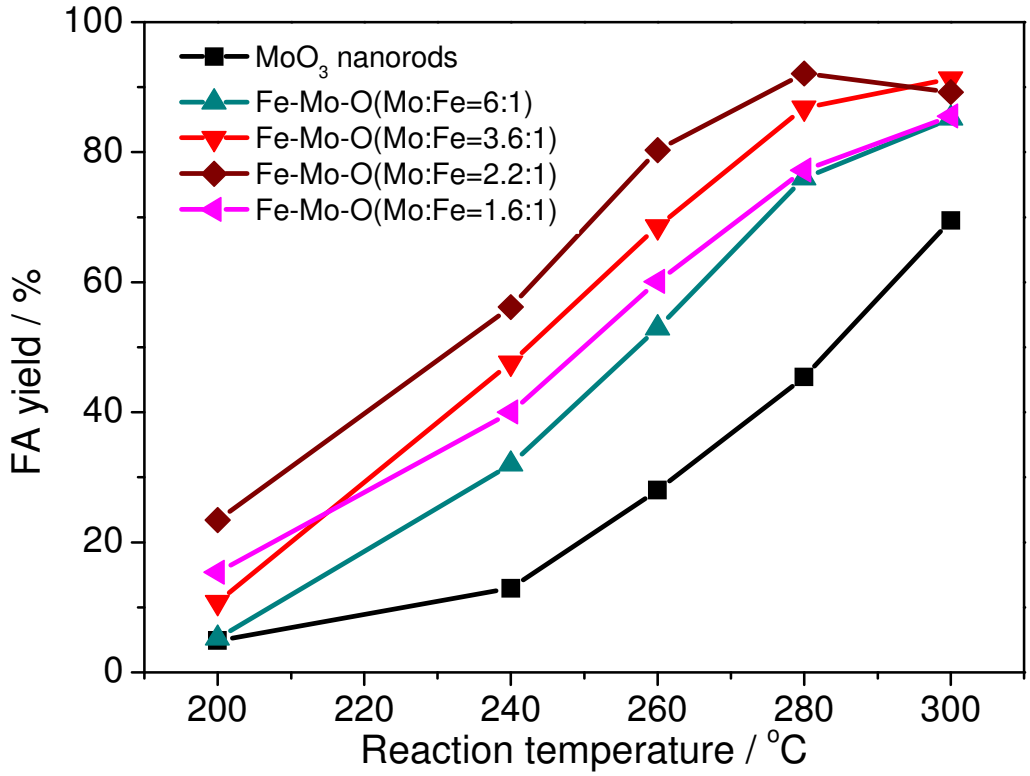

Figure 7.2 Catalytic performance of Fe-Mo-O materials prepared with different Mo:Fe ratios for the oxidation of methanol to formaldehyde. (Main by-products: CO, DME (di-methyl ether), MF (methyl formate)).

Table 7.2 BET surface areas of the Fe-Mo-O catalysts produced with different Mo:Fe atomic ratios.

Sample	**BET Surface area / $m^2.g^{-1}$**
MoO_3 nanorods	12.6
Fe-Mo-O (Mo:Fe = 6:1)	5.2
Fe-Mo-O (Mo:Fe = 3.6:1)	7.7
Fe-Mo-O (Mo:Fe = 2.2:1)	7.2
Fe-Mo-O (Mo:Fe = 1.6:1)	7.0

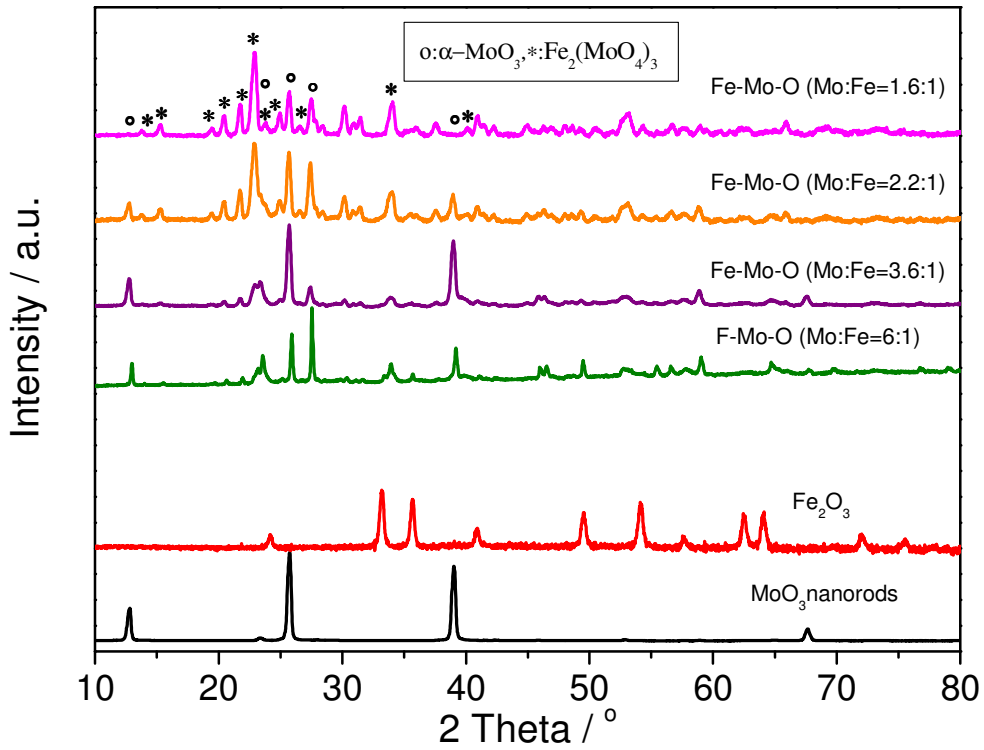

Figure 7.3 XRD patterns of the Fe-Mo-O materials prepared with different Mo:Fe ratios.

Figure 7.4 shows the Raman spectra acquired from the Fe-Mo-O nanorod catalysts prepared with different Mo/Fe atomic ratios. It shows a similar trend to that exhibited in the XRD data, namely that as the Mo/Fe ratio decreases from 6:1 to 1.6:1, the $Fe_2(MoO_4)_3$ Raman bands gradually intensify, while the MoO_3 Raman bands progressively weaken. Again absorption bands characteristic of the Fe_2O_3 phase were not detected in any of the catalyst samples.

The Raman spectra from the pure MoO_3 nanorods exhibit the expected sharp characteristic bands of crystalline MoO_3 at 997, 821, 666, 376, 336 and 284 cm^{-1}. The $Fe_2(MoO_4)_3$ phase generates Raman bands at 336, 784, 821, 937, 970 and 990 cm^{-1}. The bands at 937, 970, and 990 cm^{-1} correspond to the Mo=O symmetric stretches of the three distinct, isolated MoO_4 sites in bulk $Fe_2(MoO_4)_3$.[5] The Raman bands at 784 and 821cm^{-1}

are the associated asymmetric stretches, and the broader band at 336 cm^{-1} is the related bending mode of these species.[5] It should also be noted that the weak bands at ~ 990 and ~ 937 cm^{-1} are associated with the $Fe_2(MoO_4)_3$ phase and are not related to the MoO_3 phase. Because both $Fe_2(MoO_4)_3$ and MoO_3 possess a Raman vibration at ~ 821 cm^{-1}, the difference between these two phases is reflected only by the additional vibrations that are unique to MoO_3 (namely 997, 666 and 284 cm^{-1}).[6] For the Fe-Mo-O nanorod catalyst with excess MoO_3 (Mo/Fe= 2.2, 3.6, 6), the Raman bands of both crystalline $Fe_2(MoO_4)_3$ and MoO_3 are present. The data suggests that there is probably little or no residual MoO_3 phase present in the $Fe_2(MoO_4)_3/MoO_3$ catalyst produced with Mo/Fe=1.6:1.

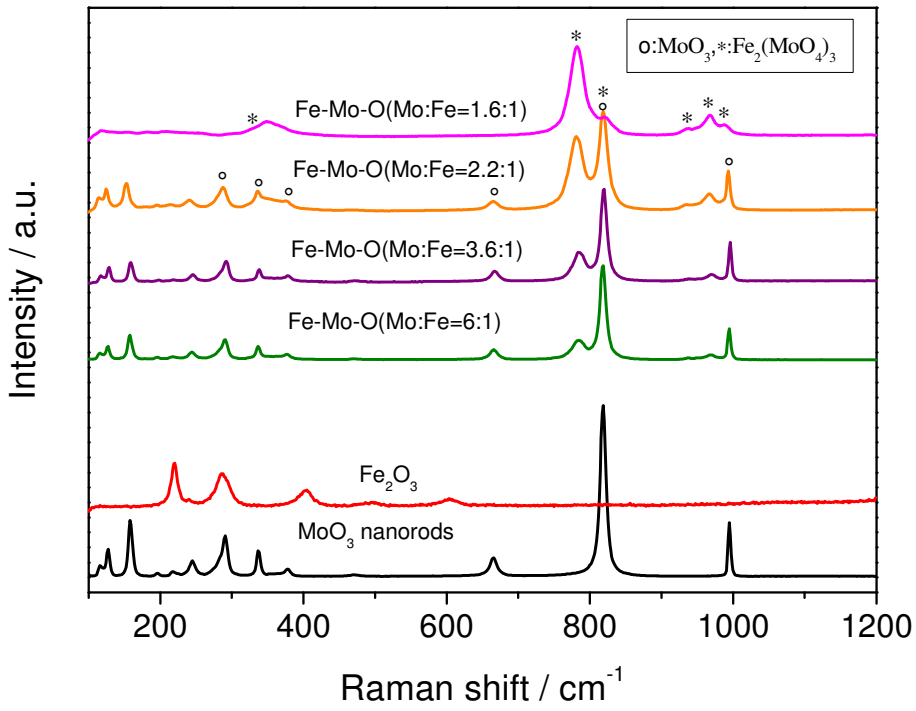

Figure 7.4 Raman spectra obtained from the Fe-Mo-O nanorod catalysts with different Mo/Fe atomic ratios. Pure Fe_2O_3 and MoO_3 nanorods are also shown as standard baseline materials.

Again absorption bands characteristic of the Fe_2O_3 phase were not detected in any of the catalyst samples. This implies that all the Fe_2O_3 has reacted with MoO_3 nanorods to form $Fe_2(MoO_4)_3$. It should be noted however that the weak Raman scattering may not be detectable for trace amounts of the dark residual Fe_2O_3 phase.

Figure 7.5 shows SEM micrographs of this set of Fe-Mo-O nanorod catalysts. When the amount of Fe is low (*i.e.* Mo:Fe= 6:1 or 3.6:1), the observed morphologies are very similar to that of the bare supports, showing MoO_3 nanorods with only a few scattered surface islands of size ranging between 20 and 100 nm as well as occasional abnormally large 200 nm particles (Figs. 7.5(a)(b)(c)(d)). As the amount of Fe is further increased to Mo/Fe=2.2:1 (Figs. 7.5(e)(f)), a significant number of larger islands with a size ranging between 50 and 100 nm appear on the surface of nanorods, which begins to look like a pretzel stick. When the amount of Fe is further increased up to Mo/Fe=1.6:1 (Figs. 7.5(g)(h)) that is close to the stoichiometric ratio 1.5:1 for pure $Fe_2(MoO_4)_3$, these surface islands tend to grow to a size larger than 100 nm. The island/nanorod morphology disappears, and these surface islands begin to coalesce. The size ranges of the surface islands for these Fe-Mo-O materials produced at different Mo:Fe atomic ratios are summarized in Table 7.3. It shows that the diameter of the surface islands increases with increasing Mo:Fe atomic ratio used in the preparation.

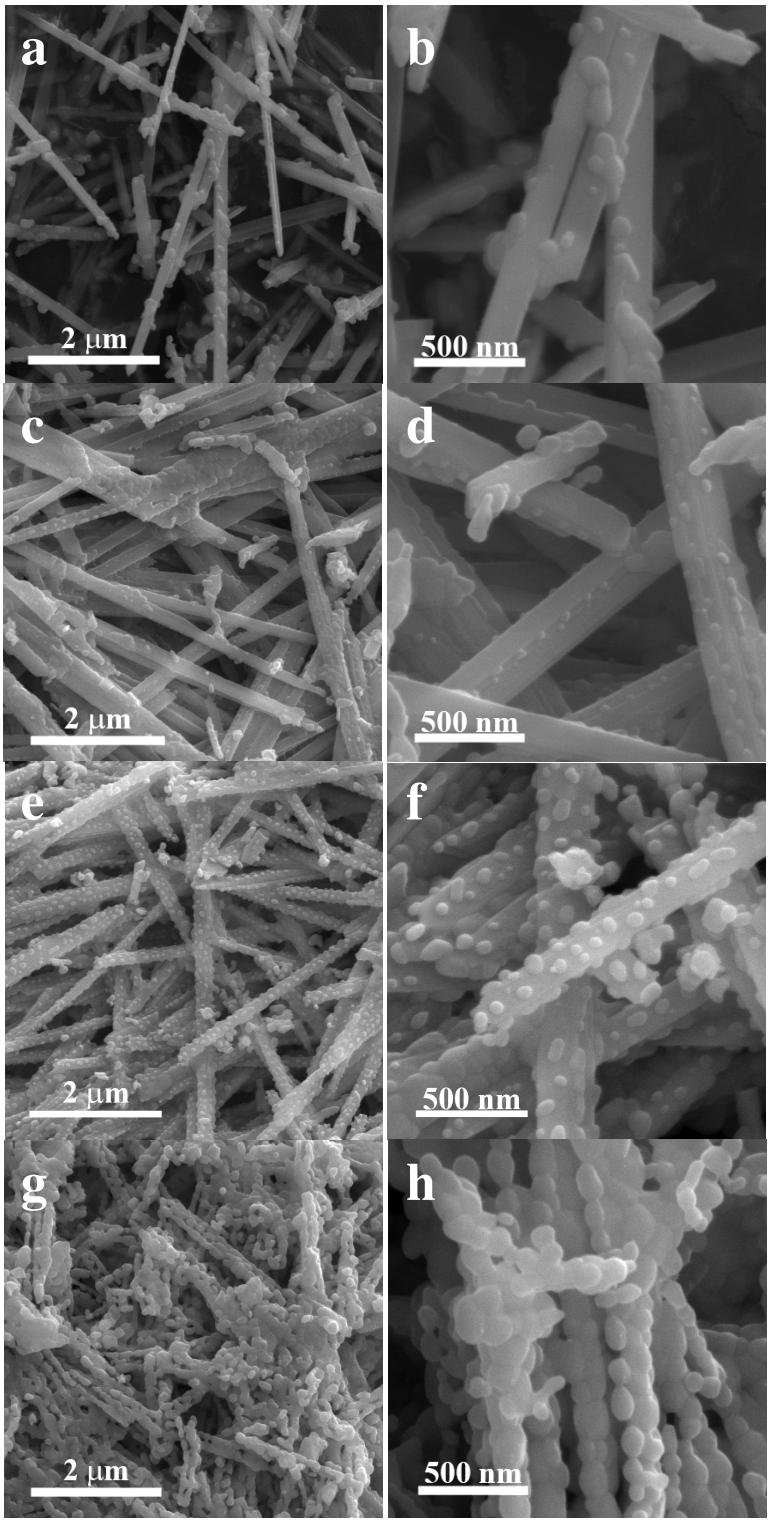

Figure 7.5 SEM micrographs of Fe-Mo-O materials prepared with different Mo/Fe ratios. A low magnification view and a higher magnification view are shown for (a,b) Mo:Fe = 6:1, (c,d) Mo:Fe = 3.6:1, (e,f) Mo:Fe = 2.2:1, (g,h) Mo:Fe = 1.6:1, respectively.

Table 7.3 Size ranges measured from SEM micrographs of the surface islands for these Fe-Mo-O materials produced at different Mo:Fe ratios.

Sample	Size range of surface islands / nm
Fe-Mo-O (Mo:Fe = 6:1)	20 - 100 nm
Fe-Mo-O (Mo:Fe = 3.6:1)	30 - 100 nm
Fe-Mo-O (Mo:Fe = 2.2:1)	50 - 100 nm
Fe-Mo-O (Mo:Fe = 1.6:1)	100 - 200 nm

Since the Fe-Mo-O catalyst prepared with a Mo:Fe atomic ratio of 2.2:1 (FeMoO-ar3) gives the best catalytic performance, our detailed transmission electron microscopy characterization was mainly focused on this particular material. BF-TEM micrographs of sample FeMoO-ar3 (Fig. 7.6(a)) shows a number of islands sitting on the nanorod surface with sizes ranging between 5 nm and 100 nm. These surface islands exist mainly on the {001}-type termination facets of the MoO_3 nanorod. An XEDS spectrum (Fig. 7.6(b)) taken from the large area incorporating an agglomerate of the nanorods exhibit major Mo L peak (at 2.293 keV) and Mo K peak (at 17.478 keV) that are mainly from the MoO_3 nanorods, and a minor Fe K peak (at 6.398 keV) that probably comes from the surface overlayer material. Higher magnification BF-TEM micrographs (Figs. 7.6(c)(d)) show that surface islands are mostly hemispherical, and three distinct micro-structural features within the nanorods, namely; (i) elongated internal voids in the MoO_3 nanorod with sizes ranging between 5 and 50 nm (#1 in Fig. 7.6(c)); (ii) a inwards concave interface between the surface island and the nanorod (#2 in Fig. 7.6(c)), and; (iii) distinct pits on the MoO_3 nanorod surface (#3 in Fig. 7.6(d)). These pits could potentially form because the surface islands were detached from the nanorod (inset, Fig. 7.6(a)), which leaves behind concave surface pits. The origin of these three micro-structural features will be discussed in detail

in sub-section 7.4.1. It should be noted that both the internal voids and the surface etch pits were not observed in the pure MoO_3 nanorods, which means that they were created during the calcination stage of the Fe-Mo-O materials.

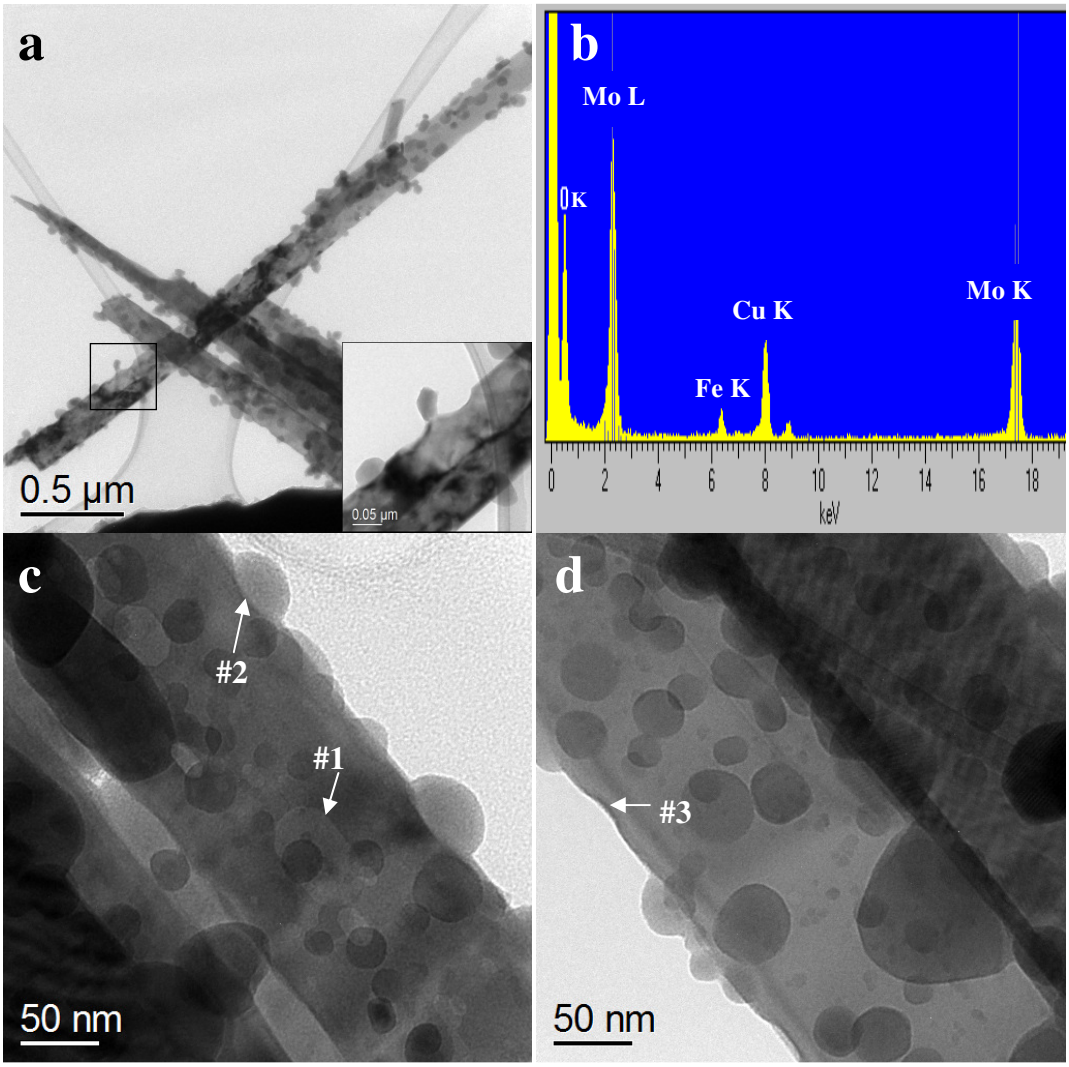

Figure 7.6 BF-TEM micrographs of FeMoO-ar3 catalyst showing (a) a typical island/nanorod morphology (inset, an enlargement of the square area delineated in (a) showing that surface island are beginning to be peeled off leaving a pit on the surface.); (c) elongated internal voids in the nanorod and (d) surface etch pits on the nanorod; (b) XEDS spectrum from the agglomerate presented in (a) showing Mo K, Mo L, Fe K and O K peaks. (Cu peaks are artifacts from the TEM copper grid.).

Figure 7.7(a) is a high magnification BF-TEM micrograph of an individual surface bump, which shows moiré fringes within the island. The HR-TEM technique

allows us to study the interfacial structure between the surface island the nanorod in more detail. An HR-TEM micrograph taken from the square area delineated in Figure 7.7(a) shows crossed fringes which correspond to the (112) and $(22\bar{2})$ lattice planes of the monoclinic $Fe_2(MoO_4)_3$ phase (PDF# 04-011-0402) with an intersection angle of 65° (Fig. 7.7(b1)). The crystalline MoO_3 nanorod shows weak crossed fringes which can be indexed to (010) and (001) lattice planes of the α-MoO_3 phase (Fig. 7.7(b2)). The weaker fringe contrast in the MoO_3 is probably due to the higher thickness of the nanorod in this region along being imaged. A careful comparison between these two FFTs (Figs. 7.7(b1) and (b2)) shows that there is a possible epitaxial relationship between the surface $Fe_2(MoO_4)_3$ island and the MoO_3 nanorod. The epitaxial relationship is as follows:- $[010]^{MoO_3}$ // $[\bar{1}\bar{1}4]^{Fe_2(MoO_4)_3}$ with a lattice spacing of 3.700 Å and 3.897 Å, respectively; and $[011]^{MoO_3}$ // $[112]^{Fe_2(MoO_4)_3}$ with a lattice spacing of 2.704 Å and 4.597 Å, respectively. A grain boundary region between the island and the nanorod is shown in Figure 7.7(c), but no obvious interfacial dislocations were detected. This could be due to the fact that the interface between the two are not flat but curved resulting in an overlap of two structures instead of a clear edge-on view. Such a curved interface could be formed during the solid-state reaction between the surface Fe species and the MoO_3 nanorod during calcination, which will be discussed in sub-section 7.4.1. It should be noted that the $Fe_2(MoO_4)_3$ phase is quite sensitive to the electron beam. An amorphous overlayer observed on the $Fe_2(MoO_4)_3$ island can be developed with increasing illumination time.

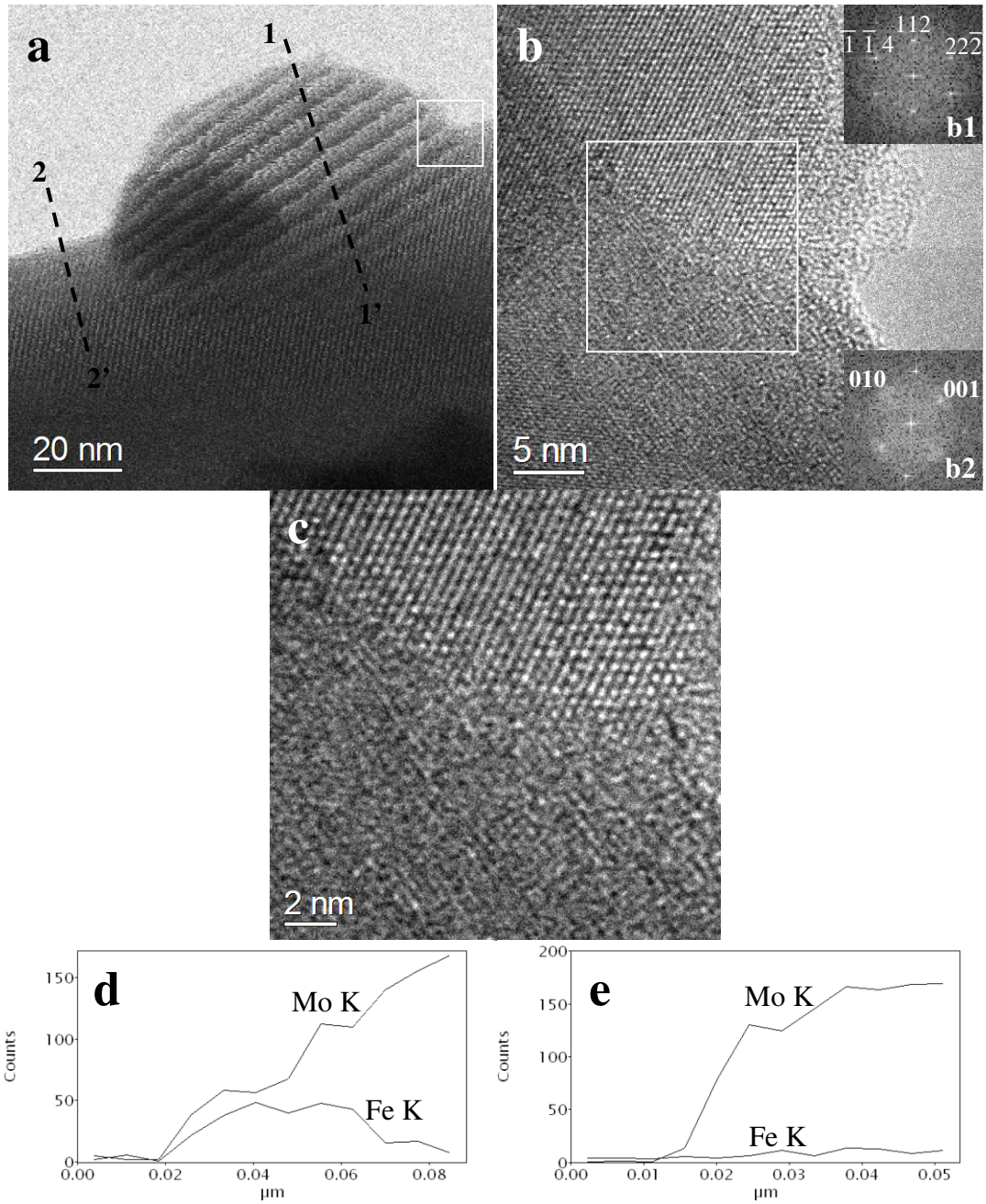

Figure 7.7 (a) BF-TEM micrograph of a surface island on the MoO_3 nanorod, (b) HR-TEM micrograph of the interfacial structure between the $Fe_2(MoO_4)_3$ island and the MoO_3 nanorod with no defect observed, (b1) FFT taken from the $Fe_2(MoO_4)_3$ island showing the (112) and $(22\bar{2})$ lattice planes of the $Fe_2(MoO_4)_3$ phase and (b2) FFT taken from the MoO_3 nanorod showing (010) and (001) lattice planes of the α-MoO_3 phase and (c) an enlargement of the interface showing a clear grain boundary; (d) XEDS line profile along 1-1' direction showing both Mo signals and Fe signals only when the electron probe is focused within the surface island and (e) XEDS line profile along the 2-2' direction showing that Mo signals are observed along this line whereas the Fe signals are absent (the step size is 4.4 nm).

STEM-XEDS line profile analysis was also performed to study the elemental distribution of Mo and Fe at the island/nanorod interface in the so-called "pretzel stick"-like material. One STEM-XEDS line profile is drawn along the 1-1' direction (Fig. 7.7(a)) which shows both Mo K signals and Fe K signals (Fig. 7.7(d)) only when the electron probe is focused within the surface island. This is expected since the HR-TEM analysis already convincingly shows these surface islands are $Fe_2(MoO_4)_3$. When another line is drawn along the 2-2' direction (Fig. 7.7(a)), Mo K signals are observed along the line whereas the Fe K signals are absent (Fig. 7.7(e)). This result indicates that Fe is not present on the terminated surface of MoO_3 nanorods away from the surface bump and these "pretzel stick"-like materials consist of MoO_3 nanorods with $Fe_2(MoO_4)_3$ islands on the surface. To strengthen this interpretation, EFTEM analysis has also been performed to map out the elemental distribution of Fe, Mo and O in these nanorod materials.

A typical island/nanorod morphology of the produced Fe-Mo-O material is shown in Figure 7.8(a) and its t/λ thickness map is displayed in Figure 7.8(b). It is normally required that the t/λ values are below unity in order for efficient collection of EELS spectra and reliable EFTEM analysis.[7] In this experiment, t/λ values in most of the area analyzed are indeed below 1, with the exception of the region at the center of the nanorod. This condition is acceptable, since the areas of interest are really the edge regions where the surface islands sit on the periphery of the nanorod. The O-K elemental map (Fig. 7.8(c)) shows that O is well dispersed in the nanorod and in the surface islands, which agrees with the fact that both are oxide phases. The Mo-$M_{4,5}$ elemental map (Fig. 7.8(d)) looks similar to the O-K elemental map in that the Mo signal is detected in both the nanorod and surface bumps. Some darker areas are also observed in the center of the

nanorod, which looks like Mo is not present. This is actually an artefact due to the increased thickness in the central part of the nanorod (Fig. 7.8(b) inset, where $t/\lambda > 1$) causing the blackout of the energy-loss signals from weak Mo-$M_{4,5}$ edges. The Fe-$L_{2,3}$ elemental map (Fig. 7.8(e)) shows a different feature from the other two elemental maps. Fe is only observed in the surface islands, which further suggests that the islands in these nanorod catalysts are indeed a mixed Fe-Mo-oxide.

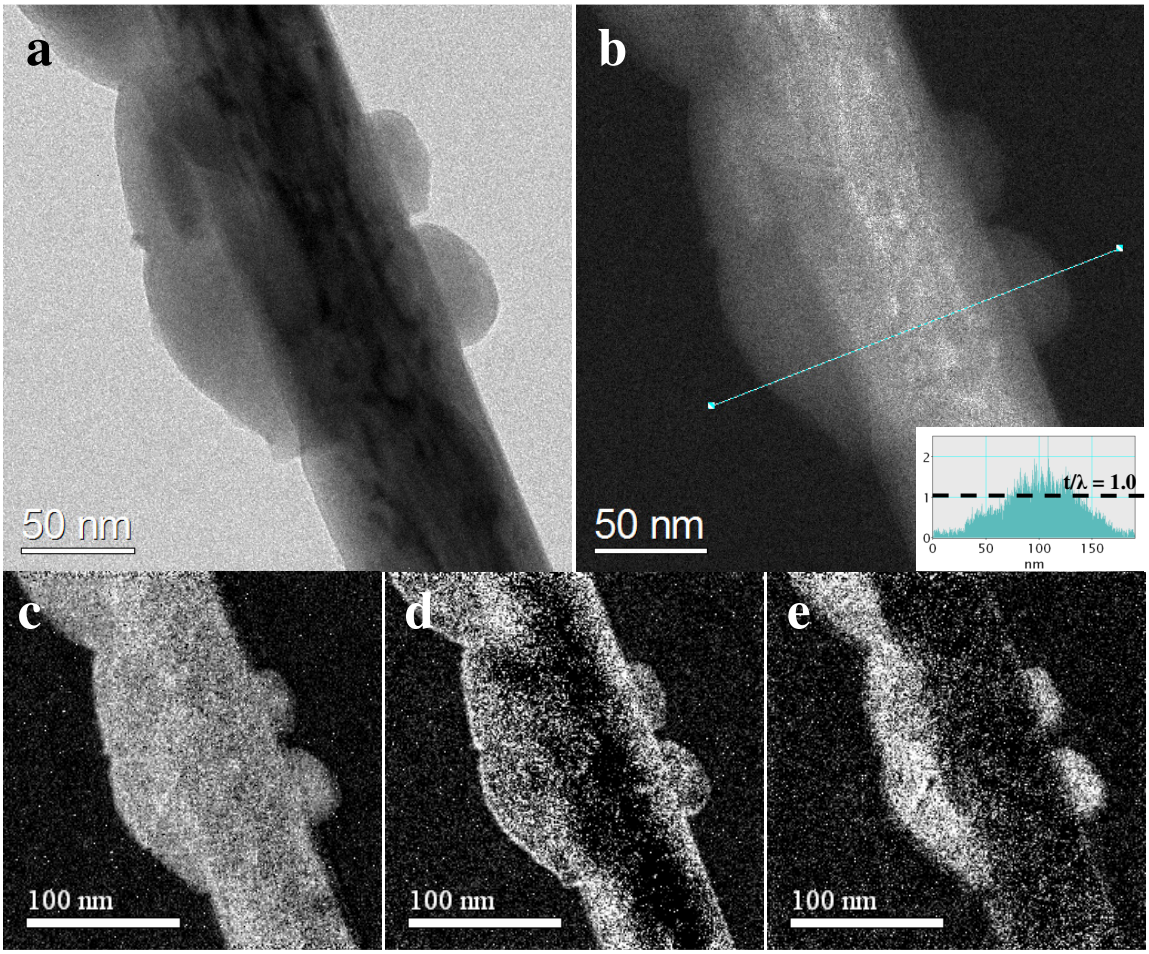

Figure 7.8 (a) BF-TEM micrograph of the FeMoO-ar3 nanorod catalyst with surface islands, (b) t/λ thickness map (inset, t/λ values along the line), (c) O-K elemental map, (d) Mo-$M_{4,5}$ elemental map and (d) Fe-$L_{2,3}$ elemental map.

The effect of the Mo/Fe atomic ratio on the produced $Fe_2(MoO_4)_3/MoO_3$ island/nanorod materials can be simply summarized as follows. With increasing amounts of Fe, more surface $Fe_2(MoO_4)_3$ islands are formed on the MoO_3 nanorods. Eventually for the larger Fe addition in the preparation stage, Fe-containing species react with MoO_3 nanorods, and form larger surface $Fe_2(MoO_4)_3$ islands which finally coalesce.

It should be noted that a small number of isolated smaller particles (~ 5 vol%) are also observed in all of these catalysts (Mo/Fe = 6:1 to 1.6:1). A typical example of this minor morphology is shown in Figure 7.9(a) having a particle size of around 100 nm. XEDS analysis (Fig. 7.9(b)) shows that they contain significant amounts of Fe, Mo and O. HR-TEM analysis from one of the smaller particles (Fig. 7.9(c)) shows that it is actually the $Fe_2(MoO_4)_3$ phase with (202) and (010) lattice planes resolved. This is supported by the simulated and indexed $[10\bar{1}]$ SADP (Fig. 7.9(d)) which shows good agreement with the experimental FFT (inset, Fig. 7.9(c)). Hence these smaller particles, which is a minor morphology compared to the nanorod materials, are also $Fe_2(MoO_4)_3$ materials. They could be formed from the reaction of Fe-containing species with small fragments of MoO_3 nanorods. One such potential MoO_3 fragment with about 100 nm in width and 400 nm in length is shown in Fig. 7.1(c), which is underlying the regular MoO_3 nanorod. Alternatively they could be the $Fe_2(MoO_4)_3$ materials that are detached from the surface of nanorod catalysts and coalesce during calcination.

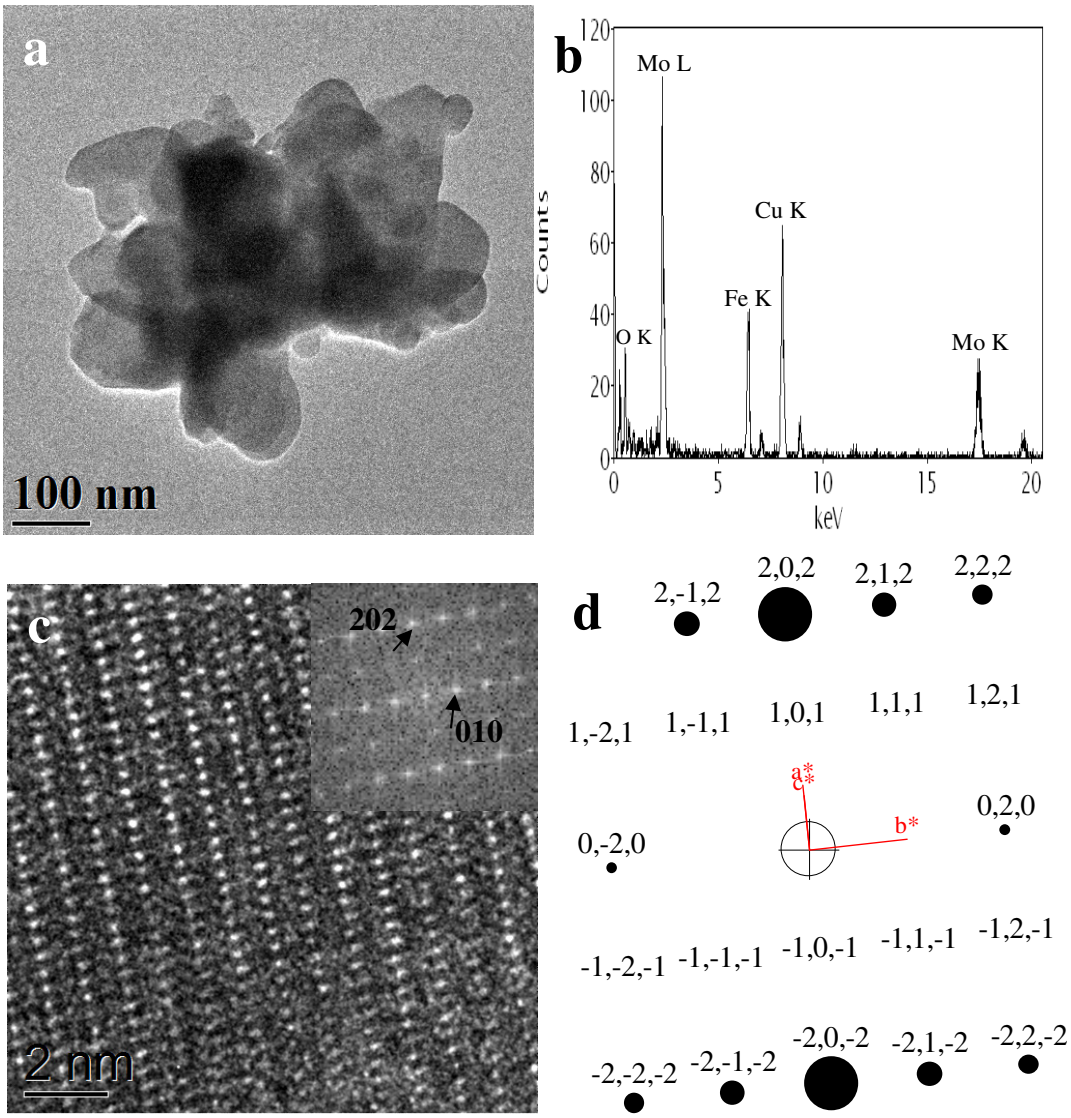

Figure 7.9 (a) BF-TEM micrograph of small particles rarely found in the nanorod catalysts, (b) XEDS spctrum taken from (a) showing Mo K, Fe K, Mo L and O K peaks, (c) HR-TEM micrograph of (a) showing (010) and (202) lattice fringes which correspond to the [10$\bar{1}$] projection of $Fe_2(MoO_4)_3$; and (d) the simulated and indexed SADP of the [10$\bar{1}$] projection of $Fe_2(MoO_4)_3$.

7.3.3 Effect of changing the calcination time on the structure, chemical composition and catalytic performance of Fe-Mo-O catalysts

The previous sub-section 7.3.2 has clearly demonstrated that these Fe-Mo-O nanorod catalysts are composite $Fe_2(MoO_4)_3/MoO_3$ island/nanorod materials, which have

a morphology analogous to that of a pretzel stick. In addition the Fe-Mo-O nanorod material produced with Mo/Fe atomic ratio = 2.2:1 gives rise to the best catalytic performance. In this sub-section, the effect of calcination time on the structure and performance of Fe-Mo-O nanorod catalysts is investigated. In this experiment the Mo/Fe atomic ratio was kept at 2.2:1 and the calcination temperature chosen was 400 ^{o}C.

Figure 7.10 shows the catalytic performance of $Fe_2(MoO_4)_3/MoO_3$ nano catalysts subjected to different calcination times for the oxidation of methanol to formaldehyde. When the reaction temperature is lower than 260 ^{o}C, the samples subjected to a shorter calcination time exhibited a higher formaldehyde yield. As the reaction temperature is increased up to 260^{o}C, all the samples show a similar formaldehyde yield. When the reaction temperature exceeded 300^{o}C, the samples subjected to longer calcination times (*i.e.* 48h) gave the highest formaldehyde yield. At 300^{o}C, the formaldehyde yield over catalysts with different calcination times showed the following trend: 48h > 18h > 12h > 6h > 3h, with corresponding formaldehyde yields of 94.7%, 93.0%, 89.1%, 88.0% and 79.1%, respectively. It is expected that longer calcination times will produce more of the active $Fe_2(MoO_4)_3$ phase which is beneficial for formaldehyde production.

The BET surface areas of the $Fe_2(MoO_4)_3/MoO_3$ catalysts calcined for different times are listed in Table 7.4. When compared with the pure MoO_3 nanorods, the surface areas of these nanorod catalysts become relatively lower and tend to range between 6.8 and 8.5 m^2/g after calcination for more than 6 h.

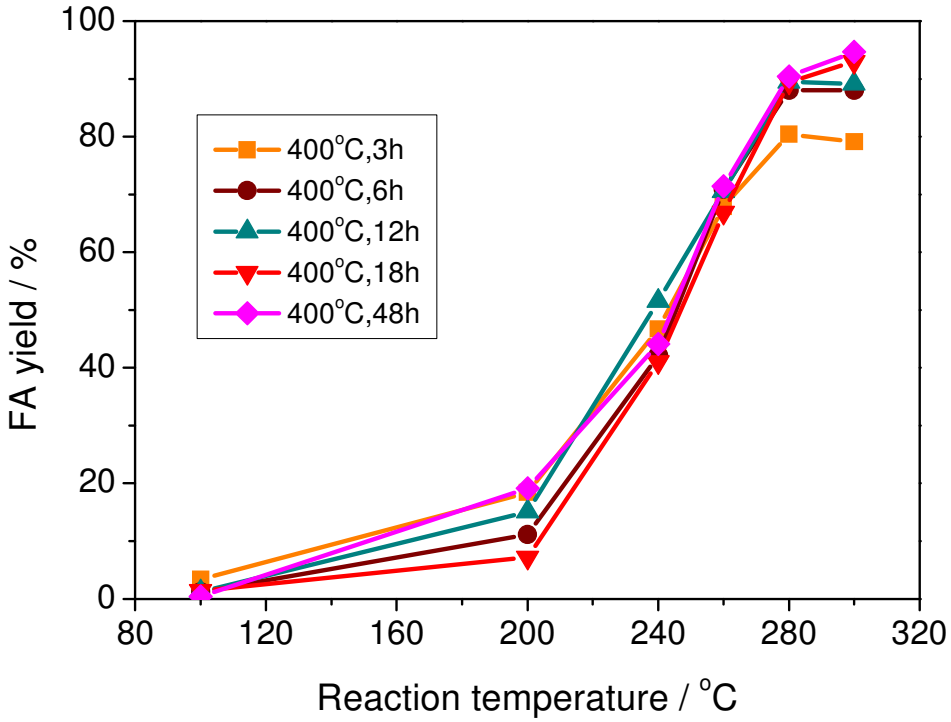

Figure 7.10 Catalytic performance of Fe-Mo-O materials prepared with different calcination times in selective oxidation of methanol to formaldehyde.

Table 7.4 BET surface areas of Fe-Mo-O catalysts calcined for different time periods at 400 °C.

Sample	BET surface area / $m^2.g^{-1}$
MoO_3 nanorods	12.6
FeMoO-ct1	12.5
FeMoO-ct2	8.5
FeMoO-ct3	7.1
FeMoO-ct4	6.8
FeMoO-ct5	7.2

XRD patterns obtained from Fe-Mo-O nanorod catalysts generated at different calcination times are shown in Figure 7.11. When samples were calcined at 400 °C, as the calcination time was prolonged, the diffraction peaks attributed to $Fe_2(MoO_4)_3$ gradually became sharper and more intense. Sample FeMoO-ct1, which was calcined for 3 h, showed only very weak diffraction peaks of $Fe_2(MoO_4)_3$. Surprisingly, no Fe_2O_3

diffraction peaks was found, which implies that the Fe-containing phase was initially dispersed in an amorphous state on the surface of the catalyst. As the calcination time was increased gradually up to 48 h, the $Fe_2(MoO_4)_3$ diffraction peaks become stronger, while the strongest MoO_3 (400) peak (at ~25.69°) still persists as compared to the reduced intensity of the (400) peak of MoO_3 observed in Figure 7.3 (Mo:Fe = 2.2:1, 500 °C, 2h). This indicates that the formation of $Fe_2(MoO_4)_3$ from the reaction of the Fe precursor and MoO_3 is not yet completed. An even longer calcination time at this lower calcination temperature may be needed in order to complete the transformation and improve the crystallinity of the $Fe_2(MoO_4)_3$ phase.

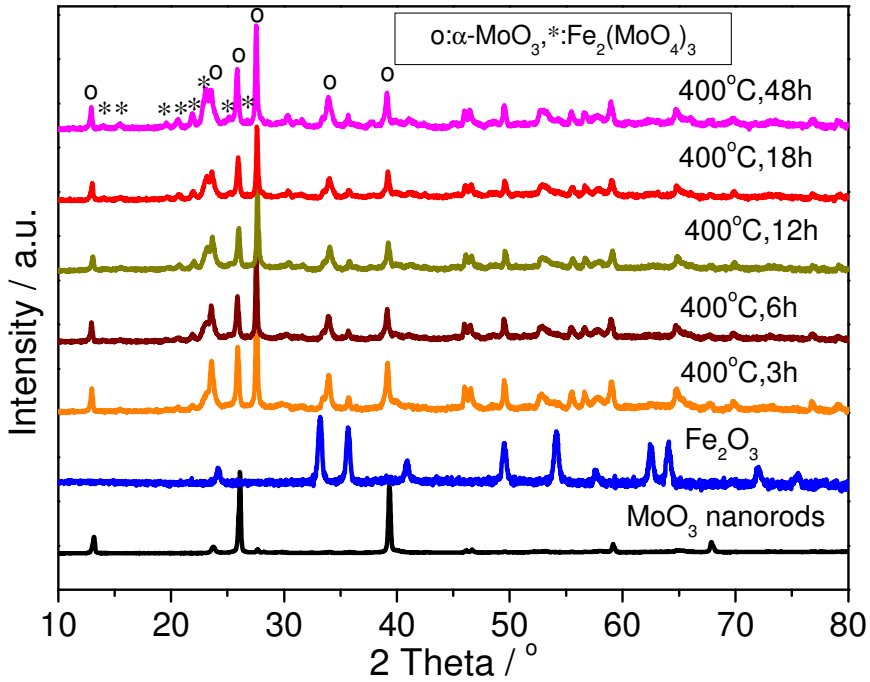

Figure 7.11 XRD patterns of Fe-Mo-O materials prepared with different calcination times at 400 °C.

As shown in Figure 7.12, when the sample was calcined at 400°C for increasing time periods, the Raman bands characteristic of the $Fe_2(MoO_4)_3$ phase gradually strengthen, while those corresponding to the MoO_3 phase weaken. This trend is similar to that found in the XRD patterns (Fig. 7.11). When the calcination time was 3h, weak absorption bands of $Fe_2(MoO_4)_3$ are noted. When calcined for 48h, strong absorption bands from $Fe_2(MoO_4)_3$ vibrations are developed. Compared with the corresponding Raman spectra of FeMoO-ar3 sample prepared at 500 °C (Mo:Fe = 2.2:1, Fig. 7.4), more intense bands of the MoO_3 phase and weaker bands of the $Fe_2(MoO_4)_3$ phase are detected after 48h calcination at 400°C. This is consistent with the XRD data indicating that even after 48h of calcination treatment at 400 °C, the surface $Fe_2(MoO_4)_3$ islands are still not completely transformed or well crystallized.

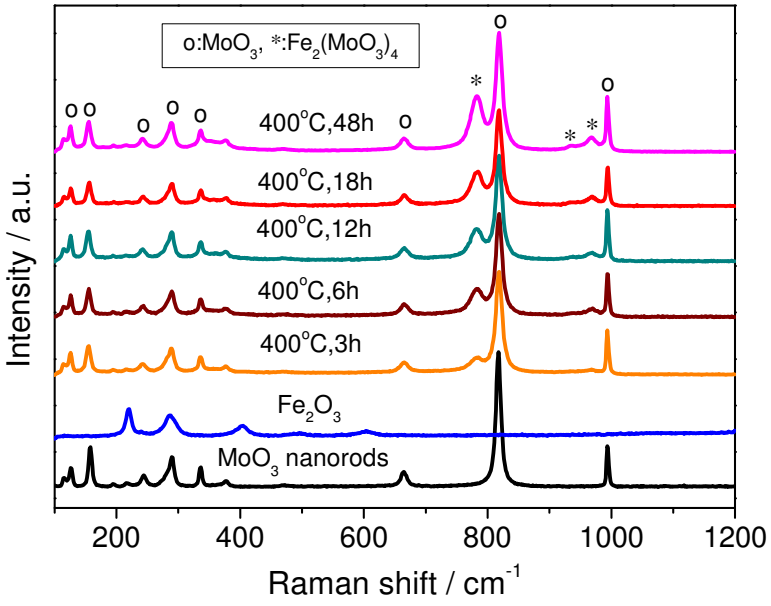

Figure 7.12 Raman spectra of $Fe_2(MoO_4)_3/MoO_3$ nanorod catalysts generated at different calcination times at 400 °C.

SEM micrographs of the Fe-Mo-O nanorod catalysts calcined at 400 ^{o}C for different time periods give a more intuitive view of microstructural development with time. As shown in Figure 7.13(a)(b)(c), when calcined at 400 ^{o}C for time periods less than 12 h, the MoO_3 nanorods are covered by semi-continuous thin films, which are probably Fe-containing species (*e.g.* Fe_2O_3, or FeOOH, or $Fe(OH)_2NO_3$, or a mixture of these compounds) from the thermal decomposition of $Fe(NO_3)_3 \cdot 9H_2O$.[8] As the calcination time is increased (eventually up to 48 h) these surface films gradually develop into surface islands on the nanorods. This also suggests that the surface Fe-containing species react with the nanorod surface to produce more crystalline $Fe_2(MoO_4)_3$ islands at longer calcination times, which is consistent with XRD and Raman data. However even after 48h calcination at 400 ^{o}C, the surface islands on the nanorod catalysts are not fully transformed, showing connected patches instead of the isolated islands that were observed in sample FeMoO-ar3 (Fig. 7.5(c)(f), 500 ^{o}C, 2 h).

It is highly probable that if these materials were calcined for an even longer time, *e.g.* 96 h, a similar morphology to that found in FeMoO-ar3 would develop. Therefore, for the lower calcination temperatures- 400^{o}C in this case, a longer calcination time is needed in order to produce completely transformed and/or well crystallized surface $Fe_2(MoO_4)_3$ islands.

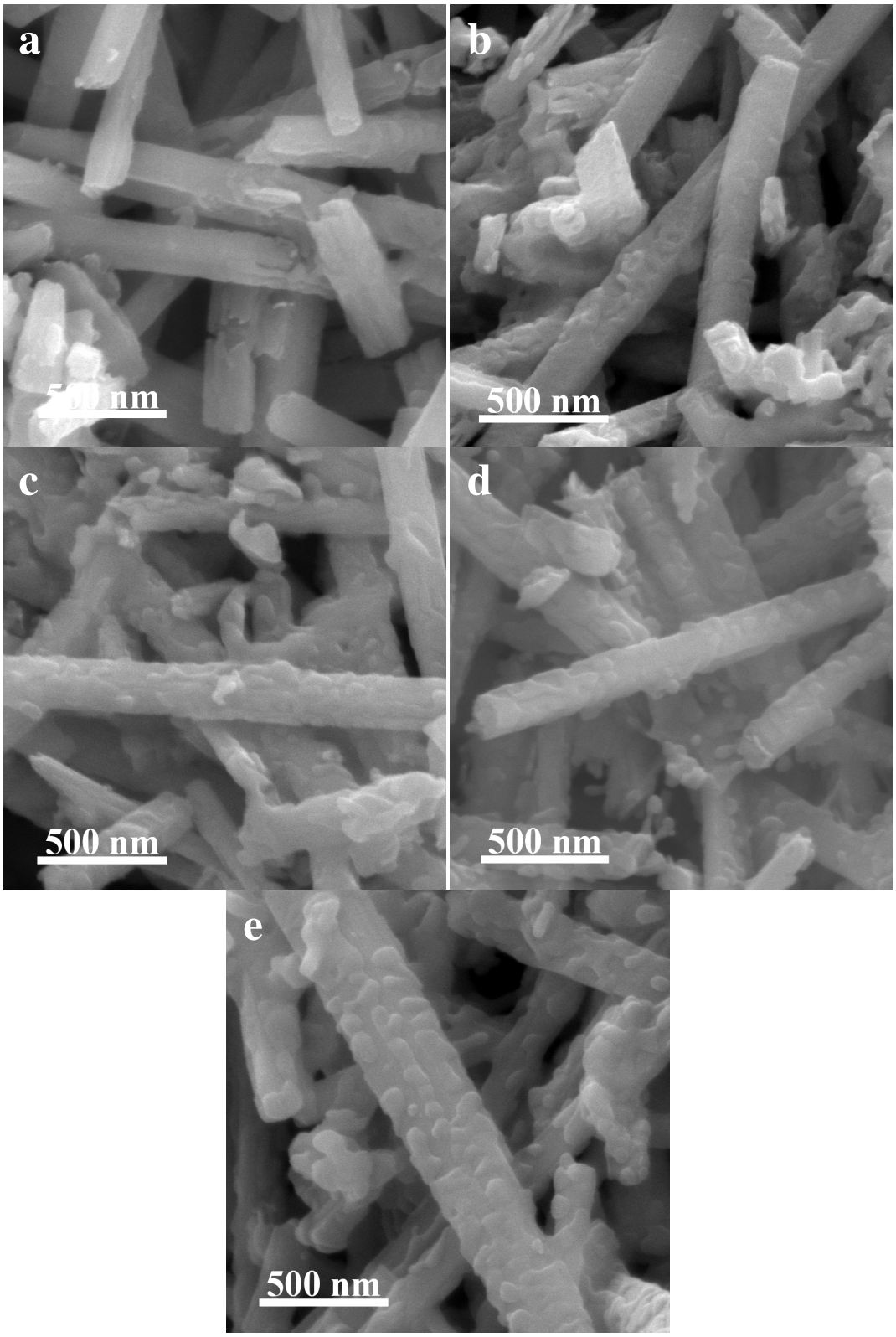

Figure 7.13 SEM micrographs of Fe-Mo-O materials prepared with different calcination times at 400 ^{o}C; (a) 3h, (b) 6h, (c) 12h, (d) 18h, (e) 48h.

In an attempt to identify the structure and composition of these semi-continuous thin films covering MoO_3 nanorods, detailed TEM analyses (Fig. 7.14) were performed on sample FeMoO-ct2, a material which was calcined for 6 h at 400^{o}C. As shown in the BF-TEM micrographs (Figs. 7.14(a)(b)), at the initial stages of calcination, a surface semi-continuous rough overlayer about 5 - 15 nm in thickness covers the whole nanorod. XEDS analysis (Fig. 7.14(c)) confirms that these films are Fe-containing compounds since a small Fe K peak at 6.398 keV was detected. The SADP (Fig. 7.14(d)) taken from a nanorod with overlayers (Fig. 7.14(b)) shows a major pattern which is close to the [100] projection of the α-MoO_3 phase, and a few extra spots that could arise from the rough overlayer. Both XRD patterns and Raman spectra of FeMoO-ct2 (400 ^{o}C, 6 h, Figs. 7.12 and 7.13) detected a small amount of crystalline $Fe_2(MoO_4)_3$ materials. Hence it is very tempting to assign some of these extra diffraction spots to the $Fe_2(MoO_4)_3$ phase. For example, the arrowed diffraction spot in Figure 7.14(d) can be tentatively assigned to be the $(32\bar{2})$ reflection of the $Fe_2(MoO_4)_3$ phase, which has an interplanar spacing of 3.46 Å.

An HR-TEM micrograph taken from the FeMoO-ct2 material is shown in Figure 7.15(b). An XEDS line profile (Fig. 7.15(c)) was acquired along the 3-3' path indicated on the Fe-Mo-O nanorod (Fig. 7.15(a)). Both Mo K and Fe K signals are detected along this line, which indicates that these semi-continuous thin films contain Fe. As can be seen from Figure 7.15(c) Fe K signal is not constant across the diameter of the nanorod, which indicates that this overlayer is not uniformly dispersed on the nanorod. This agrees with the micrograph in Figure 7.13(b), where a patchy overlayer coverage is shown. An HR-TEM image (7.15(b)) taken from the rim region of this particular nanorod shows an amorphous overlayer with a thickness of 3 - 5 nm, which would not be "visable" by the

XRD technique. It should be noted that although extreme care was taken, the possibility that some fraction of the amorphous layer was formed due to electron beam damage can not be entirely ruled out.

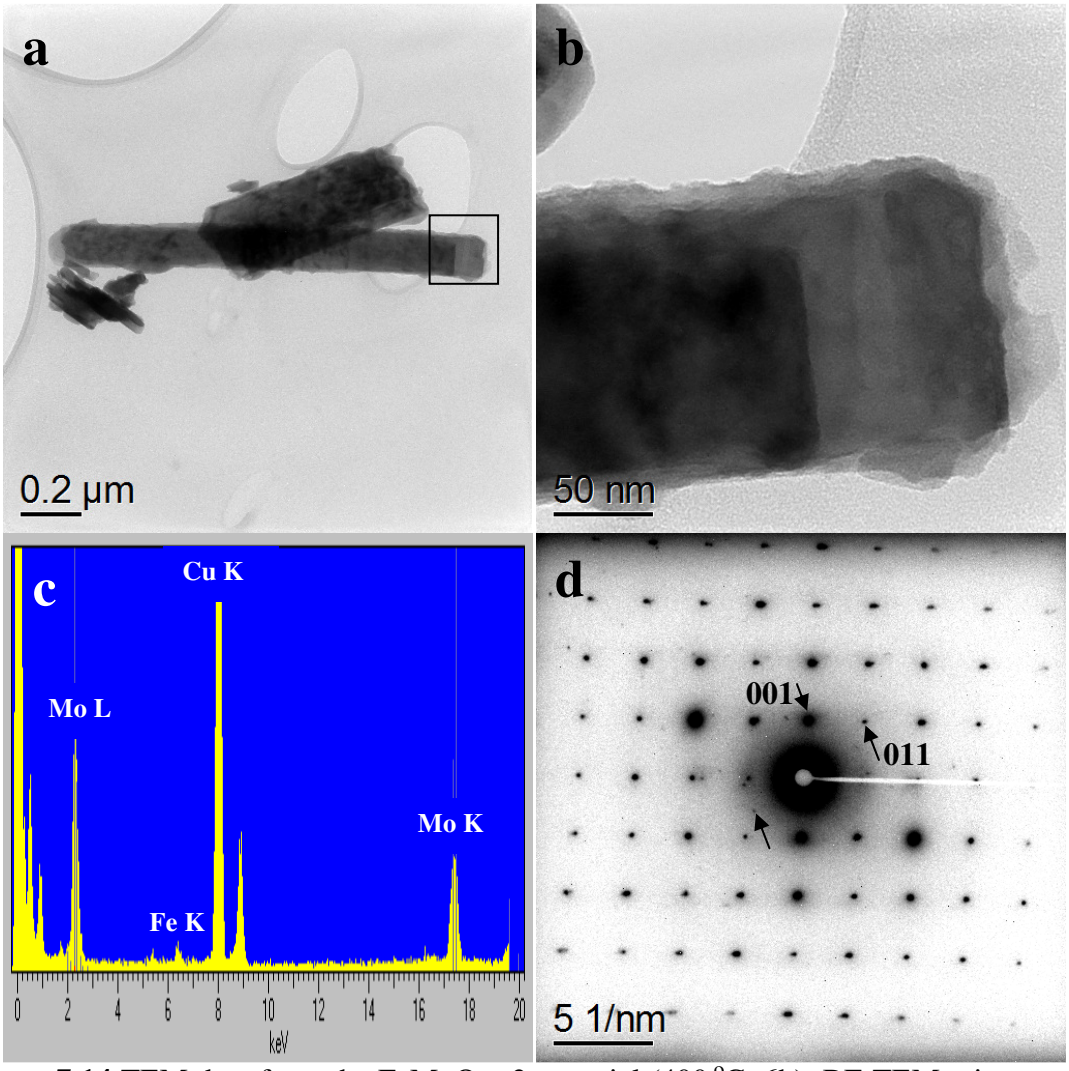

Figure 7.14 TEM data from the FeMoO-ct2 material (400 °C, 6h): BF-TEM micrographs of (a) Fe-Mo-O nanorods, (b) the enlargement of the squared area in (a) showing a semi-continuous rough overlayer covering the nanorod; (c) XEDS spectrum from (b) showing strong signals from Mo L and Mo K peaks, and weak signal from Fe L peak (Cu signals are artifacts from the TEM copper grid); and (d) SADP's from (b) exhibiting major patterns which is close to the [100] projection of α-MoO_3 and a minor spot (arrowed in (d)) that might be the $(32\bar{2})$ reflection of $Fe_2(MoO_4)_3$.

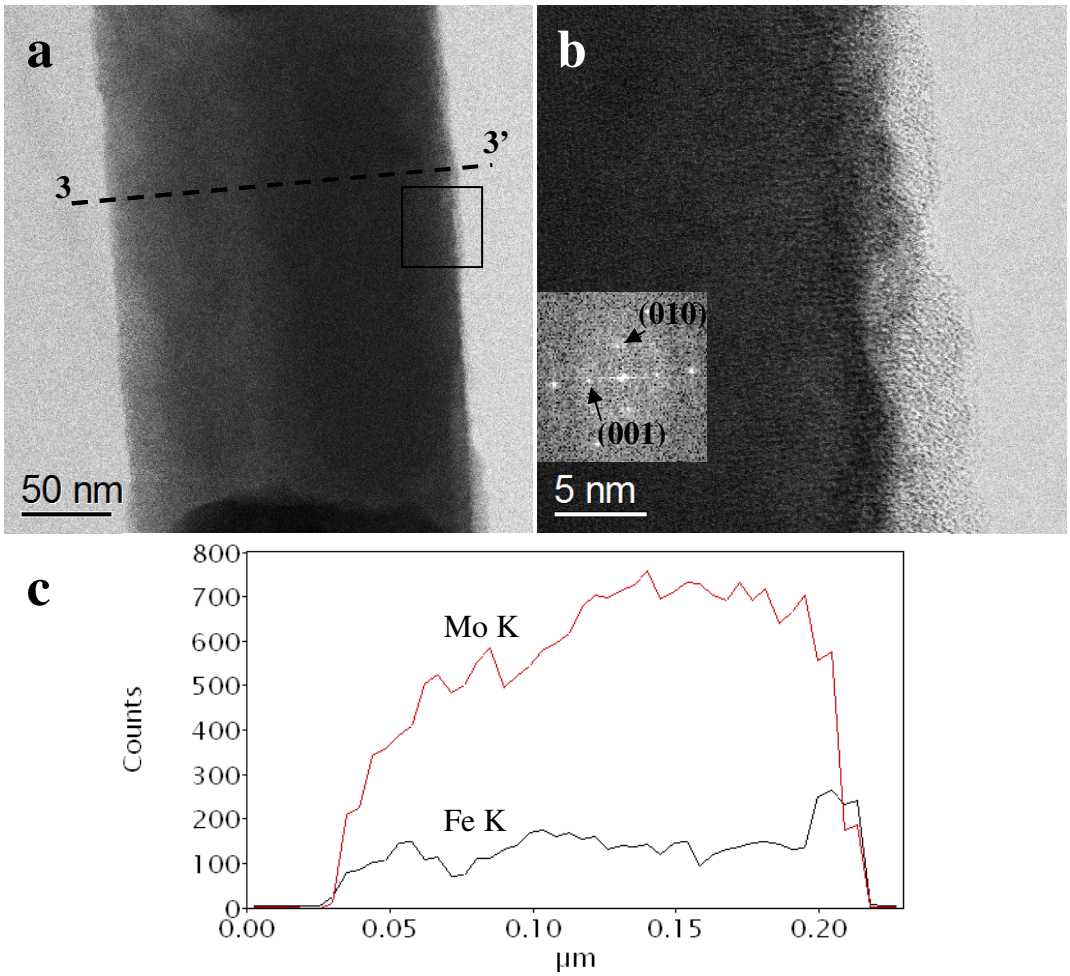

Figure 7.15 (a) BF-TEM micrograph of the sample FeMoO-ct2, (b) HR-TEM micrograph of the square area delineated in (a) showing the crystalline MoO_3 nanorod with an amorphous overlayer of 3-5 nm (inset, FFT from the nanorod showing (010) and (001) lattice planes of the MoO_3 phase) and (c) XEDS line profile taken along the 3-3' direction in (a) showing both Mo K signals and Fe K signals along the line (the step size is 4.6 nm).

From XRD patterns, Raman spectra and electron microscopy data, it can be concluded that the generation and the crystallinity of surface $Fe_2(MoO_4)_3$ materials increases with prolonged calcination time at 400 ^oC, leading to a corresponding improvement in the catalytic performance. The surface Fe-containing semi-continuous thin films exists in an amorphous state at the initial stages, and gradually react with the MoO_3 nanorods to form the crystalline $Fe_2(MoO_4)_3$ surface islands after prolonged

calcination at 400 °C. In addition, at a lower calcination temperature such as 400 °C, it takes much longer (> 48h) to generate fully transformed and well crystallized $Fe_2(MoO_4)_3$ islands.

7.3.4 Enhanced catalytic performance of the $Fe_2(MoO_4)_3/MoO_3$ nanorod catalyst compared to the standard iron molybdate catalyst

The standard iron molybdate (Fe-Mo-O) catalyst, which is structurally similar to the commercial catalyst, has a characteristic particle morphology with size ranging between 100 nm and 200 nm as shown in Figure 7.16(a)(b). SADP's acquired from an agglomerate of the standard Fe-Mo-O catalyst (Fig. 7.16(c)) exhibit characteristic the $(21\bar{2})$, $(40\bar{2})$, (024) and (420) diffraction rings expected of the $Fe_2(MoO_4)_3$ phase.

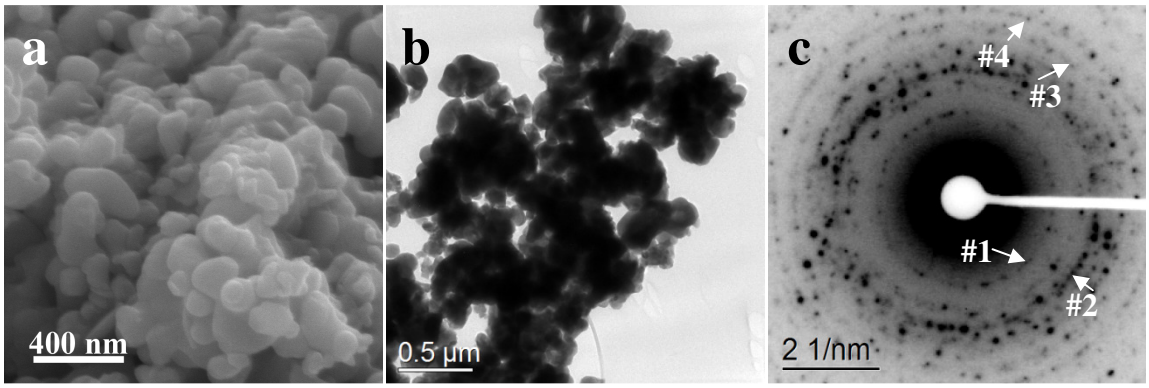

Figure 7.16 Standard Fe-Mo-O catalyst: (a) SEM and (b) BF-TEM micrographs showing smaller particles with size of 100 - 200 nm, and (c) SAED ring patterns of agglomerrates in (b) which can be indexed to the $Fe_2(MoO_4)_3$ phase (some characteristic rings are indexed as #1: $(21\bar{2})$, #2: $(40\bar{2})$, #3: (024) and #4: (420)).

Figure 7.17 shows a comparison of the catalytic performance between the Fe-Mo-O nanorod catalyst produced in this study (FeMoO-ar3) (which shows the better catalytic performance) and the standard Fe-Mo-O catalyst under the same reaction conditions. At the same reaction temperature, the conversion rate of methanol has increased by 5% to 15% over the nanorod catalyst when compared to that of the standard catalyst, while the

selectivity to formaldehyde has been maintained. The formaldehyde yield, can therefore in principle be increased by 5% to 15% depending on the reaction temperature chosen in the 240 and 280 °C range.

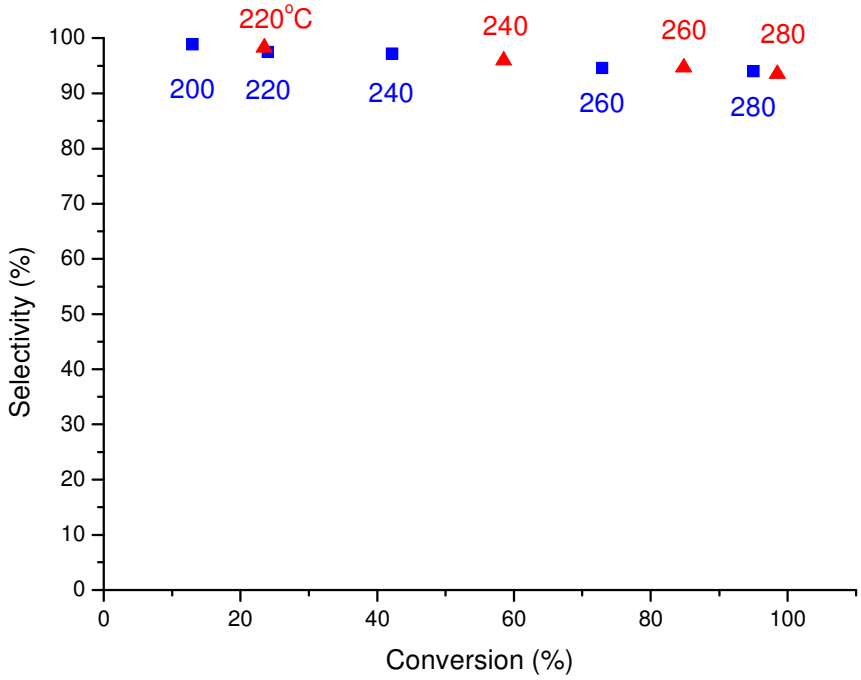

Figure 7.17 Comparison of the catalytic performance between our Fe-Mo-O nanorod catalyst (FeMoO-ar3) and the standard Fe-Mo-O catalyst at various reaction temperatures. Key: ■ standard catalyst, ▲ nano-rod catalyst.

7.4 Discussion

7.4.1 The formation mechanism of the $Fe_2(MoO_4)_3/MoO_3$ island/nanorod catalyst

In this study, the $Fe_2(MoO_4)_3/MoO_3$ "pretzel stick"-like nanorod catalysts were generated by reacting an Fe-containing precursor ($Fe(NO_3)_3{\cdot}9H_2O$) with pre-synthesized MoO_3 nanorods. It is well known that $Fe(NO_3)_3{\cdot}9H_2O$ can be decomposed into Fe-containing compounds, such as Fe_2O_3, FeOOH, or $Fe(OH)_2NO_3$ under thermal environment.[8] Hence the synthesis of the $Fe_2(MoO_4)_3$ surface island materials can be

rationalized in terms of a solid-state reaction occurring between the surface film containing Fe and the MoO_3 nanorod under the thermal environment encountered during calcination.

A similar synthesis strategy was first used by Wang *et al.*[9] to produce ferric molybdate nanotubes. In their experiments, they started from MoO_3 nanorods and then deposited $Fe(OH)_3$ onto the surface to form a core/shell $MoO_3/Fe(OH)_3$ nanorod. After heating in air, monoclinic ferric molybdate nanotubes with internal voids were generated via the Kirkendall effect. A schematic diagram illustrating the progress of this solid-state reaction sequence is shown in Figure 7.18. It should be noted that in their experiment, a thick Fe-containing precursor (*i.e.* $Fe(OH)_3$) shell, with thicknesses up to 40 nm was deposited onto the pre-synthesized MoO_3 nanorods.

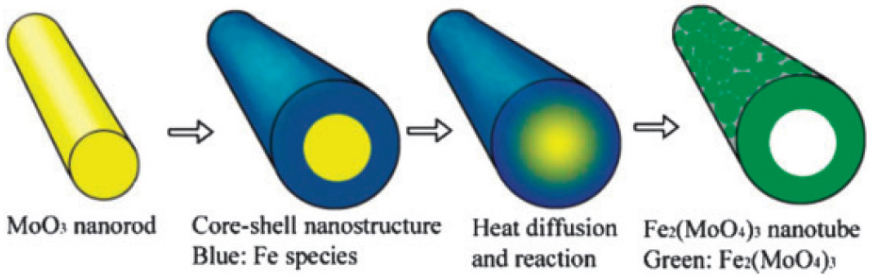

Figure 7.18 Schematic diagram showing the formation of Fe-Mo-O nanotubes by the solid-state reaction and the Kirkendall effect.[9]

However, in our study a much thinner Fe-containing film (≤ 15 nm) was deposited as shown in Figures 7.14(b) and 7.15(b). Hence after calcination, scattered surface particles are formed in our case, instead of the continuous porous shell as noted by Wang *et al.* when using a thicker Fe precursor shell. In our experiments most of the surface $Fe_2(MoO_4)_3$ islands are nearly hemispherical in nature, which indicates that the rounded surface could be a more thermally stable morphology for the $Fe_2(MoO_4)_3$

materials. This can be supported by the fact that the standard $Fe_2(MoO_4)_3$ materials are mostly rounded particles as observed by SEM and TEM (Fig. 7.16). The unique $Fe_2(MoO_4)_3/MoO_3$ island/nanorod morphology generated in our studies is probably formed following a solid-state diffusing reaction accompanied by the Kirkendall effect as described in several other studies.[10,11] It is well known that Fe-containing compounds can react with MoO_3 in the solid state to form $Fe_2(MoO_4)_3$.[3,9,12] The Kirkendall effect was first used to describe a classical phenomenon in metallurgy in which the boundary layer between two metals can move due to the difference in the diffusion rates of these two metals.[13] It is also one of the more widely accepted mechanisms invoked to explain porous nanorod formation via the reaction between two metal oxides[10,11,14]. In our experiment, surface Fe reacts with the MoO_3 nanorods to form surface $Fe_2(MoO_4)_3$ islands through two possible pathways, namely (i) the solid-state interdiffusion between the interfacial Mo (which is on the interface between MoO_3 and surface Fe) and Fe; and (ii) the solid-state interdiffusion between the internal Mo (which is originally away from the surface) and Fe.

The pathway (i) can be justified by the observation of an inwards concave interface (Fig. 7.6(c)- #2 and Fig. 7.19- #2) between the surface $Fe_2(MoO_4)_3$ islands and the MoO_3 main body. Since the interfacial Mo diffuses into the surface island at a much faster rate than that at which the external Fe diffuses into the nanorod, this results in the loss of Mo in these areas. Such Mo loss gives rise to an inwards concave morphology at the interface. In some areas, surface islands are peeled-off leaving behind concave "pits" on the surface (Fig. 7.6(d)- #3 and Fig. 7.19- #3), which supports that Mo diffuses faster and is removed from these areas of the MoO_3 nanorod. Interestingly, these surface "pits"

on MoO_3 nanorods are close to hemispherical, which means that the MoO_3 main body was trying to match with the spherical morphology of the surface $Fe_2(MoO_4)_3$ islands during calcination. Such a similar phenomenon was also observed by Posadas *et al.*[15] in the study of $TiSi_2$ islands on Si(001) facets. This curved interface morphology was attributed to the surface and interface energy minimization between the islands and the main body.

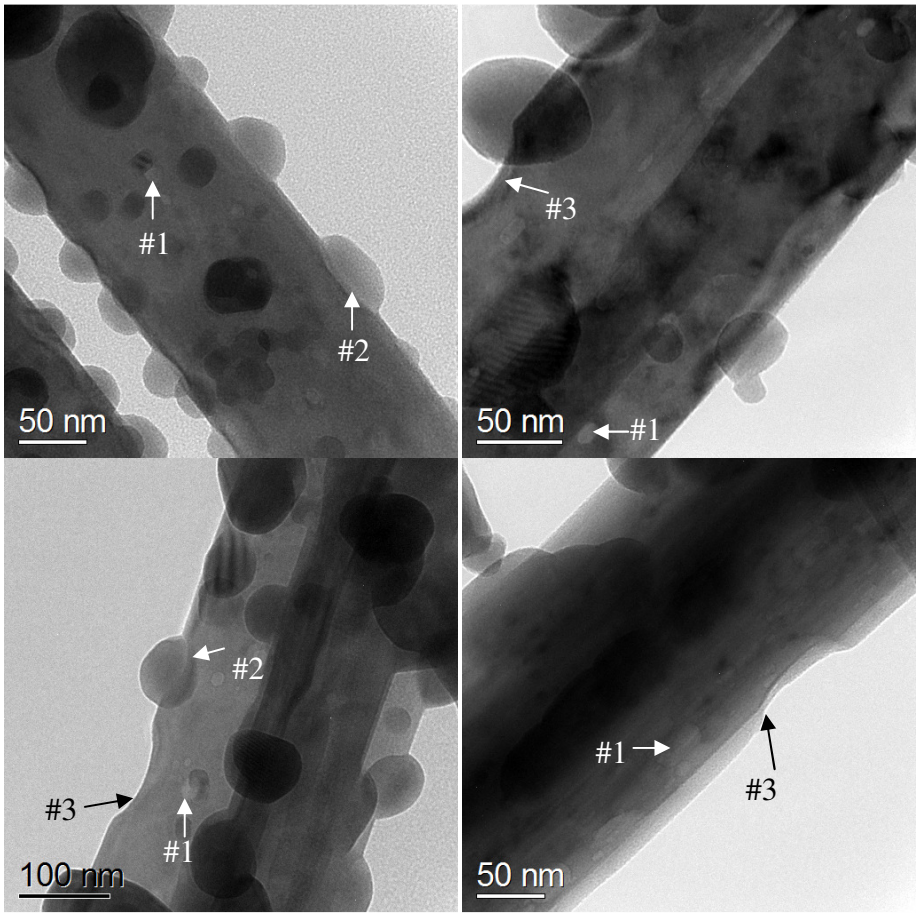

Figure 7.19 BF-TEM micrographs of $Fe_2(MoO_4)_3/MoO_3$ island/nanorod catalysts (FeMoO-ar3) observed in this experiment showing more examples of internal voids (labelled #1), concave interface (labelled #2) and surface pits (labelled #3).

Similarly in pathway (ii), internal Mo atoms originally away from the surface, diffuse to the surface at a much faster rate than that at which the surface Fe diffuses into the nanorod, which can leave internal voids within the nanorod (see Fig. 7.6- #1 and Fig. 7.19- #1). This phenomenon occurring as a result of interfacial solid-state reactions has been observed in many studies.[9-11,14] The formation of internal voids was attributed to a spatial confinement effect given by this 1D nanorod morphology. When the outward diffusion of Mo occurred, local areas having vacancy supersaturation are formed due to the spatial confinement, which then coalesce into an internal void.[9-11,14]

Hence from our observations the dominant formation mechanism for the $Fe_2(MoO_4)_3/MoO_3$ island/nanorod morphology follows the sequence:-

(i) An Fe-containing compound is deposited onto the surface of the nanorod;

(ii) During calcination at high temperature the surface Fe-containing film begins to react with underlying MoO_3 via interdiffusion to form $Fe_2(MoO_4)_3$ on the surface through a solid-state reaction;

(iii) Due to the Kirkendall effect, inwards concave interfaces and internal voids are formed with the MoO_3 and an $Fe_2(MoO_4)_3/MoO_3$ island/nanorod morphology is produced. A schematic diagram of the formation sequences observed in this study is shown in Figure 7.20.

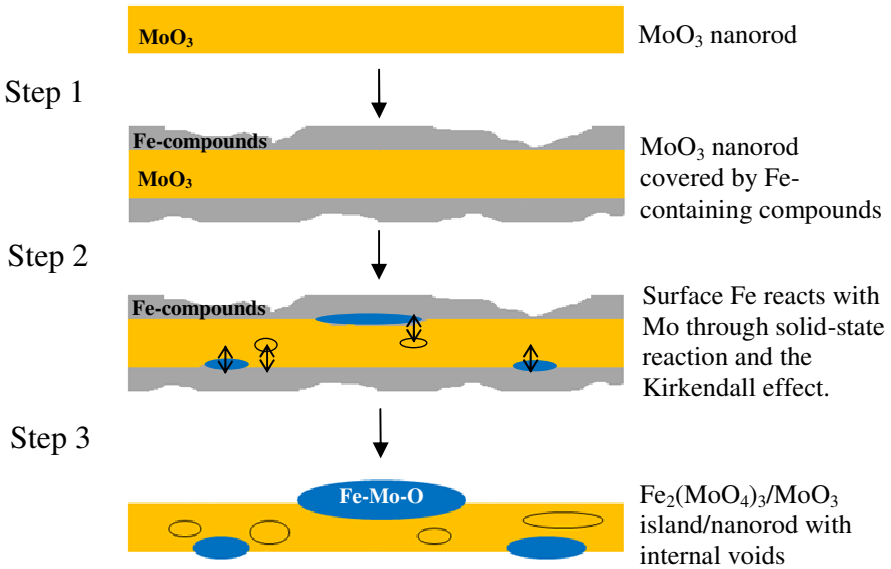

Figure 7.20 Schematic diagram depicting the formation mechanism of $Fe_2(MoO_4)_3/MoO_3$ island/nanorod catalysts through the solid-state reaction. (↕ represents the region where interdiffusion occurs between Mo and Fe; solid circles represent internal voids; yellow areas represent the MoO_3 nanorod; grey areas represent the surface Fe-containing compounds; and blue areas represent the $Fe_2(MoO_4)_3$ particles. In this diagram the relative thickness of Fe-containing compounds and the relative size of the internal voids and surface islands are exaggerated for clearer presentation, which are not in the real scale compared to the size of the MoO_3 nanorod.)

7.4.2 Possible reasons for the enhanced catalytic performance of $Fe_2(MoO_4)_3/MoO_3$ island/nanorod catalysts as compared to standard $Fe_2(MoO_4)_3$ catalysts

Most researchers believe that $Fe_2(MoO_4)_3$ is the active component of the catalyst[2,16,17] and that methanol oxidation on $Fe_2(MoO_4)_3$ follows a Mars-van-Krevelen mechanism.[18] In this mechanism lattice oxygen from the surface region of the $Fe_2(MoO_4)_3$ crystal is incorporated into the gaseous products during the reaction and leave behind vacancies. These O vacancies are then neutralized by gas-phase oxygen molecules. Alessandrini *et al.*[19] proposed that the stoichiometric $Fe_2(MoO_4)_3$ phase was the active phase. The excess Mo did not influence the specific activity of the catalyst, but

was necessary to prevent inactive iron-rich phases, such as the reduced $FeMoO_4$ phase, forming on the surface. Soares *et al.*[2] agreed that $Fe_2(MoO_4)_3$ was the active phase of the Fe-Mo-O catalyst. They proposed that excess Mo in the Fe-Mo-O catalyst could give rise to a higher selectivity to formaldehyde, which was attributed to the enhanced oxidization potential on the surface. In a recent review, Soares *et al.*[3] stated that this excess MoO_3 phase can act like a reservoir which provides mobile Mo species to regenerate the reduced surface of catalysts during the reaction. Using XEDS and XPS, the same authors[20] observed the migration of Mo from the bulk to the surface in a Mo rich Fe-Mo-O catalyst, which occurred in order to replenish the loss of surface Mo during methanol oxidation. Such a synergistic effect was also supported by Jacques *et al.*,[21] who used an ultra-rapid *in-situ* diffraction technique to analyze these materials under successive reducing (5% H_2/Ar) and oxidizing (5% O_2/Ar) environments. They found that the reduced β-$FeMoO_4$ phase can be quickly re-oxidized back to the $Fe_2(MoO_4)_3$ phase in the presence of MoO_3 as shown in eqn. 7.1.

$$2\ (\beta\text{-}FeMoO_4) + MoO_3 + \tfrac{1}{2}\ O_2 \rightarrow Fe_2(MoO_4)_3 \qquad (7.1)$$

However, some researchers attribute the enhanced catalytic performance of Fe-Mo-O catalysts with excess MoO_3 to the formation of a surface MoO_x monolayer on the $Fe_2(MoO_4)_3$ phase.[22] They believe that this surface MoO_x monolayer is the catalytically active phase. The excess crystalline MoO_3 in Fe-Mo-O catalysts is then only used to replace the surface MoO_x loss during the reaction. A more detailed literature review concerning the determination of the active sites in Fe-Mo-O catalysts for methanol oxidation can be found in Chapter 1, sub-section 1.4.4.

Obviously determining the active sites in the selective oxidation of methanol to formaldehyde over Fe-Mo-O catalysts is still a source of lively ongoing debate. In this work, the $Fe_2(MoO_4)_3/MoO_3$ island/nanorod catalyst with Mo/Fe=2.2:1 calcined at 500 °C for 2 h shows the best catalytic performance amongst all of the Fe-Mo-O catalysts produced. It achieved a formaldehyde yield of 92.1% at 280 °C. The synergistic effect between the surface $Fe_2(MoO_4)_3$ islands and MoO_3 nanorods is more likely to be the main factor for the enhanced catalytic performance. In this scenario, the MoO_3 reservoir is in close and very stable contact with the active $Fe_2(MoO_4)_3$ phase, and is always available to balance Mo losses through possible sublimation or surface diffusion during methanol oxidation. This unique and very stable island/nanorod morphology may simply provide a better synergistic effect since each single $Fe_2(MoO_4)_3$ island is connected separately to the underlying MoO_3 reservoir. It should be noted that none of techniques used in this study was sensitive enough to detect a MoO_x monolayer on the $Fe_2(MoO_4)_3$ phase. Hence it is plausible that a MoO_x monolayer may exist on the surface of $Fe_2(MoO_4)_3$ islands in our Fe-Mo-O catalysts, which would play a vital role in the oxidation of methanol.

7.5 Conclusions and suggestions for future work

Using an impregnation method to deposit materials onto pre-synthesized MoO_3 nanorods, a series of $Fe_2(MoO_4)_3/MoO_3$ island/nanorod catalysts were prepared having different Mo/Fe atomic ratios (from 6:1 to 1.6:1) and subjected to different calcination times (from 3h to 48h at 400 °C). The best Fe-Mo-O catalysts produced have a “pretzel stick”-like morphology with the MoO_3 nanorods as the main body of the pretzel and the $Fe_2(MoO_4)_3$ islands as the ‘salt grains’. This characteristic morphology develops via the

interaction between the surface Fe-containing precursor phase and the MoO_3 nanorod through the solid-state reaction coupled with the Kirkendall effect. The catalytic testing shows that the $Fe_2(MoO_4)_3/MoO_3$ island/nanorod catalyst generated with a Mo/Fe atomic ratio of 2.2:1 with a 2 h calcination time at 500 °C has the best catalytic performance, giving a formaldehyde yield of 92.1% at 280 °C. Its catalytic performance is comparable to that of the standard Fe-Mo-O catalyst and even slightly exceeds it in the 240 - 280 °C temperature range. Such an enhancement in catalytic performance may be due to a better and more stable synergistic effect provided by the unique island/nanorod morphology.

In this project two series of Fe-Mo-O materials, namely (i) an atomic ratio series and (ii) a calcination time series have been studied in some detail. In order to complete this systematic study, several more samples relating to calcination temperature series need to be studied. In this series, the calcination temperature can be adjusted from 550 to 800 °C. This would allow us to investigate the effect of the higher calcination temperature on the physical structure, chemical composition and catalytic performance of the produced catalysts. Since the identification of active sites of Fe-Mo-O catalysts for the methanol oxidation is still being hotly debated, additional techniques such as the temperature programmed reduction (TPR), *in-situ* optical spectroscopy (*e.g.* Raman and infrared) and surface analysis techniques (*e.g.* low-energy ion scattering (LEIS) and XPS) could be applied to these unique $Fe_2(MoO_4)_3/MoO_3$ island/nanorod catalysts. These potentially reveal the reaction mechanism and surface modifications occurring during the methanol oxidation reaction. It should be noted that in this project, all of the Fe-Mo-O materials studied by electron microscopy techniques were unused catalyst materials. More electron microscopy examination (*i.e.* SEM, TEM, HR-TEM and STEM) should be

performed on the "used" catalysts to investigate any micro-structural details that might change during the reaction, especially the surface structure and composition of these $Fe_2(MoO_4)_3$ islands. Ideally *in-situ* electron microscopy techniques could be used to study these materials at the atomic scale under typical reaction conditions. Only by combining the results from a variety of *in-situ* techniques, can a better understanding of the structure-performance relationships in these fascinating $Fe_2(MoO_4)_3/MoO_3$ island/nanorod catalysts be achieved.

7.6 Acknowledgements

In this study the Fe-Mo-O catalyst syntheses, BET surface area measurement, XRD experiments, Raman spectroscopy analysis and catalyst testing were performed by Dr. Guojie Jin from Shanghai Research Institute of Petrochemical Technology, and Dr. Zhongjie Lin, Dr. Nicholas F. Dummer, Dr. Jonathan K. Bartley and Dr. Stuart Taylor in Prof. Graham J. Hutchings's group at Cardiff University. Their various contributions to this work are much appreciated and gratefully acknowledged.

7.7 References

1. H. Adkins and W. R. Peterson, "The oxidation of methanol with air over iron, molybdenum, and iron-molybdenum oxides," *Journal of the American Chemical Society,* **53,** 1512-1520 (1931).

2. A. P. V. Soares, M. F. Portela, A. Kiennemann, L. Hilaire, and J. M. M. Millet, "Iron molybdate catalysts for methanol to formaldehyde oxidation: effects of Mo excess on catalytic behaviour," *Applied Catalysis A-General,* **206,** 221-229 (2001).

3. A. Soares and M. Portela, "Methanol selective oxidation to formaldehyde over iron-molybdate catalysts," *Catalysis Reviews-Science and Engineering,* **47,** 125-174 (2005).

4. L. Fang, Y. Shu, A. Wang, and T. Zhang, "Green synthesis and characterization of anisotropic uniform single-crystal alpha-MoO_3 nanostructures," *Journal of Physical Chemistry C,* **111,** 2401-2408 (2007).

5. B. Delmon and G. Froment, "Remote control of catalytic sites by spillover species: A chemical reaction engineering approach," *Catalysis Reviews-Science and Engineering,* **38,** 69-100 (1996).

6. E. Soderhjelm, M. P. House, N. Cruise, J. Holmberg, M. Bowker, J. Bovin, and A. Andersson, "On the synergy effect in MoO_3-$Fe_2(MoO_4)_3$ catalysts for methanol oxidation to formaldehyde," *Topics in Catalysis,* **50,** 145-155 (2008).

7. D. B. Williams and C. B. Carter, Transmission electron microscopy: a textbook for materials science (Springer, 2nd Edition, 2009).

8. K. Wieczorek-Ciurowa and A. J. Kozak, "The thermal decomposition of $Fe(NO_3)_3 \cdot 9H_2O$," *Journal of Thermal Analysis and Calorimetry,* **58,** 647-651 (1999).

9. L. Wang, B. Peng, X. Guo, W. Ding, and Y. Chen, "Ferric molybdate nanotubes synthesized based on the Kirkendall effect and their catalytic property for propene epoxidation by air," *Chemical Communications,* 1565-1567 (2009).

10. Y. D. Yin, R. M. Rioux, C. K. Erdonmez, S. Hughes, G. A. Somorjai, and A. P. Alivisatos, "Formation of hollow nanocrystals through the nanoscale Kirkendall effect," *Science,* **304,** 711-714 (2004).

11. Y. Yang, D. S. Kim, M. Knez, R. Scholz, A. Berger, E. Pippel, D. Hesse, U. Goesele, and M. Zacharias, "Influence of temperature on evolution of coaxial ZnO/Al_2O_3 one-dimensional heterostructures: From core-shell nanowires to spinel nanotubes and porous nanowires," *Journal of Physical Chemistry C,* **112,** 4068-4074 (2008).

12. R. R. Zakirov, B. I. Popov, and A. D. Tsyganov, "Mossbauer spectroscopic studies of interaction between iron(III) and molybdenum(VI) oxides," *Reaction Kinetics and Catalysis Letters,* **9,** 69-72 (1978).

13. A. D. Smigelskas and E. O. Kirkendall, "Zinc diffusion in alpha brass," *American Institute of Mining and Metallurgical Engineers,* **171,** 130-142 (1947).

14. H. J. Fan, M. Knez, R. Scholz, K. Nielsch, E. Pippel, D. Hesse, M. Zacharias, and U. Goesele, "Monocrystalline spinel nanotube fabrication based on the Kirkendall effect," *Nature Materials,* **5,** 627-631 (2006).

15. A. Posadas, R. Dargis, M. R. Choi, A. Slepko, A. A. Demkov, J. J. Kim, and D. J. Smith, "Formation of single-orientation epitaxial islands of $TiSi_2$ on Si(001) using Sr passivation," *Journal of Vacuum Science and Technology B,* **29,** 03C1311-03C1316 (2011).

16. M. Bowker, R. Holroyd, M. House, R. Bracey, C. Bamroongwongdee, M. Shannon, and A. Carley, "The selective oxidation of methanol on iron molybdate catalysts," *Topics in Catalysis,* **48,** 158-165 (2008).

17. A. Andersson, M. Hernelind, and O. Augustsson, "A study of the ageing and deactivation phenomena occurring during operation of an iron molybdate catalyst in formaldehyde production," *Catalysis Today,* **112,** 40-44 (2006).

18. N. Pernicone, F. Lazzerin, G. Liberti, and G. Lanzavecchia, "On the mechanism of CH_3OH oxidation to CH_2O over $MoO_3/Fe_2(MoO_4)_3$ catalyst," *Journal of Catalysis,* **14,** 293-302 (1969).

19. G. Alessandrini, L. Cairati, P. Forzatti, P. L. Villa, and F. Trifiro, "Chemical, structural and catalytic modifications of pure and doped iron (III) molybdate," *Journal of the Less-Common Metals,* **54,** 373-386 (1977).

20. A. P. V. Soares, M. F. Portela, A. Kiennemann, and L. Hilaire, "Mechanism of deactivation of iron-molybdate catalysts prepared by coprecipitation and sol–gel techniques in methanol to formaldehyde oxidation," *Chemical Engineering Science,* **58,** 1315-1322 (2003).

21. S. D. M. Jacques, O. Leynaud, D. Strusevich, A. M. Beale, G. Sankar, C. M. Martin, and P. Barnes, "Redox behavior of Fe-Mo-O catalysts studied by ultrarapid in situ diffraction," *Angewandte Chemie-International Edition,* **45,** 445-448 (2006).

22. K. Routray, W. Zhou, C. J. Kiely, W. Grünert, and I. E. Wachs, "Origin of the synergistic interaction between MoO_3 and iron molybdate for the selective oxidation of methanol to formaldehyde," *Journal of Catalysis,* **275,** 84-98 (2010).

Appendix I

Publications arising from this work

Journal Papers

W. Weng, R. Al Otaibi, J. K. Bartley, N. F. Dummer, G. J. Hutchings and C. J. Kiely, "Controlling vanadium phosphate catalyst precursor morphology by adding alkane solvents in the reduction step of $VOPO_4 \cdot 2H_2O$ to $VOHPO_4 \cdot 0.5H_2O$," *Journal of Materials Chemistry*, accepted (2011).

W. Weng, M. Davies, G. Whiting, B. Solsona, C. J. Kiely, A. F. Carley and S. H. Taylor, "Niobium phosphates as new highly selective catalysts for the oxidative dehydrogenation of ethane," *Physical Chemistry Chemical Physics,* accepted (2011).

Z. Lin, **W. Weng**, C. J. Kiely, N. F. Dummer, J. K. Bartley and G. J. Hutchings, "The synthesis of highly crystalline vanadium phosphate catalysts using a di-block copolymer as a structure directing agent," *Catalysis Today,* **157**, 211-216 (2010).

U. Sithamparappillai, J. L. Nuño, N.F. Dummer, **W. Weng**, C.J. Kiely, J.K. Bartley and G.J. Hutchings, "Effect on the structure and morphology of vanadium phosphates of the addition of alkanes during the alcohol reduction of $VOPO_4 \cdot 2H_2O$," *Journal of Materials Chemistry*, **20**, 5310-5318 (2010).

R. Al Otaibi, **W. Weng**, J. K. Bartley, N. F. Dummer, C. J. Kiely and G. J. Hutchings, "Vanadium phosphate oxide seeds and their influence on the formation of vanadium phosphate catalyst precursors," *ChemCatChem*, **2**, 443-452 (2010).

N. F. Dummer, **W. Weng**, C. Kiely, A. F. Carley, J. K. Bartley, C. J. Kiely and G. J. Hutchings, "Structural evolution and catalytic performance of DuPont V-P-O/SiO_2 materials designed for fluidized bed applications," *Applied Catalysis A: General*, **376**, 47-55 (2010).

Conference presentations and extended abstracts (selected)

W. Weng, M. Davies, B. Solsona, S. H. Taylor and C. J. Kiely, "Structural Characterization of Niobium Phosphate Catalysts used for the Oxidative Dehydrogenation of Ethane to Ethylene," *Microscopy and Microanalysis,* **17**, 1738-1739 (2011).

W. Weng, R. Al Otaibi, N. F. Dummer, J. K. Bartley, G. J. Hutchings and C. J. Kiely, "Electron microscopy studies of V-P-O catalyst precursors: defining the dihydrate to hemihydrate phase transformation," *Microscopy and Microanalysis,* **16**, 1198-1199 (2010).

W. Weng, N. F. Dummer, C. Kiely, A. F. Carley, J. K. Bartley, G. J. Hutchings and C. J. Kiely, "Evaluation and structural characterization of DuPont V-P-O/SiO_2 catalysts," *Microscopy and Microanalysis,* **15**, 1412-1413 (2009).

W. Weng, Z. Lin, N. F. Dummer, J. K. Bartley, G. J. Hutchings and C. J. Kiely, "Structural characterization of vanadium phosphate catalysts prepared using a di-block copolymer template," *Microscopy and Microanalysis,* **15**, 1438-1439 (2009).

Vita

Weihao Weng was born in Nanjing, Jiangsu, China on October 16th, 1983, the son of Guoheng Weng and Lifang Jiang. After completing his study in Nanjing No.9 Middle School in 2001, he attended Nanjing University of Technology in Nanjing, China, for undergraduate study. He graduated from Nanjing University of Technology in July, 2005, with the degree of Bachelor of Engineering in Polymer Science and Engineering. In July of 2007, he received the degree of Master of Engineering from Zhejiang University in Hangzhou, China, under the supervision of Dr. Wenjian Weng. He then started his PhD studies in the Department of Materials Science and Engineering at Lehigh University in August of 2007. Under the supervision of Dr. Christopher Kiely, he has been working on the electron microscopy studies of complex oxide catalysts since 2007, which comprises this thesis. After graduation he will begin work as an Engineer/Scientist at International Business Machines (IBM) in Hopewell Junction, NY in October.